Fakultät für Mathematik, Informatik und Naturwissenschaften | RWTH AACHEN UNIVERSITY

Nature-Inspired Biomaterials for Infection Management:

From Interactive Coatings to Phagocytic Synthetic Cells

Von der Fakultät für Mathematik, Informatik und Naturwissenschaften der RWTH Aachen University zur Erlangung des akademischen Grades einer Doktorin der Naturwissenschaften genehmigte Dissertation

vorgelegt von

Master of Science

Rosario Manuela Garay Sarmiento

aus Lima, Peru

Berichter: Prof. Dr. Ulrich Schwaneberg

Prof. Dr. César Rodriguez-Emmenegger

Tag der mündlichen Prüfung: 10.06.2024

To my parents,

Luz and Edvin.

I hereby declare that I have created this work completely on my own and used no other sources or tools than the ones listed, and that I have marked any citations accordingly.

Hiermit versichere ich, dass ich die vorliegende Arbeit selbstständig verfasst und keine anderen als die angegebenen Quellen und Hilfsmittel benutzt sowie Zitate kenntlich gemacht habe.

Aachen, den 17.06.2024

The experimental work of this thesis has been performed from March 2019 until November 2023 at the DWI – Leibniz Institute for Interactive Materials e.V. at the RWTH Aachen University under the mentorship of Prof. Dr. César Rodriguez-Emmenegger and supported by Prof. Dr. Ulrich Schwaneberg as PhD promoter.

Parts of this work have been or will be published in scientific journals:

[1] Söder, D., Garay-Sarmiento, M., Rahimi, K., Obstals, F., Dedisch, S., Haraszti, T., Davari, M.D., Jakob, F., Heß, C., Schwaneberg, U. and Rodriguez-Emmenegger, C., Unraveling the Mechanism and Kinetics of Binding of an LCI-eGFP-Polymer for Antifouling Coatings. *Macromol. Biosci*. **2021**, 21, 2100158. https://doi.org/10.1002/mabi.202100158

[2] Obstals, F., Witzdam, L., Garay-Sarmiento, M., Kostina, N. Y., Quandt, J., Rossaint, R., Singh, S., Grottke, O and Rodriguez-Emmenegger, C., Improving Hemocompatibility: How Can Smart Surfaces Direct Blood to Fight against Thrombi. *ACS Appl. Mater. Interfaces* **2021**, 13, 11696−11707. https://doi.org/10.1021/acsami.1c01079

[3] Garay-Sarmiento, M., Witzdam, L., Vorobii, M., Simons, C., Herrmann, N., de los Santos, A., Heine, E., El-Awaad, I., Lütticken, R., Jakob, F., Schwaneberg, U., Rodriguez-Emmenegger, C., Kill&Repel Coatings: The Marriage of Antifouling and Bactericidal Properties to Mitigate and Treat Wound Infections. *Adv. Funct. Mater.* **2022**, 32, 2106656. https://doi.org/10.1002/adfm.202106656. (Front cover)

[4] Witzdam, L., Meurer, Y.L., Garay-Sarmiento, M., Vorobii, M., Söder, D., Quandt, J., Haraszti, T. and Rodriguez-Emmenegger, C. (2022), Brush-Like Interface on Surface-Attached Hydrogels Repels Proteins and Bacteria. *Macromol. Biosci.* **2022**, 22, 2200025. https://doi.org/10.1002/mabi.202200025

[5] Garay-Sarmiento, M., Quandt, J., Witzdam, L., Englert, J., Rutsch, Y., Stöcker, C., Obstals, F., Grottke, O., Rodriguez-Emmenegger, C., Interactive Hemocompatible Nanocoating to Prevent Surface-Induced Coagulation in Medical Devices. *Adv. Mater. Interfaces* **2022**, 9, 2201055. https://doi.org/10.1002/admi.202201055

[6] Vorobii, M., Teixeira-Santos, R., Gomes, L.C, Garay-Sarmiento, M., Wagner, A. M., Melgulhão, F.J, Rodriguez-Emmenegger, C., Oriented immobilization of Pep19-2.5 on antifouling brushes suppresses the development of Staphylococcus aureus biofilms. *Prog. Org. Coat.,* **2022**, 106609. https://doi.org/10.1016/j.porgcoat.2021.106609

[7] Wagner, A. M., Quandt, J., Söder, D., Garay-Sarmiento, M., Joseph, A., Petrovskii, V. S., Witzdam, L., Hammoor, T., Steitz, P., Haraszti, T., Potemkin, I. I., Kostina, N. Y., Herrmann, A., Rodriguez-Emmenegger, C., Ionic Combisomes: A New Class of Biomimetic Vesicles to Fuse with Life. *Adv. Sci.* **2022**, 9, 2200617. https://doi.org/10.1002/advs.202200617. (Front cover)

[8] Palà, M., El Khannaji, H., Garay-Sarmiento M., Ronda, J. C., Cádiz, V., Galià, M., Percec, V., Rodriguez-Emmenegger, C., Lligadas, G., A green solvent-to-polymer upgrading approach to water-soluble LCST poly(N-substituted lactamide acrylate)s. *Green Chem.*, 2022, 24, 8314-8323. https://doi.org/10.1039/D2GC02780A

[9] Joseph, A., Wagner, A. M., Garay-Sarmiento, M., Aleksanyan, M., Haraszti, T., Söder, D., Georgiev, V. N., Dimova, R., Percec, V., Rodriguez-Emmenegger, C., Zwitterionic Dendrimersomes: A Closer Xenobiotic Mimic of Cell Membranes. *Adv. Mater.* 2022, 34, 2206288. https://doi.org/10.1002/adma.202206288

[10] Englert, J., Witzdam, L., Söder, D., Garay-Sarmiento, M., Joseph, A., Wagner, A. M., Rodriguez-Emmenegger, C., Synthetic Evolution of a Supramolecular Harpooning Mechanism to Immobilize Vesicles at Antifouling Interfaces. *Macromol. Chem. Phys.* 2023, 2300306. https://doi.org/10.1002/macp.202300306

[11] Garay-Sarmiento, M., Witzdam, L., Gagliardi, M., Meurer, Y. L., Rutsch, Y., Englert, J., Philipsen, S., Janem, A., Alsheghri, R., Jakob, F., Molin, D. G. M., Schwaneberg, U., van den Akker, N. M. S., Rodriguez-Emmenegger, C., Brush-Like Coatings Provide A Cloak of Invisibility to Titanium Implants. *Macromol. Biosci.* **2023**, 2300434. https://doi.org/10.1002/mabi.202300434

[12] Garay-Sarmiento, M., Wagner, A., Söder, D., Quandt, J., Wiert, F., Russo, T., Haraszti T., Kostina, N. Yu., Rodriguez-Emmenegger, C., Super-Predatory Synthetic Cells: Unlocking the Phagocytic Potential of Ionic Combisomes, **2024**. *Manuscript in preparation*

[13] Garay-Sarmiento, M., Abdulkadir, Y., Rutsch, Y., Barth, S., Jakob, F., Bergs, T., Schwaneberg, U., Rodriguez-Emmenegger, C., Hierarchically-engineered surface modification renders the surface of titanium dental implants resistant to bacterial colonization, **2024**. *Manuscript in preparation*

[14] Garay-Sarmiento, M., Wagner, A., Söder, D., Russo, T., Kostina, N. Yu., Rodriguez-Emmenegger, C., Leveraging Artificial Phagocytosis to Fight Bacteria, **2024**. *Manuscript in preparation*

[15] Garay-Sarmiento, M., Herrmann, N., Jakob, F., Schwaneberg, U., Rodriguez-Emmenegger, C., Advanced Kill&Repel Coating: Effective Combat Against Multi-Drug Resistant Bacteria in *Ex Vivo* Skin Models, **2024**. *Manuscript in preparation*

Conference Contributions:

[1] NanoBio&Med2023, Barcelona, Spain (21-23.11/**2023**)
Oral presentation: Nature-inspired biomaterials: from interactive coatings to granular hydrogels exhibiting specific interactions with living matter.

[2] 16th IBEC Symposium, Barcelona, Spain (03.10/**2023**)
Poster presentation: Kill&Repel Coatings: The Marriage of Antifouling and Bactericidal Properties to Mitigate and Treat Wound Infections.

[3] 16th IBEC Symposium, Barcelona, Spain (03.10/**2023**)
Poster presentation: Designing zwitterionic granular hydrogels towards specific interactions with living matter.

[4] 16th IBEC Symposium, Barcelona, Spain (03.10/**2023**)
Poster presentation: Super predatory ionically-linked comb polymers for engulfment of micro and nanoparticles (Best poster award).

[5] 33rd Annual Conference of the European Society for Biomaterials (ESB 23), Davos, Switzerland (04-08.09/**2023**)
Poster presentation: The Anchor Peptide Platform: Enabling robust and precise functionalization of medical devices with synergistic antifouling and antimicrobial properties.

[6] Advanced Functional Polymers for Medicine 2023, Barcelona, Spain (06-10.06/**2023**)
Poster presentation: Kill&Repel Coatings: The Marriage of Antifouling and Bactericidal Properties to Mitigate and Treat Wound Infections.

[7] Advanced Functional Polymers for Medicine 2023, Barcelona, Spain (06-10.06/**2023**)
Poster presentation: Designing zwitterionic granular hydrogels towards specific interactions with living matter.

[8] 55th DGBMT Annual Conference on Biomedical Engineering (BMT 2021), Hannover, Germany (07.10.**2021**)
Oral presentation: Kill&Repel Coatings: The Marriage of Antifouling and Bactericidal Properties to Fight Wound Infections

[9] 14th IBEC Symposium – Bioengineering for Regenerative Therapies, online (27-28.10.**2021**)

Poster presentation: Kill&Repel Coatings: The Marriage of Antifouling and Bactericidal Properties to Fight Wound Infections

[10] 13th IBEC Symposium – Bioengineering for Regenerative Therapies, online (27-28.10.**2020**)
Poster presentation: Antimicrobial and non-adhesive electrospun wound dressings of polycaprolactone.

[11] Cloud-yESAO 2020, online (07-11.09.**2020**)
Oral presentation: Antimicrobial and non-adhesive electrospun wound dressings of polycaprolactone.

[12] ESAO Winter School 2020, Lutherstadt Winterberg, Germany (26-29.02.**2020**)
Poster presentation: A universal system to control the unspecific protein and cell adhesion on electrospun polycaprolactone wound dressing.

TABLE OF CONTENTS

ABSTRACT

Despite revolutionary advances in medicine, biotechnology and the biomedical field over the last decades, the effective management of microbial infections remains a persistent challenge. Moreover, the continued emergence of antimicrobial-resistant microbes poses a serious threat and is a matter of global concern. The resistance crisis we face today is a consequence of the excessive and inappropriate use of antibiotics, as well as the lack of invention of new antimicrobial strategies. Antimicrobial stewardship is now imperative and requires innovative approaches to combat infections in a safe, sustainable, yet efficient manner. The scientific work conducted within the framework of this thesis focused on the development of non-antibiotic antimicrobial biomaterials. For this purpose, particular inspiration is drawn from some of nature's most efficient defense and survival mechanisms.

Initially, this thesis focuses on the design of coatings that confer the surface of biomedical devices with stealth properties, shielding off bacterial adhesion and thereby reducing the risk of infection development. The coatings consist of polymer brushes and brush-like structures composed of (3-Methacryloylamino-propyl)-(2-carboxy-ethyl) dimethylammonium carboxybetaine methacrylamide (CBMAA) and *N*-(2-hydroxypropyl) methacrylamide (HPMA), which create physical and energetic barriers that effectively prevent the adsorption of blood plasma proteins and the adhesion of pathogenic bacteria. Additionally, this thesis showcases a universal and readily applicable coating strategy for polymeric and metallic surfaces. This approach involves the synthesis of peptide-polymer hybrids that form a brush-like coating through site-directed adsorption on the surface, eliminating the need for laborious procedures or external energy input. Further, this thesis presents the innovative "Kill&Repel" strategy for antimicrobial coatings, which combines the synergistic effects of antifouling properties with a bacteriophage-inspired bactericidal strategy. The coating was formed *in situ* by the adsorption of peptide-polymer and peptide-endolysin hybrids on the surface. Coated surfaces effectively prevented the colonization and biofilm formation by *Streptococcus agalactiae*, *Staphylococcus epidermidis*, *Streptococcus pyogenes* and *Staphylococcus aureus*. Moreover, the coating effectively eliminated bacteria in a simulated infection without allowing residues to adhere to the surface, demonstrating a self-cleaning mechanism that enables the coating to remain active for an extended period of time. Notably, the Kill&Repel coating is completely innocuous to mammalian cells and skin tissue. Next, this thesis

introduces the unprecedented concept of accelerated “Artificial Phagocytosis”. This concept involves the usage of a new family of cell mimics based on amphiphilic ionically-linked comb polymers, which have the unparalleled ability to mimic a rudimentary form of phagocytosis. In a first stage, the engulfment of inanimate objects, such as silica and polystyrene nano- and microparticles was studied and demonstrated to be highly efficient compared to other cell mimics based on lipids as well as block and graft copolymers. It is discovered that their ability for superior and accelerated engulfment is attributed to their heterogeneous membrane composition, arising from the random sequence distribution of the polymer components along and across chains in a single batch. This results in local curvature defects within the membrane, which reduce kinetic barriers facilitating intermediate states of the engulfment process. Ultimately, the superior phagocytic behavior of these cell mimics was leveraged against the predation of bacterial pathogens, including *Escherichia coli*, *Staphylococcus aureus* and *Pseudomonas aeruginosa*, resulting in the effective killing of these pathogens within 60 min. Additionally, these cell mimics exhibited great biocompatibility with organotypic tissues throughout prolonged incubation periods, showing promise as a next-generation antimicrobial therapy that can provide a safe solution to the current antimicrobial resistance crisis.

KURZFASSUNG

Trotz revolutionärer Fortschritte in der Medizin, Biotechnologie und auf dem Gebiet der Biomedizin in den letzten Jahrzehnten bleibt das effektive Management von mikrobiellen Infektionen eine anhaltende Herausforderung. Darüber hinaus stellt das stetige Auftreten resistenter Mikroben eine ernsthafte Bedrohung dar und ist eine Problematik von globaler Bedeutung. Die Resistenzkrise, mit der wir heute konfrontiert sind, ist eine Folge des übermäßigen und unangemessenen Einsatzes von Antibiotika sowie des Mangels an Erfindung neuer antimikrobieller Strategien. Antimicrobial Stewardship ist nun zwingend erforderlich und verlangt innovative Ansätze, um Infektionen auf sichere, nachhaltige und effiziente Weise zu bekämpfen. Die wissenschaftliche Arbeit, die im Rahmen dieser Dissertation durchgeführt wurde, fokussierte sich auf die Entwicklung von nicht-antibiotischen antimikrobiellen Biomaterialien. Hierbei wurde insbesondere Inspiration aus einigen der effizientesten Abwehr- und Überlebensmechanismen der Natur geschöpft.

Diese Arbeit konzentriert sich zu Beginn auf das Design von Beschichtungen, die die Oberfläche medizinischer Geräte vor bakterieller Anhaftung schützen sollen, um das Risiko einer Infektionsentwicklung zu verringern. Die Beschichtungen bestehen aus Polymerbürsten und bürstenähnlichen Strukturen aus (3-Methacryloylamino-propyl)-(2-carboxy-ethyl) Dimethylammonium Carboxybetainmethacrylamid (CBMAA) und *N*-(2-Hydroxypropyl) Methacrylamid (HPMA), die physikalische und energetische Barrieren schaffen, welche die Adsorption von Blutplasmaproteinen und die Anhaftung von pathogenen Bakterien wirksam verhindern. Darüber hinaus präsentiert diese Arbeit eine universelle und leicht anwendbare Beschichtungsstrategie für polymere und metallische Oberflächen. Der Ansatz beinhaltet die Synthese von Peptid-Polymer-Hybriden, die durch gerichtete Adsorption auf der Oberfläche eine bürstenähnliche Beschichtung bilden und dabei die Notwendigkeit aufwendiger Verfahren oder externer Energiezufuhr eliminieren. Des Weiteren wird in dieser Arbeit die innovative „Kill&Repel“ Strategie für antimikrobielle Beschichtungen vorgestellt. Diese kombiniert die synergistischen Effekte von antifouling-Eigenschaften mit einer von Phagen inspirierten, bakteriziden Strategie. Die Beschichtung entsteht *in situ* durch die Adsorption von Peptid-Polymer- und Peptid-Endolysin-Hybriden auf der Oberfläche. Beschichtete Oberflächen verhindern effektiv die Kolonisation und Biofilmbildung durch *Streptococcus agalactiae*, *Staphylococcus epidermidis*, *Streptococcus pyogenes*, *Staphylococcus aureus* und

multiresistente *Staphylococcus aureus* (MRSA). Die Beschichtung beseitigte Bakterien in einer simulierten Infektion, ohne dass Rückstände auf der Oberfläche haften blieben. Dadurch entsteht ein selbstreinigender Mechanismus, der die Beschichtung über einen längeren Zeitraum aktiv hält. Beachtenswert ist, dass die „Kill&Repel“ Beschichtung für Säugetierzellen und Hautgewebe völlig unschädlich war. Als Nächstes wird in dieser Arbeit das neue Konzept der „beschleunigten künstlichen Phagozytose“ vorgestellt. Dieses Konzept beinhaltet die Verwendung einer neuen Familie von synthetischen Zellen, die auf amphiphilen ionisch verbundenen Kamm-Polymeren basieren und die besondere Fähigkeit besitzen, eine Art künstliche Phagozytose in hohem Niveau zu imitieren. In einem ersten Schritt wurde die Aufnahme von unbelebten Objekten, wie Silika- und Polystyrol-Nano- und Mikropartikeln, untersucht. Hier wurde gezeigt, dass sie im Vergleich zu anderen Zellimitaten auf der Basis von Lipiden, Block- oder Pfropf-Copolymeren sehr effizient waren. Es wurde gezeigt, dass ihre überlegene Aufnahmefähigkeit auf ihrer heterogenen Membranzusammensetzung beruht, die sich aus der zufälligen Sequenzverteilung des amphiphilen Kamm-Polymers ergab. Dies führte zu lokalen Krümmungsdefekten in der Membran, die kinetische Barrieren reduzierten und Intermediärzustände des Verschlingungsvorgangs begünstigten. Letztendlich wurde das überlegene phagozytäre Verhalten dieser Zellimitate gegen die Prädation von bakteriellen Krankheitserregern, einschließlich *Escherichia coli*, *Staphylococcus aureus* und *Pseudomonas aeruginosa*, eingesetzt. Diese konnten innerhalb von 60 Minuten effektiv die Krankheitserreger abtöten. Darüber hinaus zeigten diese Zellimitate über längere Inkubationszeiträume hinweg eine ausgezeichnete Biokompatibilität mit organotypischen Geweben. Somit könnte diese Technologie vielversprechend für die nächste Generation von antimikrobiellen Therapien sein und eine sichere Lösung für die aktuelle Krise der antimikrobiellen Resistenz bieten.

ACKNOWLEDGEMENTS

I take this opportunity to express my deepest appreciation to the people who have been instrumental for the successful completion of this research and without whom I would not have made it through my PhD!

First and foremost, I would like to express my sincere gratitude to my supervisor, Prof. Dr. César Rodriguez-Emmenegger for his invaluable supervision and mentorship throughout my entire Ph.D. journey and for the opportunities he has provided me to engage in diverse interdisciplinary and innovative projects. I am particularly thankful for his continuous encouragement to pursue ambitious goals and all the thought-provoking discussions that have significantly shaped my research career. His passion and curiosity for science have been and will continue to be a great inspiration for me. In addition, I would like to extend my gratitude to Prof. Dr. Ulrich Schwaneberg for his support and collaboration in cutting-edge projects, for providing valuable career advice and for taking over the role of my first doctoral examiner.

Special thanks are due to Dr. Nina Yu. Kostina, Dr. Felix Jakob and Dr. Tamás Haraszti for generously sharing their extensive expertise and offering consistent advice and support, contributing significantly to the advancement of my research. I am grateful to Niklas Herrmann and Yayci Abdulkadir for their invaluable help and intellectual contributions, extending beyond our collaborative projects.

I would like to express my deepest appreciation to the best co-workers one could have wished for: all the members of the Rodriguez-Emmenegger Lab. Thank you for all the shared conversations, both scientific and some less scientific. A special note of gratitude goes to Lena Witzdam, Fabian Obstals, Dominik Söder, Anna M. Wagner, Jonas Quandt, Anton Joseph and Jenny Englert. Throughout this time, you have been a constant source of support and motivation. Thank you for always having my back, believing in me when I could not bring myself to do so and for your constant nagging. You brought a smile to my face at times when I needed it the most. I would also like to thank my best friends, Nadja Hansen and Maria Vásques, for being such excellent people, keeping me sane during the last years and reminding me to occasionally stay up all night dancing instead of working.

I cannot begin to express my deepest gratitude to my boyfriend, Gabriel Hardt. Thank you for your love, support, kindness and patience. It has not always been easy with me, most specially during the past few weeks. Thank you for standing by my side and being a source of strength. I love you!

Finally, I am forever grateful to my parents: Luz Sarmiento and Edvin Garay. I am privileged to have you as my mentors in live. Your generous hearts, unconditional love and the pursuit of growth have been an immense source of inspiration all my life. You have always supported and believed in me and I will cherish that forever. There is nothing else for me to say to you other than THANK YOU!

Abbreviation Index

^{1}H NMR ..... Proton nuclear magnetic resonance
alb ..... Albumin
AMP ..... Antimicrobial peptides
AMR ..... Antimicrobial resistance
ATRP ..... Atom transfer radical polymerization
BAIs ..... Biomaterial-associated Infections
BIB-NHS ..... 2-bromoisobutanoic acid *N*-hydroxy-succinimide ester
BP ..... Blood plasma
BSA ..... Bovine serum albumin
CA ..... Contact angle
CBAA ..... Carboxybetaine acrylamide
CBMAA ..... (3-Methacryloylamino-propyl)-(2-carboxy-ethyl) dimethylammonium carboxybetaine methacrylamide
cryo-TEM ..... Cryogenic transmission electron microscopy
Cys ..... Cysteine residue
D ..... Lateral diffusion coefficients
DDP ..... Didodecylhydrogen phosphate
DLS ..... Dynamic light scattering
DMAPAA ..... N,N-dimethylaminopropyl acrylamide
DMEM ..... Dulbecco's Modified Eagle Medium
DOPC 1,2-dioleoyl-sn-glycero-3-phosphocholine
DP ..... Degree of polymerization
DS ..... Degree of substitution
E. coli ..... Escherichia coli
ECMO ..... Extracorporeal membrane oxygenation
eGFP ..... Enhanced green fluorescent protein
EPS ..... Extracellular polymeric substance
EthD ..... Ethidium homodimer
FBS ..... Fetal bovine serum
FRAP ..... Fluorescence recovery after photobleaching
FRET ..... Förster resonance energy transfer
HCl ..... Hydrochloric acid
HDF ..... Human dermal fibroblasts
HE ..... Hematoxylin and eosin
HEK ..... Human epidermal keratinocytes
HPLM ..... Human plasma-like medium
HPMA ..... N-(2-Hydroxypropyl) methacrylamide

iCPs ..... Ionically-linked comb polymers
LB .....Luria broth
LCI ..... Liquid chromatography peak I
LPS..... Lipopolysaccharides
MALLS-SEC ..... Multiangle laser light scattering size exclusion chromatography
MRSA .....Methicillin-resistant Staphylococcus aureus
NVA-co-NVF-co-VAm .....Poly(vinylamine-co-vinylformamide-co-vinylacetamide)
NVF ..... N-vinylformamide
OD ..... Optical density
P. aeruginosa ..... Pseudomonas aeruginosa
PB-b-PEO..... Polybutadiene-block-poly(ethylene oxide)
PBS .....Phosphate-buffered saline
PCL ..... Poly(ε-caprolactone)
PCMA ..... 2-(methacryloyloxy) ethyl phosphorylcholine
PDA ..... Polydopamine
PDMS-g-PEO .....Poly(dimethylsiloxane)-graft-poly(ethylene oxide)
PE ..... Polyethylene
PEG..... Polyethylene glycol
PFA .....Paraformaldehyde
PFPA..... Perfluorophenylazides
PFPA-NHS..... N-succinimidyl-4-azidotetra-fluorobenzoate
PMP.....Poly(4-methyl-1-pentene)
poly(CBAA-co-DMAPAA) ..... poly(carboxybetaine acrylamide-co-N,N-dimethylaminopropyl acrylamide)
ppb..... Parts per billion
PS .....Polystyrene
PU .....Polyurethane
RPMI .....Roswell Park Memorial Institute
S. agalactiae .....Streptococcus agalactiae
S. aureus .....Staphylococcus aureus
S. epidermidis .....Staphylococcus epidermidis
S. gordonii..... Streptococcus gordonii
S. pyogenes..... Streptococcus pyogenes
SBMA ..... N-(3-sulfopropyl)-N-methacroyloxyethyl-N,N-dimethylammonium betaine
SEC .....Size exclusion chromatography
SEM..... Scanning electron microscopy
SET-LRP ..... Single electron transfer-living radical polymerization
SI .....Surface-initiated
SNPs ..... Nano-sized silica particles
SPR ..... Surface plasmon resonance

STED.....Stimulated emission depletion

TFH.....Thin-film hydration

Tris.....Tris(hydroxymethyl)aminomethane

TSY.....Tryptic soy yeast

VAm..... N-vinylacetamide

WHO.....World Health Organization

XPS..... X-ray photoelectron spectroscopy

List of figures

xx

List of Schemes

List of Tables

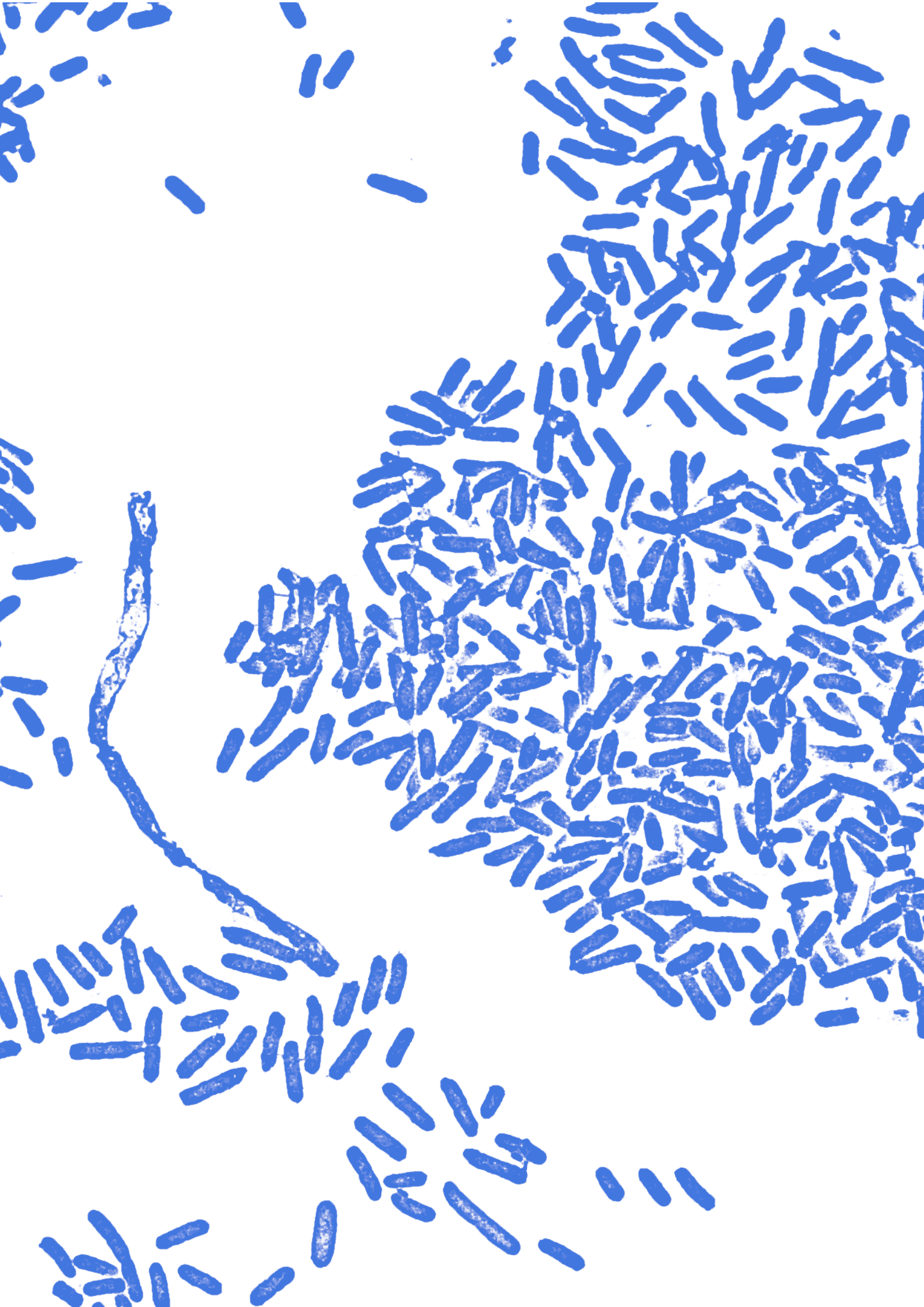

Chapter 1

Introduction

1.1 Motivation and Goal of the Thesis

"What if, every time I started to invent something, I asked, 'How would nature solve this?'"

by Janine Benyus

Nature, through its enduring process of evolution, stands as an unparalleled source of inspiration for the development of innovative materials and mechanisms. Nature has evolved unique biological systems incorporating well-engineered materials, objects and processes that function seamlessly from the macro- to the nanoscale to sense, respond, regulate, grow, regenerate, and heal.[1] Deciphering nature's blueprints can provide a powerful paradigm for the bioinspired development of solutions to mankind's most challenging problems, paving the way for transformative advances in material, environmental and medical sciences, among others.

For example, nature's ability to self-assemble at the molecular and nanoscale has inspired the engineering of nanotechnology systems capable of self-assembly, enabling the formation of complex structures and simplifying manufacturing processes. This influence has been instrumental during the COVID-19 pandemic, where membrane-mimicking formulations, such as nanodecoys, liposomes and lipid nanoparticles have demonstrated significant promise. These technologies, by mimicking natural processes and structures found in living organisms, enhance the efficiency, specificity and overall therapeutic outcomes of treatment.[2] Moreover, our world faces multiple health challenges, with the imminent menace of drug-resistant pathogens and infections, where existing antimicrobial agents are falling short. The World Health Organization (WHO) declared in 2019 that antimicrobial resistance (AMR) is one of the top ten threats to global human health[3] demanding advanced solutions. If no serious action should be taken, AMR could cause up to 10 million deaths by 2050.[4] Accordingly, the World Bank estimates that the economic repercussions of this looming antimicrobial crisis could be as devastating as the global financial crisis of 2008-2009.[5]

By delving into the intricacies of nature's artistry, ingenious solutions and design principles, in this thesis, I seek to engineer innovative biomaterials for infection management that interact seamlessly with the human body and transcend traditional antimicrobial approaches. Drawing inspiration from the exceptional antiadhesive properties of many surfaces in nature, the initial

sections of this thesis (Chapter 3 and 4) concentrate on the fabrication of different non-adhesive (antifouling) materials and coatings that create physical and energetic barriers to molecular and cellular adhesion, being capable of prohibiting microbial adhesion, thereby mitigating the risk of infection. The latter part of this thesis (Chapters 5 to 7) introduces two different active antimicrobial strategies against resistant microbes. The first strategy takes inspiration from natural viral predation on bacteria. Bacteriophages are viruses that hijack the bacterial machinery to replicate. To do so, the bacterial cell wall is disrupted for the release of progeny bacteriophages. We harness the mechanism of cell wall disruption to engineer bactericidal surface coatings. These coatings achieved efficient and targeted disruption of the bacterial cell wall while having exceptional biocompatibility with human cells, providing a potentially safe solution to combat antibiotic-resistant material-related infections. The second strategy is inspired by the cellular level defense mechanism of innate immunity. Phagocytic cells, such as macrophages and neutrophils act as frontline defenders against infections, patrolling the body to recognize, engulf and eliminate pathogens. We developed cell mimics using synthetic amphiphilic molecules that self-assemble into curved membranes and are able to replicate a rudimentary form of natural phagocytosis. These phagocytic synthetic cells are capable of disabling superbugs like *Staphylococcus aureus* and *Pseudomonas aeruginosa*.

1.2 Thesis Outline

Chapter 2 highlights the critical importance of advancing the development of antimicrobial materials. It provides a concise and comprehensive review of the *status quo* of bactericidal strategies employed in both research and clinical settings, addressing the limitations of current approaches. The chapter further emphasizes how delving into nature for antimicrobial inspiration serves as a catalyst for innovation within the realms of antimicrobial materials science and biotechnology, offering solutions that can be effective, sustainable, and considerate of the complex interactions within biological systems.

Chapter 3 elucidates the significance of antifouling surface coatings as effective measures to mitigate unwanted interactions with living matter, primarily focusing on preventing bacterial adhesion and minimizing the associated risk of material-related infections. Moreover, this chapter details the development of three different chemical routes aimed at modifying various polymeric medical devices with cutting-edge antifouling polymer brush-coatings

consisting of poly(CBMAA*co*HPMA). Bacterial adhesion studies confirmed the effectiveness of these antifouling coatings in preventing bacterial colonization on the surface, while simultaneously demonstrating excellent biocompatibility with human cells.

Chapter 4 presents a universal approach for the surface modification of a wide range of metallic and polymeric medical devices with antifouling brush-like coatings, comprising poly(CBMAA) or poly(HPMA). The coating strategy leverages the promiscuity of protein fouling to develop peptide-polymer hybrid macromolecules that can adsorb in an oriented fashion at the liquid-air interface, forming a dense brush-like coating at the periphery of the surface without the need for surface treatment processes or external energy input. This antifouling coating not only significantly minimizes non-specific protein adsorption, but also extends to the mesoscopic scale, preventing non-specific fibroblast cell adhesion and bacterial colonization with consequent biofilm formation. Additionally, this chapter provides an overview of the long-term stability and sterilization stability of this coating, along with a strategy for improving the mechanical resistance of the coating for applications in orthodontic and orthopedic implants.

Chapter 5 presents the novel Kill&Repel coating strategy, which provides simultaneous bactericidal action and antifouling properties. Built upon the versatility of the previously presented peptide-polymer hybrid coating, this coating incorporates a second hybrid macromolecule, protein-endolysin, which endows the coating with a phage-inspired antimicrobial approach. This bi-orthogonal antimicrobial action disrupts the bacterial cell wall in a specific manner, without harming human cells or promoting the development of bacterial resistance. In a plug-and-play fashion, the Kill&Repel coating is tailored to target *Streptococcus agalactiae*, *Staphylococcus epidermidis*, *Streptococcus pyogenes*, *Staphylococcus aureus* and Methicillin-resistant *S. aureus.* Wound dressings modified with the Kill&Repel coating completely eradicated bacteria in a simulated infection, without allowing residues to adhere to the surface. Additionally, this chapter highlights the potentiated antimicrobial activity of the Kill&Repel coating compared to a coating comprising solely bactericidal hybrids or a solution of molecularly dissolved hybrids (peptide-endolysin). The heightened activity results from a synergistic effect through multivalent actions and the parallel combination with antifouling properties, underlining its substantial potential for clinical applications in infection control and wound management.

Chapter 6 introduces a new family of cell mimics adept at scavenging nano and micron-sized objects through a spontaneous engulfment process, mimicking a rudimentary form of phagocytosis observed in immune cells. These Phagocytic Synthetic Cells self-assemble from amphiphilic, ionically-linked comb polymers. These polymers consist of a hydrophilic poly(carboxybetaine acrylamide-*co*-*N*,*N*-dimethylaminopropyl acrylamide) (poly(CBAA-*co*-DMAPAA)) backbone characterized by a random sequential distribution of CBAA and DMAPAA, resulting in a heterogenous composition of the membrane bilayers of PSCs. The hydrophobic alkyl side chains are appended to the DMAPAA units by electrostatic interactions. In this chapter, we delve deeper into the investigation and understanding of the physical mechanism underlying the massive uptake of silica and polystyrene particles by the PSCs. We propose that the synergistic combination of compositional heterogeneity and the non-directional nature of ionic coupling gives rise to cell mimics with local curvature defects, high fluidity and the ability for molecular topology rearrangement akin to natural cells. These inherent features reduce thermodynamic and kinetic barriers for engulfment, endowing PSCs with a superior phagocytic behavior compared to other state-of-the-art cell mimics based on liposomes, *block* or *graft* polymersomes.

Chapter 7 extends beyond the engulfment of inanimate particles, harnessing the potentiated phagocytic ability of the PSCs for the predation and killing of bacterial pathogens. Upon contact with both Gram-positive and Gram-negative biofilm-forming bacteria, PSCs efficiently engulf these pathogens into a phagosome. Notably, bacterial death can be detected already after an incubation period of 60 min. Our hypothesis posits that the antimicrobial efficacy of the PSCs relies on their close apposition to the engulfed bacterium, enabling their hydrophobic tails to insert and disrupt the integrity of the bacterial cell membrane. This bactericidal mechanism, centered on membrane disruption, is less conducive to bacterial evolution, making it less likely to contribute to the emergence of bacterial resistance. Furthermore, when PSCs were exposed to organoid microtissues, we observed high tissue viability.

Chapter 8 outlines the overarching results derived from this thesis, provides insight into potential improvements and presents a forward-looking perspective on future research efforts.

1.3 References

[1] B. Bhushan, *Philosophical Transactions of the Royal Society A: Mathematical, Physical and Engineering Sciences* **2009**, *367*, 1445-1486.

[2] B. A. Witika, P. A. Makoni, L. L. Mweetwa, P. V. Ntemi, M. T. R. Chikukwa, S. K. Matafwali, C. Mwila, S. Mudenda, J. Katandula, R. B. Walker, *Molecules* **2020**, *25*.

[3] EclinicalMedicine, *eClinicalMedicine* **2021**, *41*.

[4] B. Peng, H. Li, X.-x. Peng, *Drug Discovery Today* **2023**, *28*, 103753.

[5] O. B. Jonas, A. Irwin, F. C. J. Berthe, F. G. Le Gall, P. V. Marquez*, Vol. 2*, **2017**.

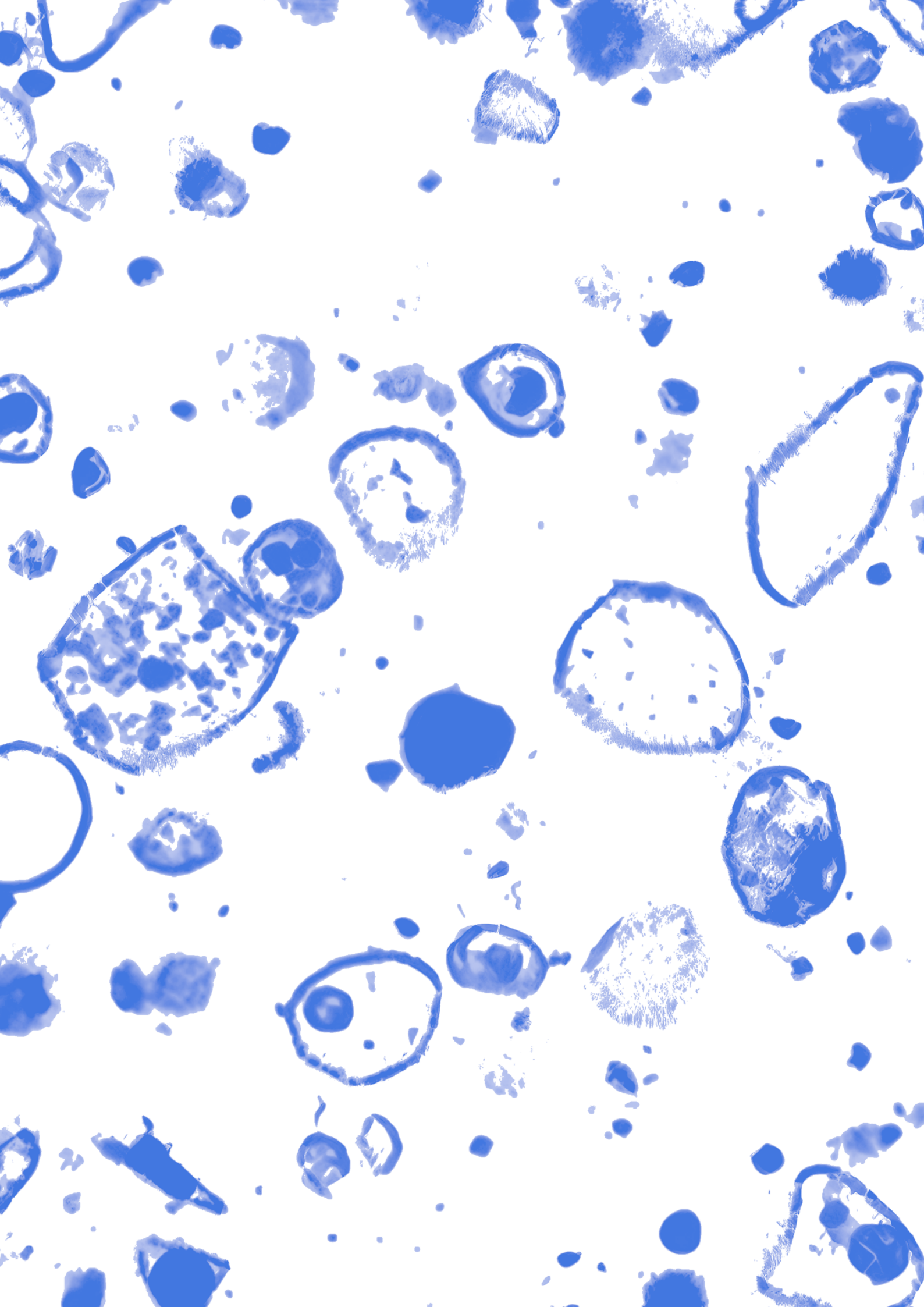

Chapter 2

State of the Art

2.1 Infections - A global Threat to Human Health

The twenty-first century has been marked by a succession of serious infectious disease outbreaks, with the most recent being the devastating COVID-19 pandemic. From January 2020 to December 2021, this pandemic was estimated to have caused nearly 15 million deaths.[1] Additionally, outbreaks of Ebola, Zika, dengue, Middle East respiratory syndrome, severe acute respiratory syndrome and influenza have contributed significantly to morbidity and mortality.[2] Furthermore, the imminent threat of rising AMR and the spread of superbugs is raising alarm bells worldwide. In 2019, the WHO declared AMR as one of the top ten deadliest threats to global human health.[3] AMR claimed the lives of 4.95 million people in 2019, surpassing the combined deaths caused by malaria and HIV.[4] If not address urgently, experts anticipate that AMR could become the leading cause of death globally, claiming the lives of up to 10 million people by 2050.[5]

2.1.1 Antimicrobial Resistance

The discovery of penicillin and other antibiotics at the beginning of the 20th century revolutionized the field of medicine, ushering a new era for the treatment and prevention of bacterial infection diseases worldwide. Since then, antibiotics have not only had a significant impact on human health but have also been widely used in the fields of agriculture, aquaculture and the food industry.[6] Antibiotics currently stand as the global gold standard for combating bacterial pathogens, showcasing diverse mechanisms of action that target specific components or processes within bacteria (Figure 2.1).**[7-9]** These mechanisms include inhibiting cell wall synthesis, disrupting cell membrane function, hindering RNA transcription, targeting the bacterial ribosome to inhibit protein biosynthesis, inhibiting nucleic acid synthesis and interfering with the folic acid metabolic pathway.

Shortly after the discovery of penicillin, Sir Alexander Fleming expressed concern about the potential overuse of antibiotics and the rise of resistance.[10] Due to the specific targeting nature of antibiotics rather than having a more gross spectrum of activity, these systems are more susceptible to resistance development. Bacteria can acquire resistance through mutations that either modify or circumvent the targeted structure or process. The main

mechanisms are degradation of the antibiotic drugs, active efflux of a drug, alteration of drug targets and changes in membrane permeability, limiting the uptake of the drug.[9, 11]

Furthermore, the overuse and misuse of these medications in medical care and agriculture coupled with a lack of development of new antibiotics have massively contributed to resistance development.[12] The last class of antibiotics that was successfully introduced into clinical use was discovered in 1987.[13] To date, unfortunately, resistance has been observed to almost all antibiotics developed and our healthcare system is experiencing an antibiotic resistant crisis, where multidrug resistant "superbugs" have emerged, posing significant challenges in terms of treatment, resulting in higher patient mortality rates and increased economic costs.[14]

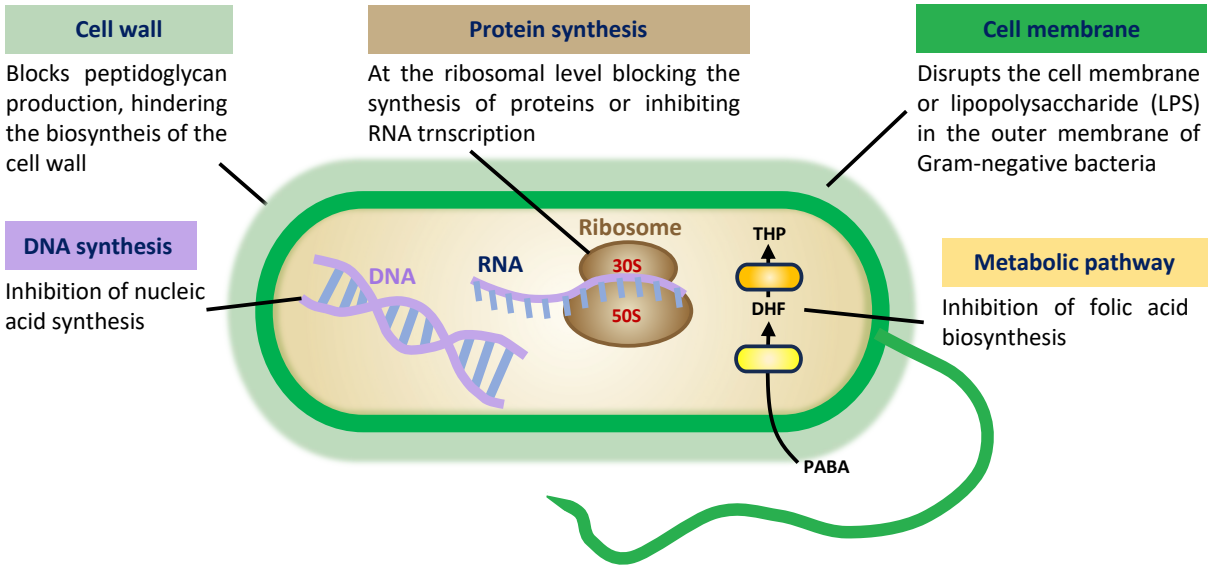

Figure 2.1. Antibiotic classes and their mode of action. Redrawn from [7].

Therefore, the establishment of a multi-sectoral antimicrobial stewardship has become imperative. Key cornerstones of this initiative encompass the reduction of antibiotic usage in agriculture, improvement in prescribing strategies within patient healthcare and the implementation of infection prevention strategies. Nevertheless, diminishing antibiotic usage demands for alternative antimicrobial strategies. Future promising approaches might consist of bacteriophage therapy, phage lysins, CRISPR-based techniques, probiotics, antimicrobial peptides, host-directed therapies, antibodies and nanotechnology.[15-17]

2.2 Biomaterial-Associated Infections

Biomaterials play a pivotal role in modern medicine facilitating the design and fabrication of indwelling medical devices and tissue scaffolds for regenerative medicine among other applications. However, device surfaces are susceptible to bacterial colonization, giving rise to biomaterial-associated infections (BAIs). BAIs have become a major postoperative complication and a leading cause of implant failure.[18-19] The onset of BAIs initiates with protein fouling at the biomaterial surface. Adsorbed proteins create a conditioning film that provides anchorage points for the attachment of bacterial cells, ultimately leading to the formation of a biofilm.[20-21] Once a biofilm develops, extracellular polymeric substances (EPSs) are secreted to create a robust chemical and physical barrier that complicates the treatment of bacterial infections 10-1000 compared to planktonic bacteria cells.[18, 22] Lastly, bacteria that are released from the biofilm may spread to the bloodstream, leading to life-threatening conditions such as bacteremia and sepsis (Figure 2.2)

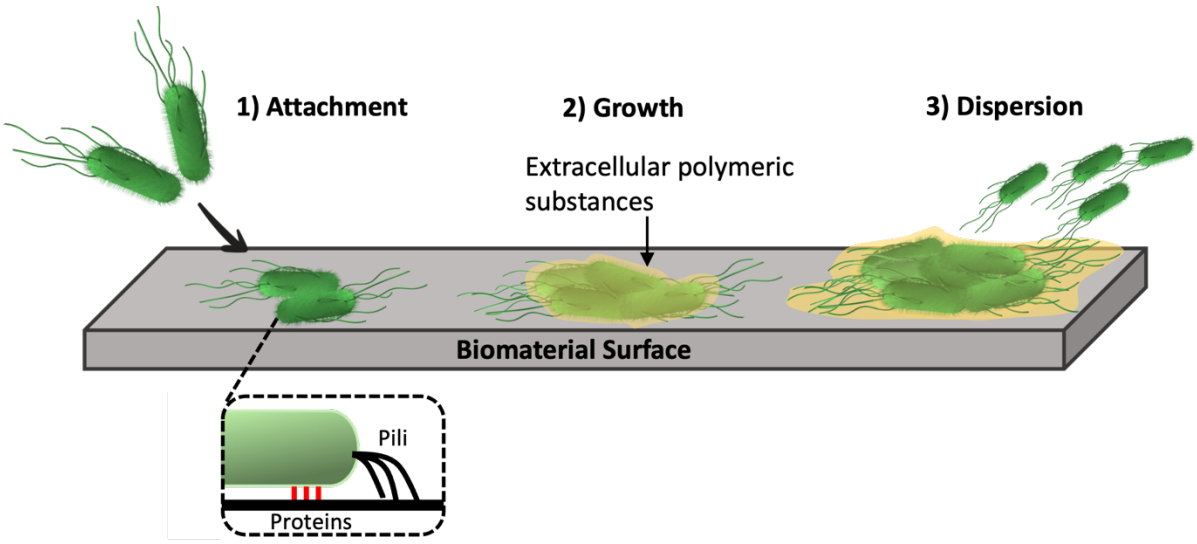

Figure 2.2. Illustration depicting the key steps of biofilm formation on biomaterials. After attaching to the surface, bacteria begin to grow forming a biofilm community until reaching a size at which it releases bacteria to spread to a different place.

Consequently, in the effort to prevent the development of BAI, antibiotics are usually prescribed. Prior to surgical procedure, patients may be provided with an antibiotic prophylaxis, or implants may be loaded with antibiotics which enable the localized delivery of these antimicrobials. However, the unnecessary and inappropriate use of antibiotics in the absence of infections creates selective pressure and contributes to the development of

antibiotic resistance. Given these challenges, alternative strategies are urgently needed for the mitigation and management of BAIs. One promising avenue is through innovative biomaterial design. The fabrication of biomaterials with inherent non-antibiotic antimicrobial properties could offer a safe prophylaxis against infections while also contributing to antibiotic stewardship.

2.2.1 The Problem of Protein Fouling

Protein fouling refers to the unwanted spontaneous adsorption of proteins on surfaces exposed to biological environments.[23] It is a ubiquitous phenomenon that, among other effects, mediates bacterial attachment and the initiation of biofilm formation on biomaterials. In this sense, the adsorption of blood proteins such as fibrinogen and fibronectin has been demonstrated to form a conditioning film that facilitates the adhesion of bacteria to the surface.[24-26] Thus, preventing protein fouling at the biomaterial surface is crucial as a preventive measure against bacterial colonization and the development of BAIs. Understanding the adsorption behavior of proteins on surfaces is pivotal for designing biomaterials resistant to bacterial colonization. Protein fouling is influenced by various factors such as protein concentration and structure (amino acids), surface hydrophilicity and charged regions of both proteins and the surface. The driving force behind protein fouling is a combination of enthalpic and entropic contributions. Enthalpic effects arise from attractive protein-surface interactions, including van der Waals forces, Coulombic forces and hydrogen bonds. Meanwhile, entropic contributions result from changes in conformation and in the state of hydration. The process of protein fouling occurs spontaneously if the change in the Gibbs energy (ΔG) of the system becomes negative ($\Delta G < 0$). [27-32] H, T and S stand for enthalpy, temperature and entropy of the system.

$$\Delta G = \Delta H - T\,\Delta S \qquad \textbf{Equation 2.1}$$

When an artificial surface is exposed to a biological environment, one of the first events is the spontaneous adsorption of water molecules and ions onto the surface. Solvated proteins migrate from the bulk aqueous medium to the surface by a combination of diffusion, thermal convection and bulk flow (Figure 2.3).

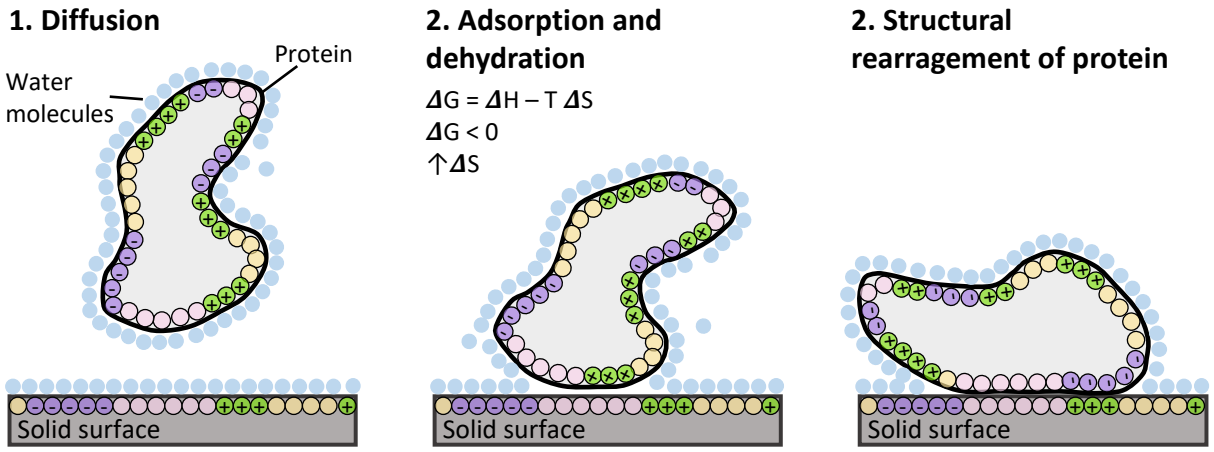

Figure 2.3. Process of protein adsorption on a solid surface. Redrawn from [33].

Proteins can then adsorb onto the solid surface through various interactions. On hydrophilic and charged surfaces, proteins adsorb trough their polar or charged regions and bind to the surface primarily via van der Waals or Coulombic interactions. On hydrophobic surfaces, proteins adsorb with their non-polar patches by means of hydrophobic interactions. Additionally, protein adsorption requires the release of interfacial water molecules (dehydration). Therefore, the structure of the water molecules covering both the surface and the protein plays a critical role and is one of the major factors governing protein adsorption. Consequently, with increasing surface hydrophilicity and stronger water binding, protein adsorption becomes less favorable as the energetic cost for dehydration rises due to a stronger water binding ability. In general, proteins tend to adsorb more readily to hydrophobic, non-polar surfaces. On these surfaces, proteins unfold by spreading their hydrophobic core on the surface, maximizing interactions and contact area with hydrophobic regions. Protein unfolding, in turn, is associated with an increase in conformational entropy and the displacement of water molecules from the surface, resulting in an additional gain in entropy.[28, 30-34]

2.3 Biomaterial-Related Strategies for the Management of Bacterial Infections

Recently, considerable attention has been directed toward the development of biomaterials and coatings that incorporate non-antibiotic antimicrobial strategies. These strategies

encompass non-adhesive (antifouling) or bactericidal materials, achieved through chemical or topographical modification approaches.[35]

2.3.1 Antifouling Materials

Antifouling surface modifications aim at preventing bacterial adhesion and mitigating infection development. These coatings rely on hydrophilic polymer coatings or low surface energy materials including fluorine- and silicon-based coatings as well as onmiphobic and super hydrophobic materials with a nanostructured topology. Herein, we will focus on the former approach based of hydrophilic polymer coatings, which aim at reducing the thermodynamic drive for protein adsorption and cell adhesion by minimizing the interfacial energy between the surface and water.

Hydrophilic antifouling polymeric coatings are mostly based on poly(ethylene glycol) (PEG) and derivates, as well as zwitterionic polymers.[36-37] The widely accepted mechanism explaining their antifouling properties is related to the formation of a tightly bound water layer on the material surface, establishing physical and energetic barriers that inhibit protein adsorption and the subsequent formation of a conditioning film conductive to bacterial attachment.[34, 36-37] In recent years, zwitterionic polymers have gained preference due to their higher hydration capacity, which is attributed to their stronger ionic solvation compared to the hydrogen bonding solvation of PEG. Consequently, zwitterionic materials have shown to exert superior antifouling properties.[38-39]

Over the years, different methods have been employed to coat the surface with antifouling polymers, including self-assembled monolayers[40], physisorption of block- and graft-copolymers,[41-43] or covalent attachment via “grafting-to” or “grafting-from” techniques.[37, 39, 44-46] In particular, the “grafting-from” approach enables the synthesis of a well-defined polymer brush coating, with a high and tunable polymer density and chain length. To date, one of the most effective antifouling coatings consist of polymer brushes based on HPMA and zwitterionic CBMAA or poly(carboxybetaine) (meth)acrylate.[47-50] These coatings have demonstrated a high level of repellency towards blood plasma proteins, bacteria, and various cell types.[50-53] Their cutting-edge antifouling performance is ascribed to the joint effect of autophobicity, high surface hydration and steric repulsion (Figure 2.4).

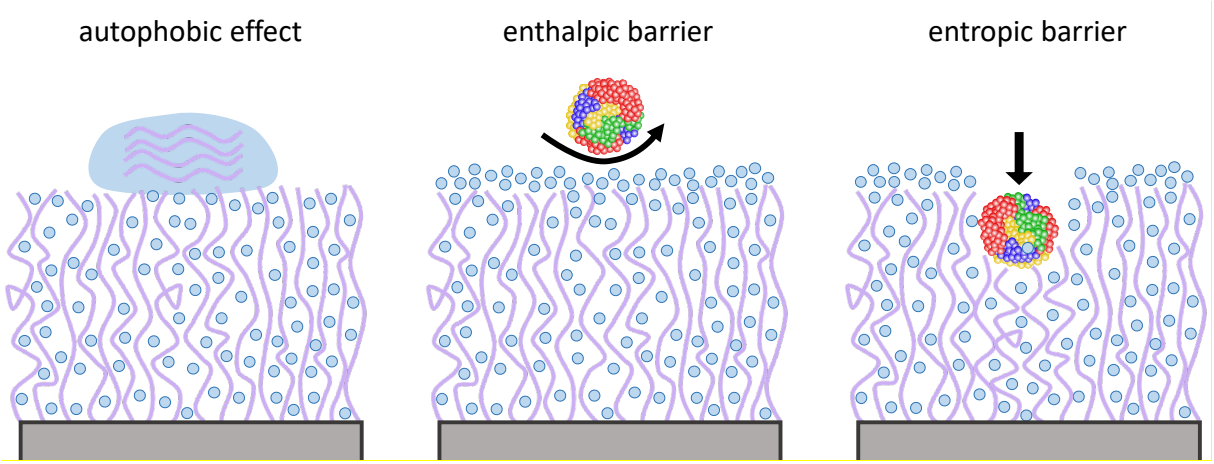

Figure 2.4. Autophobic effect as well as enthalpic and entropic repellency of polymer brushes to prevent protein adsorption.

The autophobic effect results from the difference in entropy between end-grafted and free polymers. The grafting of dense polymer brushes creates internal pressure and even a drop of a chemically identical polymer melt will not wet the densely grafted polymer brushes.[54-55] Moreover, the adhesion of biomolecules onto the brush coating would imply the unfavorable compression of the polymer chains and displacement of water molecules associated with the polymer chains into the bulk. Together these effects create significant entropic and enthalpic penalties that effectively inhibit biomolecule fouling. Polymer brushes have gained increased attention as antimicrobial coatings due their superior antifouling properties , however their realization on medical devices still remains a challenge. Their synthesis involves surface functionalization with initiator groups and requires rather stringent polymerization conditions, such as anaerobic atmosphere which is not easily to realize in clinical settings. Throughout this thesis, diverse methods will be introduced to achieve effective polymer brush-like coatings on a wide range of medical devices. These coatings exert antifouling properties on par with the best “grafting from” polymer brushes.

2.3.2 Contact-Killing materials

Contact-killing surface modification are basically able to kill bacteria on direct contact to the surface. Most of these strategies are based on cationic polymers, N-halamine polymers, antimicrobial peptides (AMPs) and enzymes.[56]

Cationic polymers: The bactericidal mechanism of cationic polymer coatings is based on the attraction of the negatively charged bacterium to the surface, where the polymers are able to disrupt the bacterial cell membrane causing bacterial death. Most cationic polymer coatings include chitosan, polyquarternary ammonium compounds or polyethylenamine.[56-57] Despite their antimicrobial efficacy, their clinical application is very limited due to a lack of selectivity in their mode of action, which can also cause toxicity to mammalian cells.[58-59]

Antimicrobial peptides: AMPs also known as host defense peptides (HDPs) are oligopeptides bearing cationic and hydrophobic regions that target the cytoplasmic membrane of bacteria and intracellular components such as nucleic acids and proteins. These peptides employ three different membrane disruption mechanisms: (1) barrel stave pores, (2) toroidal pores and (3) the carpet mechanism. In general, AMPs bind to bacteria through their cationic domains and then insert their hydrophobic regions into the bacterial membrane. In the case of barrel staves, the peptides create in this way channel-like pores in the cell membrane. Toroidal pores are formed through the interaction of the AMPs with the lipid head groups of the membrane bilayer, causing it to bend inward, resulting in the formation of a pore. The carpet mechanism, involves AMPs binding to the anionic lipids of the bilayer, causing a detergent-like disruption of the membrane into small pieces. Because of their mode of action targeting a fundamental structure of bacteria, antimicrobial peptides are active against both Gram-positive and Gram-negative bacteria. Furthermore, the likelihood of bacterial resistance development is reduced, as mutations are unlikely to result in fundamental changes to the membrane.[59-60] While AMPs represent promising alternatives to antibiotics, their clinical application has been so far precluded due to high costs of production and their susceptibility to biodegradation. Additionally, the immobilization of AMPs often results in a reduction or complete loss of activity. Unlike other antimicrobial agents, AMPs demonstrate efficient antibacterial activity only when properly oriented on the surface.[61-63]

Antimicrobial enzymes: In the past, incorporating antimicrobial enzymes into surface coatings received scarce attention. It is only recently that the significant potential of immobilized enzymes to prevent biofilm formation has been recognized. The two main categories of contact-killing antimicrobial enzymes are hydrolytic enzymes and EPS-degrading enzymes. Hydrolytic enzymes degrade the bacterial cell wall by cleaving polysaccharide chains (glycosidases) or polypeptide chains (endopeptidases) or both (amidases). EPS-degrading

enzymes target the polysaccharides, eDNA or proteins of the EPS to destabilize and eliminate biofilms. Several research groups have shown that the physical and chemical immobilization of enzymes on surfaces not only improved the thermostability and bench stability, but also led to a potentiation of the antimicrobial efficiency. Immobilizing amylase, cellobiohydrolase, pectinase, subtilisin A and β-N-acetyl-glucosaminidase (DspB) has been shown to be more effective in inhibiting biofilm formation and removing matured biofilms compared to their free forms.[64-65]

2.3.3 Antimicrobial-eluting materials

Another approach to mitigate BAIs involves modifying medical devices with coatings design to release antimicrobial agents over a period of time. Most of these materials are based on the release of antibiotics. However, in the context of this chapter, I will focus on materials that incorporate non-antibiotic bactericidal agents supporting antimicrobial stewardship. These strategies are based on the bactericidal activity of chlorhexidine, metals, antimicrobial peptides and enzymes. To date chlorhexidine is one of the most effective antimicrobial agents used in the field of orthodontics against plaque.[66-67] It is a cationic molecule that interacts with the negatively charged bacterium. Chlorhexidine is able to penetrate the cell wall via passive diffusion, reaching to the cell membrane and disrupting its integrity. Moreover, it also leads to cytoplasmic coagulation and precipitation of components like ATP and nucleic acid. Metal-based coatings most commonly incorporate the antimicrobial activity of silver, copper and zinc. Among these, the release of silver ions is a widely applied mechanism in medical device products.[68] Their exact antimicrobial mode of action is not yet clarified, but it is believed to be associated to permeabilization of the cell membrane, binding and inhibition of enzymes and proteins necessary for cell survival, interruption of DNA replication and the generation of reactive oxygen species (ROS). While silver ions exhibit considerable antimicrobial efficacy, there is growing concern about their negative impact on human health and environmental toxicity.[69-72] The same holds in the case of copper and zinc-based coatings.[72-73] Furthermore, there have been several reports of the emergence of metal-resistant bacterial isolates[74-75], underscoring the need for cautious use of these metals. It should be noted that, despite the many advantages of using antimicrobial proteins and enzymes (*vide infra*), the main drawback of their use in eluting systems is their susceptibility

to degradation, temperature and pH, which can cause their denaturation and inhibit their activity.

In general, the effectiveness of antimicrobial-eluting systems depends not only on the type of antimicrobial used, but also on the manner and rate at which they are released to their environment. It is crucial to avoid a burst release to ensure a long-term antimicrobial activity of such strategies. In particular, battling AMR and BAIs requires sustained inhibition of biofilm formation. Certainly, the formulation of multifunctional coatings that synergistically combine several non-adhesive and bactericidal phenomena may hold promise for the development of super-antimicrobial materials.[76-77] In deed, in this dissertation I will introduce a novel antimicrobial coating that combines antifouling properties with bactericidal action on contact. This coating offered improved protection against microbes compared to coatings based on a single strategy.

2.4 HDP-mimicking polymers

As mentioned before, HDP present promising alternatives to antibiotics with a broad bactericidal spectrum. However, high production costs as well as poor stability to proteases and peptidases have hindered their translation into clinical use. In a quest to circumvent these challenges, researchers have focused to design synthetic mimics of HDPs.[60, 78] These molecules should mimic the physiochemical properties of HDP but exert enhanced stability. A number of different systems have been introduced ranging from peptides composed of α-amino acids[79-80], β-amino acids[81-82], peptoids[83], aromatic oligomers[84-85] and synthetic polymers[86-90]. One of the most promising approaches involved the development of HDP-mimicking polymers, offering the advantages of large-scale productions at lower costs.[91] Moreover, they can be designed for heightened stability against enzymatic degradation, thereby improving pharmacokinetics. HDP-mimicking polymers are typically composed of cationic and hydrophobic segments and are mostly based on amphiphilic random copolymers, block copolymers or facially amphiphilic polymers.[92] In the latter system, every repeating unit features both a positively charged and a hydrophobic moiety. Mirroring natural HDPs, the cationic segments allow these molecules to adhere preferentially to the negatively charged membrane of bacteria over zwitterionic mammalian cell membranes. The hydrophobic moieties are responsible for their insertion into the lipid membrane of the microbe causing

disruption of integrity and ultimately microbial death. Thus, akin to natural HDPs, these synthetic molecules exhibit antimicrobial activity against both Gram-positive and Gram-negative bacteria with a low risk of resistance development.[60, 78, 91, 93] The key aspect in designing effective HDP-mimicking polymers is to achieve a high level of antimicrobial activity, while at the same time exert low toxicity to mammalian cells. The desired properties can be adjusted from the local monomer structure, the distribution of cationic and hydrophobic moieties in the polymer and the amphiphilic balance.[91, 94-98] For example in the latter, an overexpression of hydrophobic segments increases off-target interaction with eukaryotic cells, while too many cationic segments would result in weaker antimicrobial activities. In particular the use of facially amphiphilic polymers exerting segmented regions of cationic or hydrophobic moieties along the polymer chain have demonstrated efficient HDP-mimicking constructs, with high bactericidal abilities against a broad range of bacterial pathogens. At the same time, they maintain good cytocompatibility with eukaryotic cells.[84, 98-99] Their special amphiphilic molecular conformation, with concentrated charged and hydrophobic domains, maximizes both polar and non-polar interactions and enables these molecules to preferentially interact with the bacterial cell membrane. Although considerable research is still needed to understand the full versatility of these systems, their great potential shows that HDP-mimicking polymers hold great promise as alternatives to traditional antibiotics in healthcare.

2.5 Cell Mimics for Antimicrobial Biomedical Applications

Cell mimics or synthetic cells are artificial cell-like (compartmentalized) supramolecular structures designed to mimic some functions, interactions and structure of living cells. Bottom-up synthetic biology focuses particularly on the assembly of cell mimics from scratch with a minimal set of well-characterized building units bypassing the complexity and redundancies present in natural cells.[100-105] In this vein, natural and abiotic molecular structures such as lipids, proteins, polymers, Janus dendrimers are rationally combined to form supramolecular compartments that can mimic some of the essential functions and behaviors of natural cells (Figure 2.5). Examples include cell-mimics capable of synthesizing their own ATP[106-112], carrying out metabolic reactions[112-113], protein expression[114-115], replication[116-119], growth[120-123], division[117, 119, 121, 124-130], signaling[131-132] and motility[133-138].

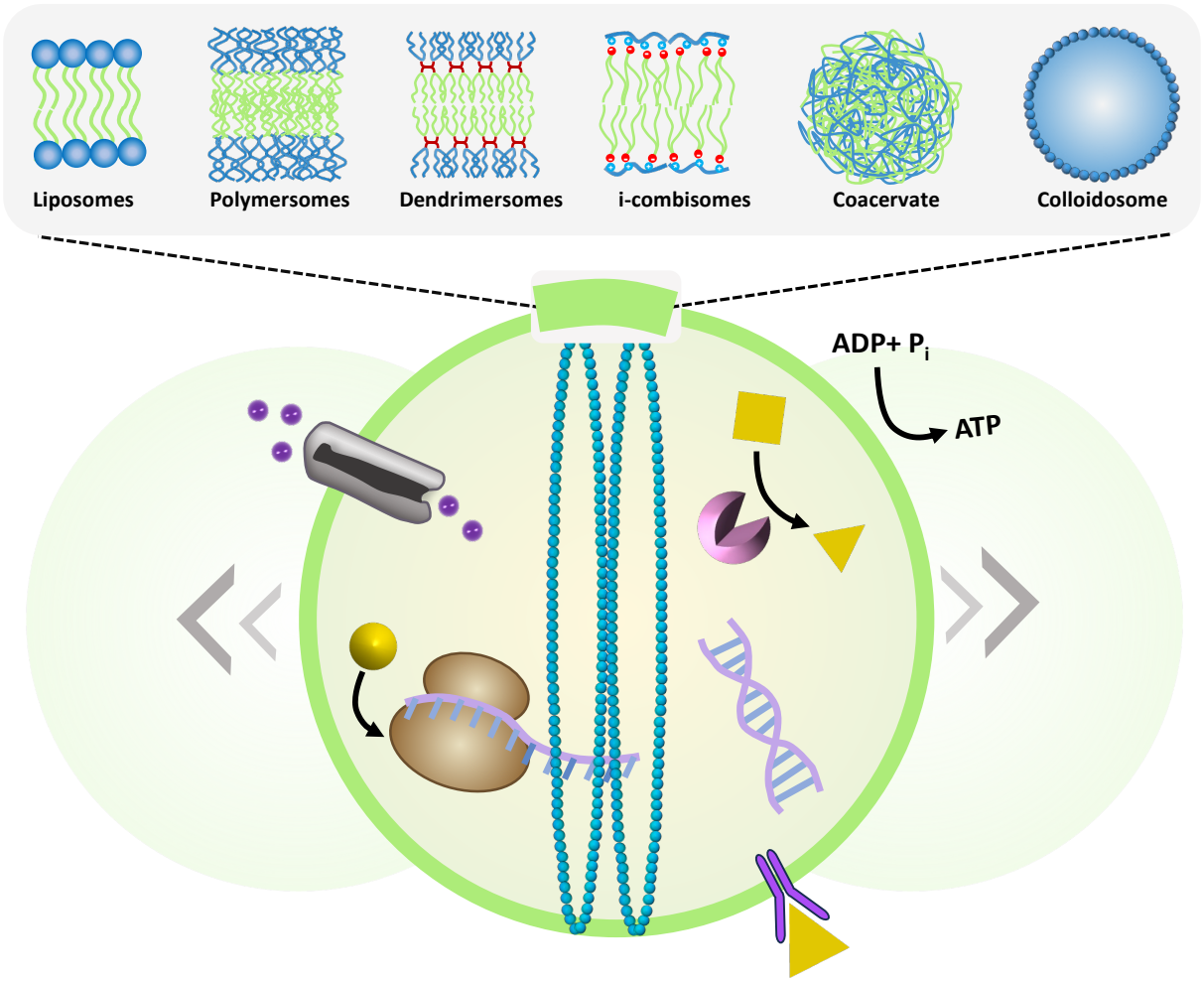

Figure 2.5. Scheme showing the life-like features of cell mimics. These synthetic cells can be composed of different structural elements.

The development of artificial cell mimics in the field of cell biology holds promise to unveil the intrinsic complexity of cellular mechanisms, address biological questions and provide insights into the origin of life. Moreover, the properties of cell mimics can extend beyond those of living systems, making them valuable as therapeutic alternatives and laying foundation for the development of the next generation of smart biomaterials with life-like behavior.[139-140] Recently, cell mimics are being explored for various biomedical applications, including immunotherapy[141-142], bone tissue engineering[143], responsive therapeutics[144-146] and for antimicrobial purposes[147-150]. In the context of the latter Tan and coworkers developed cell mimics with the ability to sense, interact and kill bacteria.[147] They achieved this by incorporating transcription–translation machinery and a quorum-sensing circuit into their lipid-based cell mimics. Upon the bacteria producing the quorum-sensing molecule *N*-Acyl homoserine lactone, the cell mimics initiate the expression of the antimicrobial peptide

Bac2A, which ultimately kills the bacteria. By expressing the Bac2A protein *in situ*, challenges related to the long-term stability of AMPs are circumvented. Furthermore, different groups have work on the development of synthetic cells with the ability to ingest and sequester objects, including bacterial pathogens.[149, 151-155] Rodriguez-Emmenegger et. al. developed cell mimics based on Janus dendrimers able to resemble a rudimentary for of endocytosis engulf *E. coli* bacteria.[149] Strikingly, engulfment was successfully achieved without the need for cellular machinery and relying only on low binding energies. Another approach for the transmembrane transport of bacteria was introduced by the research group of Sacanna.[150] They developed inorganic colloidal cell-mimics featuring a well-defined micropore through which the bacteria are captured. This involved the incorporation of an internal photoswitchable catalyst. Upon exposure to blue light and hydrogen peroxide, acting as fuel, the catalyst generates a chemical gradient that propagates through the micropore to the outside, serving as a phoretic tractor beam that pumps the bacteria inside. While both of these strategies allow for the isolation of the bacterial pathogen from the environment, they have not included yet a killing mechanism. There are only a few reports of synthetic cells that combine both mechanisms of capturing and destroying the captured microbe. One of them is the work of Spatz et. al., where they developed porous microcapsules that contained quaternary ammonium silane-modified SiO_2 microbeads in their interior.[156] This is a cationic compound that has been shown to kill bacteria upon contact. However, its bactericidal action is not specific for bacterial cells and can induce toxicity upon contact with eukaryotic cells.[157] Moreover, Huang and coworkers formulated membranized coacervate-based cell mimics capable of selectively sequestering *E.coli* bacteria within the coacervate and eradicate them.[148] The membrane was reconstituted from yeast cellular wall fragments which naturally contain mannans, a protein known to induce adhesion between yeast cells and FimH expressing bacteria. Additionally, the coacervates were composed of sodium hyaluronate and quaternized amylose, so that after adhesion and internalization of the bacteria through their interaction with the mannans present on the membrane, killing continues due to exposure to the cationic amylose derivative. Synthetic cells provide an inherently dynamic and bioactive platform that holds great potential for advancing active antimicrobials. Their modular constitution, allows for versatile configurations to enhance their specificity towards pathogens.

2.6 References

[1] W. Msemburi, A. Karlinsky, V. Knutson, S. Aleshin-Guendel, S. Chatterji, J. Wakefield, *Nature* **2023**, *613*, 130-137.

[2] R. E. Baker, A. S. Mahmud, I. F. Miller, M. Rajeev, F. Rasambainarivo, B. L. Rice, S. Takahashi, A. J. Tatem, C. E. Wagner, L.-F. Wang, A. Wesolowski, C. J. E. Metcalf, *Nature Reviews Microbiology* **2022**, *20*, 193-205.

[3] EclinicalMedicine, *eClinicalMedicine* **2021**, *41*.

[4] C. J. L. Murray, K. S. Ikuta, F. Sharara, L. Swetschinski, G. Robles Aguilar, A. Gray, C. Han, C. Bisignano, P. Rao, E. Wool, S. C. Johnson, A. J. Browne, M. G. Chipeta, F. Fell, S. Hackett, G. Haines-Woodhouse, B. H. Kashef Hamadani, E. A. P. Kumaran, B. McManigal, S. Achalapong, R. Agarwal, S. Akech, S. Albertson, J. Amuasi, J. Andrews, A. Aravkin, E. Ashley, F.-X. Babin, F. Bailey, S. Baker, B. Basnyat, A. Bekker, R. Bender, J. A. Berkley, A. Bethou, J. Bielicki, S. Boonkasidecha, J. Bukosia, C. Carvalheiro, C. Castañeda-Orjuela, V. Chansamouth, S. Chaurasia, S. Chiurchiù, F. Chowdhury, R. Clotaire Donatien, A. J. Cook, B. Cooper, T. R. Cressey, E. Criollo-Mora, M. Cunningham, S. Darboe, N. P. J. Day, M. De Luca, K. Dokova, A. Dramowski, S. J. Dunachie, T. Duong Bich, T. Eckmanns, D. Eibach, A. Emami, N. Feasey, N. Fisher-Pearson, K. Forrest, C. Garcia, D. Garrett, P. Gastmeier, A. Z. Giref, R. C. Greer, V. Gupta, S. Haller, A. Haselbeck, S. I. Hay, M. Holm, S. Hopkins, Y. Hsia, K. C. Iregbu, J. Jacobs, D. Jarovsky, F. Javanmardi, A. W. J. Jenney, M. Khorana, S. Khusuwan, N. Kissoon, E. Kobeissi, T. Kostyanev, F. Krapp, R. Krumkamp, A. Kumar, H. H. Kyu, C. Lim, K. Lim, D. Limmathurotsakul, M. J. Loftus, M. Lunn, J. Ma, A. Manoharan, F. Marks, J. May, M. Mayxay, N. Mturi, et al., *The Lancet* **2022**, *399*, 629-655.

[5] B. Peng, H. Li, X.-x. Peng, *Drug Discovery Today* **2023**, *28*, 103753.

[6] C. Kirchhelle, *Palgrave Communications* **2018**, *4*, 96.

[7] https://open.oregonstate.education/microbiology/chapter/14-2mechanisms-of-antibacterial-drugs/ 2023, 8 December.

[8] G. Kapoor, S. Saigal, A. Elongavan, *J Anaesthesiol Clin Pharmacol* **2017**, *33*, 300-305.

[9] W. C. Reygaert, *AIMS Microbiol* **2018**, *4*, 482-501.

[10] J. G. Bartlett, D. N. Gilbert, B. Spellberg, *Clinical Infectious Diseases* **2013**, *56*, 1445-1450.

[11] E. M. Darby, E. Trampari, P. Siasat, M. S. Gaya, I. Alav, M. A. Webber, J. M. A. Blair, *Nature Reviews Microbiology* **2023**, *21*, 280-295.

[12] B. Aslam, W. Wang, M. I. Arshad, M. Khurshid, S. Muzammil, M. H. Rasool, M. A. Nisar, R. F. Alvi, M. A. Aslam, M. U. Qamar, M. K. F. Salamat, Z. Baloch, *Infect Drug Resist* **2018**, *11*, 1645-1658.

[13] M. I. Hutchings, A. W. Truman, B. Wilkinson, *Current Opinion in Microbiology* **2019**, *51*, 72-80.

[14] E. Martens, A. L. Demain, *The Journal of Antibiotics* **2017**, *70*, 520-526.

[15] B. Spellberg, D. N. Gilbert, *Clin Infect Dis* **2014**, *59 Suppl 2*, S71-75.

[16] S. S. Naik, G. Anusha, K. V. Leela, S. Ravi, in *Advances in Novel Formulations for Drug Delivery*, **2023**, pp. 219-229.

[17] V. Bhandari, A. Suresh, *Frontiers in Pharmacology* **2022**, *13*.

[18] N. A. Hodges, E. M. Sussman, J. P. Stegemann, *Biomaterials* **2021**, *278*, 121127.

[19] Y. Ding, Y. Hao, Z. Yuan, B. Tao, M. Chen, C. Lin, P. Liu, K. Cai, *Biomaterials Science* **2020**, *8*, 1840-1854.

[20] S. Veerachamy, T. Yarlagadda, G. Manivasagam, P. K. Yarlagadda, *Proc. Inst. Mech. Eng., Part H* **2014**, *228*, 1083-1099.

[21] C. R. Arciola, D. Campoccia, L. Montanaro, *Nat. Rev. Microbiol.* **2018**, *16*, 397-409.

[22] T.-F. C. Mah, G. A. O'Toole, *Trends in Microbiology* **2001**, *9*, 34-39.

[23] W. Norde, J. Lyklema, *Journal of Biomaterials Science, Polymer Edition* **1991**, *2*, 183-202.

[24] R. Murga, J. M. Miller, R. M. Donlan, *J Clin Microbiol* **2001**, *39*, 2294-2297.

[25] Y. Kozuka, Z. Lu, T. Masuda, S. Hara, T. Kasama, R. Miyake, N. Isu, M. Takai, *Journal of Materials Chemistry B* **2021**, *9*, 4480-4487.

[26] W. G. Characklis, K. E. Cooksey, in *Advances in Applied Microbiology, Vol. 29* (Ed.: A. I. Laskin), Academic Press, **1983**, pp. 93-138.

[27] W. Norde, *Journal of Dispersion Science and Technology* **1992**, *13*, 363-377.

[28] W. Norde, *Macromolecular Symposia* **1996**, *103*, 5-18.

[29] W. Norde, J. Lyklema, *J Biomater Sci Polym Ed* **1991**, *2*, 183-202.

[30] F. Poncin-Epaillard, T. Vrlinic, D. Debarnot, M. Mozetic, A. Coudreuse, G. Legeay, B. El Moualij, W. Zorzi, *Journal of Functional Biomaterials* **2012**, *3*, 528-543.

[31] R. A. Latour, *Colloids Surf B Biointerfaces* **2020**, *191*, 110992.

[32] J. D. Andrade, V. Hlady, Springer Berlin Heidelberg, Berlin, Heidelberg, **1986**, pp. 1-63

[33] J. E. Contreras-Naranjo, O. Aguilar, *Biosensors* **2019**, *9*, 15.

[34] M. Thompson, C. Blaszykowski, S. Sheikh, C. Rodriguez-Emmenegger, A. de los Santos Pereira, *Biological Fluid–Surface Interactions in Detection and Medical Devices*, The Royal Society of Chemistry, **2016**.

[35] A. Uneputty, A. Dávila-Lezama, D. Garibo, A. Oknianska, N. Bogdanchikova, J. F. Hernández-Sánchez, A. Susarrey-Arce, *Colloid and Interface Science Communications* **2022**, *46*, 100560.

[36] C. Bernhard, S. J. Roeters, J. Franz, T. Weidner, M. Bonn, G. Gonella, *Physical Chemistry Chemical Physics* **2017**, *19*, 28182-28188.

[37] X. Xu, Y. Chang, Y. Gong, Y. Zhang, Y. Yu, H. Peng, C. Fu, *ACS Applied Polymer Materials* **2023**.

[38] M. Fu, Y. Liang, X. Lv, C. Li, Y. Y. Yang, P. Yuan, X. Ding, *Journal of Materials Science & Technology* **2021**, *85*, 169-183.

[39] A. Utrata-Wesołek, *Polimery* **2013**, *58*, 685-695.

[40] Y. Choi, H.-V. Tran, T. R. Lee, *Coatings* **2022**, *12*, 1462.

[41] N.-P. Huang, R. Michel, J. Voros, M. Textor, R. Hofer, A. Rossi, D. L. Elbert, J. A. Hubbell, N. D. Spencer, *Langmuir* **2001**, *17*, 489-498.

[42] G. L. Kenausis, J. Vörös, D. L. Elbert, N. Huang, R. Hofer, L. Ruiz-Taylor, M. Textor, J. A. Hubbell, N. D. Spencer, *The Journal of Physical Chemistry B* **2000**, *104*, 3298-3309.

[43] R. Guo, Y. Liu, Y. Zhang, A. Dong, J. Zhang, *Macromolecular Research* **2013**, *21*, 1127-1137.

[44] A. R. Kuzmyn, A. T. Nguyen, L. W. Teunissen, H. Zuilhof, J. Baggerman, *Langmuir* **2020**, *36*, 4439-4446.

[45] S. Edmondson, V. L. Osborne, W. T. S. Huck, *Chemical Society Reviews* **2004**, *33*, 14-22.

[46] R. Advincula, W. Brittain, K. Caster, J. Rühe, **2004**.

[47] Y. Liu, D. Zhang, B. Ren, X. Gong, L. Xu, Z.-Q. Feng, Y. Chang, Y. He, J. Zheng, *Journal of Materials Chemistry B* **2020**, *8*, 3814-3828.

[48] Y.-M. Wang, A. Kálosi, Y. Halahovets, I. Romanenko, J. Slabý, J. Homola, J. Svoboda, A. de los Santos Pereira, O. Pop-Georgievski, *Polymer Chemistry* **2022**, *13*, 3815-3826.

[49] J. Baggerman, M. M. J. Smulders, H. Zuilhof, *Langmuir* **2019**, *35*, 1072-1084.

[50] C. Rodriguez-Emmenegger, E. Brynda, T. Riedel, M. Houska, V. Šubr, A. B. Alles, E. Hasan, J. E. Gautrot, W. T. S. Huck, *Macromolecular Rapid Communications* **2011**, *32*, 952-957.
[51] C. Rodriguez-Emmenegger, S. Janel, A. de los Santos Pereira, M. Bruns, F. Lafont, *Polymer Chemistry* **2015**, *6*, 5740-5751.
[52] C. Rodriguez Emmenegger, E. Brynda, T. Riedel, Z. Sedlakova, M. Houska, A. B. Alles, *Langmuir* **2009**, *25*, 6328-6333.
[53] C. Rodriguez-Emmenegger, C. M. Preuss, B. Yameen, O. Pop-Georgievski, M. Bachmann, J. O. Mueller, M. Bruns, A. S. Goldmann, M. Bastmeyer, C. Barner-Kowollik, *Advanced Materials* **2013**, *25*, 6123-6127.
[54] L. Leibler, A. Mourran, *MRS Bulletin* **1997**, *22*, 33-37.
[55] G. Reiter, R. Khanna, *Langmuir* **2000**, *16*, 6351-6357.
[56] J. Yao, P. Zou, Y. Cui, L. Quan, C. Gao, Z. Li, W. Gong, M. Yang, *Pharmaceutics* **2023**, *15*.
[57] Y. Qiu, N. Zhang, Y. H. An, X. Wen, *The International Journal of Artificial Organs* **2007**, *30*, 828-841.
[58] H. Qiu, Z. Si, Y. Luo, P. Feng, X. Wu, W. Hou, Y. Zhu, M. B. Chan-Park, L. Xu, D. Huang, *Front Bioeng Biotechnol* **2020**, *8*, 910.
[59] Q. Song, Y. Pei, X. Ye, P. Li, W. Huang, in *Racing for the Surface: Antimicrobial and Interface Tissue Engineering* (Eds.: B. Li, T. F. Moriarty, T. Webster, M. Xing), Springer International Publishing, Cham, **2020**, pp. 115-128.
[60] H. Etayash, R. E. W. Hancock, *Pharmaceutics* **2021**, *13*.
[61] S.-C. Park, Y. Park, K.-S. Hahm, *International Journal of Molecular Sciences* **2011**, *12*, 5971-5992.
[62] Y. Cao, M. Naseri, Y. He, C. Xu, L. J. Walsh, Z. M. Ziora, *Journal of Global Antimicrobial Resistance* **2020**, *21*, 445-451.
[63] M. Riool, S. A. J. Zaat, in *Urinary Stents: Current State and Future Perspectives* (Eds.: F. Soria, D. Rako, P. de Graaf), Springer International Publishing, Cham, **2022**, pp. 245-257.
[64] F. Villa, F. Secundo, A. Polo, F. Cappitelli, *Current Microbiology* **2015**, *71*, 106-114.
[65] D. Lahiri, M. Nag, A. Dey, T. Sarkar, R. R. Ray, M. Rebezov, M. A. Shariati, M. Thiruvengadam, J. Simal-Gandara, *Biotechnology Progress* **2022**, *38*, e3281.
[66] B. D. Eden, in *Prevention in Clinical Oral Health Care* (Eds.: D. P. Cappelli, C. C. Mobley), Mosby, Saint Louis, **2008**, pp. 213-229.
[67] M. Łukomska-Szymańska, J. Sokołowski, B. Łapińska, *Czasopismo stomatologiczne* **2017**, *70*.
[68] V. Marassi, L. Di Cristo, S. G. J. Smith, S. Ortelli, M. Blosi, A. L. Costa, P. Reschiglian, Y. Volkov, A. Prina-Mello, *R Soc Open Sci* **2018**, *5*, 171113.
[69] S.-L. Abram, K. M. Fromm, *Chemistry – A European Journal* **2020**, *26*, 10948-10971.
[70] A. Frei, A. D. Verderosa, A. G. Elliott, J. Zuegg, M. A. T. Blaskovich, *Nature Reviews Chemistry* **2023**, *7*, 202-224.
[71] A. Shahid, B. Aslam, S. Muzammil, N. Aslam, M. Shahid, A. Almatroudi, K. S. Allemailem, M. Saqalein, M. A. Nisar, M. H. Rasool, M. Khurshid, *Journal of Applied Biomaterials & Functional Materials* **2021**, *19*, 22808000211040304.
[72] M. Rosenberg, K. Ilić, K. Juganson, A. Ivask, M. Ahonen, I. Vinković Vrček, A. Kahru, *PeerJ* **2019**, *7*, e6315.
[73] O. Bondarenko, K. Juganson, A. Ivask, K. Kasemets, M. Mortimer, A. Kahru, *Archives of Toxicology* **2013**, *87*, 1181-1200.

[74] A. E. M. Hosny, S. A. Rasmy, D. S. Aboul-Magd, M. T. Kashef, Z. E. El-Bazza, *Infect Drug Resist* **2019**, *12*, 1985-2001.
[75] P. Vats, U. J. Kaur, P. Rishi, *Journal of Applied Microbiology* **2022**, *132*, 4058-4076.
[76] T. Wei, Q. Yu, H. Chen, *Advanced Healthcare Materials* **2019**, *8*, 1801381.
[77] M. Mu, X. Wang, M. Taylor, A. Castillo, L. Cisneros-Zevallos, M. Akbulut, Y. Min, *Colloid and Interface Science Communications* **2023**, *55*, 100717.
[78] Y. Yang, Z. Cai, Z. Huang, X. Tang, X. Zhang, *Polymer Journal* **2018**, *50*, 33-44.
[79] M. Zasloff, *Proceedings of the National Academy of Sciences* **1987**, *84*, 5449-5453.
[80] Y. Chen, C. T. Mant, S. W. Farmer, R. E. Hancock, M. L. Vasil, R. S. Hodges, *J Biol Chem* **2005**, *280*, 12316-12329.
[81] Y. Hamuro, J. P. Schneider, W. F. DeGrado, *Journal of the American Chemical Society* **1999**, *121*, 12200-12201.
[82] E. A. Porter, X. Wang, H.-S. Lee, B. Weisblum, S. H. Gellman, *Nature* **2000**, *404*, 565-565.
[83] N. P. Chongsiriwatana, J. A. Patch, A. M. Czyzewski, M. T. Dohm, A. Ivankin, D. Gidalevitz, R. N. Zuckermann, A. E. Barron, *Proceedings of the National Academy of Sciences* **2008**, *105*, 2794-2799.
[84] D. Liu, S. Choi, B. Chen, R. J. Doerksen, D. J. Clements, J. D. Winkler, M. L. Klein, W. F. DeGrado, *Angewandte Chemie International Edition* **2004**, *43*, 1158-1162.
[85] H. Tang, R. J. Doerksen, G. N. Tew, *Chemical Communications* **2005**, 1537-1539.
[86] K. Kuroda, W. F. DeGrado, *Journal of the American Chemical Society* **2005**, *127*, 4128-4129.
[87] M. A. Gelman, B. Weisblum, D. M. Lynn, S. H. Gellman, *Organic Letters* **2004**, *6*, 557-560.
[88] B. P. Mowery, S. E. Lee, D. A. Kissounko, R. F. Epand, R. M. Epand, B. Weisblum, S. S. Stahl, S. H. Gellman, *Journal of the American Chemical Society* **2007**, *129*, 15474-15476.
[89] E. F. Palermo, I. Sovadinova, K. Kuroda, *Biomacromolecules* **2009**, *10*, 3098-3107.
[90] A. Kuroki, P. Sangwan, Y. Qu, R. Peltier, C. Sanchez-Cano, J. Moat, C. G. Dowson, E. G. L. Williams, K. E. S. Locock, M. Hartlieb, S. Perrier, *ACS Applied Materials & Interfaces* **2017**, *9*, 40117-40126.
[91] H. Takahashi, G. A. Caputo, S. Vemparala, K. Kuroda, *Bioconjugate Chemistry* **2017**, *28*, 1340-1350.
[92] G. J. Gabriel, J. A. Maegerlein, C. F. Nelson, J. M. Dabkowski, T. Eren, K. Nüsslein, G. N. Tew, *Chemistry* **2009**, *15*, 433-439.
[93] M. A. Rahman, M. Bam, E. Luat, M. S. Jui, M. S. Ganewatta, T. Shokfai, M. Nagarkatti, A. W. Decho, C. Tang, *Nature Communications* **2018**, *9*, 5231.
[94] P. R. Judzewitsch, T.-K. Nguyen, S. Shanmugam, E. H. H. Wong, C. Boyer, *Angewandte Chemie International Edition* **2018**, *57*, 4559-4564.
[95] M. A. Rahman, M. S. Jui, M. Bam, Y. Cha, E. Luat, A. Alabresm, M. Nagarkatti, A. W. Decho, C. Tang, *ACS Applied Materials & Interfaces* **2020**, *12*, 21221-21230.
[96] Y. Wu, K. Chen, J. Wang, M. Chen, Y. Chen, Y. She, Z. Yan, R. Liu, *Progress in Polymer Science* **2023**, *141*, 101679.
[97] M. Concilio, R. Garcia Maset, L. P. Lemonche, V. Kontrimas, J.-I. Song, S. K. Rajendrakumar, F. Harrison, C. R. Becer, S. Perrier, *Advanced Healthcare Materials* **2023**, *12*, 2301961.
[98] P. Pham, S. Oliver, C. Boyer, *Macromolecular Chemistry and Physics* **2023**, *224*, 2200226.

[99] G. N. Tew, D. Liu, B. Chen, R. J. Doerksen, J. Kaplan, P. J. Carroll, M. L. Klein, W. F. DeGrado, *Proc Natl Acad Sci U S A* **2002**, *99*, 5110-5114.
[100] Y. Tu, F. Peng, A. Adawy, Y. Men, L. K. Abdelmohsen, D. A. Wilson, *Chem Rev* **2016**, *116*, 2023-2078.
[101] N. Laohakunakorn, L. Grasemann, B. Lavickova, G. Michielin, A. Shahein, Z. Swank, S. J. Maerkl, *Front Bioeng Biotechnol* **2020**, *8*, 213.
[102] S. Mann, *Acc Chem Res* **2012**, *45*, 2131-2141.
[103] K. Gopfrich, I. Platzman, J. P. Spatz, *Trends Biotechnol* **2018**, *36*, 938-951.
[104] P. Schwille, *Science* **2011**, *333*, 1252-1254.
[105] B. C. Buddingh, J. C. M. van Hest, *Acc Chem Res* **2017**, *50*, 769-777.
[106] G. Steinberg-Yfrach, J. L. Rigaud, E. N. Durantini, A. L. Moore, D. Gust, T. A. Moore, *Nature* **1998**, *392*, 479-482.
[107] X. Feng, Y. Jia, P. Cai, J. Fei, J. Li, *ACS Nano* **2016**, *10*, 556-561.
[108] H. J. Choi, C. D. Montemagno, *Nano Lett* **2005**, *5*, 2538-2542.
[109] L. Otrin, N. Marušič, C. Bednarz, T. Vidaković-Koch, I. Lieberwirth, K. Landfester, K. Sundmacher, *Nano Letters* **2017**, *17*, 6816-6821.
[110] B. Pitard, P. Richard, M. Dunach, J. L. Rigaud, *Eur J Biochem* **1996**, *235*, 779-788.
[111] K. Y. Lee, S. J. Park, K. A. Lee, S. H. Kim, H. Kim, Y. Meroz, L. Mahadevan, K. H. Jung, T. K. Ahn, K. K. Parker, K. Shin, *Nat Biotechnol* **2018**, *36*, 530-535.
[112] T. E. Miller, T. Beneyton, T. Schwander, C. Diehl, M. Girault, R. McLean, T. Chotel, P. Claus, N. S. Cortina, J. C. Baret, T. J. Erb, *Science* **2020**, *368*, 649-654.
[113] P. M. Gardner, K. Winzer, B. G. Davis, *Nat Chem* **2009**, *1*, 377-383.
[114] Y. Elani, R. V. Law, O. Ces, *Phys Chem Chem Phys* **2015**, *17*, 15534-15537.
[115] M. Dwidar, Y. Seike, S. Kobori, C. Whitaker, T. Matsuura, Y. Yokobayashi, *J Am Chem Soc* **2019**, *141*, 11103-11114.
[116] H. Kita, T. Matsuura, T. Sunami, K. Hosoda, N. Ichihashi, K. Tsukada, I. Urabe, T. Yomo, *Chembiochem* **2008**, *9*, 2403-2410.
[117] K. Kurihara, M. Tamura, K. Shohda, T. Toyota, K. Suzuki, T. Sugawara, *Nat Chem* **2011**, *3*, 775-781.
[118] P. van Nies, I. Westerlaken, D. Blanken, M. Salas, M. Mencia, C. Danelon, *Nat Commun* **2018**, *9*, 1583.
[119] K. Kurihara, Y. Okura, M. Matsuo, T. Toyota, K. Suzuki, T. Sugawara, *Nat Commun* **2015**, *6*, 8352.
[120] M. D. Hardy, J. Yang, J. Selimkhanov, C. M. Cole, L. S. Tsimring, N. K. Devaraj, *Proc Natl Acad Sci U S A* **2015**, *112*, 8187-8192.
[121] J. M. Castro, H. Sugiyama, T. Toyota, *Sci Rep* **2019**, *9*, 165.
[122] N. Marusic, Z. Zhao, L. Otrin, R. Dimova, I. Ivanov, K. Sundmacher, *Macromol Rapid Commun* **2022**, *43*, e2100712.
[123] H. Terasawa, K. Nishimura, H. Suzuki, T. Matsuura, T. Yomo, *Proc Natl Acad Sci U S A* **2012**, *109*, 5942-5947.
[124] S. Deshpande, W. K. Spoelstra, M. van Doorn, J. Kerssemakers, C. Dekker, *ACS Nano* **2018**, *12*, 2560-2568.
[125] Y. Dreher, K. Jahnke, E. Bobkova, J. P. Spatz, K. Gopfrich, *Angew Chem Int Ed Engl* **2021**, *60*, 10661-10669.
[126] M. de Souza Melchiors, T. Ivanov, I. Harley, C. Sayer, P. Henrique Hermes de Araujo, L. Caire da Silva, C. Ferguson, K. Landfester, *Angew Chem Int Ed Engl* **2022**.
[127] Y. Miele, Z. Medveczky, G. Hollo, B. Tegze, I. Derenyi, Z. Horvolgyi, E. Altamura, I. Lagzi, F. Rossi, *Chem Sci* **2020**, *11*, 3228-3235.

[128] J. Steinkuhler, R. L. Knorr, Z. Zhao, T. Bhatia, S. M. Bartelt, S. Wegner, R. Dimova, R. Lipowsky, *Nat Commun* **2020**, *11*, 905.
[129] T. F. Zhu, J. W. Szostak, *J Am Chem Soc* **2009**, *131*, 5705-5713.
[130] A. M. Wagner, H. Eto, A. Joseph, S. Kohyama, T. Haraszti, R. A. Zamora, M. Vorobii, M. I. Giannotti, P. Schwille, C. Rodriguez-Emmenegger, *Adv Mater* **2022**, *34*, e2202364.
[131] O. Adir, M. R. Albalak, R. Abel, L. E. Weiss, G. Chen, A. Gruber, O. Staufer, Y. Kurman, I. Kaminer, J. Shklover, J. Shainsky-Roitman, I. Platzman, L. Gepstein, Y. Shechtman, B. A. Horwitz, A. Schroeder, *Nat Commun* **2022**, *13*, 2328.
[132] M. Weiss, J. P. Frohnmayer, L. T. Benk, B. Haller, J. W. Janiesch, T. Heitkamp, M. Borsch, R. B. Lira, R. Dimova, R. Lipowsky, E. Bodenschatz, J. C. Baret, T. Vidakovic-Koch, K. Sundmacher, I. Platzman, J. P. Spatz, *Nat Mater* **2018**, *17*, 89-96.
[133] S. M. Bartelt, J. Steinkuhler, R. Dimova, S. V. Wegner, *Nano Lett* **2018**, *18*, 7268-7274.
[134] L. Wang, S. Song, J. van Hest, L. Abdelmohsen, X. Huang, S. Sanchez, *Small* **2020**, *16*, e1907680.
[135] J. Parmar, X. Ma, J. Katuri, J. Simmchen, M. M. Stanton, C. Trichet-Paredes, L. Soler, S. Sanchez, *Sci Technol Adv Mater* **2015**, *16*, 014802.
[136] D. A. Wilson, R. J. Nolte, J. C. van Hest, *Nat Chem* **2012**, *4*, 268-274.
[137] Z. Wu, X. Lin, T. Si, Q. He, *Small* **2016**, *12*, 3080-3093.
[138] X. Arque, A. Romero-Rivera, F. Feixas, T. Patino, S. Osuna, S. Sanchez, *Nat Commun* **2019**, *10*, 2826.
[139] Q. Xu, Z. Zhang, P. P. Y. Lui, L. Lu, X. Li, X. Zhang, *Materials Today Bio* **2023**, *23*, 100877.
[140] M. H. M. E. van Stevendaal, J. C. M. van Hest, A. F. Mason, *ChemSystemsChem* **2021**, *3*, e2100009.
[141] M. Amidi, M. de Raad, D. J. A. Crommelin, W. E. Hennink, E. Mastrobattista, *Systems and Synthetic Biology* **2011**, *5*, 21-31.
[142] Y. Lu, L. Li, J. Du, J. Chen, X. Xu, X. Yang, C. Ding, C. Mao, *ACS Applied Materials & Interfaces* **2021**, *13*, 55890-55901.
[143] F. Itel, J. Skovhus Thomsen, B. Städler, *ACS Appl Mater Interfaces* **2018**, *10*, 30180-30190.
[144] R. Lentini, N. Y. Martín, M. Forlin, L. Belmonte, J. Fontana, M. Cornella, L. Martini, S. Tamburini, W. E. Bentley, O. Jousson, S. S. Mansy, *ACS Central Science* **2017**, *3*, 117-123.
[145] R. Lentini, S. P. Santero, F. Chizzolini, D. Cecchi, J. Fontana, M. Marchioretto, C. Del Bianco, J. L. Terrell, A. C. Spencer, L. Martini, M. Forlin, M. Assfalg, M. D. Serra, W. E. Bentley, S. S. Mansy, *Nature Communications* **2014**, *5*, 4012.
[146] Ö. D. Toparlak, J. Zasso, S. Bridi, M. D. Serra, P. Macchi, L. Conti, M.-L. Baudet, S. S. Mansy, *Science Advances* **2020**, *6*, eabb4920.
[147] Y. Ding, L. E. Contreras-Llano, E. Morris, M. Mao, C. Tan, *ACS Applied Materials & Interfaces* **2018**, *10*, 30137-30146.
[148] C. Zhao, J. Li, S. Wang, Z. Xu, X. Wang, X. Liu, L. Wang, X. Huang, *ACS Nano* **2021**, *15*, 10048-10057.
[149] N. Y. Kostina, K. Rahimi, Q. Xiao, T. Haraszti, S. Dedisch, J. P. Spatz, U. Schwaneberg, M. L. Klein, V. Percec, M. Möller, C. Rodriguez-Emmenegger, *Nano Letters* **2019**, *19*, 5732-5738.
[150] Z. Xu, T. Hueckel, W. T. M. Irvine, S. Sacanna, *Nature* **2021**, *597*, 220-224.
[151] L. Rodriguez-Arco, M. Li, S. Mann, *Nat Mater* **2017**, *16*, 857-863.
[152] Y. Qiao, M. Li, R. Booth, S. Mann, *Nat Chem* **2017**, *9*, 110-119.
[153] Y. Qiao, M. Li, D. Qiu, S. Mann, *Angew Chem Int Ed Engl* **2019**, *58*, 17758-17763.

[154] K. A. Smith, D. Jasnow, A. C. Balazs, *J Chem Phys* **2007**, *127*, 084703.
[155] K. Jaskiewicz, A. Larsen, D. Schaeffel, K. Koynov, I. Lieberwirth, G. Fytas, K. Landfester, A. Kroeger, *ACS Nano* **2012**, *6*, 7254-7262.
[156] R. Luo, S. Pashapour, O. Staufer, I. Platzman, J. Spatz, *Advanced Functional Materials* **2020**, *30*.
[157] Y. Jiao, L. N. Niu, S. Ma, J. Li, F. R. Tay, J. H. Chen, *Prog Polym Sci* **2017**, *71*, 53-90.

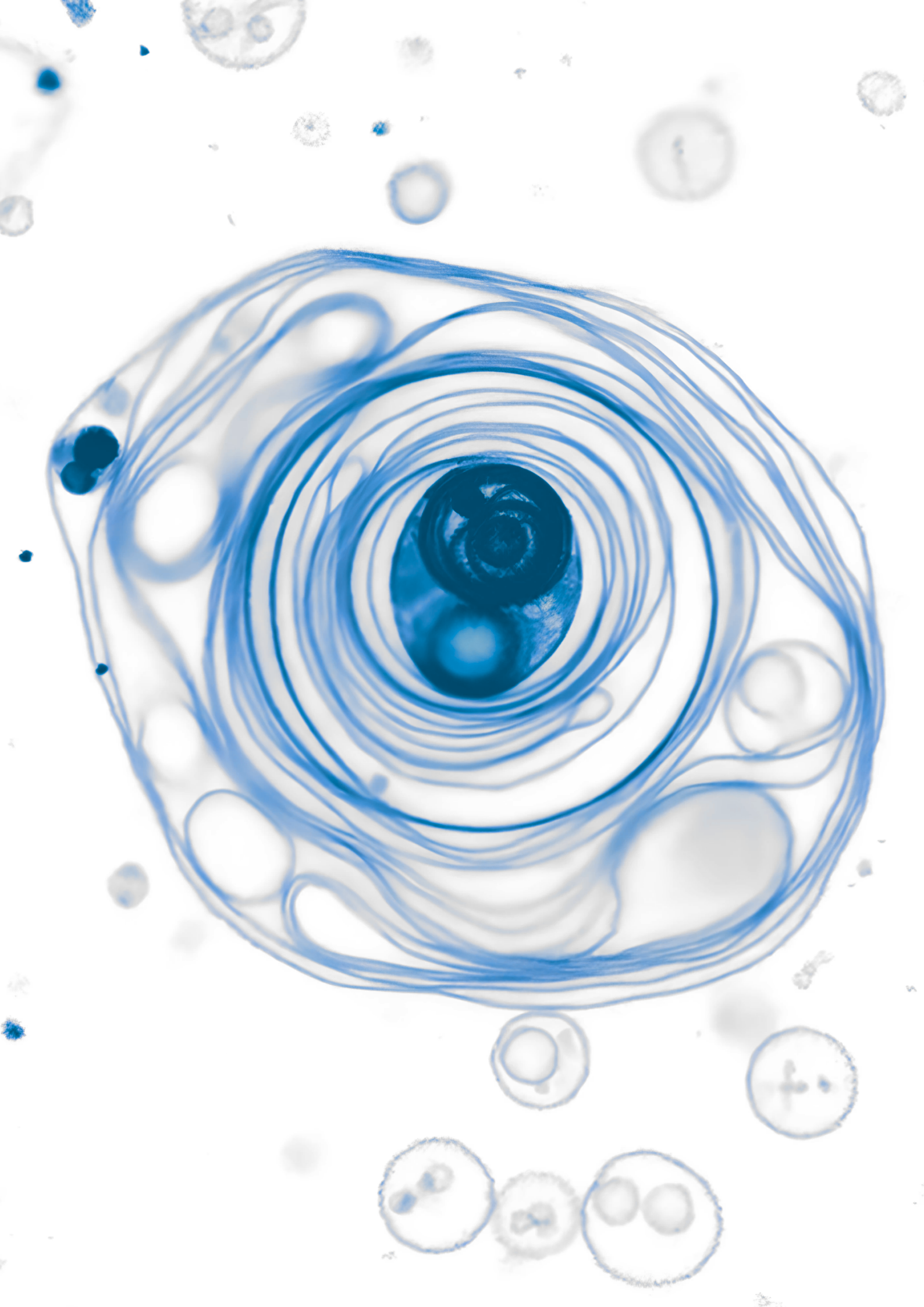

Chapter 3

Chemical Routes to Graft Polymer Brushes that Minimize Bacterial Adhesion

3.1 Introduction

Biointerfaces play a pivotal role in regulating and controlling cell-biomaterial interactions. When an exogenous material comes into contact with bodily fluids, there is immediate spontaneous adsorption of proteins at the solid-liquid interface between biomaterial surface and biological fluid. This phenomenon is known as protein fouling and is strongly dependent on the surface properties, including surface energy, polarity, charge and morphology (*vide supra*). The uncontrolled adsorption of proteins onto implants and other medical devices can trigger a series of adverse outcomes such as surface-induced coagulation, inflammatory responses, harmful immune reactions and infections. Notably, the latter is one of the main leading causes of implant failure.[1]

The onset of biomaterial-associated bacterial infections begins with protein fouling at the biomaterial surface. Adsorbed proteins create a conditioning layer that provides anchoring points for the attachment of bacterial cells ultimately leading to biofilm formation.[2-3] Therefore, it is crucial to prevent protein fouling at the biomaterial surface as a preventive measure against bacterial colonization and infection development. A leading strategy for achieving highly effective antifouling properties is the grafting of hydrophilic polymer brushes directly from the material surface at high grafting densities using surface-immobilized initiators.[4-10] These brushes create not only an enthalpic but also an entropic barrier, which successfully prohibits both the penetration and adsorption of proteins and cells.[11-16] However, given the low chemical reactivity of polymeric materials, finding an effective strategy to attach the initiator to the material surface remains an ongoing challenge. A commonly used strategy is to oxidize the surface with oxygen plasma followed by functionalization with silane-containing initiators. However, plasma treatment can cause substrate damage. Also, the generated functional groups are susceptible to diminish with time due to reorganization effects. Moreover, the formed siloxane bonds show only reduced stability under aqueous conditions which can lead to partial detachment of the polymer brushes (delamination) limiting their applicability in biological systems.[17-20]

In the upcoming chapter, I will present three different routes to achieve the incorporation of initiator groups onto the surface of a wide range of chemically inert polymeric medical devices. These include Poly(ε-caprolactone) (PCL) electrospun nanofibers, which find application as

scaffolds in tissue engineering, wound dressings and drug delivery therapeutics[21], poly(4-methyl-1-pentene) (PMP) membrane hollow fibers used in extracorporeal membrane oxygenation (ECMO) devices and Polyethylene (PE) wound contact layers.

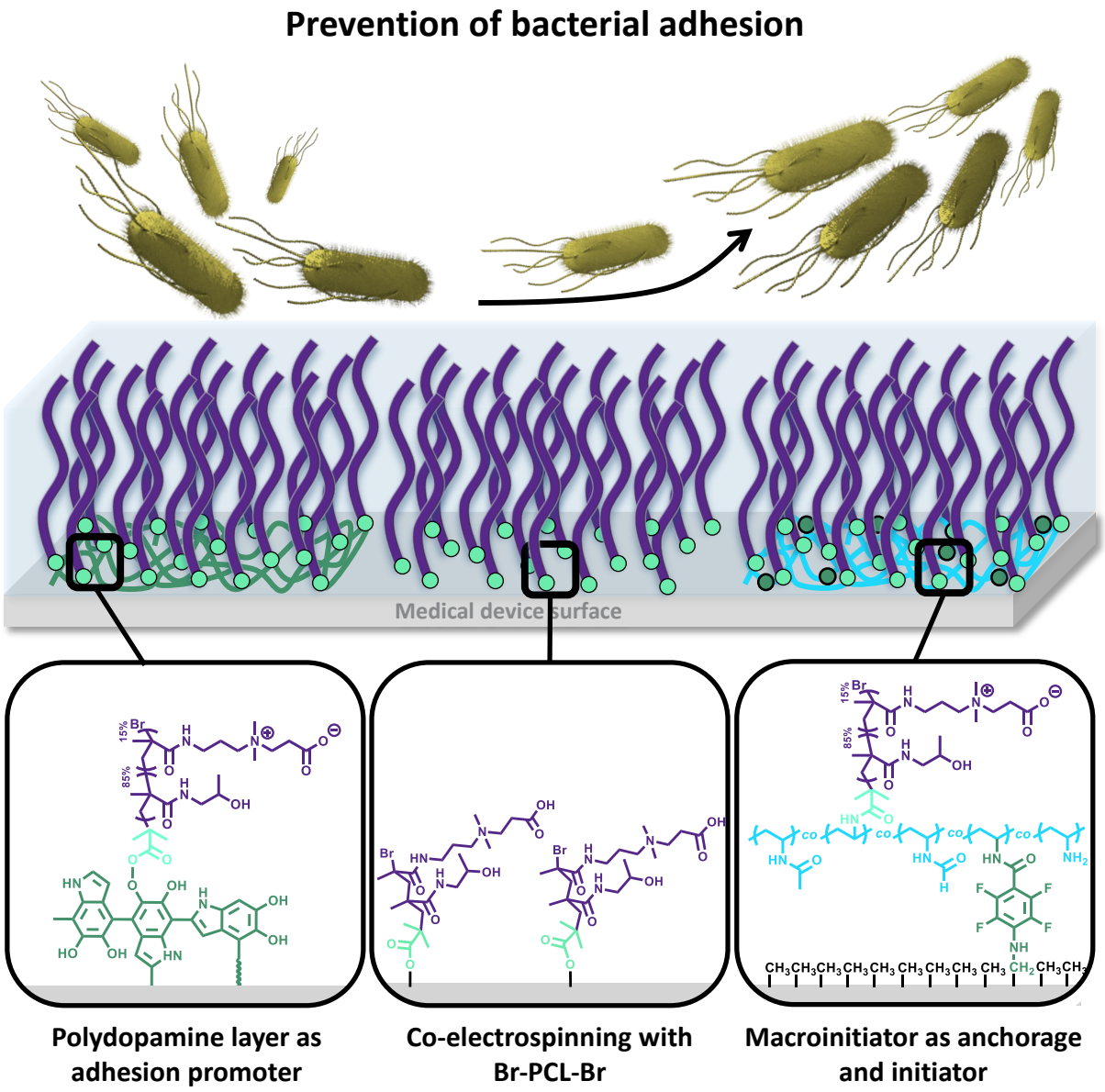

Figure 3.1. Concept figure of the chemical routes for the deposition of initiators on the surface of polymeric medical devices to graft antifouling polymer brushes

The strategies developed here include: 1) The application of a biomimetic polydopamine (PDA) adlayer and 2) The synthesis of two macroinitiators, one of which can be directly implemented in the PCL electrospinning process to generate pre-functionalized PCL fiber scaffolds in a single step. The other one is a heterobifunctional macroinitiator that binds to the surface through UV-assisted phenyl azide chemistry. To demonstrate the successful introduction of initiator

groups, poly(HPMA-*co*-CBMAA) brushes are grafted directly from the modified substrates via atom transfer radical polymerization (ATRP) or single electron transfer-living radical polymerization (SET-LRP). HPMA and CBMAA were chosen because these two polymers, when grafted as polymer brushes, have shown to exhibit the best antifouling properties against proteins from complex biological fluids.[22-24] Altogether, the three initiator deposition strategies have been proved to be safe and effective. They circumvent the need for aggressive surface activation steps and successfully enable the grafting of antifouling polymer brushes, with the goal of preventing bacterial adhesion and the associated risk of material-related infections.

3.2 Results and Discussion

3.2.1 Polydopamine Coating as a Biomimetic Strategy for the Modification of Surfaces with Antifouling Properties

Polydopamine has emerged as a versatile method for creating a multifunctional coating layer on a broad range of organic and inorganic materials.[25-28] This approach draws inspiration from the adhesive nature of catechols and amines found in the proteins that mussels secrete to adhere to surfaces underwater. PDA layers adhere through strong covalent and non-covalent interactions with substrates. The formation of PDA involves the autooxidation of dopamine hydrochloride in an alkaline medium, resulting in the generation of dopamine quinone and subsequent conversion to 5,6-dihydroxyindole, which constitutes the PDA layer.[29] Yet, the precise mechanism of layer formation and structure remains unclear.

Here, PDA surface chemistry was explored to modify electrospun PCL fiber scaffolds. As illustrated in Figure 3.2, PDA provides an anchoring layer with functional groups that enable the binding of an initiator, from which antifouling poly(HPMA-*co*-CBMAA) brushes can be subsequently grafted. To achieve this, the PDA layer was obtained by immersing the PCL fibers into a dopamine hydrochloride solution in Tris(hydroxymethyl)aminomethane (Tris) buffer (2 $mg \cdot mL^{-1}$, pH = 8.5) for 3 h. During this process, the solution was stirred in a controlled manner to maintain a continuous oxygen supply across the air-solution interface. Scanning electron microscopy (SEM) imaging of the PCL fibers was conducted before and after the application of the PDA coating (Figure 3.3A and B). The morphology of the fiber mesh was predominantly preserved, with a few small PDA aggregates present. However, occasionally larger aggregates could be observed throughout the fibers as shown in Figure 3.3B (right), despite careful efforts to keep the samples consistently in a vertical orientation, preventing in that manner the sedimentation of larger PDA aggregates on the surface. The formation of both small and large PDA precipitates hinders the formation of a smooth coating on the surface. This may not only affect the topographic features of the electrospun fibers but also impact other features, such as porosity and permeability.

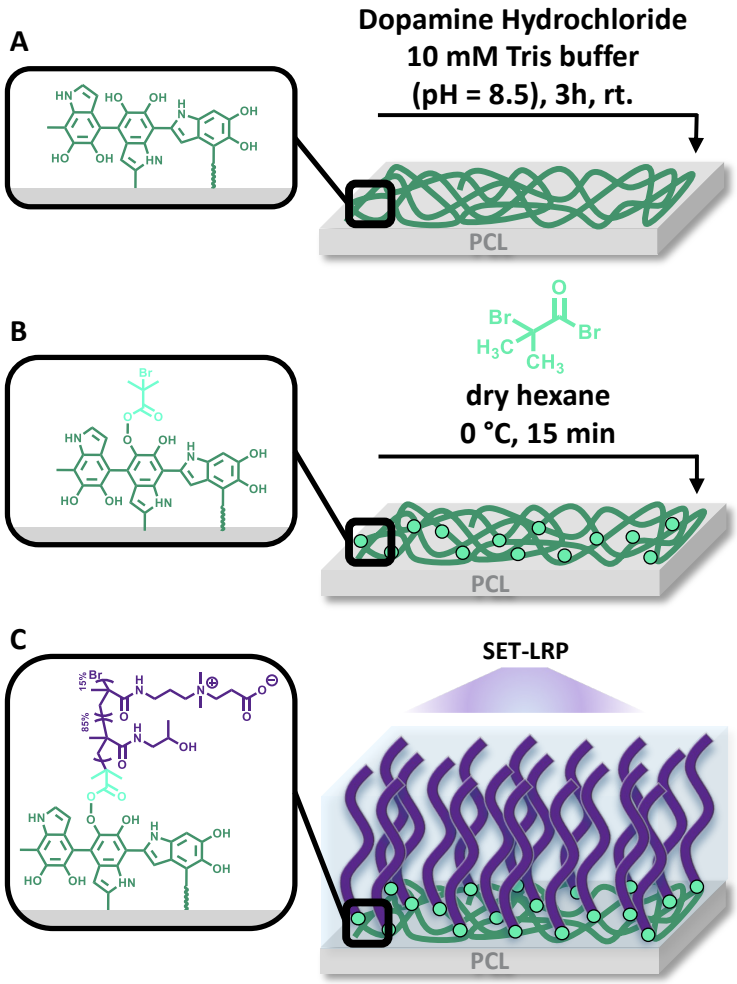

Figure 3.2. Chemical strategy for the coating of electrospun PCL nanofibers with (A) polydopamine deposition, (B) initiator functionalization and (C) the subsequent grafting of antifouling poly(HPMA-*co*-CBMAA) brushes.

To apply the antifouling polymer brushes to the PDA-coated PCL fibers, the amino and hydroxyl surface groups of PDA were functionalized through acylation with the α-bromoisobutyryl bromide (BIB) initiator. Subsequently, poly(HPMA-*co*-CBMAA) brushes were grafted from the surface via ATRP. The successful deposition of each layer was verified by X-ray photoelectron spectroscopy (XPS) analysis (Figure 3.3). The pristine PCL fibers display characteristic signals for the [C-O] and [O=C-O] groups of PCL in the C1s spectrum at 286.4 eV and 289.0 eV, respectively. As expected for pristine PCL, no signals were observed in the N1s spectrum. Upon the application of the PDA layer, a signal at 400.1 eV emerges, which can be assigned to the primary and secondary amines within PDA. Additionally, PDA leads to a slight increase of the [C-O] bonds signal at 285.0 eV, resulting from the contribution of sp2 and sp3 carbon species. The successful grafting of the poly(HPMA-*co*-CBMAA) brushes was confirmed

by the presence of [C-N] bonds at 285.8 eV and amide bonds [O=C-N] at 287.8 eV. Furthermore, the appearance of a peak at 402.7 eV, characteristic of quaternary amine [$N^+(CH_3)_2$], confirmed the integration of CBMAA. Notably, the absence of the [O=C-O] peak of PCL indicates that the surface is entirely covered by a thick polymer brush layer.

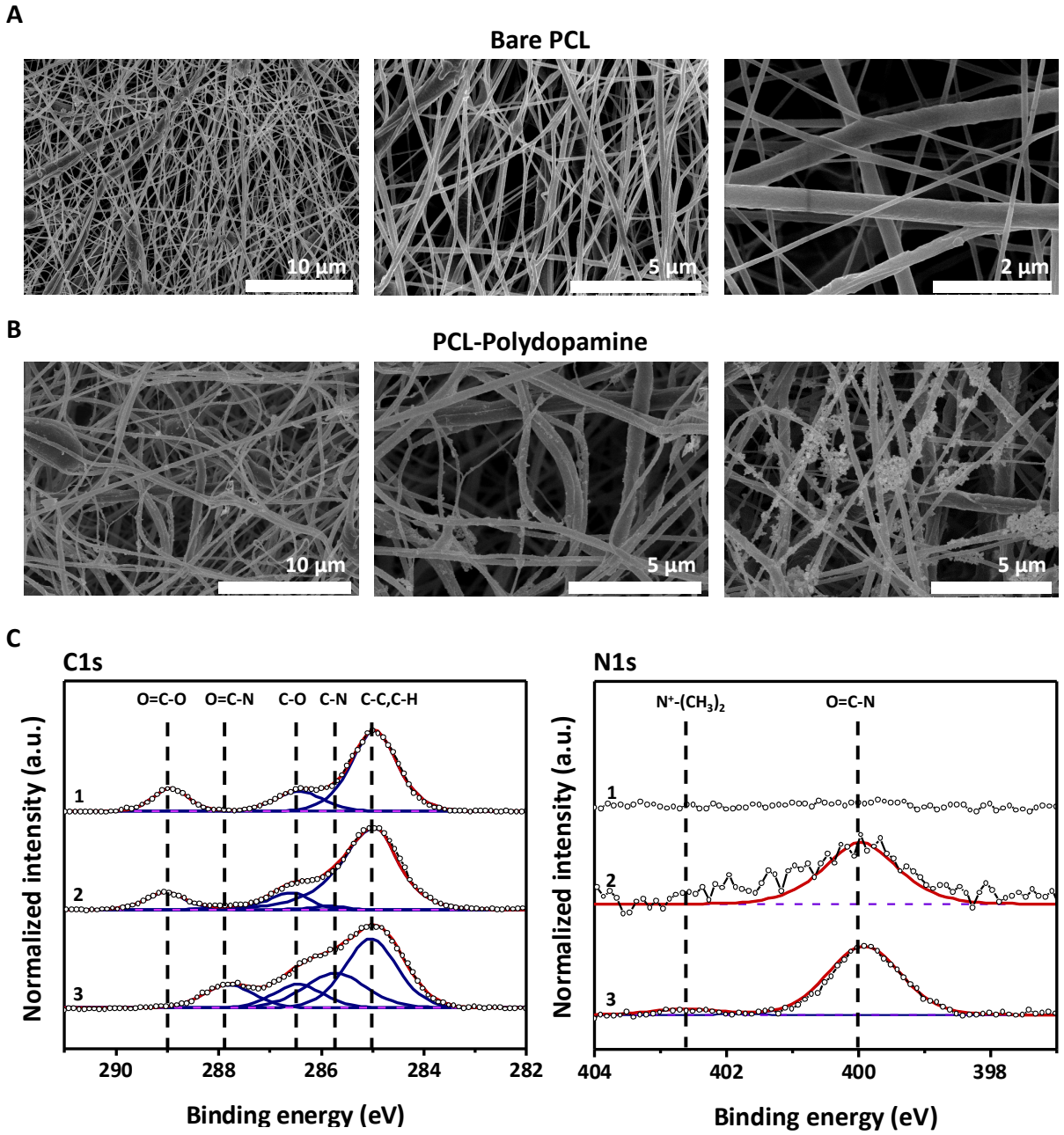

Figure 3.3. SEM-images of electrospun PCL fibers (A) before and (B) after PDA layer deposition. (C) High resolution XPS spectra, C1s (left) and N1s (right), of 1. pristine PCL fibers, 2. PDA coated fibers and 3. Poly(HPMA-*co*-CBMAA) coated fibers.

Further analysis of each coating layer was conducted by ellipsometry and dynamic contact angle (CA). These measurements were performed on Si-wafers that had been spin-coated with

an 18 ± 0.02 nm thick layer of PCL and subsequently treated in the same manner as the PCL fibers. The combined thickness of the entire PDA-poly(HPMA-*co*-CBMAA) brush coating amounted to approximately 40 nm. Advancing and receding CA measurements with water showed a transition from Θ_{adv} = 81.2.° and Θ_{rec} = 62.2° before coating to Θ_{adv} = 33.2° and Θ_{rec} = 13.7° after application of the entire coating (Table 3.1).

Table 3.1. Dry thickness as well as advancing and receding CAs of a silicon wafer spin-coated with PCL and subsequently modified with a PDA layer and poly(HPMA-*co*-CBMAA) brushes.

Surface	Thickness [nm]	Θ_{adv} [°]	Θ_{rec} [°]
PCL bare	18.5 ± 0.1	81.2	62.2
PCL-PDA	8.4 ± 0.01	72.2	40.2
PCL-PDA+brushes	31.36 ± 1.02	33.2	13.7

Overall, these results show that electrospun PCL nanofibers can be modified with a biomimetic polydopamine layer without causing significant alterations in the nanofiber morphology and topology. The PDA layer serves as a platform for grafting antifouling poly(HPMA-*co*-CBMAA) polymer brushes. These brushes hydrophilize the surface, minimizing the interfacial energy with water, and introduce enthalpic and entropic barriers, all of which are necessary to prevent non-specific protein adsorption. Nonetheless, it is important to acknowledge that this chemical approach has some significant limitations. It involves several time-consuming synthetic and washing steps to enable the grafting of the polymer brushes. Moreover, UV-initiated polymerization cannot be employed in this procedure as UV-irradiation of polydopamine leads to the formation of unwanted free hydroxyl radicals[30]. Additionally, PDA is susceptible to degradation under both visible and UV-Vis light exposure[31-32]. PDA has also a low polymerization rate and the formation of aggregates hinders the formation of a smooth coating, which could be essential when dealing with intricate submicron structures. Hence, it

is of great importance to continue investigating innovative chemical strategies for the effective functionalization of PCL fibers with antifouling polymer brushes.

3.2.2 Synthesis of a Br-PCL-Br Macroinitiator and Electrospinning of PCL Fibers with Surface-enriched Initiator Groups

Herein, I present a facile one-step approach to generate electrospun PCL fibers bearing initiator groups at their surface (Figure 3.4). Unlike conventional methods where initiating groups are incorporated after electrospinning, this strategy introduces initiator groups to the surface through the incorporation of a Br-PCL-Br macroinitiator to the PCL solution prior to the electrospinning process. During electrospinning, the alkyl bromide initiating groups [C-Br] migrate towards the periphery of the fibers due to electrostatic attraction.[33]

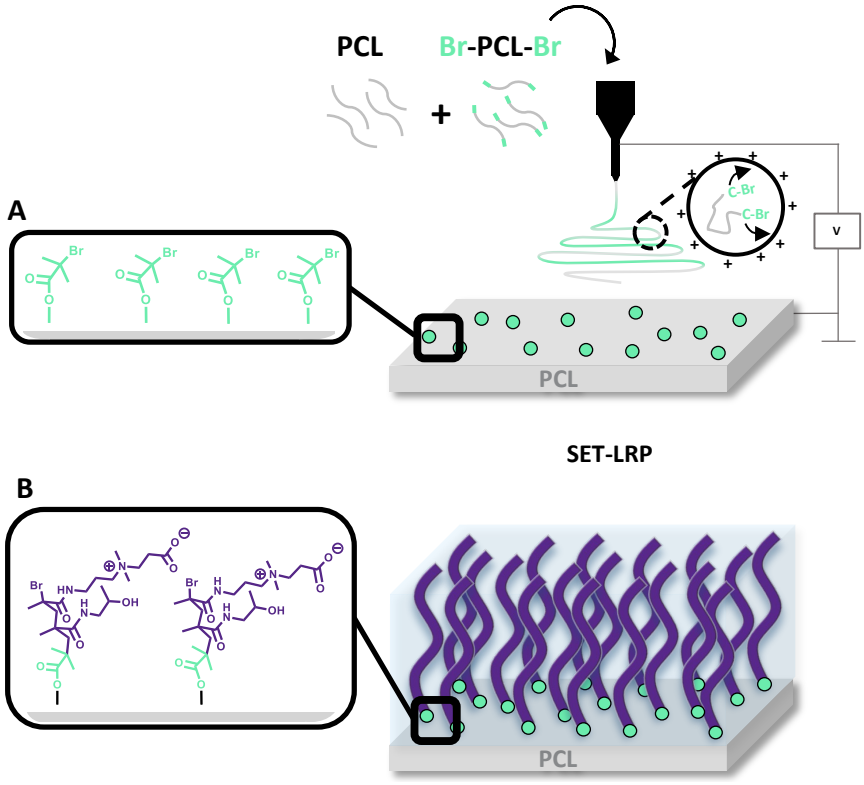

Figure 3.4. 1. Fabrication strategy of PCL electrospun nanofibers with surface-enriched alkyl bromide initiator groups. (A) During the electrospinning process the alkyl bromide groups migrate towards the liquid-air interface. (B) Surface-initiated (SI) photo-SET-LRP of poly(HPMA-*co*-CBMAA) brushes.

The Br-PCL-Br macroinitiator was synthesized by reacting Polycaprolactone diol (PCL-diol) with 2-bromoisobutyryl bromide in the presence of triethylamine in tetrahydrofuran (Scheme 3.1). Subsequently, the Br-PCL-Br macroinitiator was mixed with a high molecular weight PCL (45,000 g·mol^{-1}) and dissolved in a chloroform:methanol mixture at a ratio of 2:1.

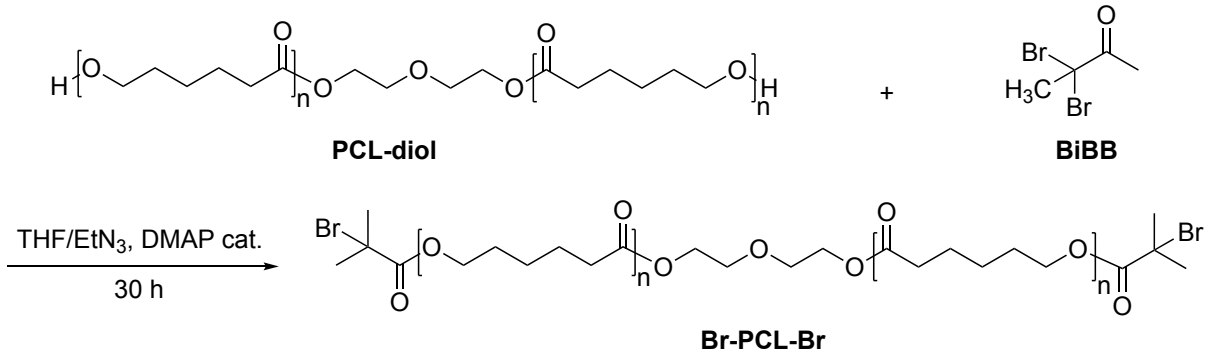

Scheme 3.1. Chemical route for the synthesis of the Br-PCL-Br macroinitiator.

This mixture was then used for the electrospinning process, resulting in the fabrication of functionalized PCL fiber scaffolds. During the electrospinning process, the cathode was positioned at the spinneret such that the surface of the polymer solution would become positively charged. As the alkyl bromide group [C-Br] is polarized, the Br atom exhibits a partial negative charge (δ^-). Consequently, the [C-Br] groups will migrate towards the positively charged polymer solution surface during electrospinning, leading to PCL electrospun fibers with surface-enriched alkyl bromide groups (Figure 3.4). SEM images (Figure 3.5A) indicate uniform electrospun nanofibers. Following electrospinning, poly(HPMA-*co*-CBMAA) brushes were grafted from the PCL fibers by SI photo-SET LRP at ambient temperature. Photo-SET-LRP was used because compared to ATRP, it only requires extremely low concentrations (ppb) of copper catalyst, reducing potential toxicity. This is a critical consideration in biomedical applications as removing high levels of toxic contaminants can be challenging and time-consuming. Additionally, photo-SET-LRP requires only about 30 min to form a 30-40 nm thick brush coating, a thickness found to be required for achieving outstanding antifouling properties in previous work.[4, 34-36]

XPS analysis confirmed the successful grafting of poly(HPMA-*co*-CBMAA) brushes. Figure 3.5B depicts the high-resolution C1s (left) and N1s (right) spectra of the fibers before and after modification with the antifouling polymer brushes. In their pristine state, the fibers exhibit three signals at 285, 286.6 and 288.9 eV corresponding to the [C−C], [C−H], [C−O] and [O−C=O]

components of PCL, respectively. As anticipated from the chemical structure of PCL, the N1s spectrum does not display any signals. After the modification with polymer brushes, the C1s spectrum reveals the contributions of [C-N] bonds at 285.99 eV and [O=C-N] bonds at 287.8 eV, which correspond to HPMA and CBMAA. Furthermore, the signal at 402.8 eV in the N1s spectrum results from the quaternary ammonium component in CBMAA.

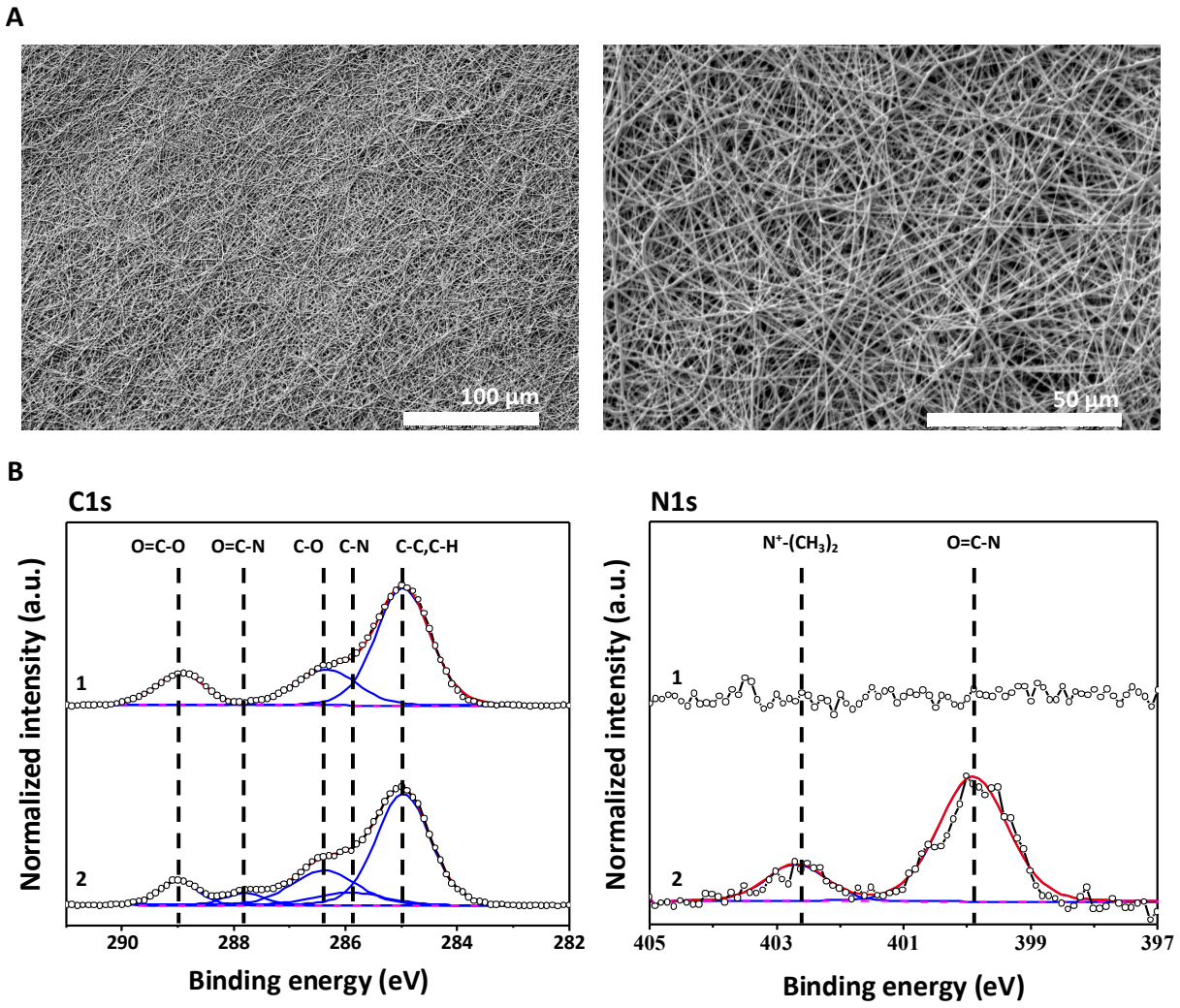

Figure 3.5. (A) SEM images of electrospun PCL nanofibers with surface-enriched alkyl bromide initiator groups from a chloroform:methanol (2:1) solvent system. (B) High resolution C1s (left) and N1s (right) XPS spectra of the fiber mats. 1. PCL/Br-PCL-Br fibers, 2. PCL/Br-PCL-Br fibers decorated with poly(HPMA-*co*-CBMAA) polymer brushes.

In conclusion, the presented data provide clear evidence that our approach of pre-functionalizing PCL with initiating groups prior to electrospinning provides a straightforward and rapid strategy for functionalizing electrospun PCL scaffolds with antifouling polymer brushes. This method preserves the inherent characteristics of electrospun structures while

also affording precise control over the spatial distribution of functionalization as both the density and localization of the functional groups can be readily adjusted. The former can be achieved by simply tuning the ratio between PCL and Br-PCL-Br. Importantly, this strategy may be extended beyond the scope of initiating group functionalization, paving the way for the production of multifunctional PCL fiber scaffolds. In this context, Stevens et al. successfully introduced bilayered PCL fiber scaffolds with dual functionality, featuring a cell-adhesive surface on one side and an antifouling non-cell-adhesive surface on the opposing side.

3.2.3 Synthesis of a Waterborne Macroinitiator for UV-assisted Surface Modification of a Broad range of Polymeric materials

In the quest of an effective way to functionalize a wide range of biomaterials with organic and inorganic domains, photoactive coupling agents have been explored, including benzophenones[37-38] and perfluorophenylazides (PFPA)[39-40]. Upon photoactivation reactive radical intermediates (carbenes and nitrenes) are formed, that can subsequently undergo insertion reactions.

Herein, I present a strategy to apply antifouling coatings on any inert polymeric material containing C-H or N-H bonds. This is accomplished by utilizing a water-soluble macroinitiator containing PFPA adhesion promoting groups and initiator groups that can be used to graft antifouling polymer brushes by SI SET-LRP. The backbone of the macroinitiator was synthesized via free radical polymerization of *N*-vinylformamide (NVF) and *N*-vinylacetamide (VAm) at equal molar concentrations. Subsequently the formamide groups in NVF were partially hydrolyzed in an aqueous solution of hydrochloric acid (HCl), generating amine groups. This reaction yielded poly(vinylamine-*co*-vinylformamide-*co*-vinylacetamide) (NVA-*co*-NVF-*co*-VAm) containing 8% residual formamide units, 44% of free amine groups and 48% of vinylacetamide entities (Scheme 3.2). The degree of polymerization (DP) was calculated to be DP = 60 from proton nuclear magnetic resonance analysis (^{1}H NMR, Figure S3.1 and Figure S3.2). Additionally, the molecular weight (M_n) was determined by size exclusion chromatography (SEC) to be $M_n = 3.87 \times 10^3$ g·mol^{-1} with a polydispersity (Đ) of Đ = 3.0 (Figure S3.3). To further functionalize NVA-*co*-NVF-*co*-VAm with initiator groups on the one hand and surface reactive groups on the other, the free amine groups were additionally reacted with 2-bromoisobutanoic acid *N*-hydroxy-succinimide ester (BIB-NHS) and *N*-succinimidyl-4-

azidotetra-fluorobenzoate (PFPA-NHS), respectively. Following purification, the resulting macroinitiator NVA-co-NVF-*co*-VAm-*co*-PFPA-*co*-BIB contained 3.5–5.0% of BIB-initiator groups and 34.5% of PFPA-adhesion promoting groups (Figure S3.4 and Figure S3.5).

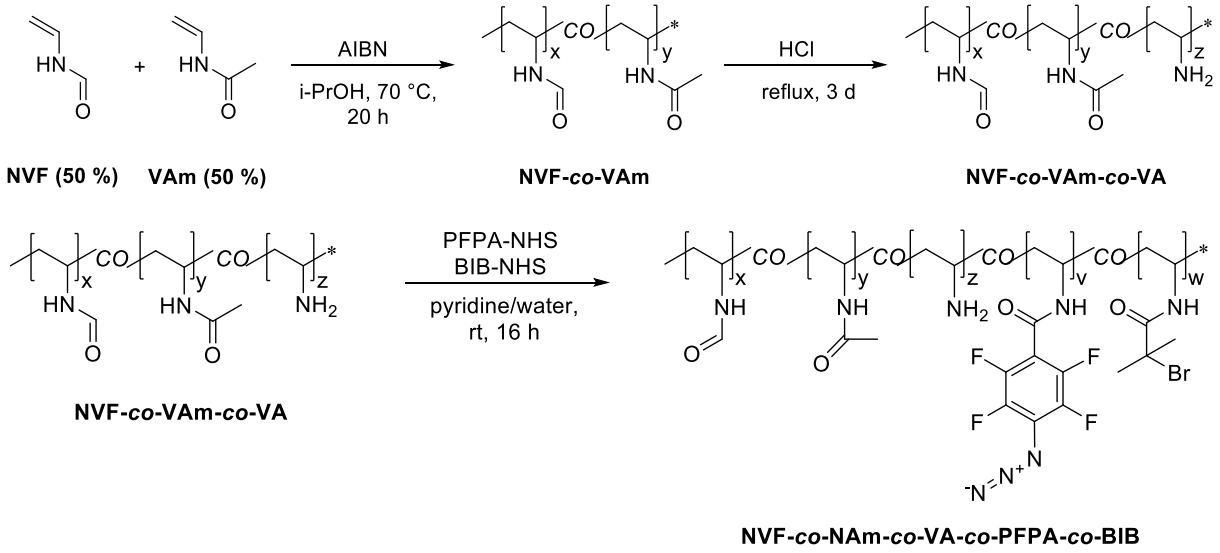

Scheme 3.2. Chemical route for the synthesis of the water-soluble NVA-*co*-NVF-*co*-VAm-*co*-PFPA-*co*-BIB macroinitiator including backbone polymerization and following functionalization with adhesion promoting (PFPA) and initiator groups (BIB).

The modular chemical design of this macroinitiator renders this strategy highly tunable, facilitating so the adjustment of the final polymer brush properties. By tweaking the ratio of initiator groups to adhesion groups during the synthesis of the macroinitiator, the grafting density of the brushes can be tailored to meet specific requirements.

3.2.4 Ligation of the Macroinitiator to the Surface and Grafting of Antifouling Poly(HPMA-*co*-CBMAA) Brushes

The NVA-*co*-NVF-*co*-VAm-*co*-PFPA-*co*-BIB macroinitiator opened up a universal and easy route for a single step modification of polymeric medical devices. Here it was utilized for the modification of PMP membrane hollow fibers, which find application in ECMO devices, electrospun PCL nanofibers, used as scaffolds in tissue engineering, wound dressings and drug delivery therapeutics as well as PE wound contact layers. The substrates were fully wetted or immersed into an aqueous solution of the macroinitiator (1 mg·mL^{-1} in Milli-Q water) and exposed to UV irradiation for 60 min. The continuous exposure to UV light triggers the

formation of nitrene radicals at the PFPA groups, which insert into C-H bonds of the substrates covalently linking the macroinitiator to the surface (Figure 3.6).

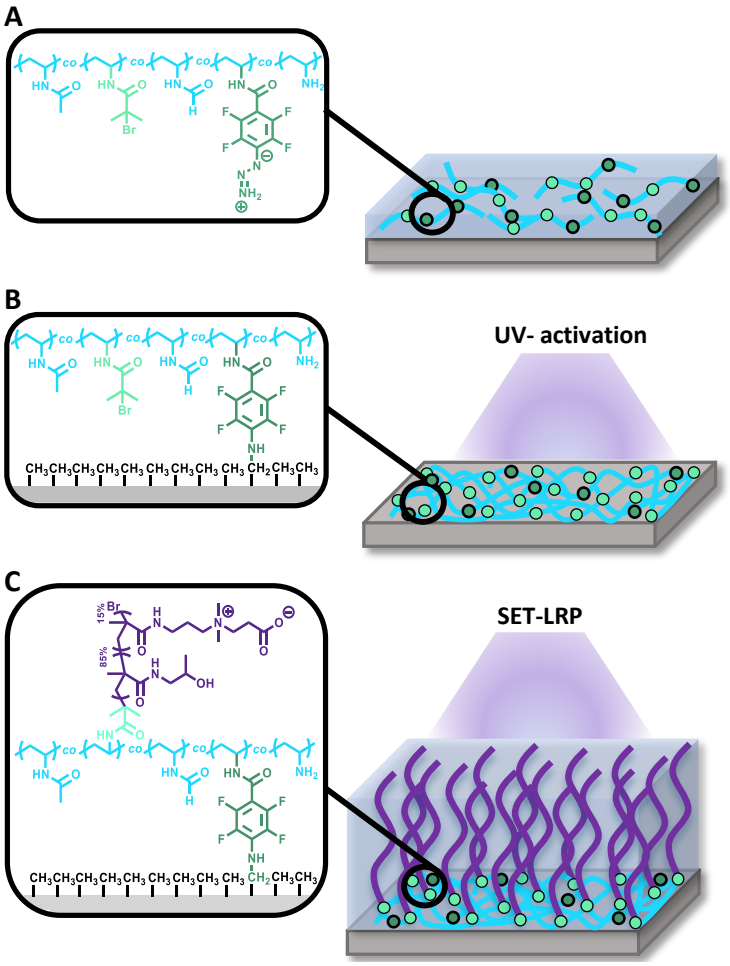

Figure 3.6. Overview of the coating process of polymeric substrates with the macroinitiator by activated UV-insertion and subsequent grafting of antifouling polymer brushes from the surface by SI SET-LRP.

Figure 3.7A depicts exemplary XPS analysis of PMP hollow fibers before and after the application of the macroinitiator layer. The C1s high-resolution spectrum shows the appearance of additional peaks at 285.7 and 286.6 eV, which correspond to [C-N] and [C-O] bonds stemming from the amine and amide groups of the macroinitiator. Furthermore, the N1s high-resolution spectrum additionally confirms the presence of amide bonds [O=C-N] at 400 eV. These results demonstrate the successful ligation of the macroinitiator to PMP. Further the linking of the hydrophilic macroinitiator should lead to a hydrophilization of the substrate surface. Advancing and receding CA measurements with water show a change from

Θ_{adv} = 122.5° and Θ_{rec} = 95.2° before the ligation to Θ_{adv} = 79.5° and Θ_{rec} = 54.2° after ligation on flat PMP membranes (Table 3.2).

After proving the feasibility of the macroinitiator ligation, polymer brushes consisting of poly(HPMA-*co*-CBMAA) were grafted from the functionalized polymeric surfaces via photo-induced SET-LRP. As confirmed by ellipsometry measurements, brushes with a thickness in the range of 30–40 nm were attained after a polymerization time of 40 min (Table 3.2). The copolymerization of HPMA (85 mol%) and CBMAA (15 mol%) was confirmed by the N1 s high-resolution spectrum of XPS analysis (Figure 3.7), which shows the characteristic quaternary amine peak [$N^+(CH_3)_2$] stemming from CBMAA at 402.6 eV. Moreover, the polymer brushes coating should further result into a decrease of interfacial tension with water. Indeed, coated PMP flat membranes exhibited Θ_{adv} = 52.9° and Θ_{rec} = 28.3°. Likewise, the non-wettable PCL surface (Θ_{adv} = 81.2° and Θ_{rec} = 62.2° with water) could be wetted by water (Θ_{adv} = 46.1° and Θ_{rec} = 23.3°) after brushes were grafted. It should be noted, that the hydrophilization of the surface, minimizing the interfacial energy with water, is essential to create an antifouling surface that prevents protein fouling.

Table 3.2. Dry ellipsometric thickness as well as advancing and receding CAs of pristine PMP hollow fiber membranes and a silicon wafer spin-coated with PCL, coated with the NVA-*co*-NVF-*co*-VAm-*co*-PFPA-*co*-BIB macroinitiator and poly(HPMA-*co*-CBMAA) brushes.

Surface	Thickness [nm]	Θ_{adv} [°]	Θ_{rec} [°]
PMP bare	12.8 ± 0.1	122.5	95.2
PMP-macroinitiator	1.7 ± 0.1	79.5	54.2
PMP-macroinitiator+brushes	32.1 ± 0.1	52.9	28.3
PCL bare	18.5 ± 0.1	81.2	62.2
PCL-macroinitiator	4.2 ± 0.1	70.8	38.7
PCL-macroinitiator + brushes	39.0 ± 0.1	46.1	23.3

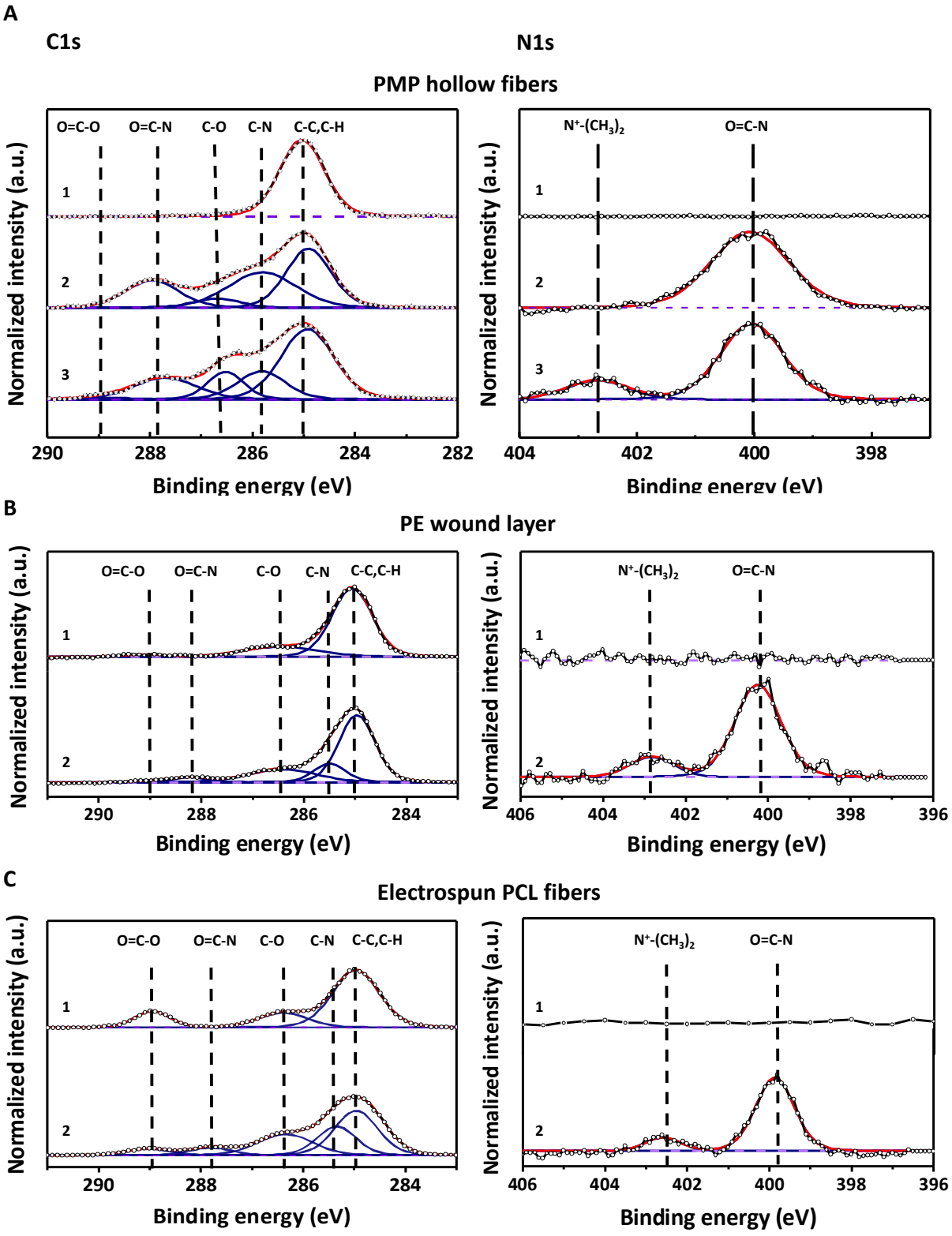

Figure 3.7. High-resolution XPS spectra C1s (left) and N1s (right) of (A) PMP hollow fibers, (B) PE wound contact layers and (C) PCL electrospun fibers. In (A) 1. Represents bare PMP hollow fibers, 2. PMP functionalized with macroinitiator and 3) PMP subsequently coated with poly(HPMA-*co*-CBMAA) brushes. In (B) and (C), 1. Represents bare substrates and 2. Substrates after the application of the poly(HPMA-*co*-CBMAA) brush-coating.

Furthermore, SEM images, as depicted in Figure 3.8, reveal that the entire coating procedure has no damaging effects on the substrates. Remarkably, given its nanometer-range thickness, the brush coating also does not affect the porosity of the PCL fibers or the PE wound contact layers.

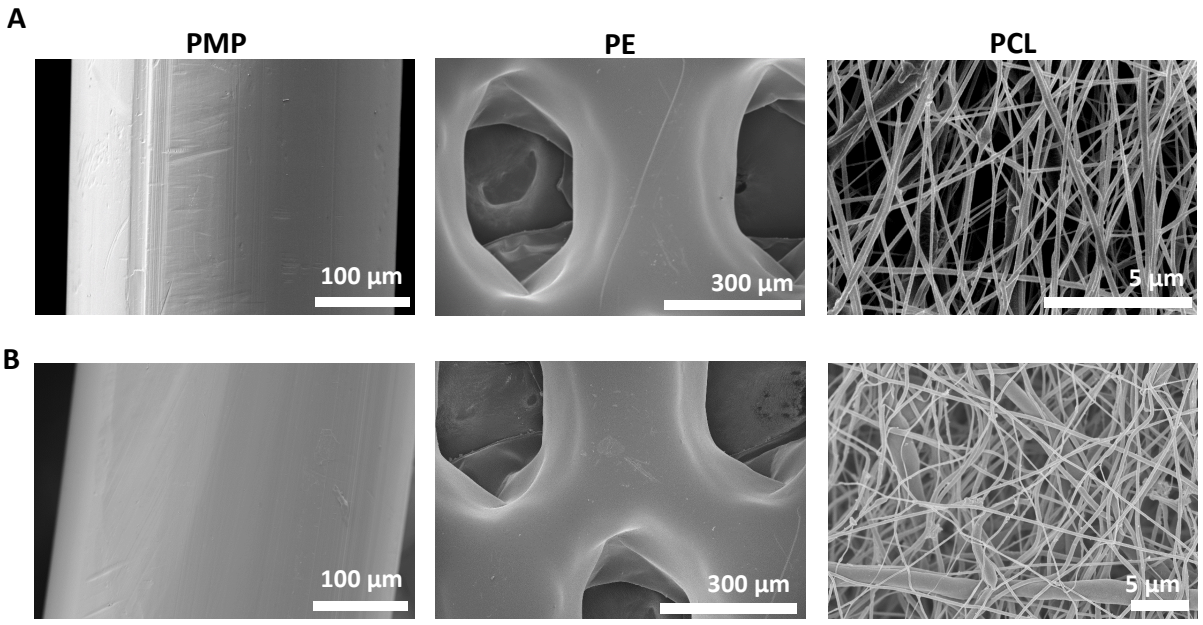

Figure 3.8. SEM micrographs of PMP hollow fibers, PCL nanofibers and PE wound contact layers (A) bare and (B) after application of poly(HPMA-*co*-CBMAA) brush coating

3.2.5 Antifouling Properties Against Blood Plasma Proteins

The initial step in achieving a truly antibacterial surface involves the prevention of protein adsorption with concomitant formation of a conditioning layer. To this end, we evaluated the antifouling properties of our coating using a highly complex bodily fluid such as undiluted blood plasma. Remarkably, using surface plasmon resonance (SPR) we observed that a substantial amount of blood plasma (BP) proteins (~ 100 ng·cm^{-2}, Figure 3.9) were able to adsorb onto the surface of uncoated (bare) PMP. The deposition of the macroinitiator reduced protein fouling by 26%. This can likely be attributed to the hydrophilization of the surface. However, as observed, hydrophilization alone is not sufficient and additional protective measures against protein adsorption are necessary. In stark contrast, the PMP coated with our poly(HPMA-*co*-CBMAA) brush-coating displayed significantly enhanced resistance to BP proteins, reducing fouling by 91% (23 ng·cm^{-2}) after 60 min of contact. This level of performance is comparable to that of the best polymer brushes directly grafted from self-

assembled monolayers of initiators. This highlights that the ease of application and versatility of this coating chemistry does not come at the expense of effectiveness.

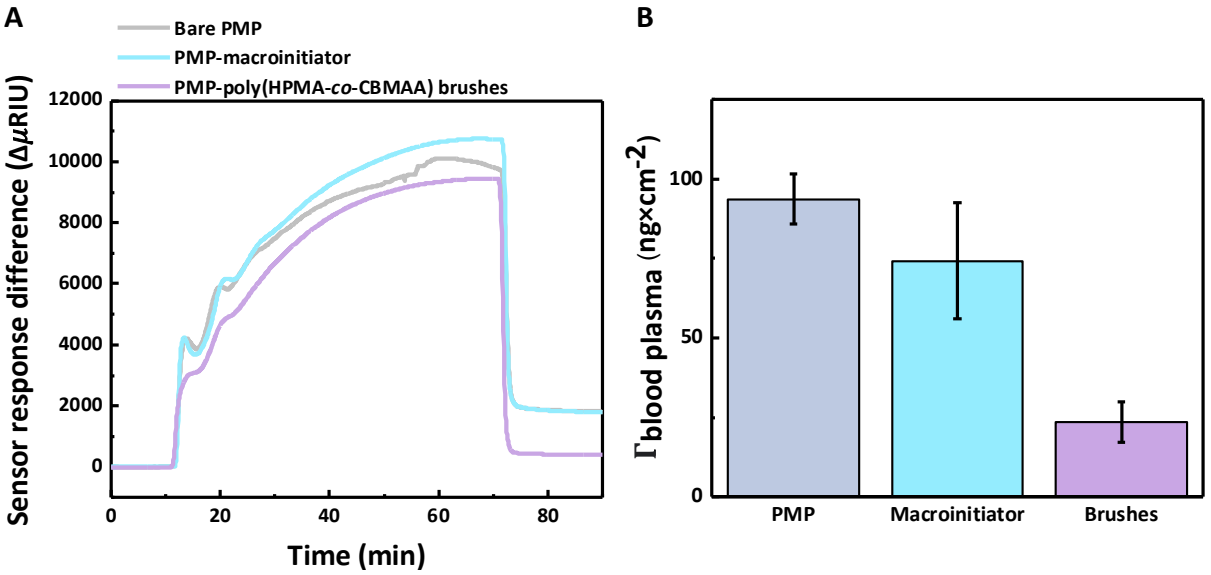

Figure 3.9. (A) SPR sensograms and (B) comparison of BP protein fouling on bare PMP-coated SPR sensors, after macroinitiator deposition and after full poly(HPMA-*co*-CBMAA) brush coating.

3.2.6 Biocompatibility

One of the primary prerequisites for any material, which in going to be exposed to the body or bodily fluids is biocompatibility, i.e. that is has no harmful effects on cells and tissue. Cytotoxicity serves as a critical indicator of biocompatibility. Here, I assessed the cytotoxicity of the coated substrates by incubating them in direct contact to a semiconfluent layer of human dermal fibroblasts (HDF) and subsequently measuring the metabolic activity of the cells via MTS assay (Figure 3.10). After 72 h of incubation, the coating did not induce toxicity and cell viability was above 95% for all PMP and PCL substrates, comparable to the positive control. In the case of PE, the pristine material itself caused a 24% reduction in cell viability, indicating that despite being a commercial wound contact layer, this material is not entirely benign to cells. However, the application of the coating did not lead to further reduction of cell viability, which remained at approximately 75%. These results confirm that neither the macroinitiator nor the poly(HPMA-*co*-CBMAA) brush coating are cytotoxic and remained entirely innocuous to connective tissue fibroblasts.

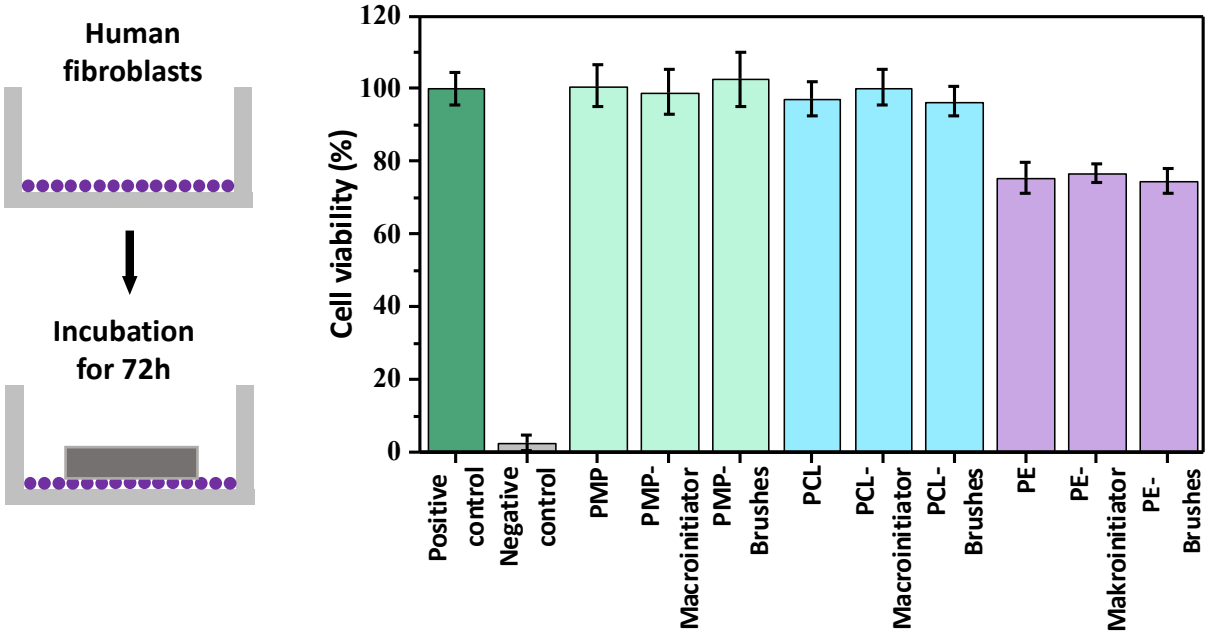

Figure 3.10. Cell viability of human dermal fibroblasts determined by MTS assay after 72 h of incubation in direct contact with substrates (n = 3, statistical significance for * $p < 0.05$). Untreated cells were used as positive control, while latex gloves were used as negative control.

3.2.7 Prevention of Bacterial Adhesion

E. coli is a common pathogen associated with nosocomial infections.[41] Even a non-pathogenic laboratory strain of these bacteria rapidly adheres to the PMP, PE, and PCL substrates, as illustrated in Figure 3.11. The surfaces of PMP and PE were covered by 22% and 42% by *E. coli*, respectively. A significant number of bacteria, could also be found within the porous structure of the PCL fibers, essentially create a bacterial cesspool from which biofilm can form. However, these results are not surprising given our previous observations that these surfaces allow significant protein adsorption, creating ideal conditions for bacterial adhesion to proceed.

In stark contrast, the coated substrates were capable of significantly reducing or completely preventing bacterial adhesion to their surfaces. Notably, almost no bacterium was capable of adhering to either the exterior or interior of the electrospun fibers. This highlights the applicability of our process, which enables to apply an antifouling brush coating to the entire intricate surface of the fiber mesh.

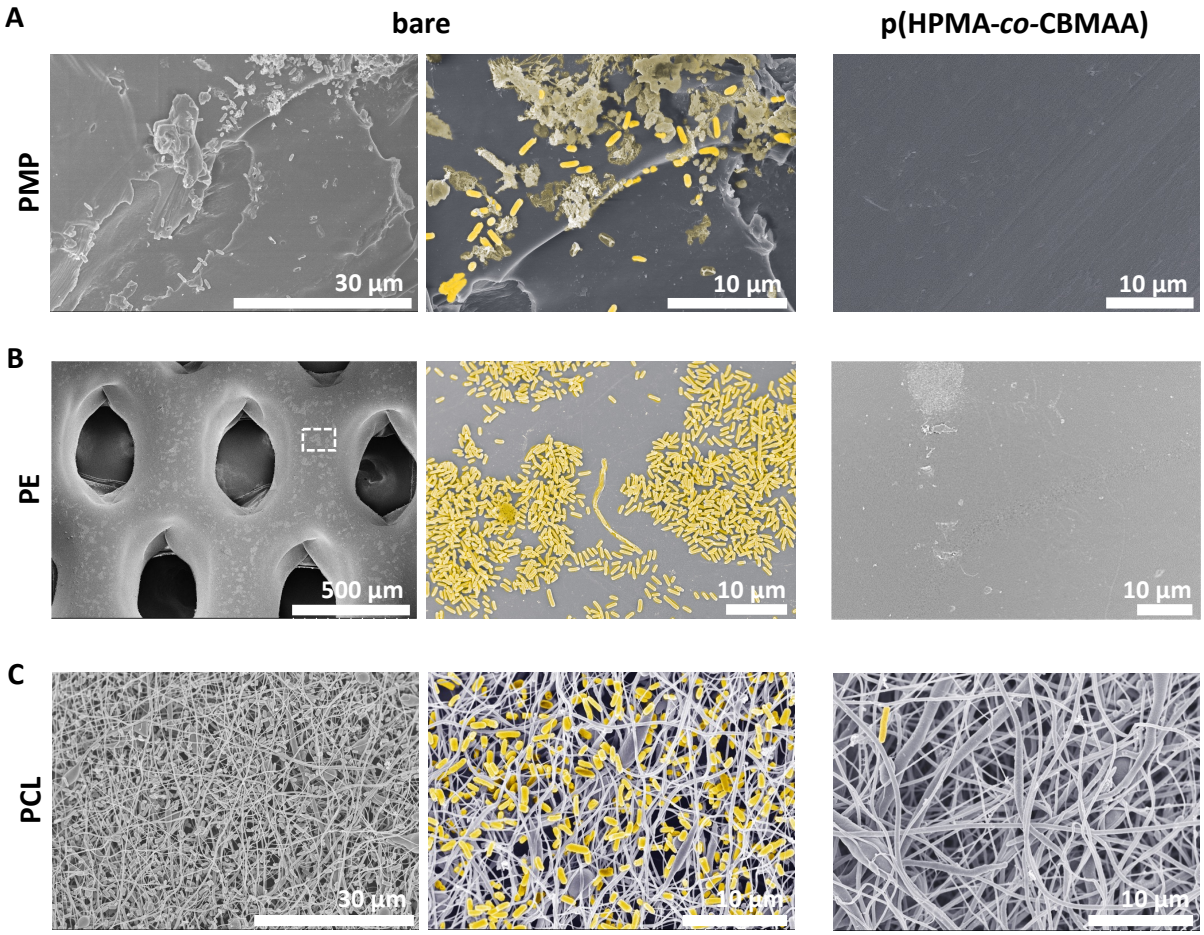

Figure 3.11. Representative SEM micrographs of bacterial adhesion on (A) pristine (left) and coated (right, poly(HPMA-*co*-CBMAA) brushes) PMP hollow fibers, (B) PE wound contact layers and (C) PCL electrospun scaffolds after incubation with a suspension of E. coli (OD_{600} = 0.1) in LB (n = 3).

3.3 Conclusion

In this chapter, I presented three different strategies for the functionalization of various biomaterials such as PCL, PMP and PE with antifouling poly(HPMA-*co*-CBMAA) brushes. The first strategy entailed a biomimetic PDA coating, which served as an anchoring layer for the introduction of initiator groups, from which the antifouling polymer brushes were grafted. While this strategy proved effective for functionalizing PCL fiber scaffolds, it still involves several time-consuming steps to achieve the polymer brush coating. Furthermore, the generation of PDA precipitates during the process is inevitable, resulting in the formation of a rough coating with occasional large PDA aggregates attached to the surface.

In light of these limitations, the second strategy involved generating pre-functionalized PCL scaffolds with alkyl bromide initiator groups on their surface. These functional fibers are fabricated by electrospinning a blend of a high molecular weight PCL and the macroinitiator Br-PCL-Br, all in a single step. During the process of electrospinning, the initiator groups segregate at the surface, facilitating the subsequent synthesis of polymer brushes from the fiber surface. This approach is particularly compelling for creating modular PCL fiber scaffolds with a hierarchical structure and customized functionality. The sequential electrospinning of different layers and ability to adjust the ratio between PCL and Br-PCL-Br macroinitiator provides spatial control over functionality and surface properties.

A third strategy was established as a universal, single step and gentle approach for coating not only PCL fiber scaffolds but different hydrophobic polymeric materials such as PMP hollow fiber membranes and PE wound contact layers. The synthesis of the dual-functional NVA-*co*-NVF-*co*-VAm-*co*-PFPA-*co*-BIB macroinitiator enables the gentle modification of the polymer substrates via UV irradiation. UV exposure triggers the formation of nitrene radicals at the PFPA groups, which insert into the C-H bonds of the substrate cross-linking the macroinitiator to the surface. Then the BIB initiator groups are exploited to graft the polymer brushes. This strategy resulted in a nanometer-thick and smooth coating that preserved the topographical and morphological features of the substrates. Remarkably, the poly(HPMA-*co*-CBMAA) brush coating was able to decrease fouling from BP proteins by over 75%. Furthermore, all coated substrates effectively prohibited the adhesion of *E. coli* bacteria.

Taken together, all of these strategies provide simple and highly versatile methods for readily generating grafting-from poly(HPMA-*co*-CBMAA) brushes on the surface of medically relevant polymers without the need for aggressive pretreatments that would otherwise damage the substrate surface. Most notably, the antifouling coatings presented herein are on par with the best polymer brushes directly grafted from self-assembly monolayers of initiators on gold surfaces. Furthermore, it was elucidated that the reduction of protein adsorption to the surface is a necessary condition to prevent bacterial adhesion.

3.4 Materials and Methods

3.4.1 Materials

All reagents were of analytical grade and used as received unless otherwise stated. Copper (II) bromide (CuBr2, 99%), ethanol (EtOH, >99.8%), acetone (>99.5%), toluene (99.8%), phosphate buffered saline tablets (PBS), citrated blood plasma, dopamine hydrochloride (98%) and Poly(ε-caprolactone) (PCL, Mn 45,000 $g \cdot mol^{-1}$) were purchased from Sigma Aldrich Chemie GmbH. Deuterated solvents (99.9%) were purchased from Deuterio GmbH. Dimethyl sulfoxide (DMSO, >99.9%) was obtained from VWR International GmbH. Tris(2-dimethylaminoethyl)amine (Me_6TREN, 99⁺%) was obtained from ThermoFisher GmbH. CBMAA and HPMA were synthesized as well according to literature procedures.[42-43] The adhesion promoter *N*-succinimidyl-4-azidotetra-fluorobenzoate (PFPA-NHS) and the SET-LRP initiator 2-Bromoisobutanoicacid *N*-hydroxy-succinimide ester (BIB-NHS) were synthesized according to literature.[44] Water used in the experiments was provided by a Millipore Milli-Q system. Silicon wafers were purchased from SIEGERT WAFER GmbH. Gold coated SPR sensor slides were purchased from Cenibra GmbH. PMP hollow fibers (Oxyplus Cross Wound Knitted Mat, PMP 90/200) were obtained from Membrana GmbH. PE substrates were cut from polymer films (150 mm x 150 mm x 0.5 mm) purchased from Goodfellow Cambridge Limited.

Cells and biochemicals. E. coli BL21-Gold (DE3) were obtained from the Leibniz Institute DSMZ-German Collection of Microorganisms and Cell Cultures GmbH, Braunschweig, Germany. These cells were grown in lysogeny broth (LB) containing 10 $g \cdot L^{-1}$ tryptone, 5 $g \cdot L^{-1}$ yeast extract and 10 $g \cdot L^{-1}$ NaCl, purchased from AppliChem GmbH. HDF were purchased from PromoCell GmbH. HDF were cultured in Dulbecco's Modified Eagle Medium (DMEM, Gibco®) supplemented with 10% fetal bovine serum (FBS, Gibco®) and 1% Penicillin-Streptomycin (Pen Strep, Gibco®), purchased from ThermoFisher GmbH. For cell viability measurements, HDF were cultured until passage 7 in 75 cm^2 cell culture flasks. Cells were then harvested by trypsin (Gibco™) treatment and seeded into 12-well plates (Greiner bio-one) at a density of 100,000 cells/well. Cultivation was carried out until 70% confluency at 37°C and in humidified, 5% CO_2 atmosphere.

3.4.2 Synthetic and Fabrication Methods

Preparation of PCL electrospun fibers. PCL meshes were prepared by the electrospinning technology using the Fluidnatek LE-500 from Bioinicia. Briefly, acetone was utilized to dissolve PCL at 35 °C and a concentration of 21% w/v. The solution was then filtered utilizing a 1 µm PTFE filter and transferred into a 20 mL syringe. The electrospinning apparatus was equipped with a round six-nozzle spinneret and 27-gauge cannulas. A 200 mm thick mandrel rotating at 100 RPM was taken as collector. It was placed 160 mm away from the spinneret. The electrospinning parameters were set to a flowrate of 9.2 $mL \cdot h^{-1}$, voltage of 20/-9 kV, temperature of 23.4 °C and humidity of 37%.

Preparation of a thin layer of PCL. A thin layer of PCL was spin-coated on silicon-chips (1.2 x 1.2 cm) and gold-coated SPR sensor chips using the Spin Coater 1001 S from Convac GmbH. PCL was dissolved in toluene at 0.6% w/v. Once a clear solution was obtained, 75 µL were taken and dropped onto the substrate while it was spinning at room temperature. The parameters were set to a duration of 60 s and speed of 2000 RPM. The coated substrates were subsequently thermally annealed at 45 °C for 3.5 h in a vacuum oven. Subsequently. The PCL layer thickness was determined by ellipsometry.

Formation of polydopamine layer. PDA was deposited on PCL electrospun fibers (4 x 2 cm). Briefly, these fibers were immersed in a 2 $mg \cdot mL^{-1}$ solution of dopamine hydrochloride in 10 mM Tris-HCl (pH 8.5) buffer for 3 h. This was performed in open glass dishes and under controlled stirring that provided a continuous supply of oxygen through the air/solution interface. In addition, the flat substrates were kept vertical to avoid sedimentation of microparticle on the PCL fibers.

Preparation of Br-PCL fibers. PCL and 5 wt% of Br-PCL-Br were dissolved in a 2:1 Chloroform: Methanol mixture. The electrospinning set-up consisted of a high voltage power supply, a glass syringe with a flat needle gauge 21 and an aluminum plate covered with aluminum foil (collector). The applied voltage varied between -15 to -18.5 kV. The flow rate was 0.5 $mL \cdot h^{-1}$ and the distance between the needle tip and collector was 13 cm.

UV-activated insertion of NVA-co-NVF-co-VAm-co-PFPA-co-BIB on polymer substrates. A solution of NVA-*co*-NVF-*co*-VAm-*co*-PFPA-*co*-BIB macroinitiator at 1 $mg \cdot mL^{-1}$ in Milli-Q-water was freshly prepared. Polymer substrates (PCL fibers, PMP hollow membrane fibers and PE

wound contact layers) were fully immersed in the macroinitiator solution. The substrates were irradiated with UV light for 60 min using a self-constructed device (144 W, 4 x 36 W lamps).

Grafting of poly(HPMA-co-CBMAA) brushes by photoinduced SET-LRP. The polymerization was performed in DMSO and lasted 30 min. First a catalyst stock solution of $CuBr_2$ (8.7 mg, 3.9 µmol) and Me_6TREN (62.5 µL, 23.4 µmol) was prepared in 10 mL DMSO and protected from light until further use. In another flask the monomer solution was prepared, briefly HPMA (1.49 mmol) and CBMAA (0.26 mmol) were dissolved in DMSO. For each milliliter of monomer solution, 44 µL of the catalyst stock solution were added. The combined solution was degassed by bubbling with N_2 for 60 min. Simultaneously, the substrates were placed into vials equipped with a septum and degassed by purging with N_2 for 60 min. PCL fiber mats were fixed from one side to a silicon wafer to prevent buoyancy of the fiber mat while polymerization. Afterwards, 1 mL of the polymerization solution was transferred into the vials containing the substrates by using a gas-tight syringe and the polymerization was conducted at room temperature by irradiating with UV light using a nail-curing device (Salon Edge, 36 W (4 x 9 W lamps), λ_{max} = 365 nm). To stop the polymerization the vials were opened and quenched with 1 mL of DMSO. The samples were then rinsed with DMSO, EtOH and Milli-Q water. Subsequently these were dried with an N_2-stream and stored until further use. Gold-coated SPR sensor slides were stored in a solution of 95 % of Milli-Q-water and 5 % of EtOH.

3.4.3 Analytical Methods

Nuclear magnetic resonance. ^{1}H-NMR spectra were obtained on a Bruker Avance III 400 spectrometer at 400 MHz.

X-ray photoelectron spectroscopy. XPS spectra were recorded using an Ultra AxisTM spectrometer (Kratos Analytical, Manchester, United Kingdom). For that, the surfaces were irradiated with a monochromated A1 Kα X-ray source (1486.6 eV) with a total power of 144 W (12 kV·12 mA). The processing software CasaXPS (Version 2.3.22, Casa Software Ltd., United Kingdom) was used to perform charge corrections. The spectra were fitted/deconvoluted with several Voigt profiles. All spectra were referenced to the C1s peak of the aliphatic carbons ([C-C], [C-H]), which was set to 285.0 eV according to literature.[45]

Ellipsometry. The dry thickness of the coatings was obtained using the RC2-D spectroscopic Ellipsometer (J.A. Woolam Co., Inc.). Measurements were performed at room temperature, at angles of incidence of 65°, 70°, and 75° and in the wavelength range of 250-1000 nm. Data analysis was done using the CompleteEASE software (Version 5.08r) applying a multilayer model.

Dynamic contact angle measurements. Measurements were performed on a Krüss contact angle measuring system. 10 oscillations of a 10 ± 3 µL drop of Milli-Q-water were used with a dosing rate of 50 $\mu L \cdot min^{-1}$ and analyzed by Tangente and Circle Fit to calculate an average value for the advancing and receding contact angles.

Scanning electron microscopy. Images were acquired using the HITACHI-S-3000N and HITACHI-S-4800 (Hitachi High-Technologies, Tokyo, Japan). Before analysis, the samples were sputtered with an 8-10 nm thick conductive layer of Au/Pd.

Assessment of blood plasma fouling. The amount of BP protein fouling was assessed by SPR on the MP-SPR NaviTM 210A VASA (BioNavis, Tampere, Finland) with a two-channel microfluidic system enabling measurement at 670nm as well as 785 nm. The system was used with the SPR-Navi Control software (Version 4.2.5.2). Briefly, the undiluted citrated BP solution in PBS was injected over the coated SPR sensor at 10 $\mu L \cdot min^{-1}$ for 60 min. Subsequently, the surface was flushed with phosphate-buffered saline (PBS) buffer to removed unbound proteins. The data were analyzed with the SPR-Navi Data Viewer (Version 4.3.5.2). Adsorbed protein mass was determined from ΔµRIU before and after injection by multiplication with a conversion factor of 0.0794 $ng \cdot cm^{-2}$ per µRIU for 670 nm.

Cell viability by direct contact. Cell viability (metabolically active cells) was determined using the colorimetric MTS assay (The CellTiter 96® AQ_{ueous} One Solution Cell Proliferation Assay (MTS), Promega). This test is based on the conversion of 5-(3-carboxymethoxyphenyl)-2-(4,5-dimethyl-thiazoly)-3-(4-sulfophenyl) tetrazolium salt into a colored formazan in the mitochondria of metabolically active cells. The amount of produced formazan is proportional to the number of living cells. Sterilization of all materials was performed prior to experiments by UV disinfection (254 nm) for 1 h. Subsequently, samples were washed three times with sterile PBS each time 5 min. For experiments, substrates were placed on top of a monolayer of HDF cells and incubated for 72 h at 37 °C in a humidified, 5% CO_2 atmosphere. Cells cultured

in complete DMEM growth medium serve as negative control, while latex gloves provide a reproducible cytotoxic response and were used as positive control. After the incubation period, the medium was exchange to equal the volumes and 20 µL of MTS reagent for every 100 µL of DMEM was added. Microplates were then left to incubate for 3 h at 37 °C in a humidified, 5% CO_2 atmosphere and the absorbance was recorded at 490 nm utilizing the multi-mode microplate reader SpectraMax® M3. The collected absorbance data was normalized, where the negative control was put as 100% reference.

Adhesion assay of E. coli. A single colony *of E. coli* was inoculated into 10 mL Luria broth (LB) and grown for 16 h (37 °C, 180 RPM). For the adhesion assay, the LB was supplemented with 10% fetal bovine serum (FBS) and the optical density (OD) was adjusted to an OD_{600} of 0.1, corresponding to approximately 10^8 CFU·mL^{-1}. Bare and coated substrates were placed in 15 mL Falcon tubes and covered with 3 mL of bacterial suspension (OD_{600} = 0.1). All substrates were tested in triplicate. The tubes were closed and placed inside the incubator for 24 h at 37 °C and 180 RPM. Planktonic cells were removed by pipetting out the cell suspension. Substrates were washed four times with 2 mL of PBS (5 min) and fixed with 3% glutaraldehyde in PBS (overnight, 4 °C). All samples were dehydrated through a graded ethanol series (25%, 50%, 70%, 90% and 100% dry, 15 min each step, 2 × 100%) and air dried with hexamethyldisilazane. Adhesion of *E. coli* was visualized by SEM.

3.5 Supplementary results

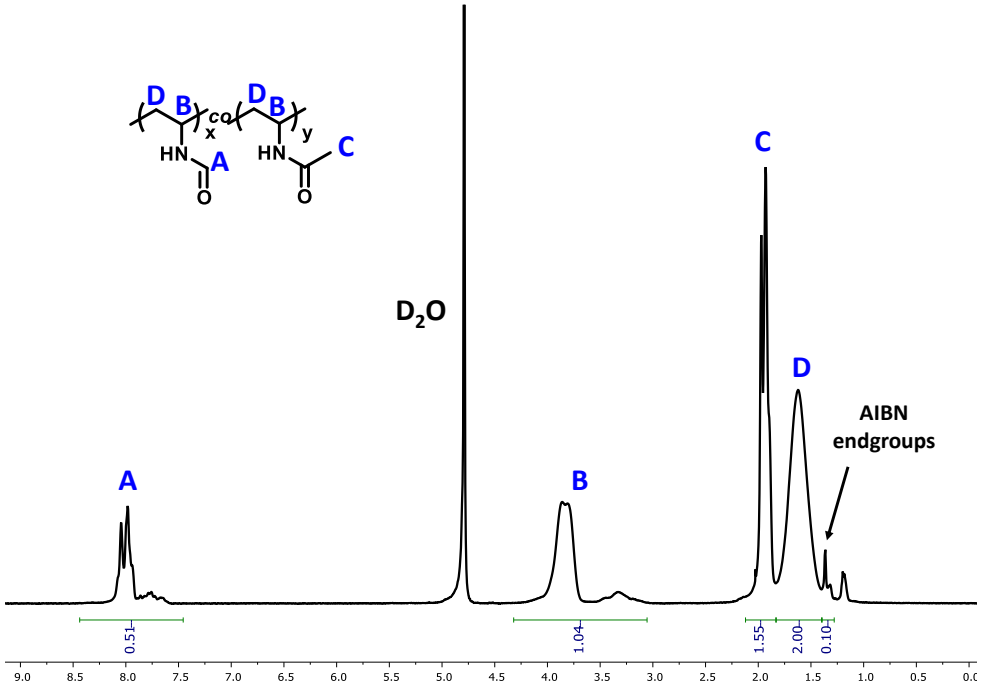

Figure S3.1. ^{1}H NMR spectrum of poly(NVF-*co*-VAm). Assignment of signals to the corresponding structural units by capital letters.

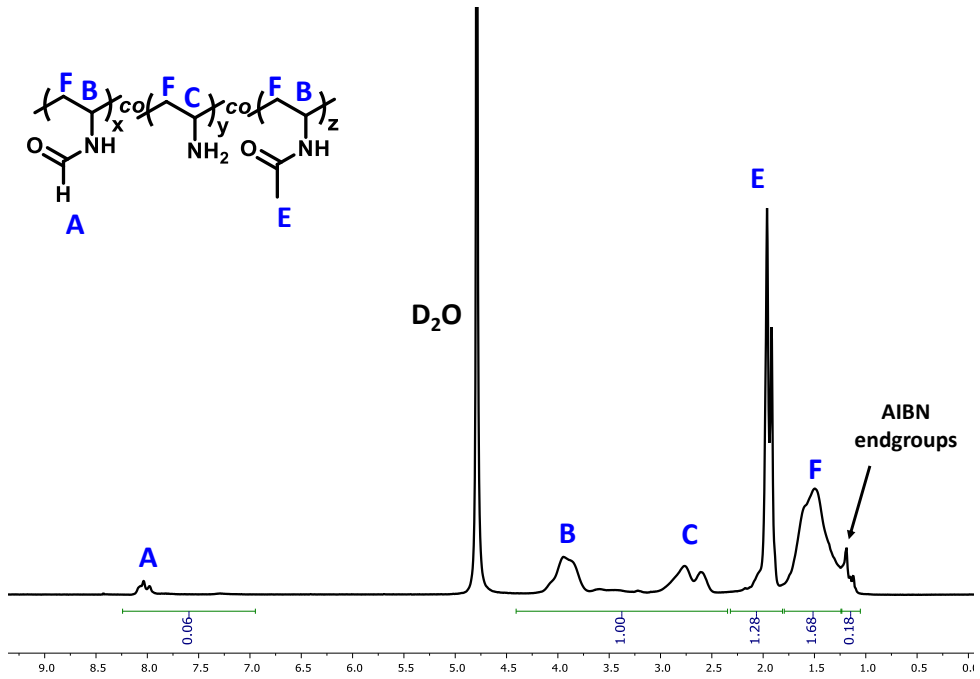

Figure S3.2. ^{1}H NMR spectrum of the poly(NVA-*co*-NVF-*co*-VAm) backbone after hydrolysis. Assignment of signals to the corresponding structural units by capital letters.

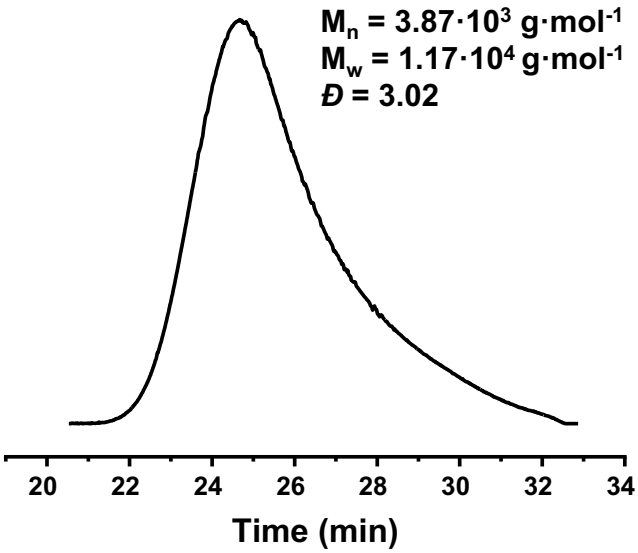

Figure S3.3. SEC elugram of poly(NVA-*co*-NVF-*co*-VAm) prior to functionalization with PFPA and BIB**.**

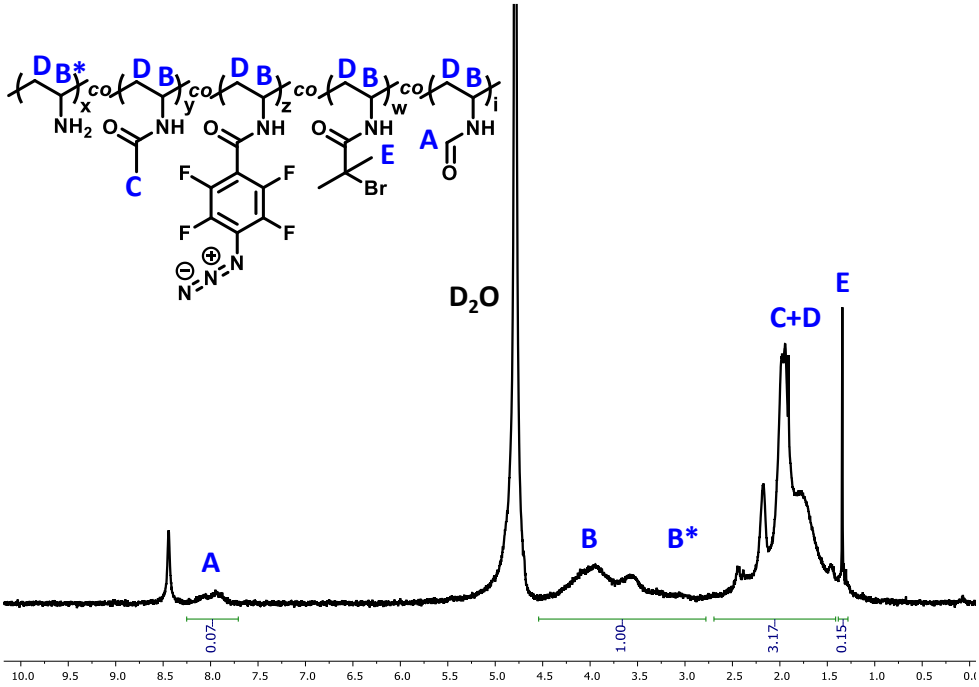

Figure S3.4. ^{1}H NMR spectrum of the macroinitiator after introduction of PFPA and BIB groups. Assignment of signals to the corresponding structural units by capital letters.

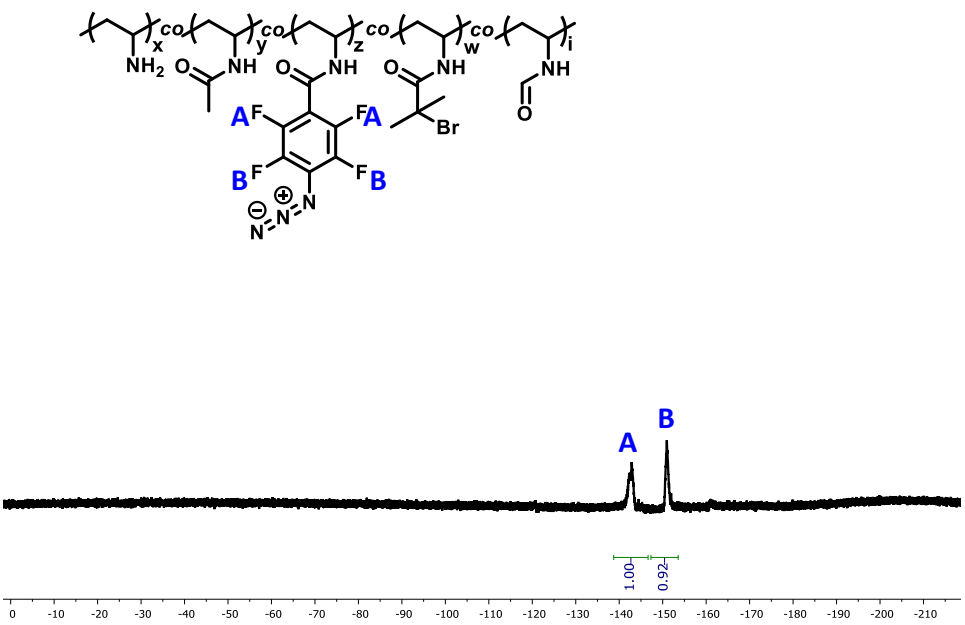

Figure S3.5. ^{19}F NMR spectrum of the macroinitiator

3.6 Declaration of Contributions

Parts of this chapter were adapted with permission from the publication “Interactive Hemocompatible Nanocoating to Prevent Surface-Induced Coagulation in Medical Devices” in Advanced Materials Interfaces (Quandt, J., Garay-Sarmiento, M., Witzdam, L., Englert, J., Rutsch, Y., Stöcker, C., Obstals, F., Grottke, O., Rodriguez-Emmenegger, C., Interactive Hemocompatible Nanocoating to Prevent Surface-Induced Coagulation in Medical Devices. Adv. Mater. Interfaces 2022, 9, 2201055; https://doi.org/10.1002/admi.202201055; Copyright © 2022 The Authors. Advanced Materials Interfaces published by Wiley-VCH GmbH). Moreover, some of the results were also published in the master thesis entitled “Assessment of immobilized antibody against a blood coagulation factor” at RWTH Aachen University by Jonas Quandt.

As for Subchapter 3.2.1: I performed PDA coating studies and surface characterization by SEM imaging and ellipsometry analysis. Jonas Quandt and I performed the grafting of polymer brushes via ATRP and XPS analysis. Furthermore, Jonas Quandt performed CA analysis.

As for Subchapter 3.2.2: I performed electrospinning experiments, SEM and XPS analysis. Jonas Quandt and I performed the synthesis of the Br-PCL-Br macroinitiator.

As for the subchapters 3.2.3 to 3.2.7: I performed electrospinning experiments, SEM analysis, biocompatibility and *E. coli* adhesion studies. Jonas Quandt synthesized antifouling polymer brushes and performed SPR as well as CA studies. Jonas Quandt and I performed XPS analysis. Jan Tenbusch provided the precursor poly(vinylamine-*co*-vinylformamide-*co*-vinylacetamide) copolymer (NVA-*co*-NVF-*co*-VAm) and its molecular characterization by ^{1}H-NMR and SEC.

Prof. César Rodriguez-Emmenegger supervised all of these projects.

3.7 References

[1] N. A. Hodges, E. M. Sussman, J. P. Stegemann, *Biomaterials* **2021**, *278*, 121127.

[2] S. Veerachamy, T. Yarlagadda, G. Manivasagam, P. K. Yarlagadda, *Proc. Inst. Mech. Eng., Part H* **2014**, *228*, 1083-1099.

[3] C. R. Arciola, D. Campoccia, L. Montanaro, *Nat. Rev. Microbiol.* **2018**, *16*, 397-409.

[4] C. Rodriguez-Emmenegger, E. Brynda, T. Riedel, M. Houska, V. Šubr, A. B. Alles, E. Hasan, J. E. Gautrot, W. T. S. Huck, *Macromolecular Rapid Communications* **2011**, *32*, 952-957.

[5] A. R. Kuzmyn, A. T. Nguyen, L. W. Teunissen, H. Zuilhof, J. Baggerman, *Langmuir* **2020**, *36*, 4439-4446.

[6] J. Ladd, Z. Zhang, S. Chen, J. C. Hower, S. Jiang, *Biomacromolecules* **2008**, *9*, 1357-1361.

[7] A. d. l. S. Pereira, C. Rodriguez-Emmenegger, F. Surman, T. Riedel, A. B. Alles, E. Brynda, *RSC Advances* **2014**, *4*, 2318-2321.

[8] C. Rodriguez-Emmenegger, S. Janel, A. de los Santos Pereira, M. Bruns, F. Lafont, *Polymer Chemistry* **2015**, *6*, 5740-5751.

[9] G. Cheng, Z. Zhang, S. Chen, J. D. Bryers, S. Jiang, *Biomaterials* **2007**, *28*, 4192-4199.

[10] A. de los Santos Pereira, S. Sheikh, C. Blaszykowski, O. Pop-Georgievski, K. Fedorov, M. Thompson, C. Rodriguez-Emmenegger, *Biomacromolecules* **2016**, *17*, 1179-1185.

[11] I. Szleifer, *Biophysical journal* **1997**, *72*, 595-612.

[12] A. Halperin, *Langmuir* **1999**, *15*, 2525-2533.

[13] H. Lee, W. Lee, Y. Soo Han, E. Kim, D. Y. Ryu, *Polymer Journal* **2016**, *48*, 503-507.

[14] L. Leibler, A. Mourran, *MRS Bulletin* **1997**, *22*, 33-37.

[15] R. Zhang, Y. Liu, M. He, Y. Su, X. Zhao, M. Elimelech, Z. Jiang, *Chemical Society Reviews* **2016**, *45*, 5888-5924.

[16] P. G. de Gennes, *Macromolecules* **1980**, *13*, 1069-1075.

[17] S. Tugulu, H.-A. Klok, *Biomacromolecules* **2008**, *9*, 906-912.

[18] J. Wang, H.-A. Klok, *Angew. Chem., Int. Ed.* **2019**, *58*, 9989-9993.

[19] N. C. Ataman, H.-A. Klok, *Macromolecules* **2016**, *49*, 9035-9047.

[20] M. Ozdemir, C. U. Yurteri, H. Sadikoglu, *Crit. Rev. Food Sci. Nutr.* **1999**, *39*, 457-477.

[21] A. Azari, A. Golchin, M. Mahmoodinia Maymand, F. Mansouri, A. Ardeshirylajimi, *Adv Pharm Bull* **2022**, *12*, 658-672.

[22] C. Rodriguez-Emmenegger, E. Brynda, T. Riedel, M. Houska, V. Šubr, A. B. Alles, E. Hasan, J. E. Gautrot, W. T. S. Huck, *Macromol. Rapid Commun.* **2011**, *32*, 952-957.

[23] C. Rodriguez-Emmenegger, M. Houska, A. B. Alles, E. Brynda, *Macromol. Biosci.* **2012**, *12*, 1413-1422.

[24] A. de los Santos Pereira, C. Rodriguez-Emmenegger, F. Surman, T. Riedel, A. B. Alles, E. Brynda, *RSC Adv.* **2014**, *4*, 2318-2321.

[25] O. Pop-Georgievski, Š. Popelka, M. Houska, D. Chvostová, V. Proks, F. Rypáček, *Biomacromolecules* **2011**, *12*, 3232-3242.

[26] H. Lee, S. M. Dellatore, W. M. Miller, P. B. Messersmith, *Science* **2007**, *318*, 426-430.

[27] B. H. Kim, D. H. Lee, J. Y. Kim, D. O. Shin, H. Y. Jeong, S. Hong, J. M. Yun, C. M. Koo, H. Lee, S. O. Kim, *Advanced Materials* **2011**, *23*, 5618-5622.

[28] N. Y. Kostina, O. Pop-Georgievski, M. Bachmann, N. Neykova, M. Bruns, J. Michálek, M. Bastmeyer, C. Rodriguez-Emmenegger, *Macromolecular Bioscience* **2016**, *16*, 83-94.

[29] J. H. Ryu, P. B. Messersmith, H. Lee, *ACS Appl Mater Interfaces* **2018**, *10*, 7523-7540.

[30] Z. Wang, F. Tang, H. Fan, L. Wang, Z. Jin, *Langmuir* **2017**, *33*, 5938-5946.

[31] T. Wang, M. Xia, X. Kong, *Catalysts* **2018**, *8*, 215.

[32] J.-H. Lin, C.-J. Yu, Y.-C. Yang, W.-L. Tseng, *Physical Chemistry Chemical Physics* **2015**, *17*, 15124-15130.
[33] G. D. Fu, J. Y. Lei, C. Yao, X. S. Li, F. Yao, S. Z. Nie, E. T. Kang, K. G. Neoh, *Macromolecules* **2008**, *41*, 6854-6858.
[34] C. Rodriguez-Emmenegger, M. Houska, A. B. Alles, E. Brynda, *Macromolecular Bioscience* **2012**, *12*, 1413-1422.
[35] F. Obstals, M. Vorobii, T. Riedel, A. de los Santos Pereira, M. Bruns, S. Singh, C. Rodriguez-Emmenegger, *Macromolecular Bioscience* **2018**, *18*, 1700359.
[36] O. Pop-Georgievski, C. Rodriguez-Emmenegger, A. d. l. S. Pereira, V. Proks, E. Brynda, F. Rypáček, *Journal of Materials Chemistry B* **2013**, *1*, 2859-2867.
[37] O. Prucker, C. A. Naumann, J. Rühe, W. Knoll, C. W. Frank, *Journal of the American Chemical Society* **1999**, *121*, 8766-8770.
[38] P. Samyn, M. Biesalski, O. Prucker, J. Rühe, *Journal of Photochemistry and Photobiology A: Chemistry* **2019**, *377*, 80-91.
[39] L.-H. Liu, M. Yan, *Accounts of Chemical Research* **2010**, *43*, 1434-1443.
[40] O. Sterner, Â. Serrano, S. Mieszkin, S. Zürcher, S. Tosatti, M. E. Callow, J. A. Callow, N. D. Spencer, *Langmuir* **2013**, *29*, 13031-13041.
[41] S. A. Ferry, S. E. Holm, H. Stenlund, R. Lundholm, T. J. Monsen, *Scand. J. Infect. Dis.* **2004**, *36*, 296-301.
[42] C. Rodriguez-Emmenegger, B. V. K. J. Schmidt, Z. Sedlakova, V. Šubr, A. B. Alles, E. Brynda, C. Barner-Kowollik, *Macromol. Rapid Commun.* **2011**, *32*, 958-965.
[43] M. Vorobii, A. de los Santos Pereira, O. Pop-Georgievski, N. Y. Kostina, C. Rodriguez-Emmenegger, V. Percec, *Polym. Chem.* **2015**, *6*, 4210-4220.
[44] J. F. W. Keana, S. X. Cai, *The Journal of Organic Chemistry* **1990**, *55*, 3640-3647.
[45] J. F. Watts, *Surf. Interface Anal.* **1993**, *20*, 267-267.

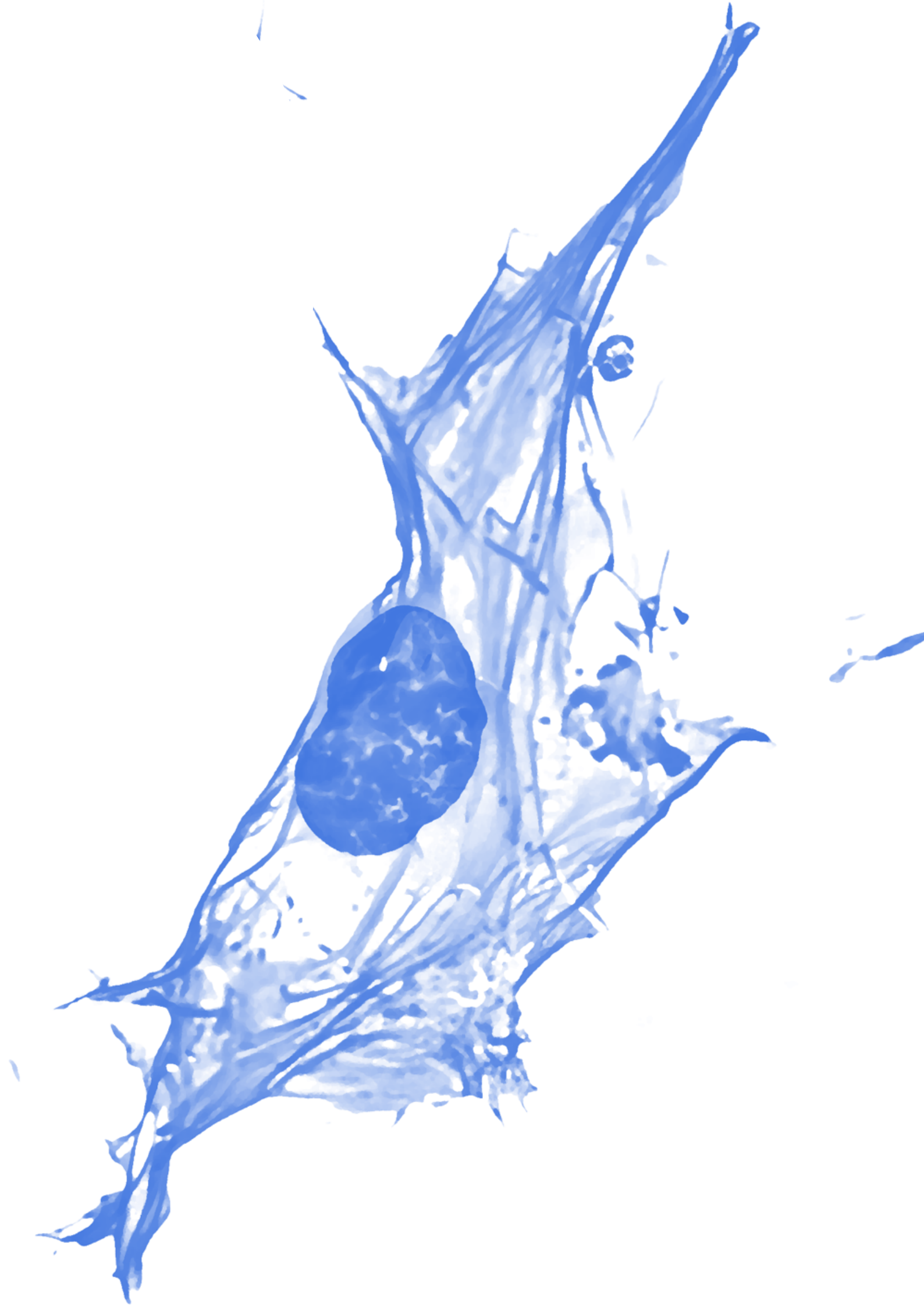

Chapter 4

Leveraging Protein Adsorption for Surface Functionalization

4.1 Introduction

The most promising method for achieving highly effective antifouling surface coatings to date is the grafting-from approach, where polymer brushes are directly grown from the substrate surface at a high density. In the previous Chapter, I presented various mild strategies that facilitate the functionalization of a wide range of materials used in medical devices with functional groups that can initiate the polymerization reaction. However, a significant limitation persists: the strict polymerization conditions required for growing these polymer brushes. Their synthesis demands inert gas atmosphere, which involves careful deoxygenation of solvents and polymerization vessels. As these conditions are difficult to realize in large-scale setups and impose limitations on substrate size and shape, they have so far precluded their translation to practical applications. Several research groups have introduced concepts to simplify the formation of a brush-like coating to achieve antifouling properties. Common strategies include the physisorption of amphiphilic copolymers[1], crosslinking of star-shaped PEG[2], electrostatic adsorption of graft copolymers[3-4] and the use of different surface binding groups, such as catechol derivates[5-7] and phosphonate groups[8]. Although these methods have been widely applied in research, many have limitations for widespread practical use such as the requirement for charges on the substrate surface or the need for chemical specificity between functional groups and surfaces. But above all, the biggest limitation is that most of these strategies do not achieve high grafting densities or a homogeneous coating, hence their antifouling properties are limited when challenged with complex biological fluids like blood plasma.

Recently, the generation of antifouling coatings with efficacy on par to the best grafting-from polymer brushes was achieved by surface-attached hydrogels[9-11] Briefly, a hydrogel precursor polymer bearing benzophenone crosslinking groups is applied to the surface of the substrate. Upon UV irradiation, the benzophenone forms biradical intermediates that insert into carbon-hydrogen bonds via C, H-insertion mechanisms crosslinking the polymer to the surface and in solution. With this method even geometrically challenging substrates, such as blood collecting tubes could be coated. However, this strategy is limited to polymeric substrates containing C-H bonds and still requires energy input for the cross-linking reaction to take place at the surface.

As previously discussed, proteins are macromolecules with high binding promiscuity, capable of adsorbing to the surface of materials within seconds of contact. They are amphiphilic in nature and have the ability to change their conformation (shape) very easy. When dissolved in water, they conceal amino acid residues unfavorable to water into their core but in the presence of an artificial surface, they adapt their conformation very fast to display those amino acids that maximize interactions with the surface, leading to their attachment and reduction of the surface's Gibbs free energy. Given this binding. promiscuity of protein, why not leverage their adhesion advantage to address the long-standing challenge of enabling the functionalization of technical surfaces that cannot be functionalized through conventional means?

As such, surface passivation of medical devices is often carried out through the spontaneous adsorption of albumin (alb) to the surface.[12] However, alb is susceptible to adsorption- and aging-induced unfolding, which can ultimately activate platelet adhesion and coagulation.[13-17] Nonetheless, protein adsorption has opened up new avenues for applying coatings without requiring external energy input for surface or reactant activation steps.[18-19] Peptides, in particular, have been found to be advantageous, as they have the unique characteristic of forming highly ordered assemblies.[20-21] In this vein, peptide-polymer hybrids are being used to achieve functionalization of multiple materials.[19, 22-24]

In this chapter, I will present a coating strategy based on the surface binding promiscuity of the antimicrobial peptide, liquid chromatography peak I (LCI). AMPs are amphipathic peptides which are very promising surface binding promoters by virtue of their bactericidal action. LCI is a novel thermally stable β-structure AMP with hydrophobic (22 aa), negatively charged (4 aa) and positively charged regions (7 aa).[25] Its directional self-assembly at the liquid-solid interface allows the functionalization of a wide range of materials ensuring strong adhesion and precise spatial arrangement.[22-23, 26-31] Herein, LCI-polymer biohybrids are leveraged to create a dense antifouling polymer brush-like coating on medical devices such as PCL wound dressings, polyurethane foam dressings, venous catheters and metallic orthopedic implants entirely through physical interactions. The LCI peptide is genetically fused to an enhanced green fluorescent protein (eGFP), which contains an available cysteine group (position 69) from where the maleimide initiator, (2-(2,5-dioxo-2,5-dihydro-1H-pyrrol-1-yl) ethyl 2-bromo-2-methylpropanoate), is conjugated via thiol-Michael click reaction. Therefrom polymer

chains of HPMA, CBMAA, *N*-(3-sulfopropyl)-*N*-methacroyloxyethyl-*N*,*N*-dimethylammonium betaine (SBMA) and 2-(methacryloyloxy)ethyl phosphorylcholine (PCMA) are grafted by SET-LRP in PBS buffer. The biohybrid coating is formed from an aqueous solution through the physisorption of these hybrids to the surface without requiring external energy input. The adsorption process is driven solely by the LCI peptide, ensuring an oriented type of immobilization that segregates the polymer chain into a dense brush-like structure at the periphery.[23]

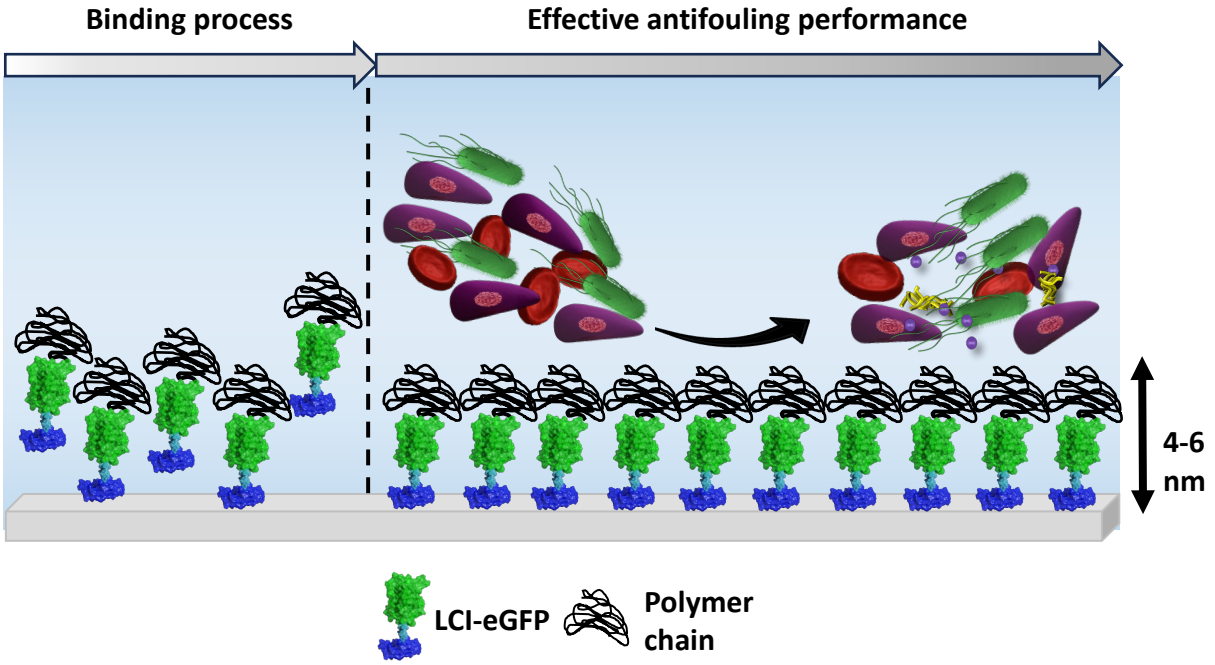

Figure 4.1. Surface directed adsorption of LCI-eGFP-Polymer hybrids from aqueous solution forming a dense coating that effectively resists the adsorption of protein and adhesion of eukaryotic cells and pathogenic bacteria.

Despite having a thickness of only a few nanometers (4-6 nm), this coating exhibits antifouling properties comparable to the best grafting-from polymer brushes. Coated substrates effectively resist the nonspecific adsorption of proteins from BP and were able to prevent the adhesion of fibroblasts and pathogenic *E. coli* bacteria. Furthermore, this biohybrid coating exerts exceptional biocompatibility and stability to sterilization by gamma irradiation.

4.2 Results and Discussion

4.2.1 Synthesis of the LCI-eGFP-Polymer Hybrid Library

The LCI-eGFP fusion protein was produced in *E. coli* BL21 Gold (DE3) cells as it has been previously described by Schwaneberg et. al.[26-27] The LCI-eGFP-Polymer hybrids were synthesized by SET-LRP. This controlled polymerization technique was chosen because it enables the reaction to proceed in aqueous system utilizing only minimal amount of catalyst while achieving high conversion rates and retention of chain-end fidelity.[32-33] Furthermore, in previous work by our group, it was confirmed by circular dichroism that the mild conditions of SET-LRP enabled polymerization without affecting the secondary structure of the LCI-eGFP construct.[22-23]

In order to carry out the polymerization, the LCI-eGFP construct had to be conjugated to an initiator group. As depicted in Figure 4.2A, the eGFP has two free cysteine residues (Cys, position 69 and 91) that provide thiol functional groups, from where initiator molecules can be conjugated. However, from computational modelling analysis and experimental work, it has been identified that the Cys at position 91 is hidden within the eGFP and therefore not accessible for polymerization purposes.[22] Thus, Cys at position 69 served to conjugate the maleimide Initiator (2-(2,5-dioxo-2,5-dihydro-1H-pyrrol-1-yl) ethyl 2-bromo-2-methylpropanoate) to LCI-eGFP via thiol-Michael addition. After careful purification, polymer chains consisting of CBMAA, HPMA, SBMA and PCMA were grafted from the functionalized LCI-eGFP construct to obtain LCI-eGFP-p(CBMAA)$_{DP}$, LCI-eGFP-p(HPMA)$_{DP}$, LCI-eGFP-p(SBMA)$_{DP}$ and LCI-eGFP-p(PCMA)$_{DP}$, respectively. DP indicates the degree of polymerization. Polymerization was carried out at 30 °C using a hydrazine-activated copper wire as catalyst. A library of various hybrids with different degrees of polymerization was synthesized by adjusting the ratio of initiator to monomer (Table S4.1). The respective conversion ratios and DPs were calculated from ^{1}H-NMR analysis of the crude polymerization solutions (Figure S4.1 and Figure S4.2). Notably, poly(CBMAA) and poly(HPMA) led to conversions of 68% and 65% in 18 h, while p(PCMA) and p(SBMA) reached full conversion (100%) in the same time. This is presumably due to the methacrylamide backbone.[34] Furthermore, the retention of green fluorescence from eGFP was considered an indicator that the secondary structure of this protein was not affected during the polymerization procedure.

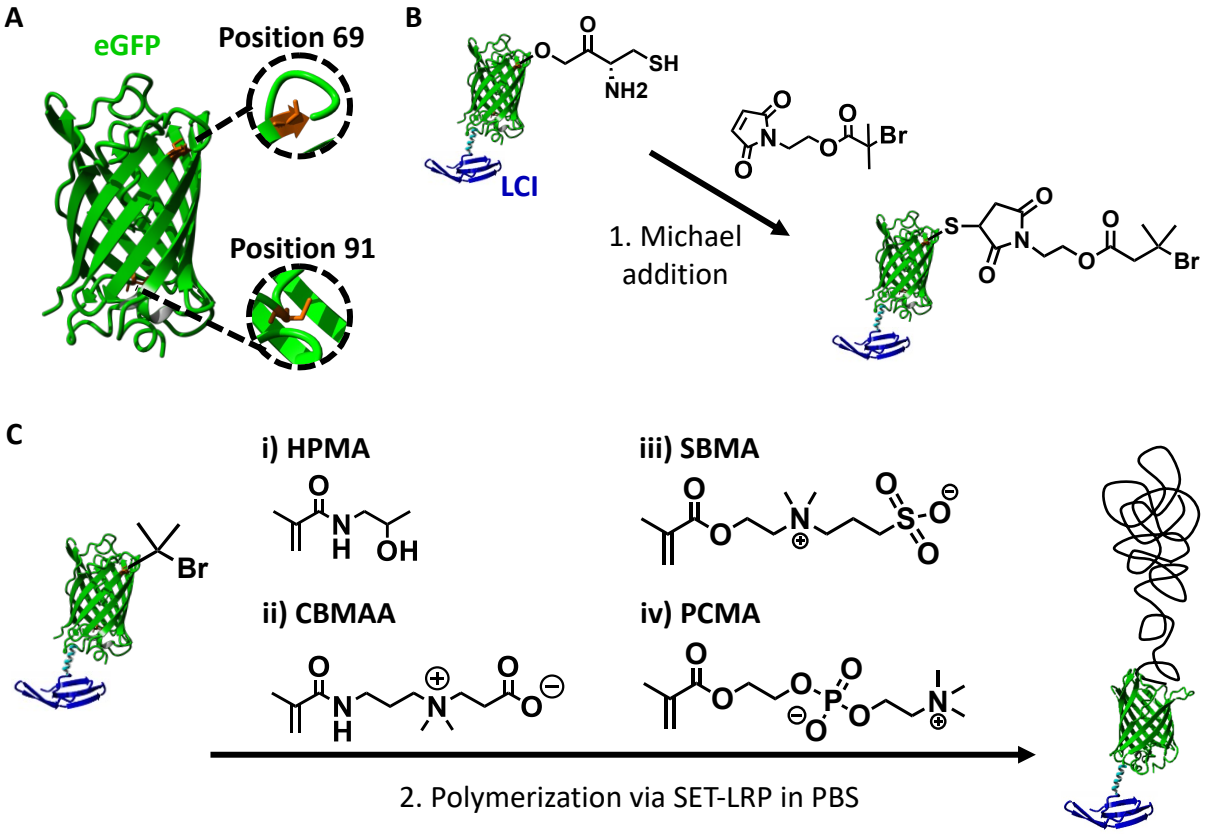

Figure 4.2. (A) Crystal structure of eGFP (PDB ID:2Y0G). Cysteine positions are highlighted in Orange (determined by YASARA – Yet Another Scientific Artificial Reality Application – v16.3.5) Schematic depiction of (B) the functionalization route of LCI-eGFP with the maleimide initiator and (C) polymerization of LCI-eGFP-p(HPMA), LCI-eGFP-p(CBMAA), LCI-eGFP-p(SBMA) and LCI-eGFP-p(PCMA) via SET-LRP.

After purification steps the hybrids were once again analyzed by ^{1}H-NMR and multiangle laser light scattering size exclusion chromatography (MALLS-SEC) to confirm purity and obtained molecular weights. Figure 4.3 depicts three exemplary ^{1}H-NMR spectra of purified LCI-eGFP, LCI-eGFP-p(CBMAA)$_{912}$ and LCI-eGFP-p(HPMA)$_{792}$. The absence of signals at a chemical shift between 5.4 and 6.0 ppm confirms that monomer remains were successfully removed during the purification process. Additionally, MALLS-SEC analysis reveals molecules with unimodal molecular weight distribution and no traces of free LCI-eGFP-Initiator, indicating quantitative initiation efficiency. Notably, the polydispersity of the hybrid macromolecules only increased slightly from 1.012 for LCI-eGFP to 1.27 for LCI-eGFP-p(HPMA)$_{340}$ and 1.33 for LCI-eGFP-p(CBMAA)$_{336}$ even though the molecular weights more than tripled (Figure S4.3).

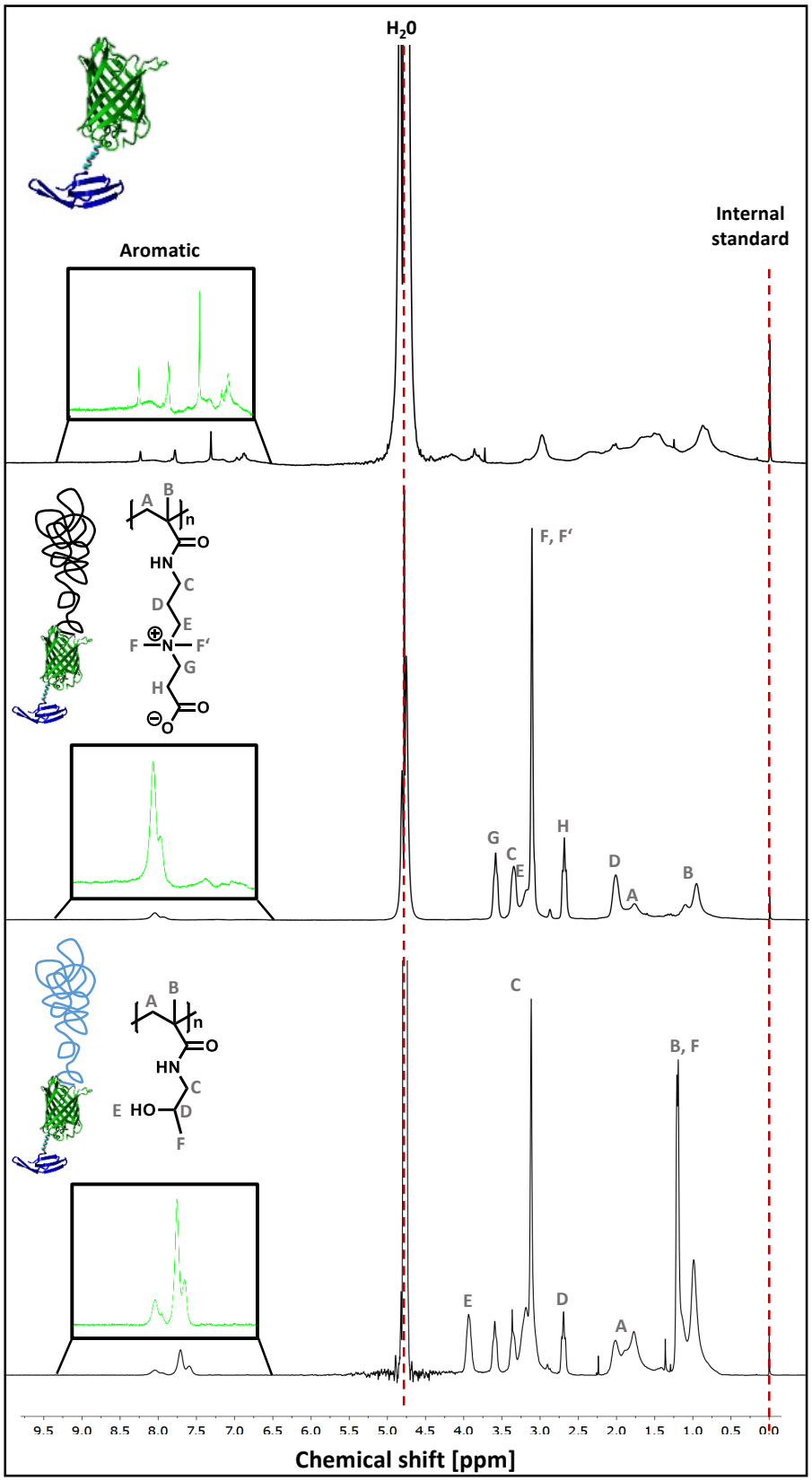

Figure 4.3. ^{1}H-NMR spectra of purified LCI-eGFP, LCI-eGFP-p(HPMA)$_{792}$ and LCI-eGFP-p(CBMAA)$_{912}$ indicating no monomer contamination. Reprinted and modified from Ref. [35].

4.2.2 Influence of Chemical Composition and Degree of Polymerization on Antifouling Properties

Various LCI-eGFP polymer hybrids based on four different types of antifouling monomers were synthesized: CBMAA, HPMA, SBMA and PCMA, as these represent the main chemical approaches to minimize protein fouling by polymer brushes. In a first step, we aimed to compare the effectiveness of the different chemical compositions in terms of their antifouling properties. For these studies we selected gold as a model surface and the hybrids LCI-eGFP-$CBMAA_{864}$, LCI-eGFP-$HPMA_{780}$, LCI-eGFP-$SBMA_{1176}$ and LCI-eGFP-$PCMA_{1200}$, since these hybrids have similar DP. The hybrid coatings were formed *in-situ* inside the flow cell on the SPR by loading the different hybrid solutions at a flow rate of 10 µL min^{-1} and a concentration of 1 mg mL^{-1} in PBS. Figure 4.4 depicts the binding kinetics of LCI-eGFP-$HPMA_{780}$ on the gold-coated SPR sensor chip. The physisorption of the hybrid to the surface begins immediately upon contact reaching saturation already after 30 min and at last generating a coating with a hybrid molecule density of 90 ng·cm^{-2} (0.60 pmol·cm^{-2}). All hybrid molecules were able form dense layers of approximately 90-190 ng cm^{-2} (Table 4.1).

Table 4.1. Hybrid molecule densities of the different coatings calculated from SPR spectroscopy.

Hybrid	Coating density [ng·cm^{-2}]	Coating density [pmol·cm^{-2}]
LCI-eGFP-$pCBMAA_{864}$	115	0.47
LCI-eGFP-$HPMA_{780}$	90	0.60
LCI-eGFP-$SBMA_{1176}$	246	0.67
LCI-eGFP-$PCMA_{1200}$	190	0.48

Following hybrid adsorption, a 10% diluted solution of BP proteins in PBS was injected and the amount of protein fouling was calculated (Figure 4.4B). $pCBMAA_{864}$ and $pHPMA_{780}$ were able to reduce protein fouling by at least 85%, while $pPCMA_{1200}$ achieved only 32%. In the case of

pSBMA$_{1176}$, protein fouling was reduced by 88%, comparable to the performance of pCBMAA$_{864}$ and pHPMA$_{780}$, however relying on a much higher DP, i.e., steric repulsion. Based on these observations, the ranking of antifouling performance is as follows: LCI-eGFP-pHPMA ≥ LCI-eGFP-pCBMAA > LCI-eGFP-pSBMA > LCI-eGFP-pPCMA >> gold surface. This ranking is consistent with literature[36] and shows that the chemical composition plays a pivotal role in the fouling process. The poor performance of LCI-eGFP-pPCMA may be attributed to specific interactions with plasma components or to a different morphology of the hybrid coating. Furthermore, as for now it is not fully understood why HPMA works as well or even better than zwitterionic polymers. Since compared to CBMAA and SBMA, it forms coatings that are only moderately hydrophilic.[37] Zuilhof et al. propose that the improved antifouling performance of pHPMA might result from the formation of hydrogen bond bridges between water molecules and the hydroxyl and amide groups within the same monomer unit, leading to a strong interaction with water.[37]

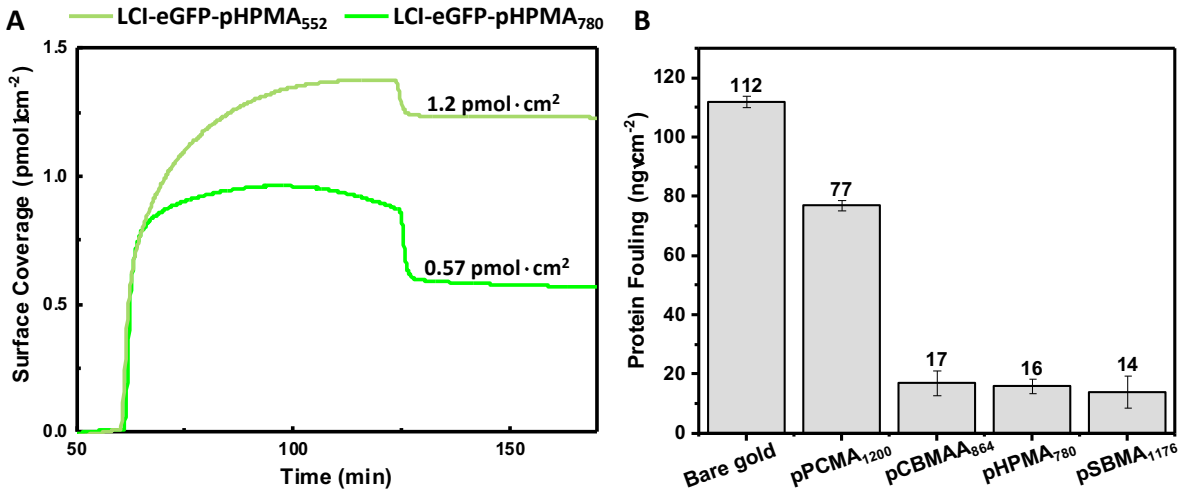

Figure 4.4. (A) SPR sensograms of the adsorption of LCI-eGFP-pHPMA hybrids on gold-coated SPR sensor chips. (B) BP fouling measured by SPR spectroscopy of different hybrid coatings on gold-coated SPR sensor chips.

Based on our findings, we concluded that LCI-eGFP-pHPMA and LCI-eGFP-pCBMAA provided the most effective antifouling coatings. Furthermore, we examined the influence of the DP on the antifouling properties. As shown in Figure 4.4A, the adsorption of LCI-eGFP-pHPMA$_{552}$ yielded a hybrid molecule density of 1.2 pmol·cm^{-2}, which is twice that of LCI-eGFP-HPMA$_{780}$ achieved (0.57 pmol·cm^{-2}). This is related to the change of packing of the hybrid molecules at the surface with a higher degree of polymerization and also to the larger excluded volume

effects, due to a larger polymer chain. In previous work by our group, we elucidated by X-ray reflectivity that the packing of cylindrical eGFP controls the assembly of the hybrids at the gold surface. eGFPs are shown to be tilted toward the surface and not completely parallel to it. As the DP increases, the tilt increases, resulting in a larger interface between the eGFP and the poly(HPMA).[23]

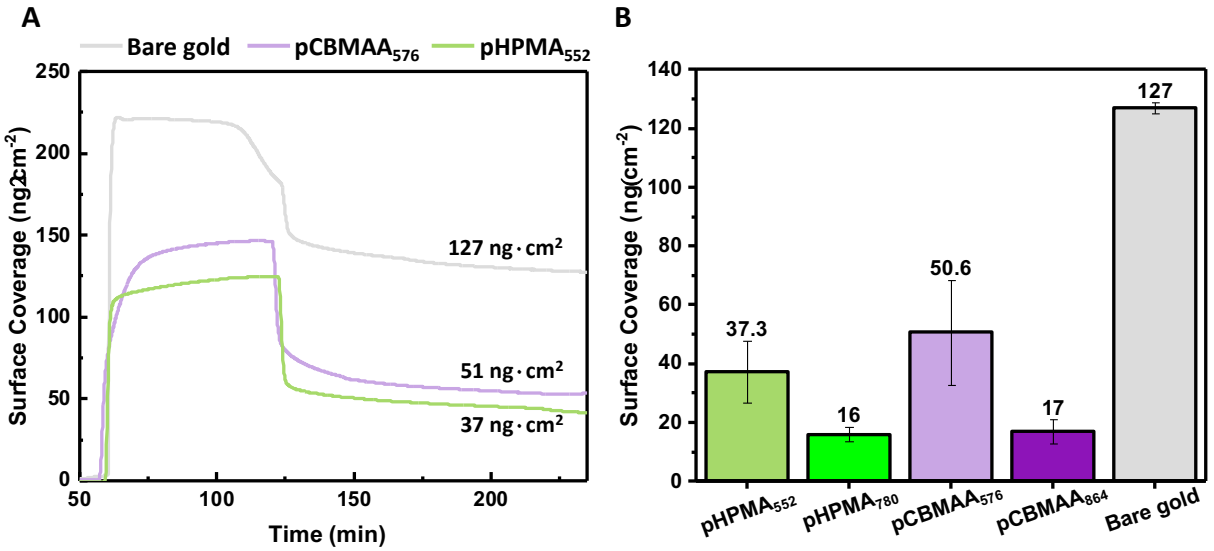

Figure 4.5. (A) SPR sensograms of BP fouling on different hybrid coatings and bare gold-coated SPR sensor chips. (B) BP fouling measured by SPR spectroscopy of different hybrid coatings on gold-coated SPR sensor chips.

As for the antifouling properties, LCI-eGPF-Polymer hybrids demonstrated improved capability in preventing non-specific absorption of proteins from 10% BP with increasing DP, i.e., the steric repulsion (Figure 4.5B). Figure 4.6A depicts an exemplary BP fouling measurement by SPR spectroscopy using 10% BP in PBS. LCI-eGFP-pHPMA$_{552}$ and LCI-eGFP-pCBMAA$_{576}$ reduced fouling only by 71 and 59%, respectively. Hence, both the chemical composition and the length of the grafted polymer chains play a crucial role in the fouling process.

Under more challenging conditions, namely exposure to undiluted blood plasma, both LCI-eGFP-pHPMA$_{780}$ and LCI-eGFP-pCBMAA$_{864}$ reduced protein fouling by at least 70% when compared to bare gold. (Gold: 197 ng·cm^{-2}; LCI-eGFP-pHPMA$_{780}$: 60 ng·cm^{-2}and LCI-eGFP-pCBMAA$_{864}$: 58 ng·cm^{-2}). Notably, this outstanding resistance to protein fouling is comparable to the best antifouling polymer brushes grafted directly from the substrate. Yet, the hybrid coating presented here is much easier to apply to the surface without the need for laborious coating procedures or surface activation steps, holding promise for clinical applications.

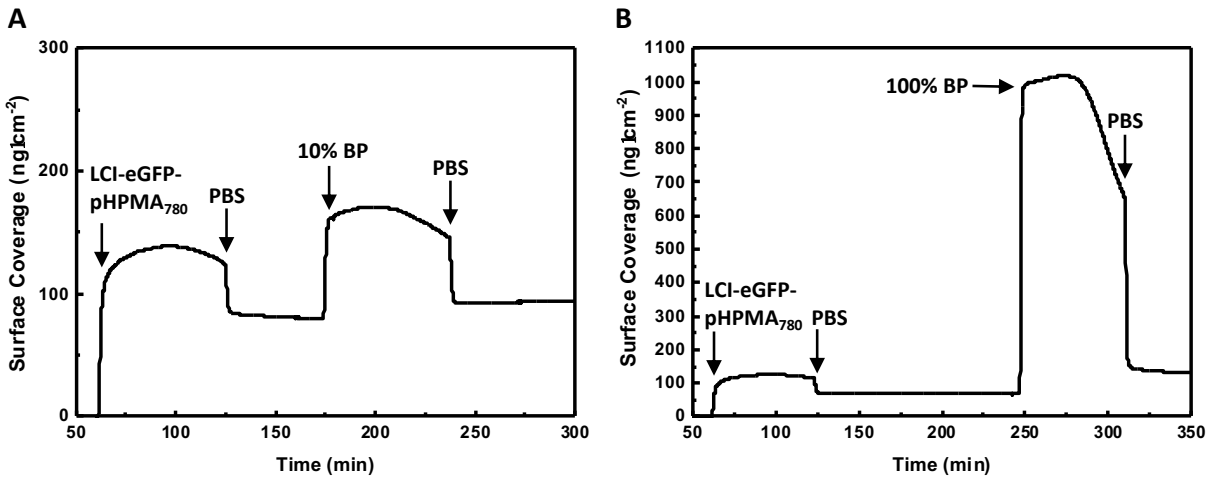

Figure 4.6. SPR sensograms capturing the adsorption of LCI-eGFP-pHPMA$_{780}$ onto gold-coated sensor chips and subsequent fouling from (A) 10% BP and (B) 100% BP.

4.2.3 Transfer of the LCI-eGFP-Polymer Coating to Relevant Medical Materials

The next step was to investigate the transfer of LCI-eGFP-Polymer coatings to various medical materials, especially polymers and metals. As the coating formation is based only on the physisorption of the hybrids onto the surface, the application does not require expensive equipment or specially trained personnel.

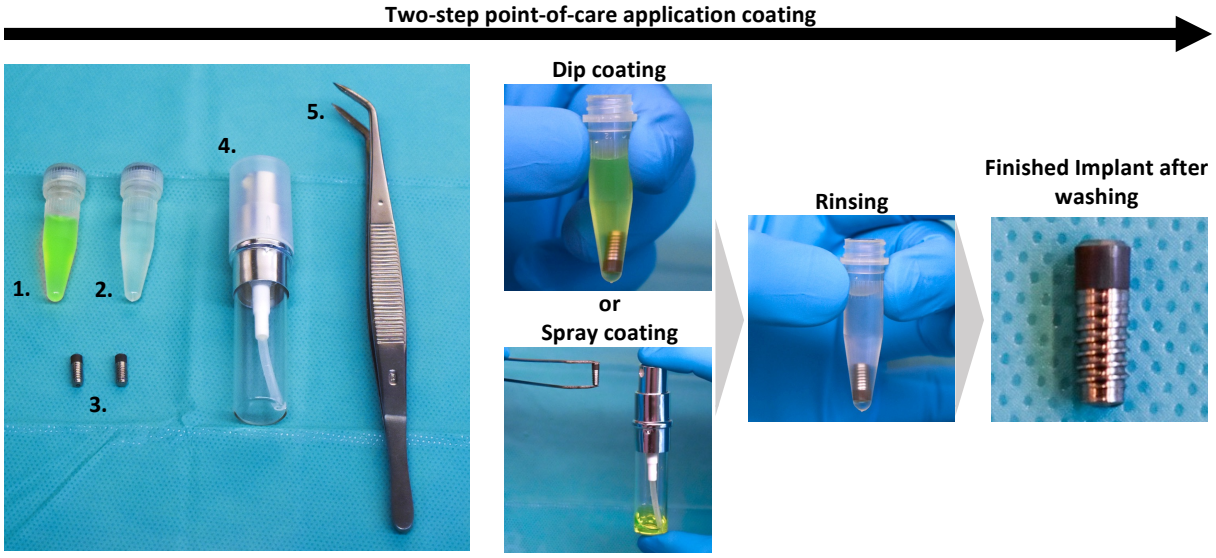

Figure 4.7. Demonstration of LCI-eGFP-Polymer hybrid coating technology of a titanium dental screw. A 1 mg mL^{-1} hybrid solution (1) is provided along with a PBS rinsing solution (2). The titanium dental implant (3) is immersed in the hybrid solution or sprayed with it using the

spray bottle (4). Following 45 min of contact time, the implant is washed with the supplied rinsing solution and the modified implant is obtained.

A simple setup, as illustrated in Figure 4.7, is all that is needed. The coating is applied in two steps using a diluted aqueous solution of LCI-eGFP Polymer hybrids (1 mg·mL^{-1} in PBS). First, the substrate to be coated is immersed in or sprayed with the hybrid solution. After 45 min of contact time, which is sufficient time to establish a fully saturated and dense coating, as confirmed with SPR analysis, the substrate can be washed to rinse off any unbound hybrid molecules. If aseptic conditions are required, the hybrid solution can be sterilized by filtration (0.2 μm) beforehand.

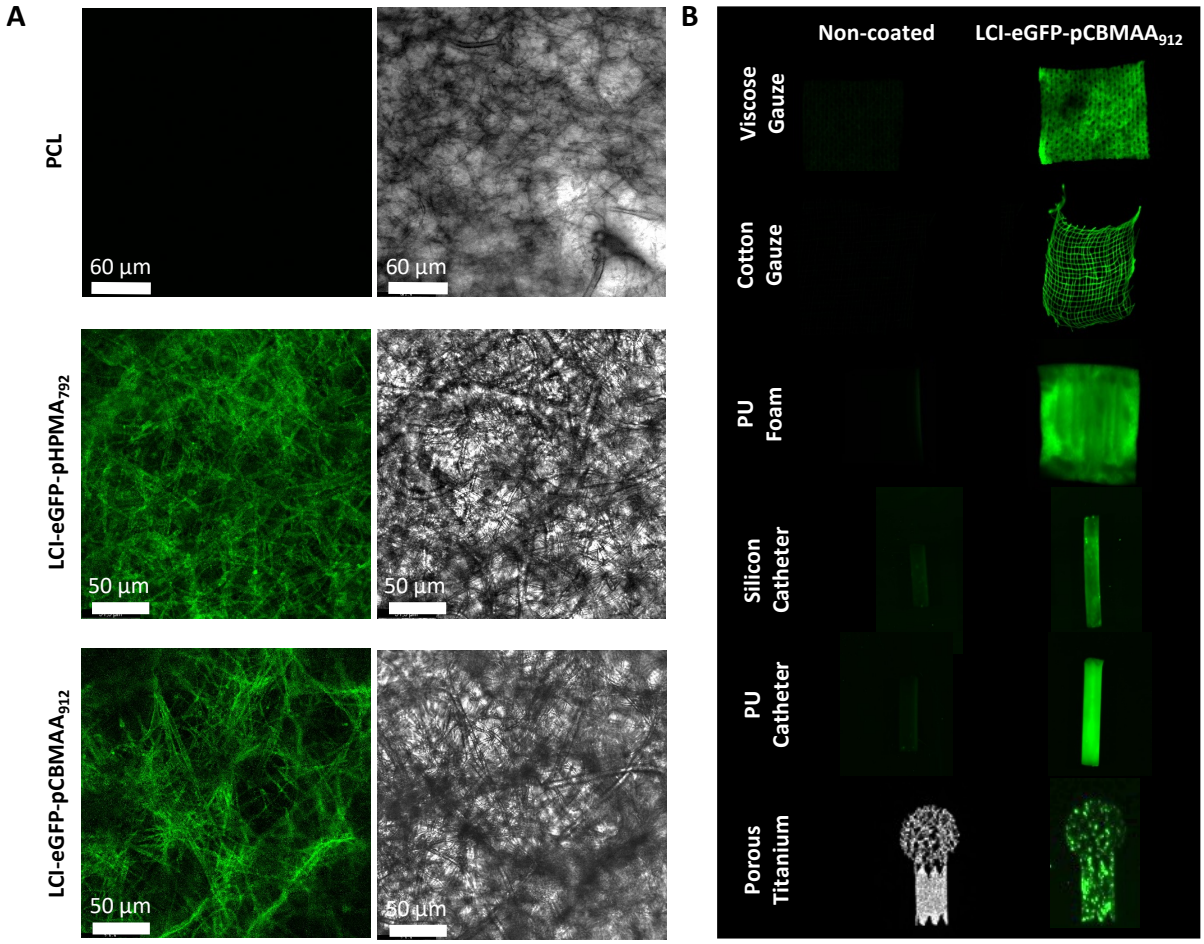

Figure 4.8. Fluorescent images taken (A) by confocal laser scanning microscopy (CLSM) or (B) a ChemiDoc MP Imaging System at 488 nm demonstrating the successful coating of a wide range of medical materials. The green fluorescence of eGFP was taken as reporter for a successful coating application. Non-coated substrates served as fluorescence control.

In this manner, we coated a wide range of different materials used in the medical industry. Figure 4.8 shows fluorescence images of some of these materials, including viscose and cotton wound dressings, polyurethane (PU) foam, silicone and PU venous catheters and porous titanium. We used the green fluorescence of eGFP as a reporter of successful coating formation. Control materials not exposed to the coating solution showed negligible to no fluorescence.

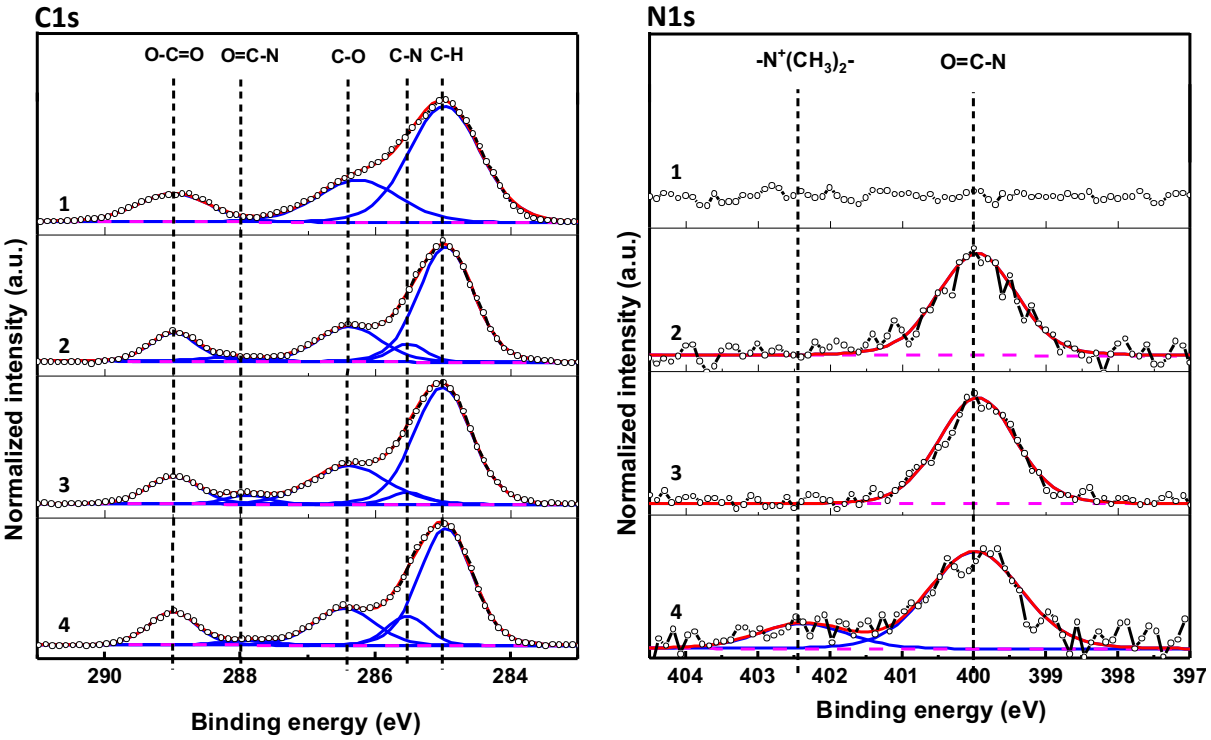

Figure 4.9. High resolution XPS spectra, C1s (left) and N1s (right), of 1. pristine PCL fibers, PCL coated with (2) LCI-eGFP, (3) LCI-eGFP-pHPMA$_{792}$ and (4) LCI-eGFP-pCBMAA$_{912}$.

Additionally, the chemical composition of the different hybrid coatings was assessed by XPS. Figure 4.9 illustrates exemplary high-resolution C1s and N1s spectra of pristine and modified (LCI-eGFP, LCI-eGFP-pHPMA$_{792}$ and LCI-eGFP-pCBMAA$_{912}$.) electrospun PCL wound dressings. The pristine PCL spectrum displays characteristic signals for the [C-O] and [O=C-O] groups of PCL at 286.4 eV and 289.0 eV, respectively. No signals were observed in the N1s spectrum, which is consistent with the chemical structure of PCL. After the adsorption of LCI-eGFP and LCI-eGFP-Polymer hybrids, signals at 285.6 and 288 eV arise referring to the presence of [C−N] and [O=C-N] bonds, respectively. The amide bond contributions derive from both the protein and the polymers. Additionally, the amide contributions can be further evidenced in the N1s

spectra by the appearance of the corresponding signal at 400 eV. In the case of LCI-eGFP-pCBMAA$_{912}$, a signal arises at 402.7 eV corresponding to the quaternary amine [$N^+(CH_3)_2$].

Notably, the high-resolution C1s spectra of the polymer surfaces show a strong predominance of [C-H] contributions stemming from the PCL substrate even after the application of the hybrid coatings. This is because the information depth of XPS is up to 10 nm and the thickness of the hybrid coatings is below this threshold, as determined by ellipsometry analysis (Table 4.2).

Table 4.2. Dry thickness of LCI-eGFP-Polymer hybrid coatings determined by ellipsometry.

Hybrid	Thickness [nm]
LCI-eGFP-pCBMAA$_{864}$	6.58
LCI-eGFP-HPMA$_{780}$	4.33

4.2.4 Stability of the LCI-eGFP-Polymer Coating

We also investigated the long-term stability of our hybrid coating in both isotonic solution, PBS, and in a nutrient-rich environment such as LB supplemented with 10% FBS. The latter is of particular interest because FBS contains various proteases and enzymes that can degrade peptides. As illustrated in Figure 4.10A, our hybrid coating remained visible on the PCL wound dressings even after 32 days of incubation in both PBS and LB+FBS. Remarkably, the hybrid coating could still be detected on the PCL dressings using XPS even after an extended 180 days of incubation. Figure 4.10B reveals that all characteristic signals of the coating are present in both the C1s and N1s spectra.

Another crucial factor to consider is the stability of the coating when exposed to sterilization methods. Gamma irradiation is a particularly attractive method for sterilizing medical devices and pharmaceuticals because it can operate at low temperatures and the sterilized materials can be used immediately, as no post-process quarantine period is required because the process leaves no toxic residues.[38] We sterilized PCL wound dressings coated with LCI-eGFP-pCBMAA$_{912}$ by gamma irradiation with a dose of 25 kGy, which is considered the gold standard for medical devices. Subsequent analysis using XPS confirmed the continued presence of the

coating on the sterilized wound dressings. These results underscore the remarkable stability of our coating technology, which is tied to the strong binding properties of the hybrids.

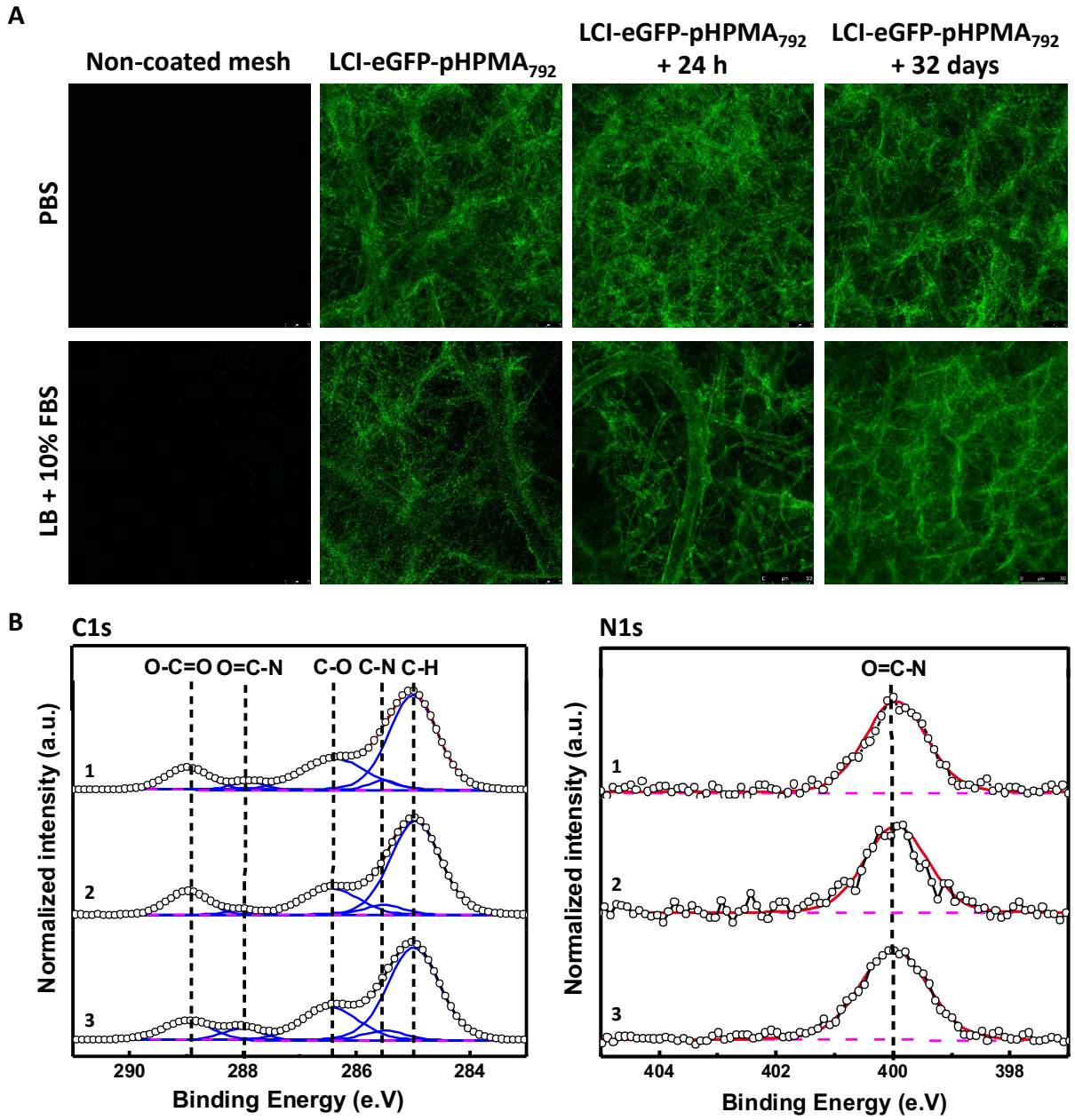

Figure 4.10. (A) CLSM images of PCL wound dressings coated with LCI-eGFP-HPMA$_{792}$ and stability studies in PBS and LB supplemented with 10% FB. (B) High resolution C1s and N1s XPS spectra of (1) freshly coated PCL wound dressings with LCI-eGFP-pHPMA$_{792}$ and after incubation for 180 days in (2) PBS and (3) LB supplemented with 10% FBS. All spectra were normalized to maximum intensity.

Collectively, these findings emphasize the potential and suitability of this coating for practical clinical applications.

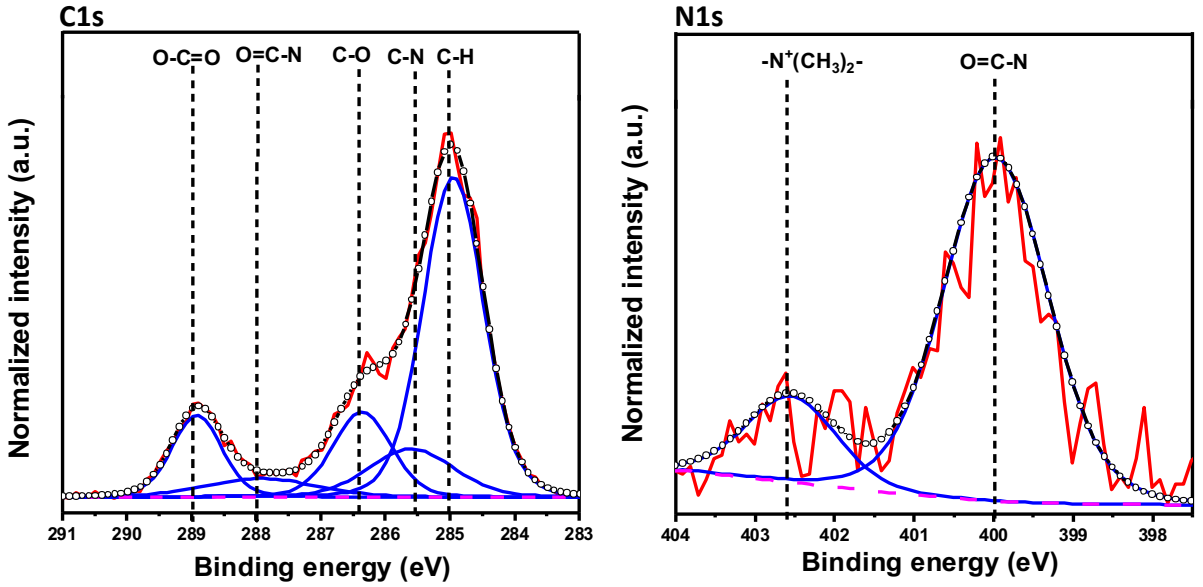

Figure 4.11. High resolution C1s and N1s XPS spectra of PCL-LCI-eGFP-pCBMAA$_{912}$ after sterilization by gamma irradiation (25 kGy).

4.2.5 Stealth Coating for PCL Wound Dressings

Having successfully confirmed that our hybrid coatings are readily applicable to a wide range of medical materials, we aimed to explore their suitability and effectiveness in a clinically relevant application, particularly in the context of wound care. Wound management is a major global challenge that imposes an enormous financial burden.[39] Hence, there is a pressing global demand for the development of advanced, cost-effective wound dressings that can mitigate and treat infections in an effective yet safe manner. In addition to providing a barrier of protection against infection, the ideal wound dressing should provide the most optimal conditions for healing and prevent further injury. That said, introducing antifouling properties on the surfaces of wound dressings can be advantageous. Certainly, it may be essential to prevent uncontrolled adhesion of skin cells, immune cells and pathogens to the dressing surface. This would otherwise lead to the release of excessive amounts of proinflammatory cytokines, which exacerbates inflammation impairing the healing process.[40-41] In addition, it would help prevent conglutination of the dressing to the wound and consequent tissue injury when the dressing is exchanged. But above all it would be advantageous to provide a strong barrier against bacterial infiltration.

Herein, we developed antifouling wound dressings based on PCL fiber meshes and our LCI-eGFP-Polymer hybrid coating technology. Electrospun PCL non-wovens were utilized because

of their large surface area, advantageous for functionalization purposes and their inherent porosity enabling high oxygen permeability necessary for wound healing. Moreover, PCL is highly biocompatible and non-toxic and is approved by both the US Food and Drug Administration and European Medicine Agency for healthcare applications.[42]

First, we performed quantitative evaluation of the hybrid coating formation on PCL surfaces via SPR spectroscopy analysis. This analysis was crucial for establishing the exact quantity of hybrids required to create a dense coating on these hydrophobic surfaces. Such an evaluation holds paramount significance for the practical implementation of this technology, as it is essential to determine whether the coating offers a cost-effective solution for real applications. For these studies a thin film of PCL was spin-coated onto gold-coated SPR sensor chips to mimic the surface of PCL nanofibers. The thickness of the PCL film was determined to be 17 nm by ellipsometry. The LCI-eGFP-Polymer coatings were formed inside the flow cell of the SPR by injecting the different hybrid solutions at a concentration of 1 $mg \cdot mL^{-1}$ in PBS and at a flow rate of 10 $\mu L \cdot min^{-1}$. The hybrid molecular densities of the coatings on PCL were approximately 0.50 and 0.77 $pmol \cdot cm^{-2}$ for LCI-eGFP-$pHPMA_{792}$ and LCI-eGFP-$pCBMAA_{912}$. This is equivalent to 76 and 199 $ng \cdot cm^{-2}$, respectively. Hence ,1 g of the hybrid coating solution would be sufficient to coat a PCL surface of 5000 m^2. The straightforward and cost-effective application process of the hybrid coating makes it even more advantageous for the clinical market.

To confirm the antifouling capabilities of the modified PCL dressings, we challenged them to a solution of bovine serum albumin (BSA). Albumin is a major protein component of BP and is found in wound exudate. Therefore, it is commonly used as a simulant for wound exudate in laboratory research and medical device testing. The BSA solution was spiked at 1 mol% with a fluorescently labeled BSA in order to visualize protein adsorption by CLSM (Figure 4.12A). Strong protein adsorption occurred on bare PCL dressings after an incubation time of 60 min. In contrast, no BSA fluorescence was observed on the coated dressings after the same incubation time, indicating minimal to no protein adsorption. Furthermore, protein fouling was also tested against a more complex wound exudate surrogate, namely BP (Figure 4.12B). The LCI-eGFP-$pHPMA_{792}$ and LCI-eGFP-$pCBMAA_{912}$ coatings were capable of significantly reducing fouling by as much as 96% (8 $ng \cdot cm^{-2}$) or even preventing it from occurring entirely.

In this case, we were also able to confirm that increasing the degree of polymerization, i.e., the steric repulsion, improves the antifouling performance (Figure 4.12C).

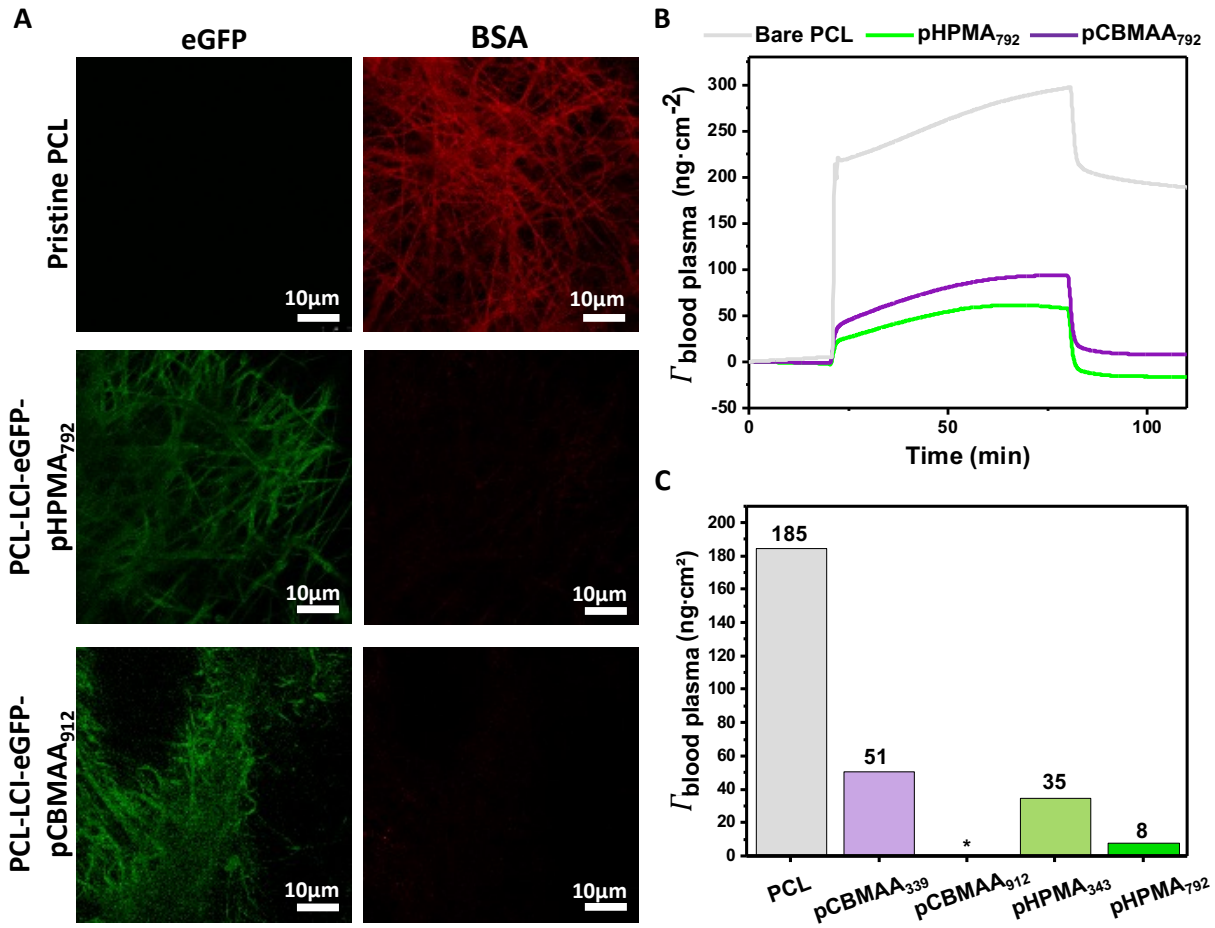

Figure 4.12. (A) BSA fouling visualized by CLSM. (B) Exemplary SPR sensograms of 10% BP fouling measured by SPR spectroscopy. (C) Comparison of BP protein fouling on the different hybrid coatings with varying DP.

4.2.5.1 Prevention of Fibroblast Adhesion

Adhesion of epithelial and endothelial cells to the dressing can lead to the dressing adhering to the wound bed, causing pain and tissue damage each time the dressing is exchanged. Moreover, the non-specific and uncontrolled adhesion of fibroblasts and immune cells to the dressing can trigger an inflammatory response that may ultimately impede wound healing. Consequently, we assessed the capacity of our hybrid coating to prevent the undesired adhesion of fibroblasts to the PCL wound dressings. To do this, we seeded 200,000 HDF onto both pristine and coated dressings. To create more challenging conditions, the cell culture medium was supplemented with 10% FBS, a protein cocktail that facilitates cell adhesion. The

samples were then incubated for 24 h at 37°C and 5% CO_2, providing the cells with sufficient time and optimal conditions for growth and adhesion. Following incubation, the samples were fixed and immunostaining of the cells proceeded to visualize the adhesion by CLSM (Figure 4.13B). The cell nuclei are depicted in blue (DAPI), f-actin as marker for the cytoskeleton in green and focal adhesion protein vinculin in red.

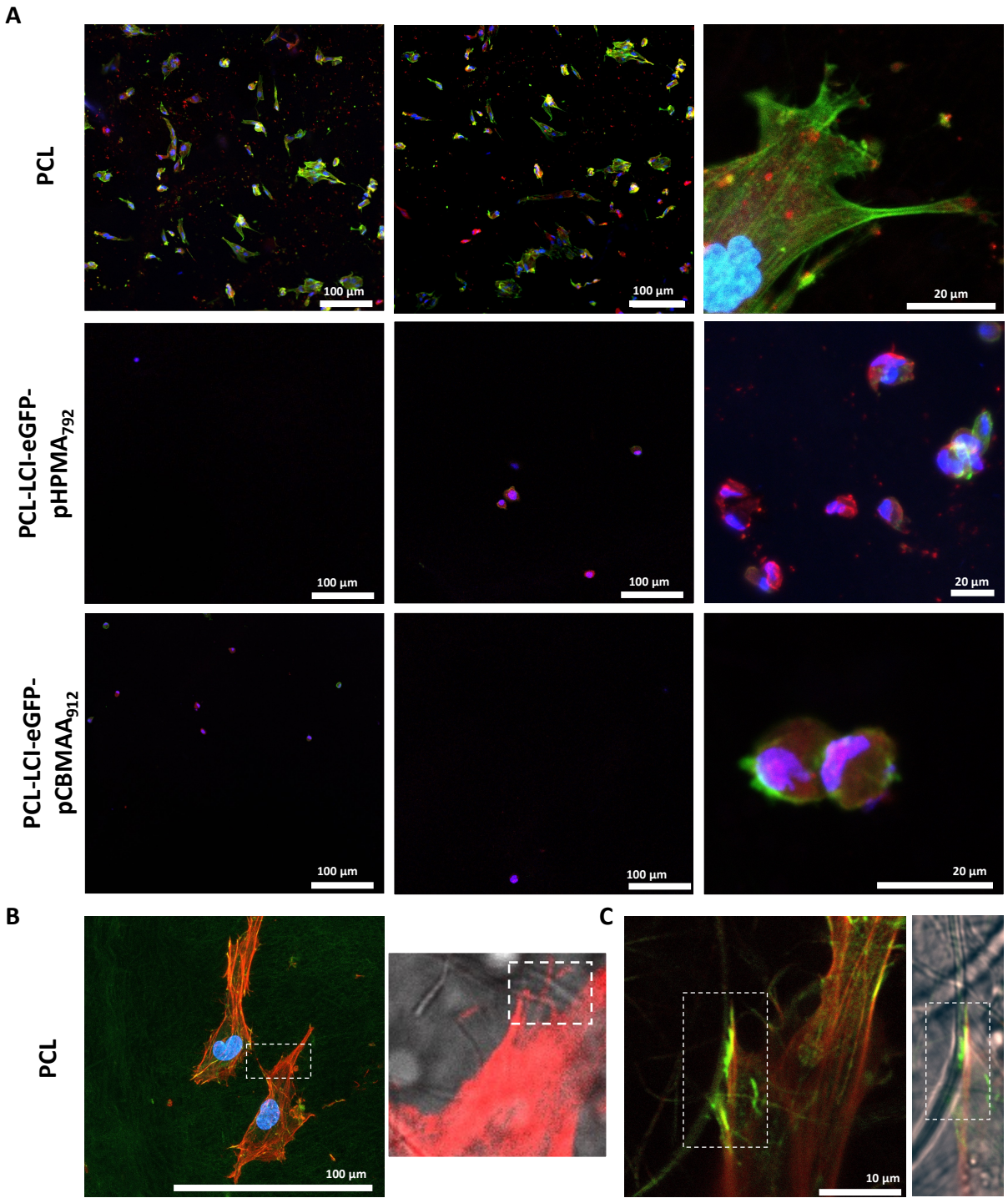

Figure 4.13. (A) Adhesion of HDF on bare and coated PCL wound dressings visualized via CLSM (nuclei: blue, actin filaments: green and vinculin: red). (B), (C) CLSM and STED microscopy

images depicting clear colocalization of the cells along the PCL fibers. Cell nuclei: blue, actin: red, vinculin: green and fibers: grayscale.

A large number of fibroblasts was able to adhere to the bare PCL dressings. CLSM images reveal spindle-shaped fibroblasts with cytoplasmic extensions aligned along the PCL fibers (actin staining). By employing stimulated emission depletion (STED) microscopy, we could clearly visualize focal adhesion points at the ends of actin fibers that were colocalized around and above the PCL fiber surface (vinculin staining). In fact, we occasionally observed that fibroblasts were able to wrap around the PCL fibers (Figure 4.13C). These results clearly demonstrate the promiscuity of fibroblasts for adhering onto surfaces previously fouled by proteins. In contrast, only very few cells were found in the fibers coated with LCI-eGFP-Polymers. These cells were round with no apparent cytoplasmic extensions or focal adhesion points along the PCL surface. It is likely that they are rather mechanically entrapped within the PCL mesh and not attached to the surface. These findings highlight that the antifouling properties of our hybrid coating extend into the mesoscopic range providing resistance to nonspecific fibroblast cell adhesion. This is an essential condition for the development of advanced non-adhesive wound dressings.

4.2.5.2 Prevention of Bacterial Adhesion and Colonization

Advanced wound dressings must act as effective barriers against pathogens and infection development. Bacterial adhesion to the dressing's surface can lead to the formation of biofilms, which are complex communities of microorganisms embedded in a protective extracellular matrix. Biofilms shield bacteria from the immune system and antibiotics, making these infections challenging to treat. We assessed the potential of our hybrid coating to deter bacterial infiltration and adhesion to the surface, thereby reducing the risk of material-related infections. For these studies, we exposed our coated PCL wound dressings to a clinical isolate strain of *E. coli* capable of forming biofilm. *E.coli* is known to be one of the most common pathogens for later stages of chronic wounds capable of substantial tissue damage.[43] The *E.coli* was suspended in LB medium at a concentration of 10^7 CFU. LB was enriched with 10 vol% FBS to simulate the wound exudate and provide proteins necessary for cell attachment. Following 24 h of incubation at 37 °C, the samples were fixed and prepared for SEM imaging.

Remarkably, hardly any bacteria were able to adhere to the coated PCL wound dressings. Occasionally, only single bacteria cells were observed, as shown in Figure 4.14 (PCL-LCI-eGFP-pHPMA$_{792}$). In stark contrast, control experiments with non-coated (bare) PCL dressings revealed a large number of bacteria adhering to the surface of the dressings. Bacterial colonization was extensive enough to cover nearly the entire PCL dressing surface, including the interstitial spaces between the fibers (bare PCL). Additionally, the presence of extracellular polymers was evident, signifying the formation of a biofilm.

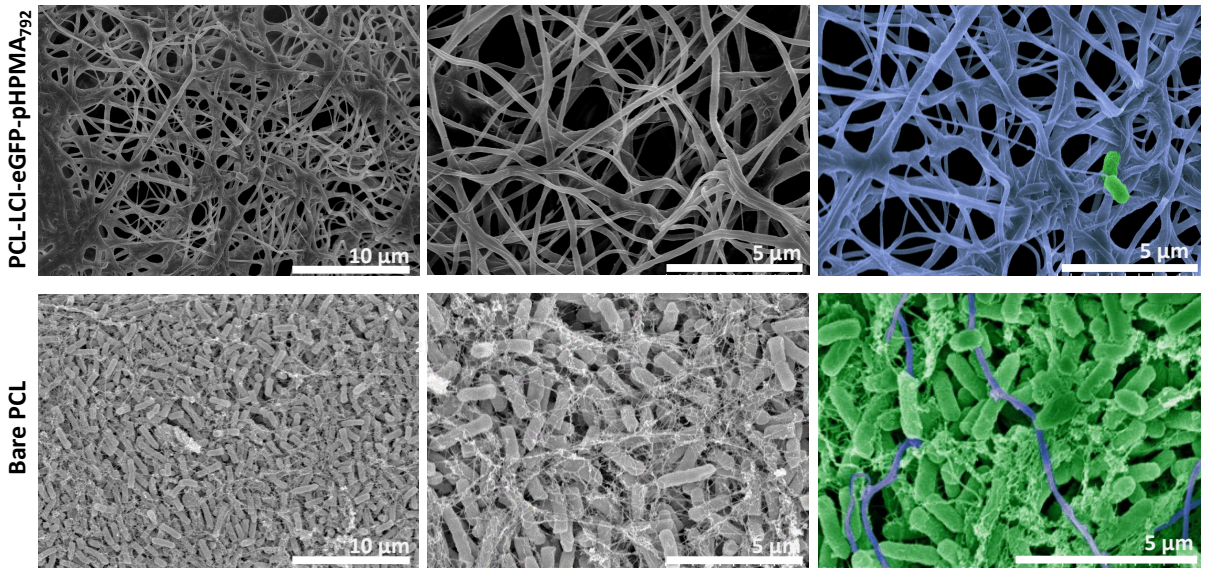

Figure 4.14. SEM micrographs of bare and coated PCL wound dressings (LCI-eGFP-HPMA$_{792}$) after incubation with *E. coli* (DSM-1103, 10^7 CFU) for 24h. Images are false-colored to enhance visualization of *E. coli* (green) and PCL fibers (blue). Adapted and modified from Ref. [35].

Furthermore, when our hybrid coating was applied to PU foam dressings via the spraying method, bacterial colonization could even be prevented in the intricate porous structure of the foam (Figure 4.15). Additionally, we successfully transferred this coating to the surfaces of both PU and silicone venous catheters, and these surfaces remained free from bacterial contamination (Figure 4.16).

In Summary, these findings underscore the potential of our hybrid coating for application in health care management. The coating not only effectively prevents undesired fibroblast adhesion but also demonstrates the ability to mitigate the infiltration of pathogenic bacteria. Surprisingly, all uncoated substrates allow the infiltration of bacteria on their surface, acting as bacterial reservoirs from where infections with biofilm formation can develop. Given this

scenario, it is not surprising to observe the frequent occurrence of implant-associated infections. Therefore, it is imperative to modify implant surfaces with effective bacterial-repellent coatings. This is a *sine qua non* to ensure appropriate healthcare management and improve patient outcomes.

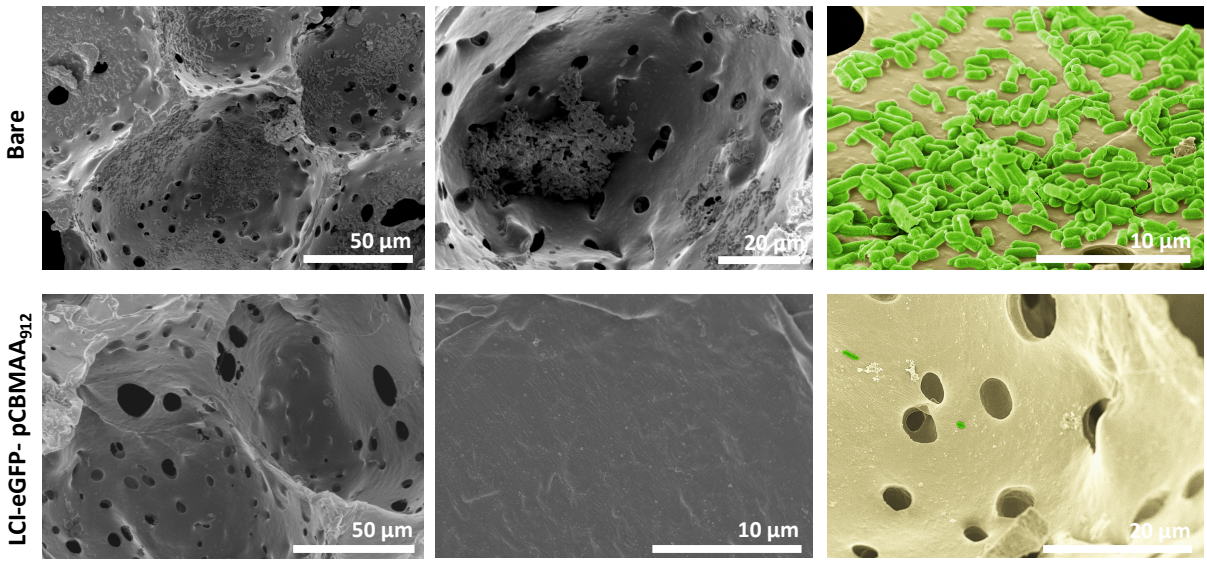

Figure 4.15. SEM micrographs of bare and coated PCL wound dressings (LCI-eGFP-HPMA$_{792}$) after incubation with *E. coli* bacteria for 24 h. Images are false-colored to enhance visualization of *E. coli* (green).

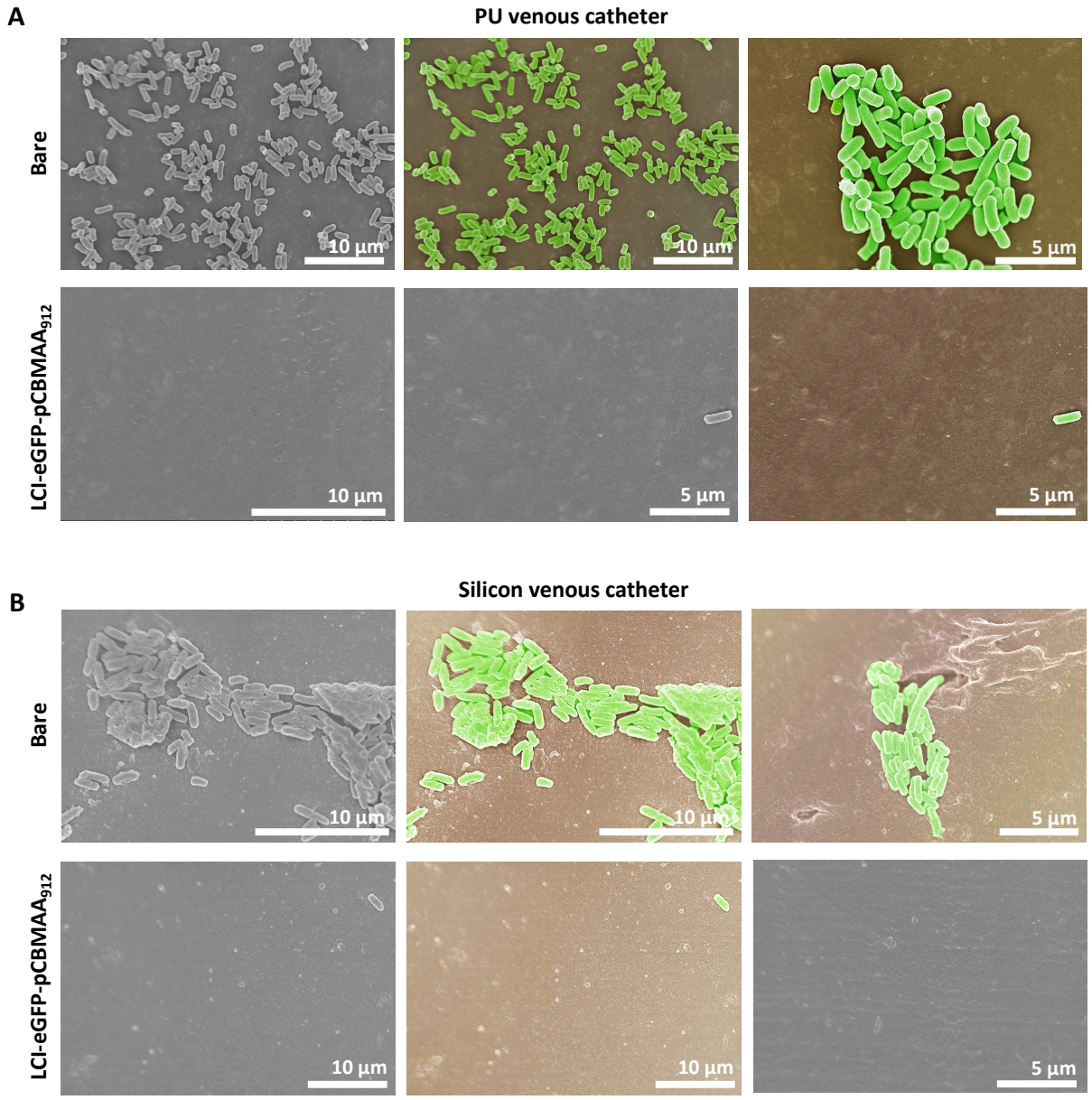

Figure 4.16. SEM micrographs of *E. coli* bacteria adhesion on bare and coated PU as well as silicone venous catheters after incubation for 24 h. Images are false-colored to enhance visualization of *E. coli* (green).

4.2.6 Stealth Coating for Orthopedic and Orthodontic Titanium Implants

Titanium and its alloys are the go-to material for orthopedic and orthodontic implants because of their excellent mechanical properties, exceptional biocompatibility, and ability to promote osseointegration.[44] However, Titanium has a high surface energy[45-46], which makes it highly susceptible to protein adsorption and bacterial adhesion. Not surprisingly, material-associated infections and biofilm formation are the leading causes of orthopedic and orthodontic implant failure.[47-48]

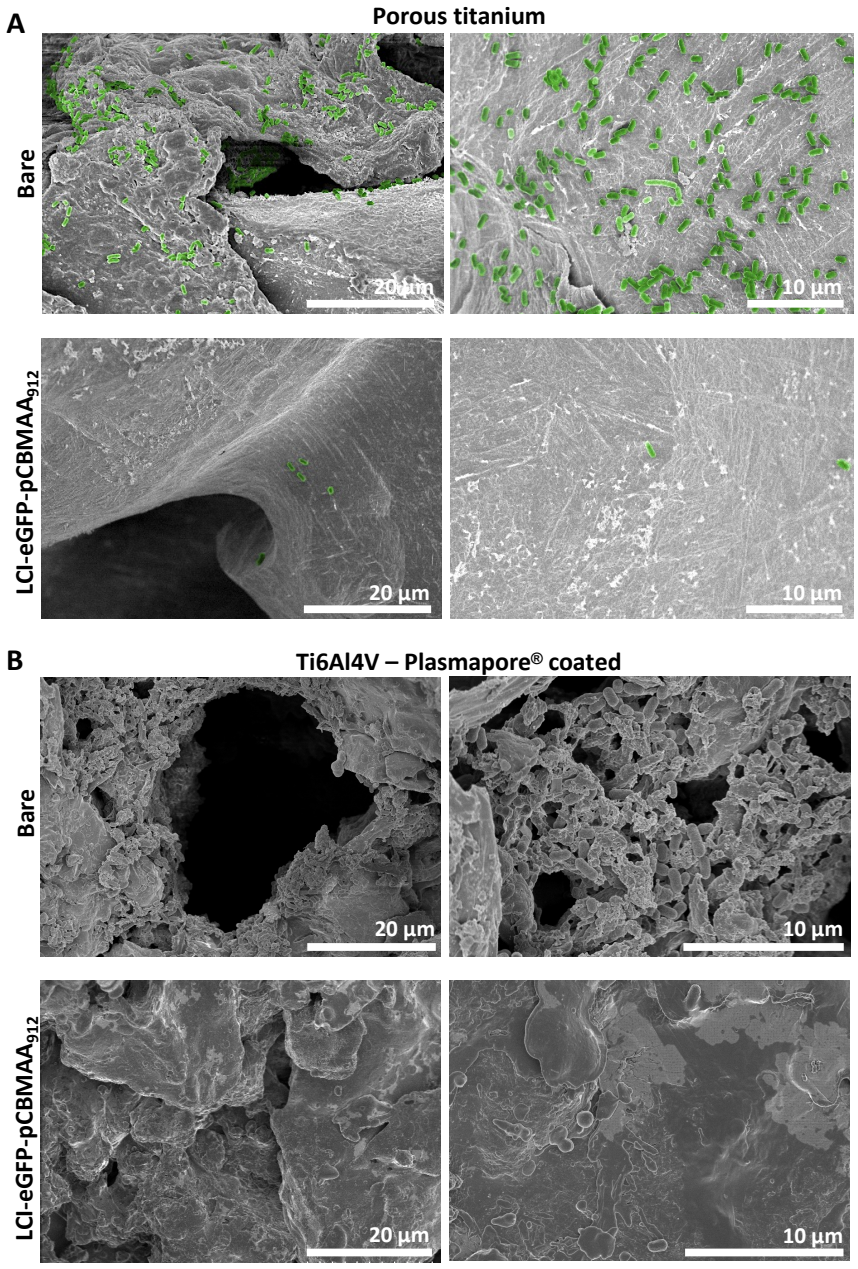

Figure 4.17. SEM micrographs of bare and LCI-eGFP-pCBMAA$_{912}$ coated (A) porous titanium and (B) Ti6Al4V-Plasmapore coated substrates after exposure to *E. coli* bacteria (MG1655) for 24 h. Images are false-colored to enhance the visualization of E. coli bacteria (green).

While I have previously demonstrated qualitatively (Figure 4.8) that our hybrid coating can be applied to titanium, the critical question is whether it can effectively deter bacterial colonization on these substrates. To address this question, we exposed both coated and non-coated titanium and titanium alloy materials to a concentrated solution of *E. coli* bacteria (MG1655). As it was expected, after 24 h of contact, we observed a significant number of *E. coli* adhered on the uncoated substrates. Notably, the coated substrates remained free of

bacterial contamination. Therefore, despite its nanometer-thin thickness, our coating provides a sufficiently robust barrier to inhibit bacterial colonization, even on complex surfaces such as titanium.

4.2.6.1 Stability to Mechanical Abrasion

Orthopedic and orthodontic implants endure continuous mechanical stresses. Hip implants, for instance, face friction and wear when subjected to joint movement during activities like walking. Furthermore, dental implants are subjected to abrasion forces resulting from chewing and cleaning processes. Therefore, for the successful application of our coating onto orthopedic and orthodontic materials, it must be able to endure abrasion forces to ensure the effectiveness of the implant.

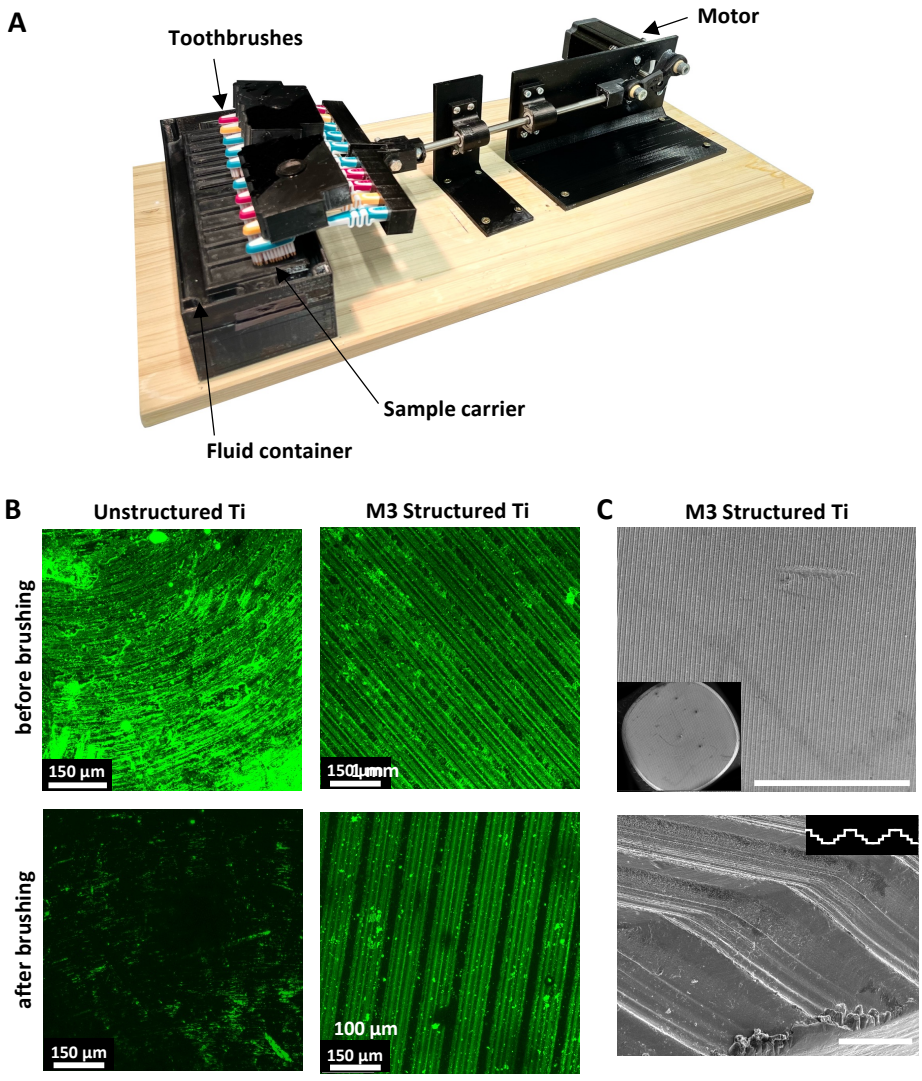

Figure 4.18. (A) Brushing test stand. (B) CLSM images of hybrid coated titanium coins with and without structure after the brushing test. (C) SEM images of the selected M3 structure.

To meet this challenge, we worked with the Laboratory for Machine Tools and Production Engineering (WZL) at RWTH Aachen University to investigate the incorporation of different surface micro- and nanostructures onto titanium substrates that can help to strategically protect the coating from abrasive forces. The effectiveness of these structures in protecting the hybrid coating was assessed by a standard brushing test method, which is commonly used to assess the abrasion resistance of coatings, paints, and surfaces. (Figure 4.18). It involves using a motorized brushing mechanism, that moves toothbrush bristles back and forth over the substrate's surface. This setup subjects the coating to controlled mechanical abrasion forces similar to conditions such as during oral hygiene practices. Following the brushing test, we examined whether the coating was still present on the surface of the substrates by CLSM using the green fluorescence of eGFP as a reporter. It should be noted that these studies were performed utilizing hybrid macromolecules, where the surface affine peptide LCI was replaced by LCI-Y29R/G35R (LCI-KR2). LCI-KR2 is a recombinant variant of LCI, which was tailored via Knowledge-gained directed evolution approach to achieve increased binding strength (Figure S4.4).[49]

As shown in Figure 4.18B, the hybrid coating on the unstructured titanium surfaces was removed during the abrasion test. As we will see later, this can lead to rapid bacterial invasion of the unprotected implant surface. However, in the titanium sample that was previously structured with microgrooves (M3), the coating remained almost intact, indicating that the structure was able to shield the coating from abrasion.

4.2.6.2 Prevention of Bacterial Adhesion and Colonization

We investigated whether the synergistic combination of the structure and our hybrid coating could withstand both mechanical abrasion and subsequent bacterial colonization. For this purpose, we coated unstructured and microgroove-structured (M3) titanium coins with LCI-KR2-eGFP-pCBMAA$_{702}$ hybrids and subjected them to the brushing test for 40 min. Subsequently, the samples were immersed in a concentrated solution of *Streptococcus gordonii* and incubation proceeded for 24 h. *S. gordonii* is a commensal bacterium found in the oral cavity and is known to be an early colonizer that initiates biofilm formation by adhering to tooth and implant surfaces. Additionally, if it is able to enter the circulatory system, it has the potential to cause bacterial endocarditis.[50] We also included pristine

unstructured and structured coins as control samples. Following incubation, the samples were fixed with 3% glutaraldehyde and bacterial adhesion was imaged by SEM (Figure 4.19). As anticipated, the uncoated substrates exhibited a substantial number of *S. gordonii* adhered to their surface. Notably, the structured titanium displayed a higher susceptibility to bacterial adhesion, attributed probably to the increased surface area created by the structure. Moreover, the application of our hybrid coating effectively prevented the adhesion of *S. gordonii* to the surface. However, it is evident that after brushing the coating is removed from the surface of the unstructured coins, allowing bacteria to adhere in substantial numbers. In stark contrast, when the titanium surface was structured with the microgrooves structure (M3), the hybrid coatings remained of the surface after the brushing test and prevented bacterial adhesion. This is evidenced by the low number of bacteria found throughout this samples compared to the uncoated structured surfaces (Figure 4.19).

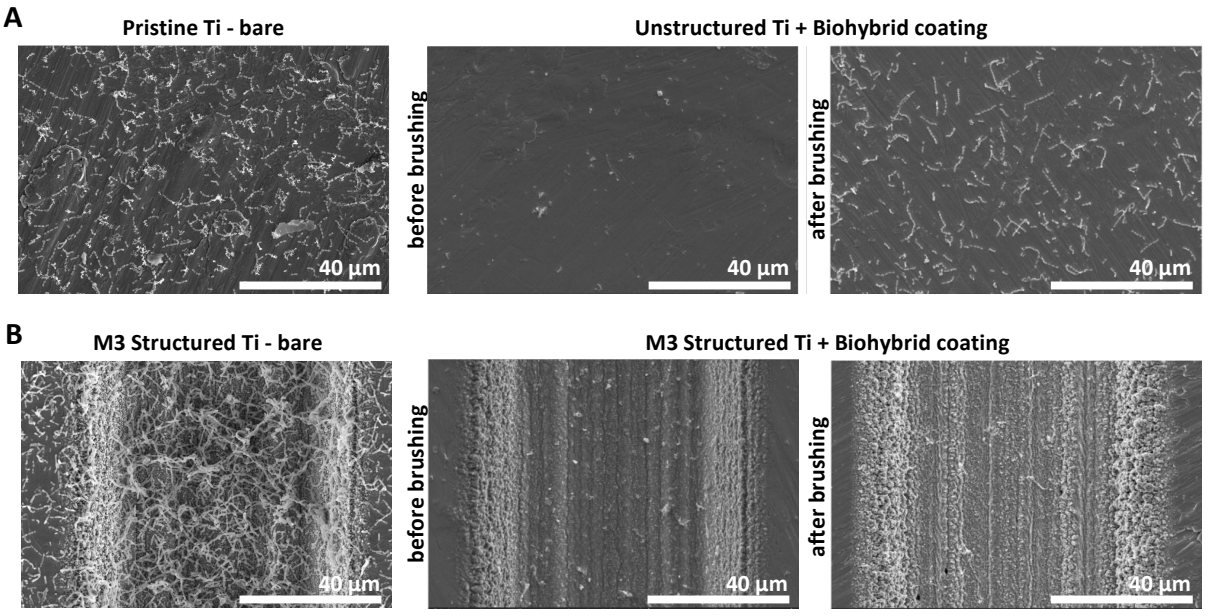

Figure 4.19. SEM images of bacterial adhesion experiments on (A) unstructured and (B) microgroove-structured (M3) titanium coins. Coins were coated with the LCI-KR2-eGFP-pCBMAA$_{702}$ hybrids and subjected to the brushing test. Pristine coins were used as control.

4.2.6.3 Proof of Concept on Dental Screws

Our aim was to validate the potential of our combined coating on actual dental screws. For this purpose, the flat surface of the screw was structured with the selected microgroove structuring and subsequently coated with the LCI-KR2-eGFP-pCBMAA$_{702}$ hybrids. Mechanical

abrasion test using our brushing test stand was performed for 40 min. During the brushing studies the screws were completely immersed in an aqueous solution of artificial saliva to make the conditions more similar to that in practice. The implants were then inoculated with *S. gordonii* bacteria and incubated for 24 h under optimal conditions for bacterial growth. The surface of the screws was then inspected by SEM (Figure 4.20. Notably, the modified implants remained clean from bacteria, highlighting that the combined effect of substrate structure and our hybrid coating rendered the surface of screw implants resistant to both mechanical abrasion and bacterial colonization.

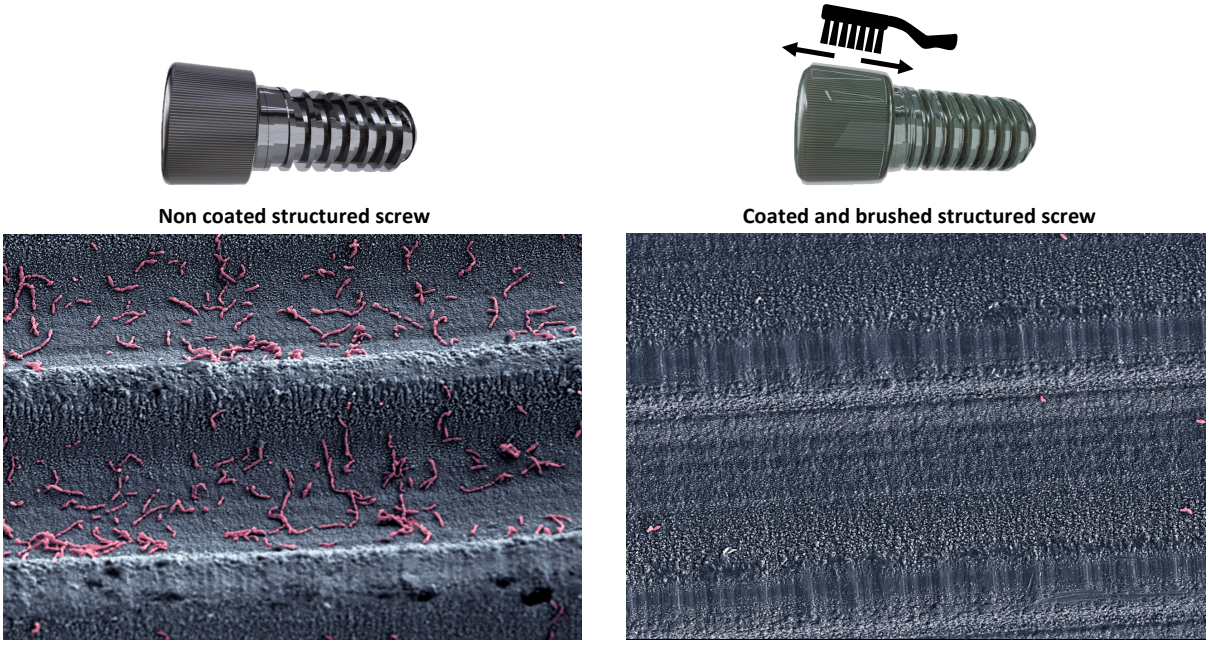

Figure 4.20. SEM images of bacterial adhesion test on dental screw demonstrator. Images are false-colored to enhance the visualization of *S. gordonii* bacteria (pink).

4.2.7 Safety of LCI-eGFP-Polymer Hybrid Coating

The application and translation of the hybrid coating technology demands inertness and outstanding biocompatibility of the coating. Therefore, we thoroughly evaluated the safety of this coating through both direct contact and extraction tests in accordance with ISO-10993. The direct contact assays were performed with HDF. PCL wound dressings were coated with the LCI-eGFP-pHPMA$_{792}$ and LCI-eGFP-pCBMAA$_{912}$ hybrids and then placed on top of a 70% confluent layer of fibroblast cells. After 24 h of contact, the dressings were carefully removed and live/dead (calcein/ EthD) staining was carried out (Figure 4.21A). Ethidium homodimer (EthD, red) is a membrane impermeable dye that stains DNA. Hence it stains only dead cells

with damaged membranes. On the other hand, calcein acetoxymethyl (green) passively crosses the cell membrane and is hydrolyzed by living cells to green-fluorescent calcein. Hence it only stains living cells with intact membrane.

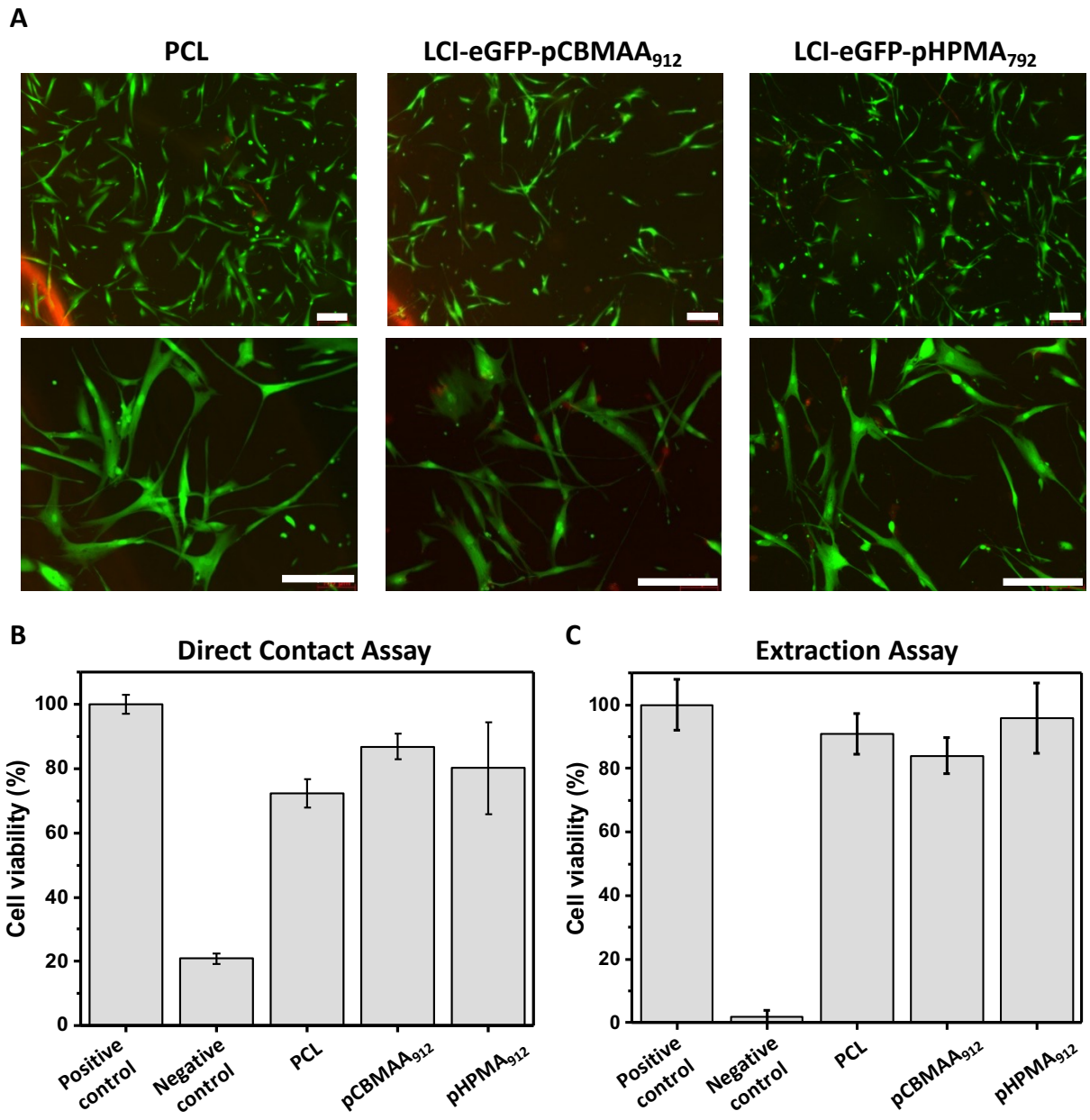

Figure 4.21 (A) Live/dead staining of cells after direct contact to coated PCL dressings for 24 h. Scale bars represent 200 µm. (B) Viability of dermal fibroblasts after direct contact to coated PCL dressings for 48 h. No significant statistical difference ($p < 0.05$) between the bare PCL fibers and the coated ones. (C) Viability of HDF after extraction assay according to ISO-10993. Untreated cells were set as negative control, while latex gloves serve as positive control.

As expected, the PCL dressings alone were not toxic to the cells. Notably, the coated PCL dressings also did not affect cell viability, as hardly any red fluorescence was visible similar to the result from PCL dressings alone. Furthermore, the fibroblast cells maintained their characteristic spindle-like shape and show no changes in morphology. Cell viability was further assessed after 48 h of direct contact time using the MTS assay (Figure 4.21B). This assay is based on the reduction of a tetrazolium salt ((5-(3-carboxymethoxyphenyl)-2-(4,5-dimethyl-thiazoly)-3-(4-sulfophenyl)) into a colored formazan. Only metabolically active (living) cells are capable of this conversion, and the amount of formazan produced is proportional to the number of viable cells in culture. For these studies, untreated cells cultured for the same duration were used as a negative control. As a positive control, cells were exposed to latex, as latex reliably induces a cytotoxic response. A reduction in cell viability was observed after treatment with bare PCL dressings. However, this may be due to cell damage during dressing removal rather than a toxic effect of PCL. As readily visible, the application of the hybrid coating did not induce changes in the metabolic activity of the cells. Viability remained above 80%, concluding that the coating remained non-toxic and safe to human fibroblasts.

Additionally, we conducted an extraction assay in accordance with ISO 10993 to evaluate the biological safety of our hybrid coating. This testing method is widely recognized as the gold standard for assessing the toxicity and biocompatibility of medical devices. The extraction procedure involved incubating the substrates in DMEM for 72 h. Following this incubation period, the samples were removed, and the conditioned extraction medium was collected for subsequent cell culture experiments. Once more, there was no evidence of any toxic effects caused by the coating. This is in agreement with direct contact studies and further confirms the excellent cytocompatibility of the LCI-eGFP-Polymer coating towards human fibroblast.

In collaboration with the University of Maastricht, we conducted further in-depth biocompatibility studies of our hybrid coating when applied to titanium substrates. Following the previously described extraction method according to ISO 10993, we analyzed the response of HUVECs, monocytes, M1 macrophages, M2 macrophages, UMR-106 cells, osteoblasts, osteoclasts and RAW264.7 cells when exposed to different dilutions of the conditioned extracted media (Figure 4.22). As a negative control we used untreated cell culture medium. All cells exhibited viability above 80% when compared to the negative control. Notably, no significant changes in viability were observed between the bare titanium and coated samples

proving once again the non-toxic nature of our coating. In a next step, we performed a series of cell activity tests, to verify that not only was cell viability unaffected but also that cell functionality remained uncompromised.

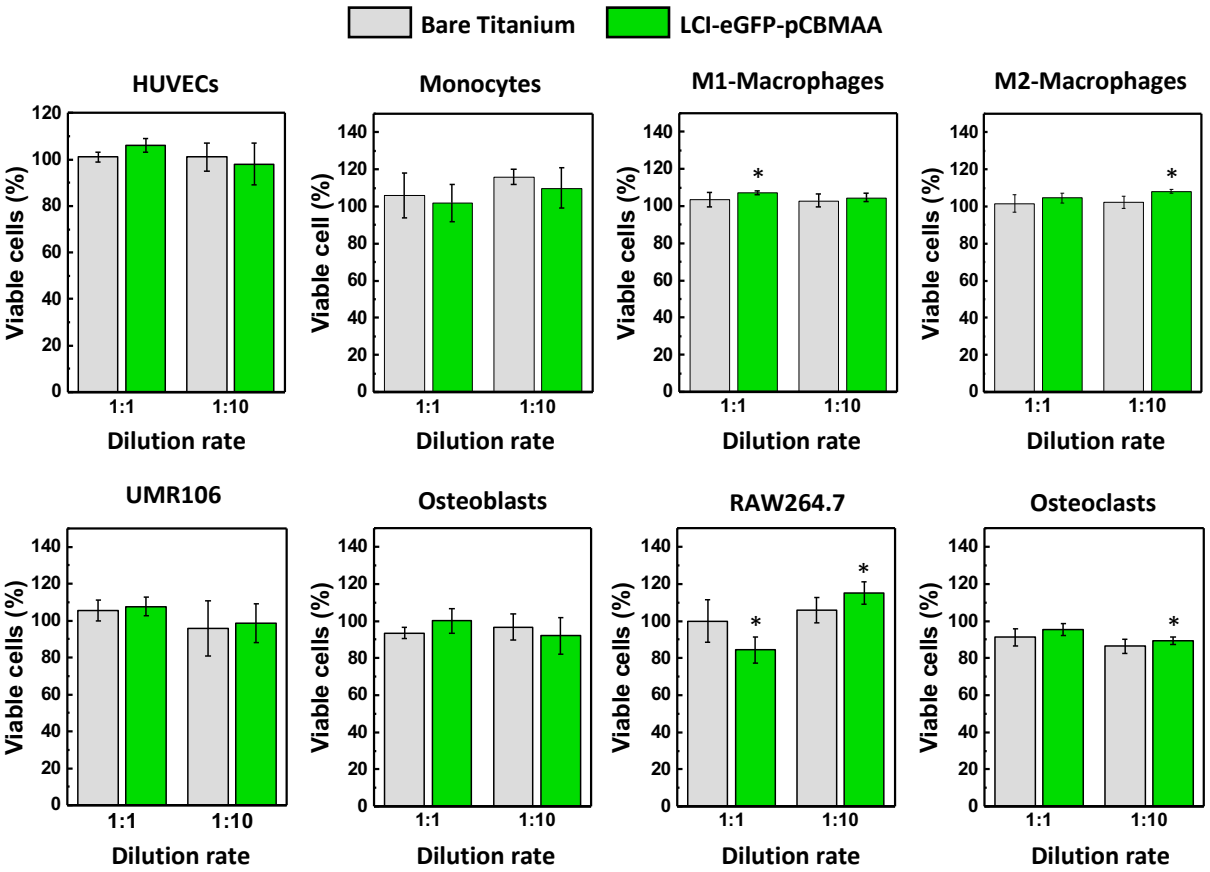

Figure 4.22. Cytotoxicity determined according to ISO 10993 and the extraction method. Cells were incubated with different dilutions of untreated cell culture medium (negative control) and extract medium for 24 h. Results were tested for significance vs. untreated culture control (100%). *p-value < 0.05 is considered significant.

The production of collagen fibers by fibroblasts is a fundamental step of the wound healing process. It is a major component of the extracellular matrix providing a scaffold that facilitates the recruitment of cells necessary for tissue repair. Moreover, collagen plays a pivotal role in wound contraction promoting wound closure.[51-52] Therefore, proper collagen production and organization are crucial for tissue integration. We analyzed the ability of fibroblasts to produce collagen (with and without the addition of ascorbic acid) after exposure to the conditioned extracted media for 24 h (Figure 4.23A). Fluorescent images readily demonstrated that collagen fiber formation was not impaired by both bare titanium or hybrid coated titanium

substrates. Moreover, the quantification of the mean collagen fiber length revealed no changes produced by our coating (Figure 4.23C).

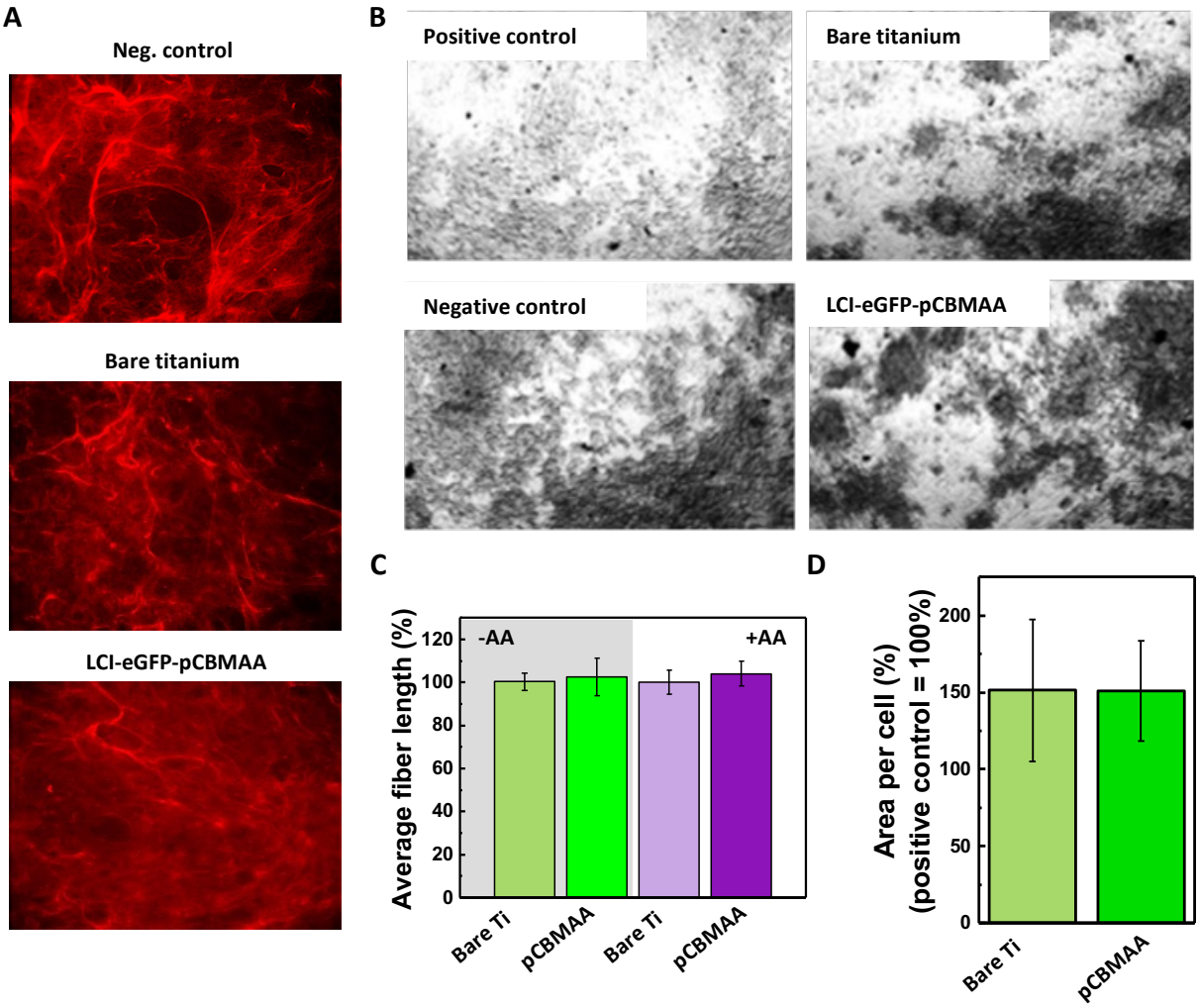

Figure 4.23. (A) Collagen production by fibroblasts visualized by staining with CBA-35-AF567 after incubation with ascorbic acid supplemented (+AA) extract media for 24 h. (B) Von Kossa staining for calcium phosphate deposition by osteoblasts. (C) Mean collagen fiber length calculated from microscopy images. (D) Quantification of hydroxyapatite deposition by osteoblasts using the OsteoImage ™ assay.

Apart from collagen formation in the fields of orthopedics and orthodontics, osseointegration (bone adherence) is crucial to maintain implant functionality and long-term clinical success. Osteoblasts are specialized bone-forming cells and they play a key role in the production and mineralization of the bone matrix, which includes hydroxyapatite, a naturally occurring calcium phosphate mineral.[53] After treatment of UMR-106 cells with the conditioned extracted media during their differentiation into osteoblast, we investigated their ability in

calcium phosphate deposition and hydroxyapatite production. Von Kossa staining revealed unaltered calcium phosphate deposition after treatment with the conditioned media, indicating that osteoblast functionality was maintained (Figure 4.23B). The extent of mineralization was quantified using the OsteoImage™ fluorescent assay (Figure 4.23D). Briefly, the fluorescent OsteoImage™ reagent specifically stains the hydroxyapatite portion of mineralized bone nodules deposited by the cells. Notably, hydroxyapatite deposition remained unaltered after treatment with hybrid coating extraction.

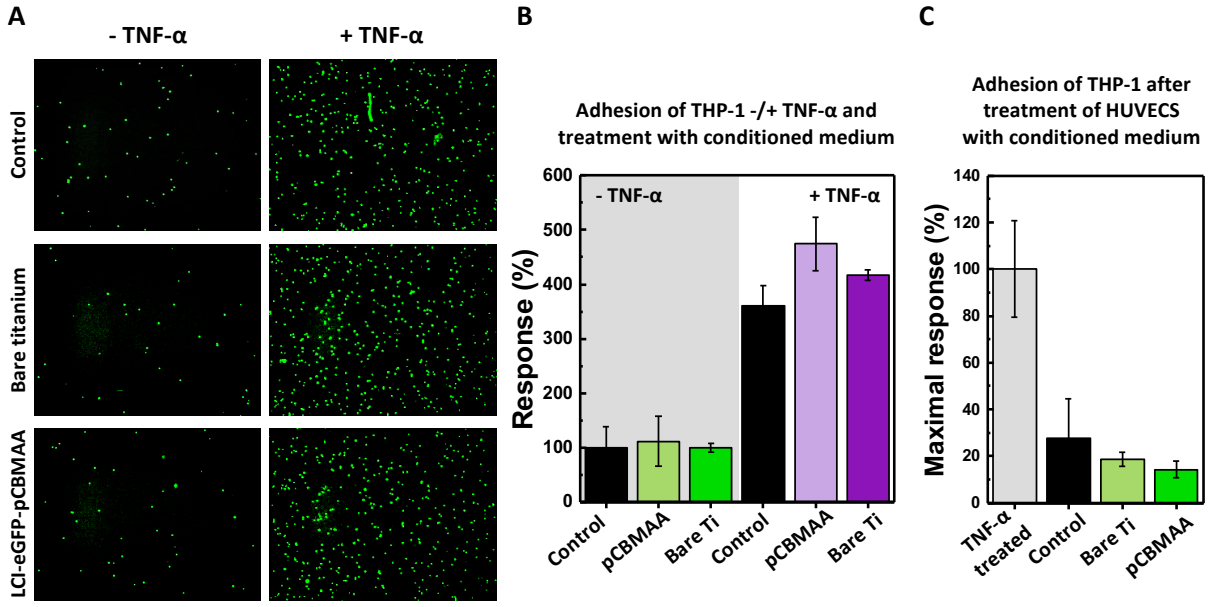

Figure 4.24. (A) Visualization of the adhesion of THP-1 cells (calcein staining, green) to inflamed and non-inflamed HUVECS. (B) Quantification of adhered THP-1 cells to non-inflamed and inflamed HUVECs (n=3). Adhesion of THP-1 cells treated with unconditioned cell culture medium to non-inflamed HUVECs is set as reference (100%). (C) Adhesion of HUVECs treated with cell culture extract to THP-1 cells (n=3). HUVECs treated with unconditioned cell culture medium served as negative control. THP-1 adhesion to inflamed HUVECs was set as reference (100%).

Lastly, ensuring that the presence of the coating does not trigger an excessive or harmful inflammatory response is essential for the biocompatibility of the final modified implant. Inflammatory reactions can lead to rejection of implants or the formation of fibrous capsules around the implant. We investigated the adhesion of THP-1 monocytes to HUVECs as a measure of the inflammatory capacity that our coating may induce. For this purpose, the THP-1 cells were treated with the conditioned extracted media under absence or supplementation

of TNF-α. The latter was done to mimic the inflammatory signals and activate THP-1 cell adhesion to endothelial cells. Unconditioned medium was taken as negative control. The THP-1 cells were stained with calcein to monitor their adhesion. As evidenced in Figure 4.24A the treatment with TNF-α induced their activation and adhesion to HUVECs. Treatment with our coating did not induce further activation nor alleviation of the inflammatory response. In the absence of TNF-α only minimal inflammatory response was observed even after treatment with the coating extract. In a subsequent experiment, HUVECs were treated with extraction medium or TNF-α to investigate the release of inflammatory cytokines that would induce THP-1 cell adhesion. Similarly, only a minimal inflammatory response was observed in comparison to TNF-α treated cells.

In summary, these findings demonstrates that the presence of our coating does not cause activation of the inflammatory response, underscoring the immuno-stealth and superior biocompatibility of our hybrid coating technology.

4.3 Conclusion

In this chapter, I introduced a coating strategy that leverages the inherent promiscuity of protein absorption to create a highly effective antifouling coating onto a wide array of medical devices. This coating is formed by the molecular adsorption of LC-eGFP-pCBMAA and LCI-eGFP-pHPMA hybrids to the surface of the substrates, eliminating the need for surface activation steps or additional energy input. This oriented type of adsorption driven by the LCI peptide, results in a brush-like coating at the outer part of the surface that exhibits antifouling properties comparable to the best grafting-from polymer brushes in spite of being only few nanometers thick. Notably, the antifouling properties of this coating extent to the mesoscopic scale being able to successfully mitigate the attachment of fibroblast cells and the adhesion of pathogenic biofilm-forming bacteria. The latter is particularly important to avoid bacterial colonization with concomitant infection development at the wound site. Moreover, our hybrid coating was shown to be completely immuno-stealth and innocuous to endothelial, connective tissue and osteoprogenitor cells.

Importantly, this hybrid coating technology may be extended beyond the scope of pure antifouling functionalization. For instance, LCI-eGFP can be fused with antimicrobial enzymes or peptides, making it a promising universal platform for generating multifunctional coatings.

Lastly, we believe that this coating technology represents a safe, cost-effective and readily applicable strategy with significant potential for clinical application.

4.4 Materials and Methods

4.4.1 Materials

All reagents were of analytical grade and used as received unless otherwise stated. Copper (II) bromide (CuBr2, 99%), ethanol (EtOH, >99.8%), acetone (>99.5%), PBS tablets, artificial saliva, bovine serum albumin, citrated blood plasma, and PCL (M_n 45,000 g·mol^{-1}) were purchased from Sigma Aldrich Chemie GmbH. Deuterated solvents (99.9%) were purchased from Deuterio GmbH. Dimethyl sulfoxide (DMSO, >99.9%) was obtained from VWR International GmbH. Tris(2-dimethylaminoethyl)amine (Me_6TREN, 99$^+$%) was obtained from ThermoFisher GmbH. CBMAA, HPMA, SBMA and PCMA were synthesized according to literature procedures. The maleimide initiator, 2-(2,5-dioxo-2,5-dihydro-1H-pyrrol-1-yl) ethyl 2-bromo-2-methylpropanoate, was synthesized according to literature.[54] MTT assay was purchased from Promega GmbH. Water used in the experiments was provided by a Millipore Milli-Q system. Silicon wafers were purchased from SIEGERT WAFER GmbH. Gold-coated SPR sensor chips were purchased from Cenibra GmbH. Cotton (Noba Gauze, NOBAMED Paul Danz AG) and viscose/polyester gauzes (Vliwasoft®, Lohmann & Rauscher GmbH & CoKG) as well as PU-foam dressings (Allevyn® Polyurethane Foam Dressing, Smith and Nephew GmbH) were acquired over the counter at the drug store. Porous titanium substrates were kindly provided by Stryker European Operations BV, Amsterdam, The Netherlands. Flat and structured titanium coins were provided by the Laboratory for Machine Tools and Production Engineering (WZL) at RWTH Aachen University. PCL Wound Dressings were prepared as previously described in Chapter 3.

Cells and Biochemicals. E. coli (MG1655), *E. coli* (DSM-1103) and *S. gordonii* (DSM 6777) were obtained from the Leibniz Institute DSMZ-German Collection of Microorganisms and Cell Cultures GmbH, Braunschweig, Germany.

E. coli BL21-Gold (DE3) was used as protein expression system and purchased from Agilent Technologies Inc., Santa Clara, United States. *E. coli* (MG1655) was grown in lysogeny broth (LB) containing 10 g·L^{-1} tryptone, 5 g·L^{-1} yeast extract and 10 g·L^{-1} NaCl, purchased from AppliChem GmbH. *E. coli* (DSM-1103) and *S. gordonii* were grown in Mueller Hinton Broth (MHB) and Trypticase Soy Yeast (TSY) medium, respectively. Hoechst 33342 and calcein AM and LIVE/DEAD staining kit were purchased from ThermoFisher Scientific, Waltham, United

States. Ethidium Homodimer-1 (EtHD-1), Phorbol-12-myristate-13-acetate (PMA) and 2-Phospho-L-ascorbic acid trisodium salt, L-Ascorbic (99%) acid, β-Glycerophosphate (≥99%), sodium thiosulfate (≥98.0%) and calcein were received from Sigma Aldrich Chemie GmbH, Steinheim, Germany. Silver nitrate (10% aqueous solution) was received from Klinipath, Duiven, The Netherlands. HUVEC cells were purchased from BD Bioscience Europe, Erembodegem, Belgium. THP-1 cells, UMR-106 cells as well as RAW 264.7 cells were received from ATCC, Manassas, United States. *PSA as well as* OsteoImage™ Mineralization assay *was purchased from Lonza AG, Basel, Switzerland, t*umor necrosis factor alpha *(TNF-α) was received from ReliaTech GmbH, Wolfenbüttel, Germany.* Collagen-binding adhesion protein 35-AF567 (CNA35-AF567) were synthesized by the group of Prof. Molin from Maastricht university according to literature.[55] HDF were purchased from PromoCell GmbH. HDF were cultured in Dulbecco's Modified Eagle Medium (DMEM, Gibco®) supplemented with 10% fetal bovine serum (FBS, Gibco®) and 1% Penicillin-Streptomycin (Pen Strep, Gibco®), purchased from ThermoFisher GmbH. Roswell Park Memorial Institute (RPMI) 1640 medium was purchased from ThermoFisher Scientific, Waltham, United States and supplemented with 10% FBS and 1% PSA. HUVEC medium (EBM™-2 Basal Medium with addition of EGM™-2 MV SingleQuots™ kit) was received from Lonza AG, Basel, Switzerland. DMEM supplemented with glucose (4.5 $g \cdot L^{-1}$), L-glutamine, sodium pyruvate and $NaHCO_3$ (1.5 $g \cdot L^{-1}$) was purchased from Pan-Biotech GmbH, Aidenbach, Germany.

4.4.2 Synthetic and Fabrication Methods

Production and purification of LCI-eGFP. The LCI-eGFP fusion protein was produced in *E. coli* BL21-Gold (DE3) cells as previously described.[27] After expression, the cell culture was centrifuged at 3200 g for 20 min at 4 °C and the remaining cell pellet was resuspended in PBS buffer at 0.17 $g \cdot mL^{-1}$ and lysed by ultrasonication (20 x 15 s intervals, amplitude 60%, Vibra-Cell™ VCX 130, Sonics). The cell lysate was then centrifuged at 3200 g for 15 min at 4° C. Subsequently, it was filtered using a 0.8 µm cellulose-acetate filter. The fusion protein LCI-eGFP was then purified via affinity chromatography using a ÄKTAprime with a prepared nickel-charged ion metal affinity chromatography (IMAC) column. Additionally, the LCI-eGFP was eluted with 500 mM imidazole. The protein solution was desalted using the disposable PD 10 desalting columns and eluted in PBS buffer. Lastly the LCI-EGFP was desalted tenfold with PBS using Amicon® Ultra centrifugal filters with a cut-off of 10 kDa (Merck Millipore Ltd.). The

concentration of the purified LCI-eGFP was determined via microvolume spectrophotometry (Nanodrop™ 2000, ThermoFisher Scientific). PBS buffer was used as reference.

Synthesis of LCI-eGFP-Polymer hybrids: The maleimide initiator 2-(2,5-dioxo-2,5-dihydro-1H-pyrrol-1-yl)ethyl 2-bromo-2-methylpropanoate was conjugated to the cysteine residue (position 69) of eGFP by Michael addition (LCI-eGFP-Initiator) as previously described.[56] For the polymerization of the LCI-eGFP-Polymer hybrids, a 10 mL Schlenk tube was filled with the necessary amount of HPMA, CBMAA SBMA or PCMA , $CuBr_2$ (0.05 eq.), Me_6TREN (0.55 eq.) and 0.5 mL PBS. 4.5 cm of hydrazine-activated Cu wire was wrapped around a magnetic stirring bar and fixed at the neck of the Schlenk tube using a magnet. The tube was degassed by six freeze-pump-thaw circles and backfilled with Argon. The LCI-eGFP-Initiator solution (1 mL, 1 eq.) was degassed for 1 h by Argon stripping. The polymerization was started by transferring the LCI-eGFP-Initiator solution to the Schlenk tube utilizing a gas-tight Hamilton syringe. The stirring bar was dropped and the polymerization continued for 18 h at 31 °C. The polymerization was stopped by exposing the solution to air and the addition of 0.5 mL of PBS. The reaction mixture was purified with Amicon® Ultra Centrifugal Filters (10 kDa). The conversion and purity of the hybrids was determined via ^{1}H-NMR spectroscopy (Table S1 and Figure S1).

Preparation of a thin layer of PCL. A thin layer of PCL was spin-coated on silicon-chips (1.2 x 1.2 cm) and gold-coated SPR sensor chips using the Spin Coater 1001 S from Convac GmbH. PCL was dissolved in toluene at 0.6% w/v. Once a clear solution was obtained, 75 µL was taken and dropped onto the substrate while it was spinning at room temperature. The parameters were set to a duration of 60 s and speed of 2000 RPM. The coated substrates were subsequently thermally annealed at 45 °C for 3.5 h in a vacuum oven. Subsequently. The PCL layer thickness was determined by ellipsometry.

Formation of the coating on substrates: The coating was formed by immersing the substrates or spraying them with an LCI-eGFP-Polymer solution in PBS (4-6 µmol·L^{-1} in PBS). After 45-60 min of incubation, the meshes were washed with copious amounts of PBS (3 x 5 min).

4.4.3 Analytical Methods

Nuclear magnetic resonance. ^{1}H-NMR spectra were obtained on a Bruker Avance III 400 spectrometer at 400 MHz. Monomer conversion was determined directly from the crude polymerization solution after the addition of D_2O (Figure S4.1and Figure S4.2). Spectra of the pure LCI-eGFP-Polymer hybrids were acquired after purification procedure with Amicon® Ultra centrifugal filters. For this, D_2O supplemented with 1% deuterated Trimethylsilylpropanoic acid (TSP) was used as solvent. The measurement was conducted using suppression of the water signal.

MALLS-SEC. Multi-angle laser light scattering size exclusion chromatography of the purified LCI-eGFP and LCI-eGFP-Polymer hybrids was measured using a Superose 6 column and online Wyatt T-rEX differential refractometer and Wyatt Dawn Heleos II Multi-angle laser light scattering detector. The mobile phase consisted of sodium acetate buffer (0.3 M, pH 6.5) containing 1 $g \cdot L^{-1}$ of sodium azide. The flow rate was set to 0.5 $ml \cdot min^{-1}$.

Ellipsometry. The dry thickness of the spin-coated PCL layer and LCI-eGFP-Polymer hybrid coatings was obtained using the RC2-D spectroscopic ellipsometer (J.A. Woollam Co., Inc.). Measurements were performed at room temperature, at angles of incidence of 65°, 70°, and 75° and in the wavelength range of 250-1000 nm. Data analysis was done using the CompleteEASE software (Version 5.08r). Fitting was applied using the B-spline model for both the PCL layer and the hybrid coating.

Quantification of hybrid absorption via SPR. A solution of LCI-eGFP-Polymer hybrids in PBS (6.64 $nmol \cdot mL^{-1}$) was flown over the PCL coated SPR sensor chip for 45-60 min. Afterwards, PBS was injected to washed out unbound hybrids. To quantify the amount of adsorbed hybrids the change in baseline refractive index before and after injection of the hybrid solution was monitored.

Assessment of blood plasma fouling. The amount of BP protein fouling was assessed by surface plasmon resonance (SPR) on the MP-SPR NaviTM 210A VASA (BioNavis, Tampere, Finland) with a two-channel microfluidic system enabling measurement at 670 nm as well as 785 nm. The system was used with the SPR-Navi Control software (Version 4.2.5.2). Briefly, a freshly prepared BP solution in PBS was injected over the coated SPR sensor at 10 $\mu L \cdot min^{-1}$ for 60 min. Subsequently, the surface was flushed with PBS buffer to removed unbound proteins. The

data were analyzed with the SPR-Navi Data Viewer (Version 4.3.5.2). Adsorbed protein mass was determined from ΔμRIU before and after injection by multiplication with a conversion factor of 0.0794 ng·cm^{-2} per μRIU for 670 nm.

X-ray photoelectron spectroscopy. XPS spectra were recorded using an Ultra AxisTM spectrometer (Kratos Analytical, Manchester, United Kingdom). For that, the surfaces were irradiated with a monochromated A1 Kα X-ray source (1486.6 eV) with a total power of 144 W (12 kV·12 mA). The processing software CasaXPS (Version 2.3.22, Casa Software Ltd., United Kingdom) was used to perform charge corrections. The spectra were fitted/deconvoluted with several Voigt profiles. All spectra were referenced to the C1s peak of the aliphatic carbons ([C-C], [C-H]), which was set to 285.0 eV according to literature.[57] All spectra were normalized to maximum intensity for better visualization.

Mechanical abrasion test. The titanium substrates were previously coated with the LCI-KR2-eGFP-pCBMAA$_{702}$ hybrids by the immersion method and under aseptic conditions. They were stored in dry state at 4°C until further use. Prior to the brushing experiments, the samples were incubated in artificial saliva or PBS for 15 min to allow the coating to hydrate. The coated substrates were then carefully placed in the 3D printed holders and the fluid reservoir of the brushing test rig was filled with PBS or artificial saliva until the samples were completely covered. The toothbrushes were placed directly on the substrates and the motor was turned on to start the brushing experiments. After 38-40 min, the experiment was stopped and the samples were dried at ambient conditions and stored at 4 °C until further use for bacterial adhesion studies.

Confocal laser scanning microscopy. CLSM was utilized to visualize the LCI-eGFP-Polymer coating on PCL meshes. Adsorptive binding was performed by immersing the meshes in the LCI-eGFP-Polymer solution at a concentration of 1.0 mg·mL^{-1} in PBS for 60 min at 4 °C. Subsequently, the surfaces were rinsed with copious amounts of PBS and Milli-Q water. For stability assessment, the coating process was performed under aseptic conditions. The meshes were sterilized by UV irradiation (254 nm) for 60 min. Hybrid solutions were sterile filtered using a 0.2 μm cellulose acetate filter. Incubation in sterile PBS and LB supplemented with 10% FBS was performed at 4 °C for 32 and 180 days. Images were acquired using a TCS SP8 (Leica Microsystems CMS GmbH, Mannheim, Germany) equipped with an argon laser (10% intensity). The excitation wavelength was set to 488 nm. The emitted fluorescence was

detected by a PMT detector at the wavelength range 500-565 nm. BSA adsorption was conducted by immersing the coated meshes for 1 h in a BSA solution in PBS at a concentration of 10 mg·mL^{-1}. The BSA solution was spiked at 1 mol% with a FITC-BSA for visualization. Images were acquired using a TCS SP8 (Leica Microsystems CMS GmbH, Mannheim, Germany) equipped with an argon laser (10% intensity). The excitation wavelength was set to 488 nm. The emitted fluorescence was detected by a PMT detector at the wavelength range 500-565 nm.

Adhesion assay of E. coli (DSM-1103) and E. coli (MG1655). A single colony *of E. coli* (DSM-1103) was inoculated in 10 mL MHB and grown for 12 h (37 °C, 180 RPM). For the adhesion assay, the MHB was supplemented with 10% FBS and the optical density was adjusted to OD_{600} of 0.1, corresponding to approximately 10^8 CFU·mL^{-1}. In the case of *E. coli* (DSM-1103), a single colony *of E. coli* was inoculated into 10 mL LB and grown for 16 h (37 °C, 180 RPM). For the adhesion assay, the LB was supplemented with 10% FBS and the optical density was adjusted to an OD_{600} of 0.1, corresponding to approximately 10^8 CFU·mL^{-1}. The bare and functionalized substrates (1 cm × 1 cm) were placed in 15 mL Falcon tubes and covered with 3 mL of bacterial suspension (OD_{600} = 0.1). All types of meshes were tested in triplicates. The tubes were closed and placed inside the incubator for 24 h at 37 °C and 180 RPM. Planktonic cells were removed by pipetting out the cell suspension. The samples were washed two to four times with 2 mL of PBS (5 min) and fixed in 3% glutaraldehyde in PBS (overnight, 4 °C). All samples were dehydrated through a graded ethanol series (25%, 50%, 70%, 90% and 100% dry, 15 min each step, 2 × 100%) and air dried using hexamethyldisilazane. Adhesion of *E.coli* was visualized by SEM.

Adhesion assay of S. gordonii (DSM-6777). A single colony *of S. gordonii* (DSM-6777) was inoculated in 15 mL tryptic soy yeast (TSY) medium and incubated without aeration for 24 h at 37 °C. For the adhesion assay, the saturated culture was diluted to an optical density of OD_{600} = 0.1. The bare and functionalized substrates were placed in well plates and covered with the bacterial suspension (OD_{600} = 0.1). In case of 96-well plates 150 µl of the bacterial suspension were added. For the experiments with dental screws 24-well plates were utilized and around 1 ml of the bacterial solution was added. Incubation proceeded without shaking at 37 °C for 24 h. Subsequently, the samples were immersed twice in 150 µL or 1 mL of PBS (5 min) and fixed in 3% glutaraldehyde in PBS (overnight, 4 °C). All samples were dehydrated

through a graded ethanol series (25%, 50%, 70%, 90% and 100% dry, 15 min each step, 2 × 100%) and air dried using hexamethyldisilazane. *S. gordonii* adhesion was visualized by SEM.

Scanning electron microscopy. Images were acquired using the HITACHI-S-3000N and HITACHI-S-4800 (Hitachi High-Technologies, Tokyo, Japan). Before analysis, the samples were sputtered with an 8-10 nm thick conductive layer of Au/Pd.

Adhesion assay of HDF. Bare and modified substrates were incubated overnight in PBS at 37 °C prior to cell adhesion experiments. Cells were cultured until passage 6 in DMEM supplemented with 10% FBS and harvested by trypsinization. PBS was removed and 200,000 fibroblasts in DMEM were seeded onto each substrate (300 µL DMEM). Samples were incubated for 24 h at 37 °C in a humidified atmosphere containing 5% CO_2. The cells were washed, fixed and permeabilized for staining of cellular components. Microscopic evaluation was performed using a Leica TCS SP8 confocal microscope (Wetzlar, Germany).

Immunostaining of fibroblasts. Cell fixation was performed by exposure to 4% paraformaldehyde in PBS (pH 7.4) for 15 min at ambient conditions. Cells were washed three times with cold PBS and permeabilized by incubation 0.1% Triton X-100 for 5 mins. Cells were then carefully washed with PBS (3x 5min) blocking step proceeded for 30 mins with 1% BSA in PBS. Immunostaining was performed using Vinculin Monoclonal Antibody (7F9), eFluor 570 (10 µg·mL), Alexa Fluor™ Plus 647 Phalloidin (1 µM) and DAPI (0.1 mg·mL^{-1}). For STED imaging, cells were stained with TRITC Phalloidin (196 nM), Vinculin Monoclonal Antibody (VLN01, 2 µg·mL^{-1}) and Goat anti-Mouse IgG (H+L), Alexa Fluor Plus 647 (2 µg·mL^{-1}).

Viability test by direct contact. All substrates (1.9 cm^2) were previously sterilized by UV disinfection (254 nm) for 1 h. Hybrid solution was sterilized by filtration using 0.2 µm cellulose acetate syringe filters (x2). Subsequently, all meshes were washed five times with PBS (5 min each) and then placed on top of a monolayer of HDF cells (80% confluence, 12-well plate) and incubated for 48 h at 37 °C in a humidified, 5% CO_2 atmosphere. Cell viability was visualized by live/dead staining and an ApoTome fluorescence microscopy. Quantification of cell viability was performed by colorimetric MTS assay.

Preparation of conditioned cell culture medium. Sterilization of all materials was performed by UV disinfection (254 nm) for 1 h. Subsequently, samples were washed three times with sterile

PBS (5 min). Conditioned extract media were prepared under aseptic conditions according to ISO 10993-12. Briefly, the substrates were immersed in DMEM growth medium at 37 °C in a humidified atmosphere containing 5% CO_2 for 72h ± 2 h. PCL wound dressings were extracted at a ratio of 3 $cm^2 \cdot mL^{-1}$. As a negative control, growth medium was incubated without the addition of any material under the same conditions. The positive control, a piece of latex glove, provides a reproducible cytotoxic response and was extracted at a ratio of 6 $cm^2 \cdot mL^{-1}$.

Viability test according to ISO 10993-5. For experiments with HDF, the cells were harvested by trypsin (GibcoTM) treatment and seeded into 96-well plates (Greiner bio-one) at a density of 8,000 cells·$well^{-1}$. Cells were then cultured for 24 h to 80% confluence and subsequently treated with 100 µL of the test specimen extracts for 24 h. The determination of cell viability (metabolically active cells) was carried out using the colorimetric MTS assay. After incubation, the medium was exchange to equal volumes and 20 µL of MTS reagent (100/20) was added. The microplates containing the treated cells and control were left to incubate for 3 h at 37 °C in a humidified, 5% CO_2 atmosphere and the absorbance was recorded at 490 nm using the multi-mode microplate reader SpectraMax® M3. The collected absorbance data were normalized with the untreated cells as the 100% reference.

For experiments with HUVEC and UMR-106 cells, culture was carried out at 5000 cells per well in Falcon 96 well-plates with HUVEC or osteoblast medium, respectively. After incubation of 72 h at 37 °C in a humidified 5% CO_2 atmosphere, half of the medium was removed and cells were treated with the conditioned extracted media at a final dilution of 1:1 or 1:10. Pristine culture media served as negative control (100%). After 24 h incubation, the viable cell fraction was determined by counting the amount of Hoechst-only positive cells. The viable cells were plotted as an average viable cell number per condition (n = 9).

For experiments with monocytes and macrophages, cells were seeded at a density of 120,000 or 100,000, respectively in 96 well-plates with monocyte or Roswell Park Memorial Institute (RPMI) 1640 medium. The conditioned and control media were added directly to the THP-1 cells at dilution rates of 1:1 and 1:10 and incubated for 24 h at 37 °C and 5% CO_2. As for the macrophages, THP-1 cells were stimulated with PMA (5 ng·mL^{-1}, 24 h) to induce initial macrophage differentiation. The cell medium was then changed to monocyte medium and the cells were incubated for an additional 24 h at 37 °C and 5% CO_2. Afterward, half of the medium was removed and (un)conditioned cell culture medium with either water (control), IFN-γ

(20 ng·mL^{-1}) and LPS (250 ng·mL^{-1}, to generate M1-like macrophages) or IL-4 (20 ng·mL^{-1}, to generate M2-like macrophages) was added. After 24 h of incubation, the viable cell fraction was determined as described above.

For experiments with osteoblasts, UMR-106 cells were differentiated into osteoblasts through stimulation with L-Ascorbic Acid (50 µM), β-Glycerophosphate (10 mM) and Dexamethasone (10 nM) for two weeks twice a week. The experiments were started with 5000 per well. After two weeks of stimulation the conditioned and control cell culture media was added and after 24 h of incubation viable cell fraction was determined as explained above.

For experiments with RAW264.7 cells, seeding at a density of 1600 cells per well (5000 cells·cm^{-2}) was carried out. Incubation proceeded in DMEM containing L-glutamine (4 mM), glucose (4.5 g·L^{-1}), sodium pyruvate (1 mM), and sodium bicarbonate (1.5 g·L^{-1}), 10% FBS and 1% PS (Osteoclast medium). To induce osteoclast differentiation RANKL (30 ng·mL^{-1}) was added. Following a 72 h incubation period at 37 °C and in humified 5% CO_2 atmosphere, conditioned and control media were added and the same protocol as described above was followed.

Assessment of collagen production. Primary bovine fibroblast cells were seeded in well-plates (Falcon 96) in DMEM medium at a density of 5000 cells/well. After 6 h, the conditioned cell culture media (n = 9) were added to the wells at a 1:1 or 1:10 dilution ratio and 2-Phospho-L-ascorbic acid trisodium salt (2-PAA, 300 µM) was added to induce collagen formation. Cells were left to incubate for 96 h at 37 °C in a humidified atmosphere containing 5% CO_2. Following incubation, the cells were fixed with 2% paraformaldehyde (PFA) for 15 min. They were then washed with PBS twice and stained with Hoechst 33342 (3.25 µM) and collagen-binding adhesion protein 35-AF567 (CNA35-AF567). Imaging was performed using a BD Pathway 855 high content analyzer. Analysis was done with the MetaXpress software (Molecular Devices). The nuclei and collagen fibers per imaged area were segmented and the average fiber length was determined. The average fiber length of the bare coin condition was set as the 100% reference.

Assessment of HUVEC:THP-1 cell interaction. The adhesion of THP-1 cells to HUVECs was used as a measure for inflammatory capacity. THP-1 or HUVEC cells were treated with the conditioned extracted media and the effect of the coatings on the individual cellular components was evaluated. To test the effect of coatings on THP-1 cells, 15 x 10^6 THP-1 cells

were incubated with 6 mL of conditioned cell culture medium and let to incubate for 24 h. 36,000 HUVECs per channel were seeded on IBIDI VI 0.4 Luer slides and incubated for 24 h at 37 °C and humidified atmosphere containing 5% CO_2. Half of the channels were then stimulated with TNF-α (80 ng·mL^{-1}) for 16 h. To test the effect of the coatings on HUVECs, 36,000 HUVECs per channel were seeded on IBIDI VI 0.4 Luer slides and incubated for 24 h at 37 °C and 5% CO_2. Then, the channels were treated with TNF-α (80 ng·mL^{-1}, positive control) or the conditioned media for 24 h. Unconditioned media served as negative control. THP-1 cells stained with calcein AM (5 µg·mL^{-1}) for 30 min at 37 °C and 5% CO_2. The cells were then washed with HUVEC medium, counted and diluted to a final concentration of 1 x 10^6 THP-1 cells·mL^{-1}. Subsequently, the solution containing the cells was flown over the corresponding HUVEC channels for 4 min at a speed of 0.44 mL·min^{-1}. Next, channels were washed with HUVEC medium (0.22 mL·min^{-1}) for 2.5 min. Imaging was performed with a BD Pathway 855 high content analyzer. The images were segmented with the MetaXpress software (Molecular Devices), where calcein stained THP-1 cells were counted.

Deposition of calcium phosphate and hydroxyapatite by osteoblasts. UMR-106 cells were differentiated into osteoblasts as described above. During this process the conditioned cell culture medium was added to the wells at each stimulation step with a final dilution of 1:10. After two weeks of stimulation, the cells were washed twice with PBS, fixed with 4% PFA for 40 min at room temperature and stained with the von Kossa stain or with the OsteoImageTM Mineralization Assay. For the von Kossa staining, a 5% silver nitrate solution was added and the plate was placed in a Jelight UVO-Cleaner 42-220 for 8 min. Cells were washed thrice with ultrapure water and incubated with a 5% sodium thiosulphate solution at ambient temperature for 5 min. Subsequently, the cells were washed with ultrapure water and imaged with an EVOS XL digital inverted microscope (n = 6 per condition). The OsteoImage™ Mineralization Assay was carried out according to the protocol provided by the manufacturer. Further, cell nuclei were stained with 3.25 µM Hoechst 33342 for 15 min. The plates were then imaged on a BD Pathway 855 high content analyzer. Segmentation of the images was performed with the MetaXpress software (Molecular Devices). The average area per cell was calculated by dividing the OsteoImage stained area by the total amount of cells per well. The average area per cell of the control sample was set as 100% reference. (n = 6).

4.5 Supplementary Results

Synthesis of LCI-eGFP-Polymer hybrids

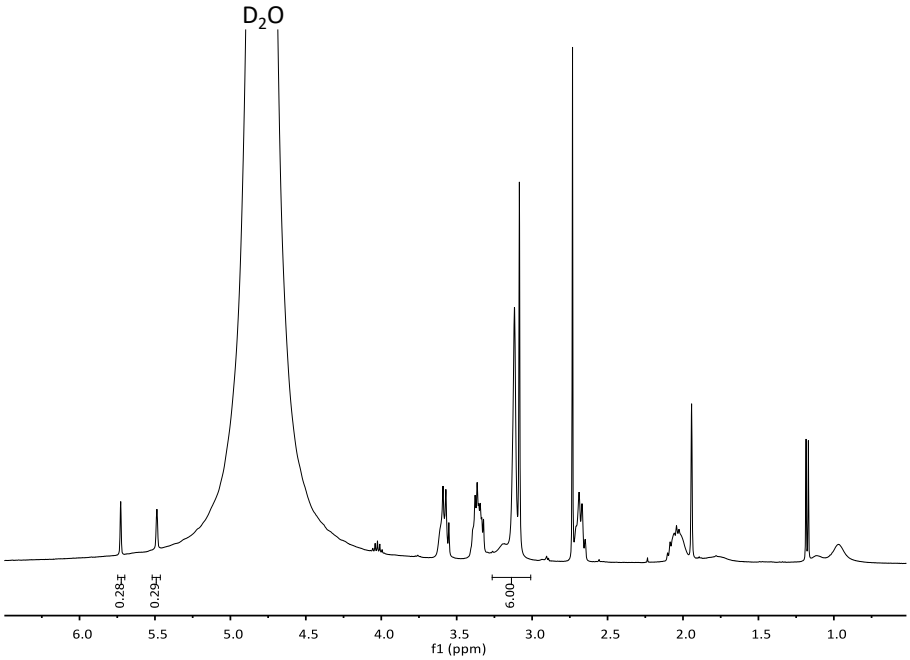

Figure S4.1. ^{1}H NMR spectrum after polymerization of LCI-eGFP-pCBMAA$_{864}$ to determine conversion.

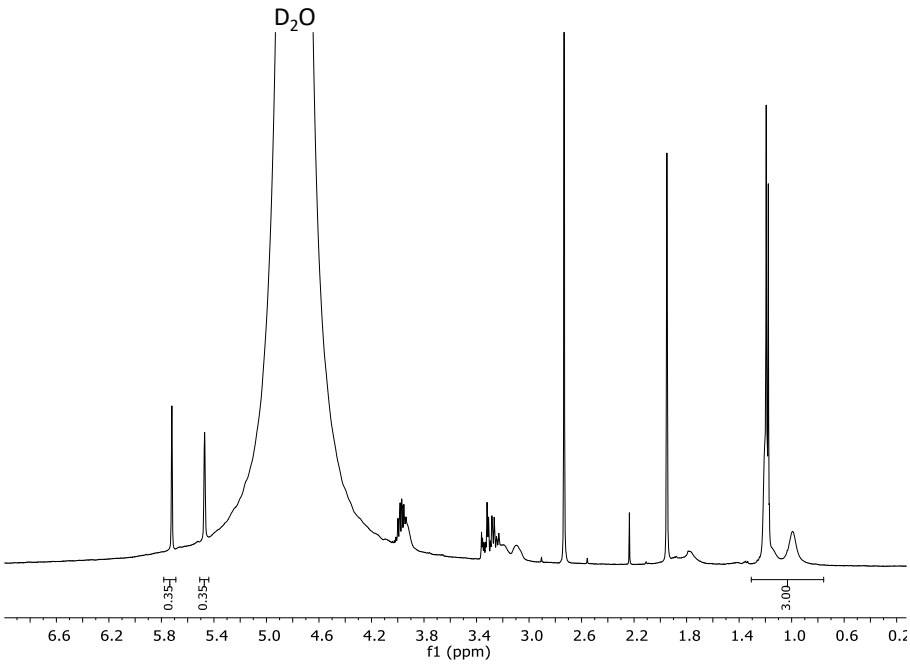

Figure S4.2. ^{1}H NMR spectrum after polymerization of LCI-eGFP-pHPMA$_{780}$ to determine conversion.

Table S4.1. List of LCI-eGFP-Polymer library

Hybrid	C [%]	DP	M_{theo} [kg·mol^{-1}]	M_{GPC} [kg·mol^{-1}]	$\frac{M_w}{M_n}$
LCI-eGFP-pCBMAA	48	576	177	143.9	1.66
LCI-eGFP-pHPMA	46	552	119	48.5	1.464
LCI-eGFP-pHPMA*co*CBMAA	33	400	98.2	65	1.474
LCI-eGFP-pCBMAA	72	864	235	193.2	1.91
LCI-eGFP-pHPMA	65	780	149	87.6	1.746
LCI-eGFP-pSBMA	98	1176	365	-	-
LCI-eGFP-pPCMA	100	1200	391	-	-
LCIK2-eGFP-pCBMAA	58.5	702	207	118.6	1.849
LCIK2-eGFP-pHPMA	76	912	168	102.4	1.864

Molecular characterization of LCI-eGFP-Polymer hybrids

Polydispersity of 1.33 for the LCI-eGFP-pHPMA$_{340}$ and 1.27 for LCI-eGFP-pCBMAA$_{336}$ hybrids measured by MALLS-SEC.

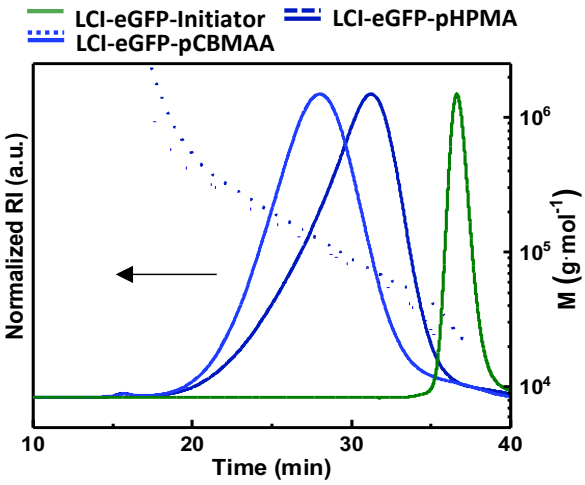

Figure S4.3. MALLS-SEC of LCI-eGFP (green) and the hybrids: LCI-eGFP-pHPMA$_{340}$ (dark blue) and LCI-eGFP-pCBMAA$_{336}$ (light blue). The solid lines indicate the normalized change in

refractive index (RI) with time, while the dashed lines show the corresponding molecular weight.

Recombinant variant LCI-KR2

The recombinant variant LCI-KR2 was generated through site-directed mutagenesis at positions Y29 and G35. Tyrosine (T) was exchanged to arginine (R).

LCI-Y29R/G35R (LCI-KR2)

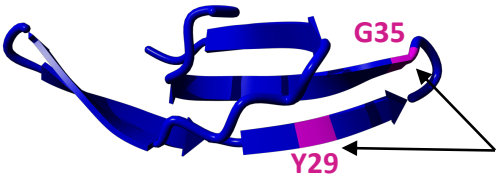

Amino acid substitutions Y29R and G35R were recombined in variant LCI-KR-2

Sequence 5' → 3'

CGAATGGTAATTTTGCAGCAAGCTTTGTRCTGGARGGCACCAAATGGATCTTCAAAAGCA
AATACTATGACAGCAGCAAAGGTTATTGGGTGGGTATTTATGAAGTGTGGGATCGCAAA

A multiplicity of weak interactions (H-bonding, hydrophobic effect, ionic interactions) enables the physisorption of the LCI and LCI-KR2 peptides from aqueous solution onto a wide range of polymeric and metal surfaces.

Figure S4.4. Amino acid sequence of the recombinant LCI-KR2 peptide. Amino acid substitutions are highlighted in pink.

Bacterial adhesion

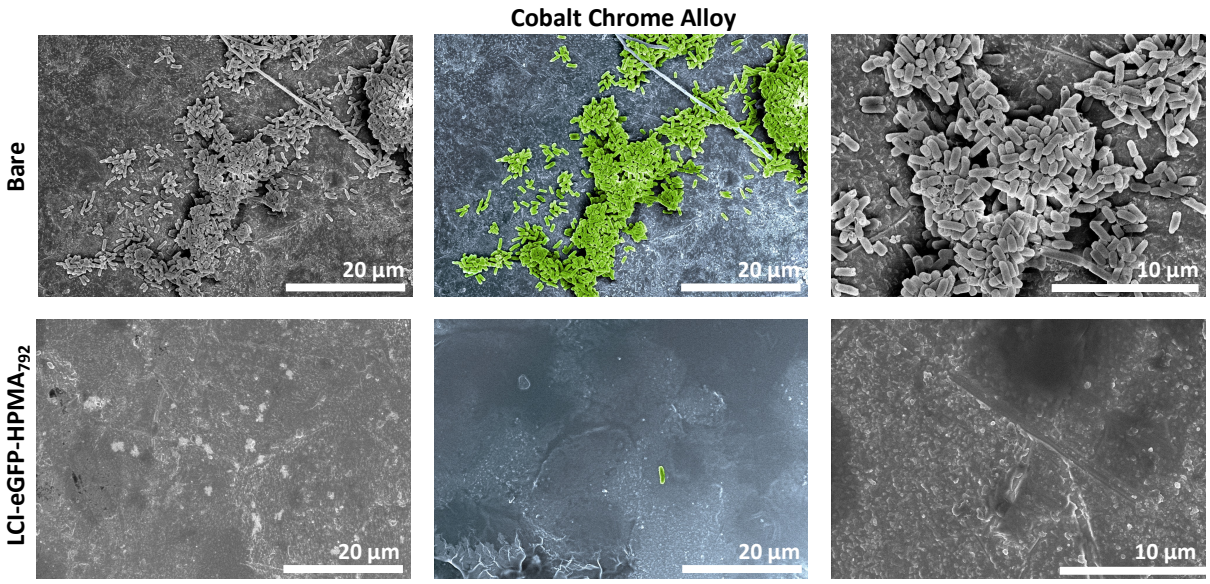

Figure S4.5. SEM micrographs of bare and LCI-eGFP-pCBMAA$_{912}$ coated (A) Cobalt Chrome Alloy surfaces after exposure to *E. coli* bacteria for 24 h. Images are false-colored to enhance the visualization of *E. coli* bacteria (green).

4.6 Declaration of Contributions

Parts of this chapter were adapted with permission from the publication “Kill&Repel Coatings: The Marriage of Antifouling and Bactericidal Properties to Mitigate and Treat Wound Infections” in Advanced Functional Materials (Garay-Sarmiento, M., Witzdam, L., Vorobii, M., Simons, C., Herrmann, N., De los Santos Pereira, A., Heine, E., El-Awaad, I., Lütticken, R., Jakob, F., Schwaneberg, U., Rodriguez-Emmenegger, C., Kill&Repel Coatings: The Marriage of Antifouling and Bactericidal Properties to Mitigate and Treat Wound Infections. Adv. Funct. Mater. 2022, 32, 2106656; https://doi.org/10.1002/adfm.202106656; Copyright © 2021 The Authors. Advanced Functional Materials published by Wiley-VCH GmbH). Moreover, some of the results were also published in the master thesis entitled “Development of an advanced Kill&Repel coating for polymeric and metallic surfaces” at RWTH Aachen University by Yannik Rutsch.

The synthesis of the LCI-eGFP-Polymer hybrid macromolecules and SPR measurements to determine hybrid adsorption and BP protein fouling were performed by me and my former master student Yannik Rutsch. I performed ^{1}H-NMR characterization, ellipsometry and XPS analysis. Dr. Andres de los Santos Pereira performed the MALLS-SEC measurements of the different LCI-eGFP-Polymer Hybrid macromolecules. Further, I performed long-term stability studies, BSA adsorption assay, fibroblast adhesion studies and their characterization by CLSM. I also performed the bacterial adhesion studies and subsequent SEM characterization of the following samples: PCL wound dressings, PU foam dressings, venous catheters, porous titanium, Ti6Al4V coins, cobalt chrome substrates and dental titanium screws. Bacterial adhesion tests and mechanical abrasion tests on titanium coins were performed together with Yayci Abdulkadir. Stephan Rütten recorded the images of the samples afterwards via SEM. I performed experiments involving the dental screw demonstrator. Moreover, I carried out the cell viability studies with fibroblasts in direct contact and according to the extraction method from ISO 10993. As for the biocompatibility studies involving HUVECs, monocytes, M1 macrophages, M2 macrophages, UMR-106 cells, osteoblasts, osteoclasts and RAW264.7 cells, these were performed by the research group of Prof. Daniel Molin under the supervision of Dr. Nynke van den Akker from Maastricht University. Furthermore, the Laboratory for Machine Tools and Production Engineering (WZL) at RWTH Aachen University is acknowledge

for the design and building of the brushing test stand and the structuring of the titanium coins as well as dental screw demonstrator.

The LCI-eGFP and LCI-KR2-eGFP proteins were produced by Christian Simmons, Niklas Herrmann and Yayci Abdulkadir.

Prof. César Rodriguez-Emmenegger supervised all of these projects.

4.7 References

[1] R. Guo, Y. Liu, Y. Zhang, A. Dong, J. Zhang, *Macromolecular Research* **2013**, *21*, 1127-1137.

[2] J. Groll, E. V. Amirgoulova, T. Ameringer, C. D. Heyes, C. Röcker, G. U. Nienhaus, M. Möller, *Journal of the American Chemical Society* **2004**, *126*, 4234-4239.

[3] N.-P. Huang, R. Michel, J. Voros, M. Textor, R. Hofer, A. Rossi, D. L. Elbert, J. A. Hubbell, N. D. Spencer, *Langmuir* **2001**, *17*, 489-498.

[4] G. L. Kenausis, J. Vörös, D. L. Elbert, N. Huang, R. Hofer, L. Ruiz-Taylor, M. Textor, J. A. Hubbell, N. D. Spencer, *The Journal of Physical Chemistry B* **2000**, *104*, 3298-3309.

[5] X. Han, Z. Yuan, Y. Niu, X. Chen, H. Liu, *Biointerphases* **2021**, *16*.

[6] B. Malisova, S. Tosatti, M. Textor, K. Gademann, S. Zürcher, *Langmuir* **2010**, *26*, 4018-4026.

[7] Â. Serrano, S. Zürcher, S. Tosatti, N. D. Spencer, *Macromolecular Rapid Communications* **2016**, *37*, 622-629.

[8] V. Zoulalian, S. Zürcher, S. Tosatti, M. Textor, S. Monge, J.-J. Robin, *Langmuir* **2010**, *26*, 74-82.

[9] N. Bentley, F. D. Scherag, T. Brandstetter, J. Rühe, *Advanced Materials Interfaces* **2022**, *9*, 2102359.

[10] L. Witzdam, Y. L. Meurer, M. Garay-Sarmiento, M. Vorobii, D. Söder, J. Quandt, T. Haraszti, C. Rodriguez-Emmenegger, *Macromolecular Bioscience* **2022**, *22*, 2200025.

[11] J. Englert, L. Witzdam, D. Söder, M. Garay-Sarmiento, A. Joseph, A. M. Wagner, C. Rodriguez-Emmenegger, *Macromolecular Chemistry and Physics*, *n/a*, 2300306.

[12] J. N. Mulvihill, A. Faradji, F. Oberling, J. P. Cazenave, *J Biomed Mater Res* **1990**, *24*, 155-163.

[13] B. Sivaraman, R. A. Latour, *Biomaterials* **2010**, *31*, 832-839.

[14] B. Sivaraman, R. A. Latour, *Biomaterials* **2011**, *32*, 5365-5370.

[15] G. J. Ma, A. R. Ferhan, T. N. Sut, J. A. Jackman, N.-J. Cho, *Colloids and Surfaces B: Biointerfaces* **2020**, *194*, 111194.

[16] B. Sivaraman, R. A. Latour, *Langmuir* **2012**, *28*, 2745-2752.

[17] K. K. Goli, O. J. Rojas, J. Genzer, *Biomacromolecules* **2012**, *13*, 3769-3779.

[18] M. Meißler, A. Taden, H. G. Börner, *ACS Macro Letters* **2016**, *5*, 583-587.

[19] G. P. Sakala, M. Reches, *Advanced Materials Interfaces* **2018**, *5*, 1800073.

[20] M. Reches, E. Gazit, *Nat Nanotechnol* **2006**, *1*, 195-200.

[21] A. Arul, S. Sivagnanam, A. Dey, O. Mukherjee, S. Ghosh, P. Das, *RSC Adv* **2020**, *10*, 13420-13429.

[22] S. Dedisch, F. Obstals, A. de los Santos Pereira, M. Bruns, F. Jakob, U. Schwaneberg, C. Rodriguez-Emmenegger, *Advanced Materials Interfaces* **2019**, *6*, 1900847.

[23] D. Söder, M. Garay-Sarmiento, K. Rahimi, F. Obstals, S. Dedisch, T. Haraszti, M. D. Davari, F. Jakob, C. Heß, U. Schwaneberg, C. Rodriguez-Emmenegger, *Macromolecular Bioscience* **2021**, *21*, 2100158.

[24] H. Steiner, D. Andreu, R. B. Merrifield, *Biochim Biophys Acta* **1988**, *939*, 260-266.

[25] W. Gong, J. Wang, Z. Chen, B. Xia, G. Lu, *Biochemistry* **2011**, *50*, 3621-3627.

[26] S. Dedisch, A. Wiens, M. D. Davari, D. Söder, C. Rodriguez-Emmenegger, F. Jakob, U. Schwaneberg, *Biotechnology and Bioengineering* **2020**, *117*, 49-61.

[27] K. Rübsam, B. Stomps, A. Böker, F. Jakob, U. Schwaneberg, *Polymer* **2017**, *116*, 124-132.

[28] R. A. Meurer, S. Kemper, S. Knopp, T. Eichert, F. Jakob, H. E. Goldbach, U. Schwaneberg, A. Pich, *Angewandte Chemie International Edition* **2017**, *56*, 7380-7386.
[29] D. B. Gehlen, L. C. De Lencastre Novaes, W. Long, A. J. Ruff, F. Jakob, T. Haraszti, Y. Chandorkar, L. Yang, P. van Rijn, U. Schwaneberg, L. De Laporte, *ACS Appl Mater Interfaces* **2019**, *11*, 41091-41099.
[30] P. Winnersbach, A. Hosseinnejad, T. Breuer, T. Fechter, F. Jakob, U. Schwaneberg, R. Rossaint, C. Bleilevens, S. Singh, *Membranes* **2022**, *12*, 73.
[31] J. Dittrich, C. Brethauer, L. Goncharenko, J. Bührmann, V. Zeisler-Diehl, S. Pariyar, F. Jakob, T. Kurkina, L. Schreiber, U. Schwaneberg, H. Gohlke, *ACS Applied Materials & Interfaces* **2022**, *14*, 28412-28426.
[32] G. Lligadas, S. Grama, V. Percec, *Biomacromolecules* **2017**, *18*, 1039-1063.
[33] X. Jiang, B. M. Rosen, V. Percec, *Journal of Polymer Science Part A: Polymer Chemistry* **2010**, *48*, 2716-2721.
[34] F. Obstals, M. Vorobii, T. Riedel, A. de los Santos Pereira, M. Bruns, S. Singh, C. Rodriguez-Emmenegger, *Macromolecular Bioscience* **2018**, *18*, 1700359.
[35] M. Garay-Sarmiento, L. Witzdam, M. Vorobii, C. Simons, N. Herrmann, A. de los Santos Pereira, E. Heine, I. El-Awaad, R. Lütticken, F. Jakob, U. Schwaneberg, C. Rodriguez-Emmenegger, *Advanced Functional Materials* **2022**, *32*, 2106656.
[36] C. Rodriguez Emmenegger, E. Brynda, T. Riedel, Z. Sedlakova, M. Houska, A. B. Alles, *Langmuir* **2009**, *25*, 6328-6333.
[37] E. van Andel, S. C. Lange, S. P. Pujari, E. J. Tijhaar, M. M. J. Smulders, H. F. J. Savelkoul, H. Zuilhof, *Langmuir* **2019**, *35*, 1181-1191.
[38] R. Singh, D. Singh, A. Singh, *World J Radiol* **2016**, *8*, 355-369.
[39] R. Dong, B. Guo, *Nano Today* **2021**, *41*, 101290.
[40] X. Zhang, D. Brodus, V. Hollimon, H. Hu, *Chem Cent J* **2017**, *11*, 18.
[41] B. O. Ode Boni, L. Lamboni, T. Souho, M. Gauthier, G. Yang, *Materials Horizons* **2019**, *6*, 1122-1137.
[42] R. Pawar, A. Pathan, S. Nagaraj, H. Kapare, P. Giram, R. Wavhale, *Polymers for Advanced Technologies* **2023**, *34*, 3296-3316.
[43] Ž. Petkovšek, K. Eleršič, M. Gubina, D. Žgur-Bertok, M. S. Erjavec, *Journal of Clinical Microbiology* **2009**, *47*, 1811-1817.
[44] R. Van Noort, *J. Mater. Sci.* **1987**, *22*, 3801-3811.
[45] M. Ask, J. Lausmaa, B. Kasemo, *Appl. Surf. Sci.* **1989**, *35*, 283-301.
[46] P. Tengvall, I. Lundström, *Clin. Mater.* **1992**, *9*, 115-134.
[47] J. G. S. Souza, M. M. Bertolini, R. C. Costa, B. E. Nagay, A. Dongari-Bagtzoglou, V. A. R. Barão, *iScience* **2021**, *24*, 102008.
[48] N. A. Hodges, E. M. Sussman, J. P. Stegemann, *Biomaterials* **2021**, *278*, 121127.
[49] K. Rübsam, M. D. Davari, F. Jakob, U. Schwaneberg, *Polymers* **2018**, *10*, 423.
[50] N. Mosailova, J. Truong, T. Dietrich, J. Ashurst, *Case Rep Infect Dis* **2019**, *2019*, 7127848.
[51] G. C. Gurtner, S. Werner, Y. Barrandon, M. T. Longaker, *Nature* **2008**, *453*, 314-321.
[52] R. Fitridge, M. Thompson, *Mechanisms of Vascular Disease*

A Reference Book for Vascular Specialists, University of Adelaide Press, **2011**.
[53] V. Šromová, D. Sobola, P. Kaspar, *Cells* **2023**, *12*, 2576.
[54] C. Rodriguez-Emmenegger, C. M. Preuss, B. Yameen, O. Pop-Georgievski, M. Bachmann, J. O. Mueller, M. Bruns, A. S. Goldmann, M. Bastmeyer, C. Barner-Kowollik, *Adv. Mater.* **2013**, *25*, 6123-6127.

[55] K. T. Cheng, M. A. Van Zandvoort, *Molecular Imaging and Contrast Agent Database (MICAD)* **2008**.
[56] S. Dedisch, F. Obstals, A. de los Santos Pereira, M. Bruns, F. Jakob, U. Schwaneberg, C. Rodriguez-Emmenegger, *Adv. Mater. Interfaces* **2019**, *6*, 1900847.
[57] J. F. Watts, *Surf. Interface Anal.* **1993**, *20*, 267-267.

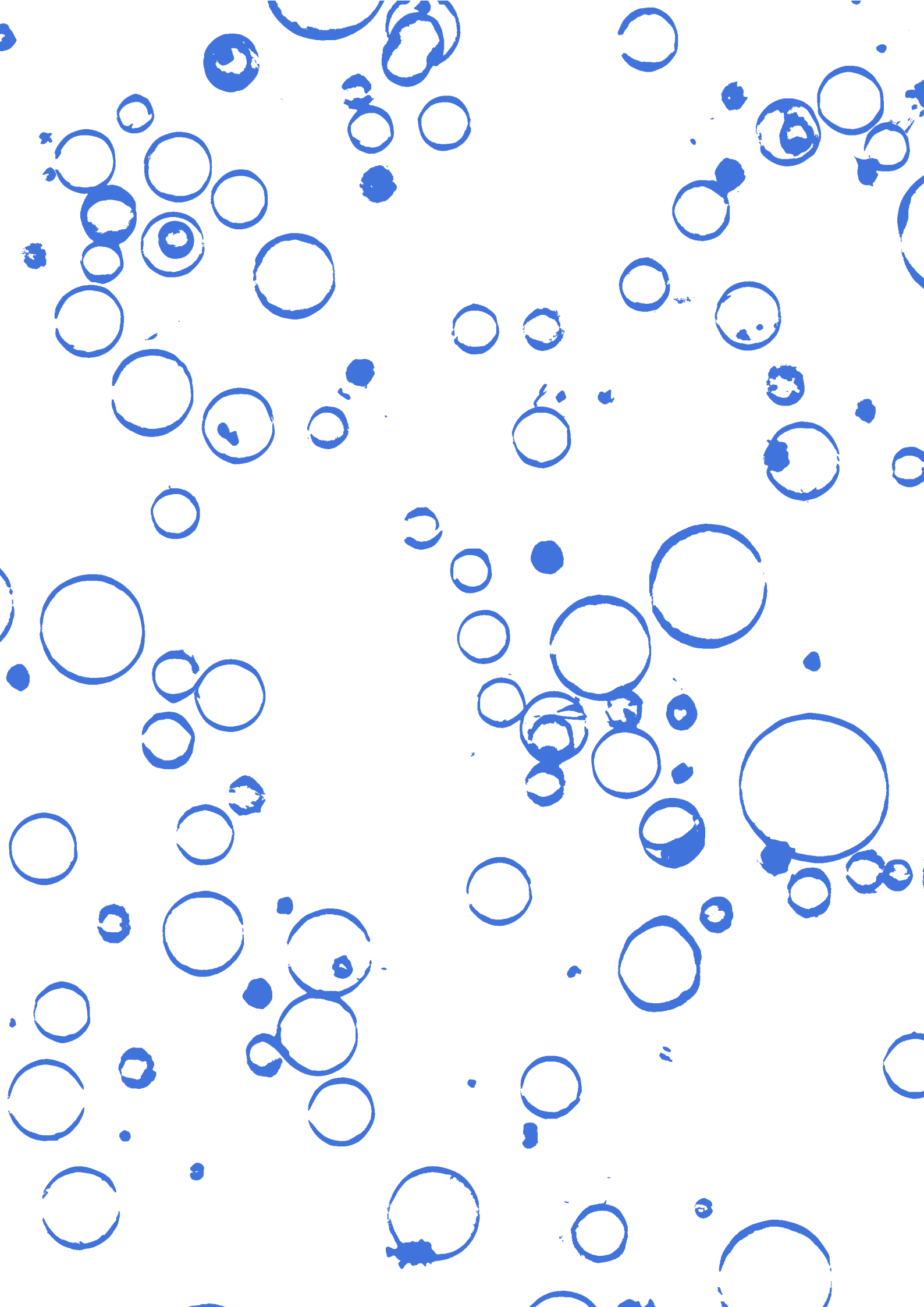

Chapter 5

The Kill&Repel Coating: The Synergistic Combination of Antifouling and Bactericidal Properties

5.1 Introduction

Conventional antibacterial surface coatings typically rely on two primary strategies to prevent bacterial colonization of biomaterial surfaces.[1-2] The first strategy, antifouling, involves creating enthalpic and entropic barriers that prevent bacterial attachment, as described earlier. The second strategy, bactericidal, focuses on eradicating microorganisms through the release of chemical agents or direct contact with the adhered bacteria. While, these two strategies mark a significant advancement in managing material-related infections, relying solely on either one does not provide sufficient long-term protection.[2-3] Although, antifouling coatings can effectively deter bacterial adhesion, they fall short in preventing the growth of these pathogens. In cases where bacteria manage to breach the repellent barrier, the coating surface becomes contaminated, bacteria can persist ultimately compromising the antifouling properties. Conversely, pure bactericidal coatings employ two approaches: the release of bacteria-killing compounds, such as silver ions and antibiotics, and coatings based on polycations.[4-5] The latter approach relies on the electrostatic attraction between cationic polymers and negatively charged bacteria cells to disrupt their cell membrane. However, this approach is often non-specific to bacteria and the same physical principle can be harmful to eukaryotic cells, limiting its practical use.[6-7] The utilization of silver ions (Ag^+) and antibiotics is widespread in clinical applications; nevertheless, their effectiveness has proven to be limited.[8-11] For instance, the release and spread of these bactericidal agents occur even in the absence of an infection, which can be harmful to neighboring tissue[12-14], compromise the innate immune system[15-16] and contribute to the emergence of drug-resistant bacteria. The latter is further aggravated due to the lack of specificity in currently used antimicrobial agents.[17] Additionally, the concentrations of antimicrobial agents administered directly at the wound site are often insufficient to prevent infections[18] and remaining viable bacteria can still colonize the surface due to the lack of antifouling properties.

Each of these strategies exhibits its unique limitations, emphasizing the need to combine their most advantageous aspects to advance future antibacterial coatings. Consequently, advanced antimicrobial coatings should incorporate multiple antibacterial mechanisms designed to thwart both bacterial adhesion and the accumulation of bacterial debris. Simultaneously, they should provide an effective and secure mechanism for eradicating bacterial pathogens

without fostering the development of antimicrobial resistance. Herein, I present a new concept for an antimicrobial coating that synergistically combines bacterial repellent properties (antifouling) with a phage-inspired biorthogonal bactericidal strategy. We termed this approach the Kill&Repel surface coating strategy.

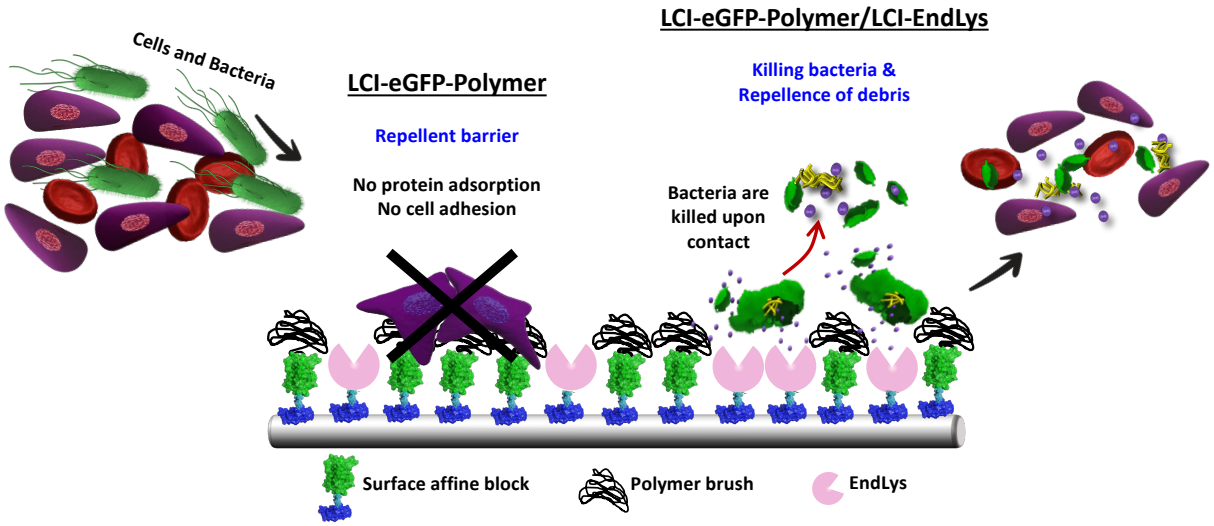

Figure 5.1. The Kill&Repel coating strategy: LCI-eGFP-Polymer hybrids prevent unwanted protein adsorption as well as fibroblast and bacterial adhesion, creating a strong barrier to bacterial colonization. However, in the event that bacteria should breach this initial barrier, the coating incorporates bactericidal enzymes, endolysins, which break down the peptidoglycan layer of the bacterial cell wall causing bacterial death. Simultaneously, the repellent properties avoid the build-up of bacterial debris on the surface, providing a self-cleaning mechanism for the active antimicrobial coating.

We leverage the versatility and modularity of our LCI-eGFP-Polymer hybrid coating strategy and introduce a bactericidal hybrid consisting of the same surface affine peptide genetically fused to a bacteriophage endolysin (LCI-EndLys). Endolysins are bacteriolytic enzymes that can cleave specific bonds within the peptidoglycan layer, causing the bacterial cell wall to rupture and ultimately cell death. This class of enzymes are becoming increasingly important in the fight against bacterial infections and antibiotic-resistant bacteria, as they offer a targeted and effective way to kill pathogenic bacteria without harming human cells.[19-21] Moreover, endolysins are less likely to induce antibiotic resistance in bacteria because they target essential bacterial structures that are difficult for the bacteria to mutate without compromising their own survival.[22]

The surface-oriented physisorption of both hybrids at the liquid-solid interface generates a densely packed, antifouling brush-like coating functionalized with endolysins (10-20 mol%). Thanks to the inherent modularity of our hybrid coating strategy, we could readily swap the LCI-EndLys hybrids in a plug-and-play fashion to target distinct bacterial strains, including Methicillin-resistant *Staphylococcus aureus* (MRSA). When applied to PCL wound dressings, our nanometer-thick coating effectively resolved an *in vitro* simulated wound infection. Notably, the surface of the coated wound dressings remained free from the accumulation of bacterial debris, ensuring prolonged accessibility and activity of the endolysin. In particular, our Kill&Repel coating strategy demonstrates that the synergistic combination of a strong repellent barrier with a biorthogonal bactericidal mechanism has the potential to provide long-lasting antibacterial activity coupled with excellent biocompatibility and safety.

5.2 Results and Discussion

5.2.1 Formation of the Kill&Repel Coating

For the formulation of our Kill&Repell coatings, we selected the endolysins PlyGBS94 as well as ClyF. We selected them because they are able to target *Streptococcus agalactiae* (*S. agalactiae*), *Staphylococcus epidermidis* (*S. epidermidis*), *Staphylococcus aureus* (*S. aureus*), *and Streptococcus pyogenes* (*S. pyogenes*), which are among the most relevant and dangerous bacterial pathogens in skin wounds. Accordingly, we synthesized the following bactericidal LCI-EndLys hybrids: LCI-PlyGBS94 and LCI-KR2-ClyF, respectively.

The Kill&Repel coating solutions were formulated by combining 80-90 mol% LCI-eGFP-Polymer with 10-20 mol% of LCI-EndLys hybrids. Importantly, the goal was to develop a coating formulation with just enough LCI-EndLys hybrids to achieve a high rate of bacterial killing without excessively impacting the antifouling properties of the coating. Moreover, our hypothesis was that since both hybrids have the same surface binding moiety governing the binding process, their adsorption kinetics should be similar. This would enable us to control the molecular ratio at the surface by adjusting the LCI-eGFP-Polymer:LCI-EndLys ratio in solution.

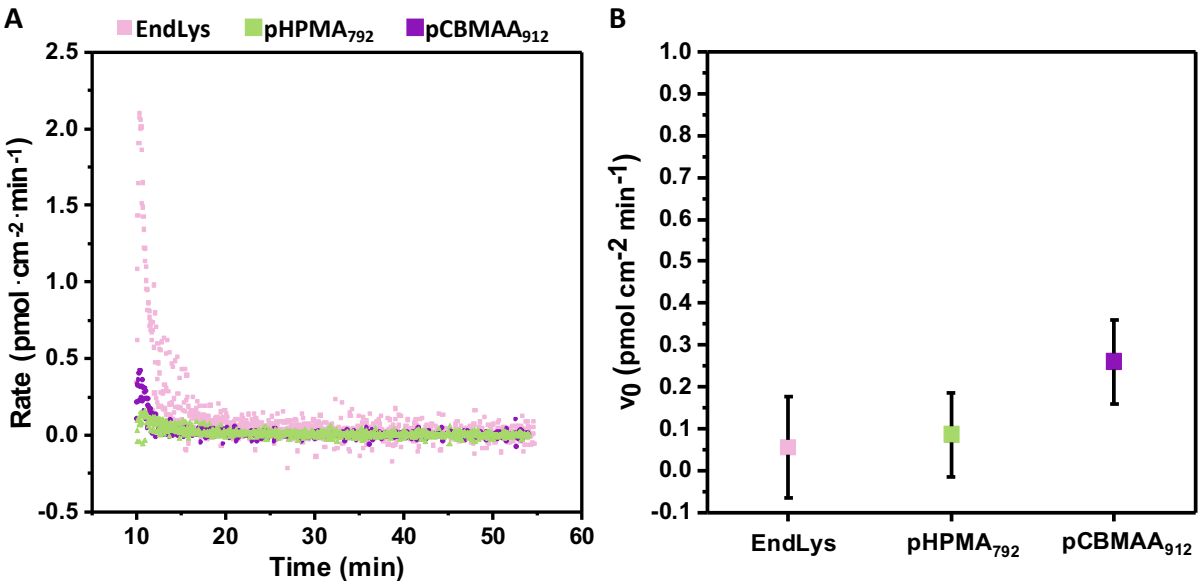

Figure 5.2. Comparison of the adsorption rates of LCI-EndLys (PlyGBS94), LCI-eGFP-pHPMA$_{792}$, and LCI-eGFP-pCBMA$_{912}$ measured by SPR spectroscopy, demonstrating that all hybrids exhibit

similar adsorption rates across the entire adsorption process. (B) Initial rate of hybrid adsorption, V_0, calculated by numerical differentiation of the binding curves and extrapolation to t=0.

Using SPR spectroscopy, we followed the binding kinetic in real time and confirmed that both the antifouling and bactericidal hybrids exhibited similar adsorption rates throughout the entire adsorption process, despite variations in their chemical composition and molecular weight (Figure 5.2 and Figure S5.1). This adsorption behavior ensures that the adsorption process is exclusively driven by the LCI or LCI-KR2 peptide in an oriented fashion. This is crucial not only to adjust the ratios of the different hybrid on the surface but also to guarantee that the endolysin is facing away from the surface, ensuring accessibility. Nevertheless, enzyme immobilization on non-polar surfaces remains a persistent challenge due to the risk of enzyme denaturation, which may lead to a significant reduction or complete loss of enzymatic activity. We assessed the lytic activity of the LCI-EndLys hybrids after their immobilization on PCL wound dressings. For that, we used a FRET-labeled synthetic peptide (γ-Glu-Lys-D-Ala-Ala-Ala-Lys) that mimics the amino acid sequence of the cross-bridges in group B streptococcal peptidoglycan.[23] The endolysin PlyGBS94 should exert high endopeptidase activity towards this specific sequence. Upon cleavage of the sequence between D-Ala↓-Ala by PlyGBS94, the distance between the FRET pair (Abz/Lys(Dnp)) increases significantly, activating the fluorophore Abz. Consequently, measuring the fluorescence signal allows the quantification of the endolysin's activity.

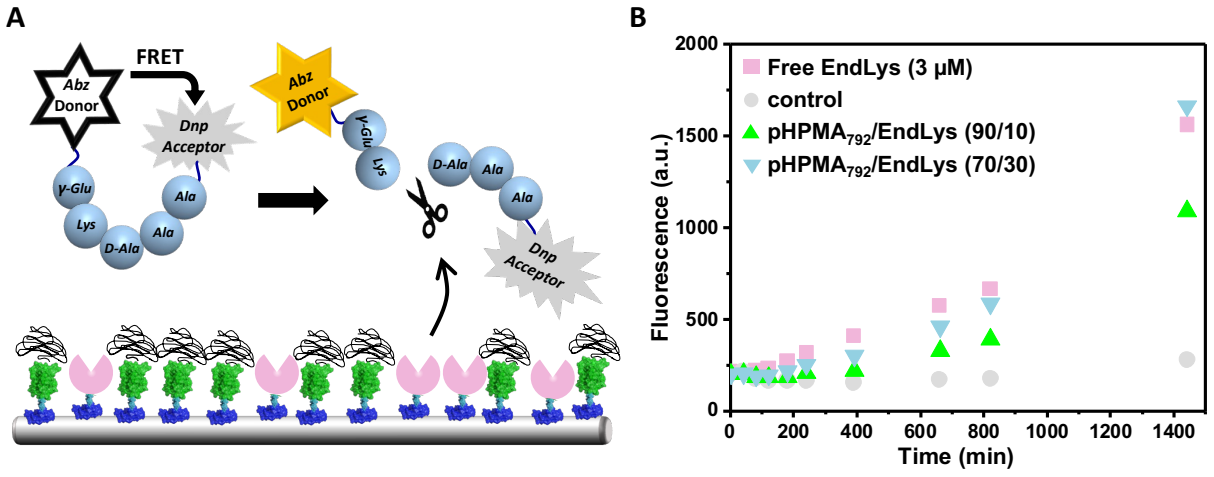

Figure 5.3. (A) Schematic representation of the cleavage of the Förster resonance energy transfer (FRET) peptide resulting in the activation of the Abz fluorophore. (B) Evaluation of the

enzymatic activity kinetics of both free and immobilized LCI-EndLys (PlyGBS94) by monitoring the rise in fluorescence intensity.

As evidenced by the continuous rise in fluorescence over time, the molecularly dissolved LCI-EndLys hybrid in PBS effectively cleaved the FRET peptide, confirming the enzymatic activity of EndLys (Figure 5.3B). Similarly, LCI-EndLys hybrids immobilized at 10 and 30 mol% in combination with LCI-eGFP-pHPMA$_{792}$ displayed enzymatic activity. Notably, the immobilized LCI-EndLys hybrids at 30 mol% exhibited enzymatic activity comparable to the molecularly dissolved LCI-Endlys (free EndLys), in spite of the substantially lower overall amount. For comparison, the hybrid solution used to coat these meshes had a total LCI-EndLys concentration of less than 2 μM, while the concentration of free EndLys reached a final concentration of 3 μM. These remarkable results indicate that the enzymatic activity of LCI-Endlys is not hindered upon immobilization; instead, LCI-Endlys displays enhanced activity when co-immobilized with LCI-eGFP-pHPMA hybrids. We propose that this boosting effect results from the close proximity to pHPMA which may induce favorable interactions, structural changes or improve the stability of the endolysin, enhancing its enzymatic performance. Such heightened enzymatic activity resulting from the combination with polymers has been reported previously for other enzymes.[24-26]

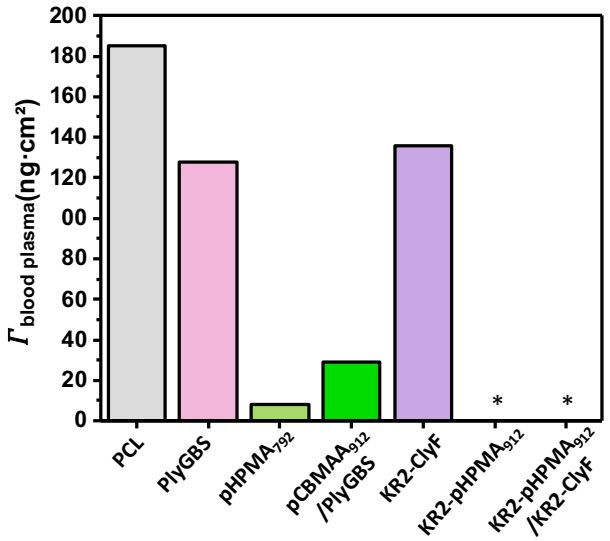

Figure 5.4. Evaluation of blood plasma fouling (10%) of the individual hybrids and the final Kill&Repel coatings.

Additionally, we assessed whether the combined use of antifouling hybrids with bactericidal hybrids in the Kill&Repel coating had a drastic effect on the coating's ability to reduce protein

adsorption, a crucial factor to prevent bacterial attachment and concomitant biofilm formation. As depicted in Figure 5.4, a coating composed solely of LCI-EndLys hybrids (LCI-PlyGBS94 and LCI-KR2-ClyF) displayed less fouling than bare PCL, which is presumably due to the hydrophilization of the surface. However, it only had a very limited capacity in preventing protein fouling from blood plasma (~73% fouling), which would result in the attachment of bacterial debris and blockage of the active bactericidal surface. However, when combined with the antifouling hybrids, even though in a diluted concentration (80-90%), the coating was able to significantly reduce protein fouling. In the case of hybrids based on the LCI-KR2 surface affine peptide, fouling from 10% BP could be entirely prevented, which is presumably due to the heightened binding strength of LCI-KR2 and the formation of a denser coating on PCL (Figure S5.3). Moreover, the repellent properties of the Kill&Repel coating extended to the mesoscopic scale, successfully resisting the nonspecific adhesion of fibroblasts cells (Figure S5.4).

5.2.2 Antimicrobial Activity Against *S. agalactiae*

S. agalactiae is a major pathogen known for causing sepsis and neonate meningitis.[27-29] Moreover, it is increasingly associated with severe subcutaneous and soft tissue infections as well as chronic wounds in the adult population to the extent of resulting in tissue necrosis and bacteremia.[28, 30-32] This, together with the mounting prevalence of multidrug-resistant strains poses a significant risk for public health, underscoring the imperative need for the development of effective treatment options.

We engineered a Kill&Repel coating design to effectively target *S. agalactiae.* This coating comprised 90 mol% LCI-eGFP-pHPMA and 10 mol% LCI-EndLys hybrids, where the LCI peptide was genetically fused to the endolysin PlyGBS94 (Kill&Repel$_{PlyGBS94}$)—a mutant lysin with enhanced killing activity, featuring solely the endopeptidase domain found in the N-terminal region of the wild-type PlyGBS94. To evaluate its efficacy against planktonic bacteria, we exposed the coated PCL dressings to a highly concentrated *S. agalactiae* solution (OD_{550} = 0.8). Within one hour, the Kill&Repel$_{PlyGBS94}$ coating successfully eliminated 92% of the bacteria. In comparison, molecularly dissolved LCI-PlyGBS94 (free PlyGBS94) at concentrations of 1 μM and 2 μM killed 41% and 52% of the bacteria cells, respectively. These findings corroborate the heightened activity of the Kill&Repel$_{PlyGBS94}$ coating, consistent with previous observation

of increased enzymatic activity. We hypothesize that this improved performance may result from a synergistic effect of potentiation through co-immobilization with pHPMA and multivalent actions. Namely, the immobilization of the endolysin results in a high interfacial concentration on the fiber surface, enabling numerous endolysin entities to simultaneously target the same region of an incoming bacterium, inflicting targeted damage to the peptidoglycan. This concerted action may produce a more lethal effect than the free enzyme, as illustrated in Figure 5.5.

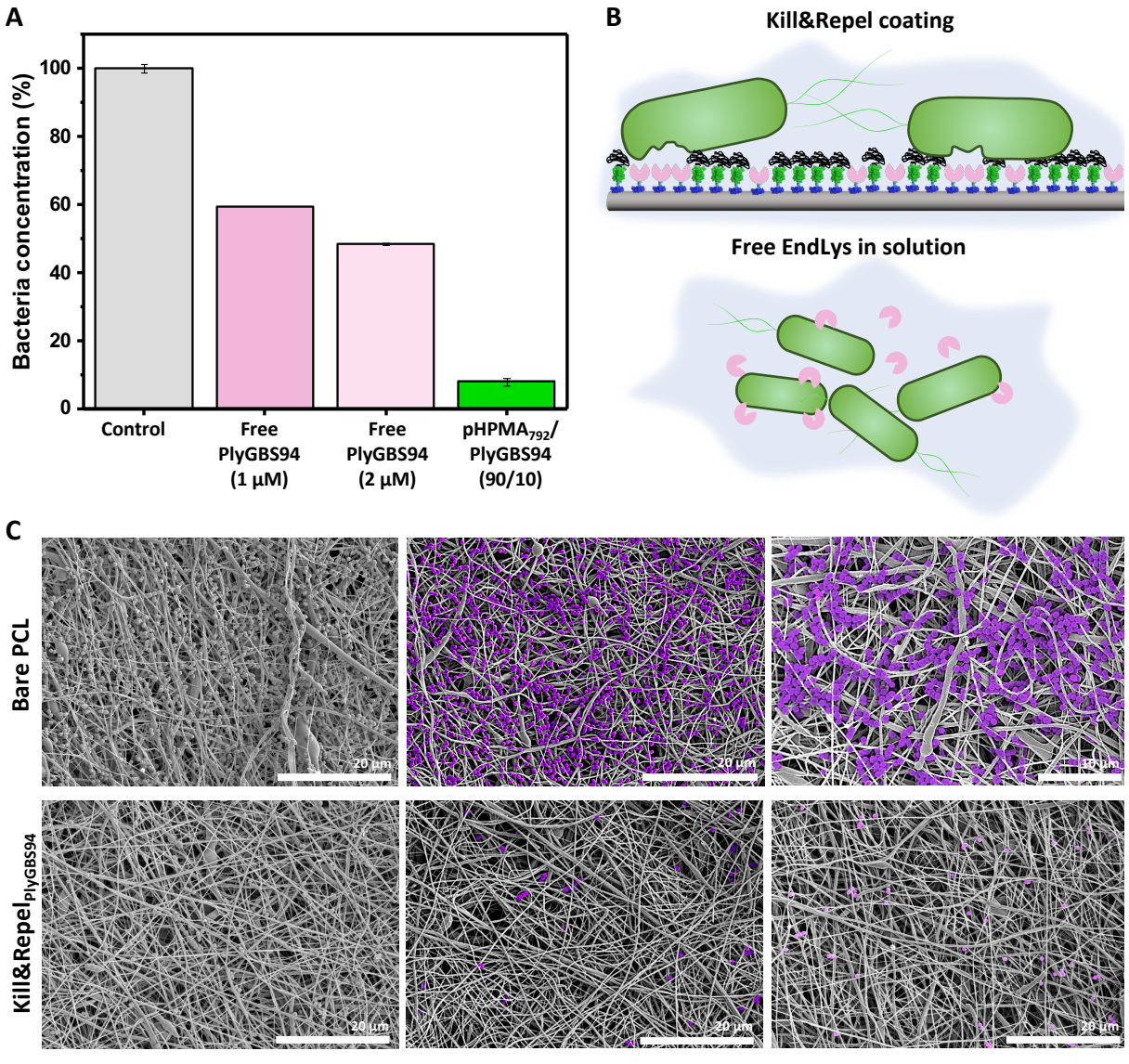

Figure 5.5. (A) Killing efficiency of the Kill&Repel$_{PlyGBS94}$ coating against *S. agalactiae*. The coating was able to eradicate bacteria more efficiently than the free enzyme. (B) Hypothesized killing mechanism rendering the Kill&Repel coating with heightened lytic activity compared to the free LCI-EndLys. (C) SEM images of the Kill&Repel$_{PlyGBS94}$ coated PCL fibers after exposure to a concentrated suspension *of S. agalactiae* (OD_{550} = 0.8).

Following exposure to bacteria, SEM analysis of the surfaces confirmed that the reduction of bacterial concentration was indeed caused by the antimicrobial action of the Kill&Repel$_{PlyGBS94}$ coating and not the adhesion of the bacteria to the PCL meshes, as the surface of these modified fibers exhibited only minimal adherence of bacteria cells (Figure 5.5C and Figure S5.5). Furthermore, we also evaluated the ability of our Kill&Repel$_{PlyGBS94}$ coating to eradicate simulated infections caused by *S. agalactiae.* For these experiments, we mimic a simplified wound infection *in vitro* by seeding bacteria onto agar plates and applying the Kill&Repel$_{PlyGBS94}$ wound dressings to the contaminated area (Figure 5.6A). Pristine PCL dressings were used as a control to assess the absence of bactericidal action.

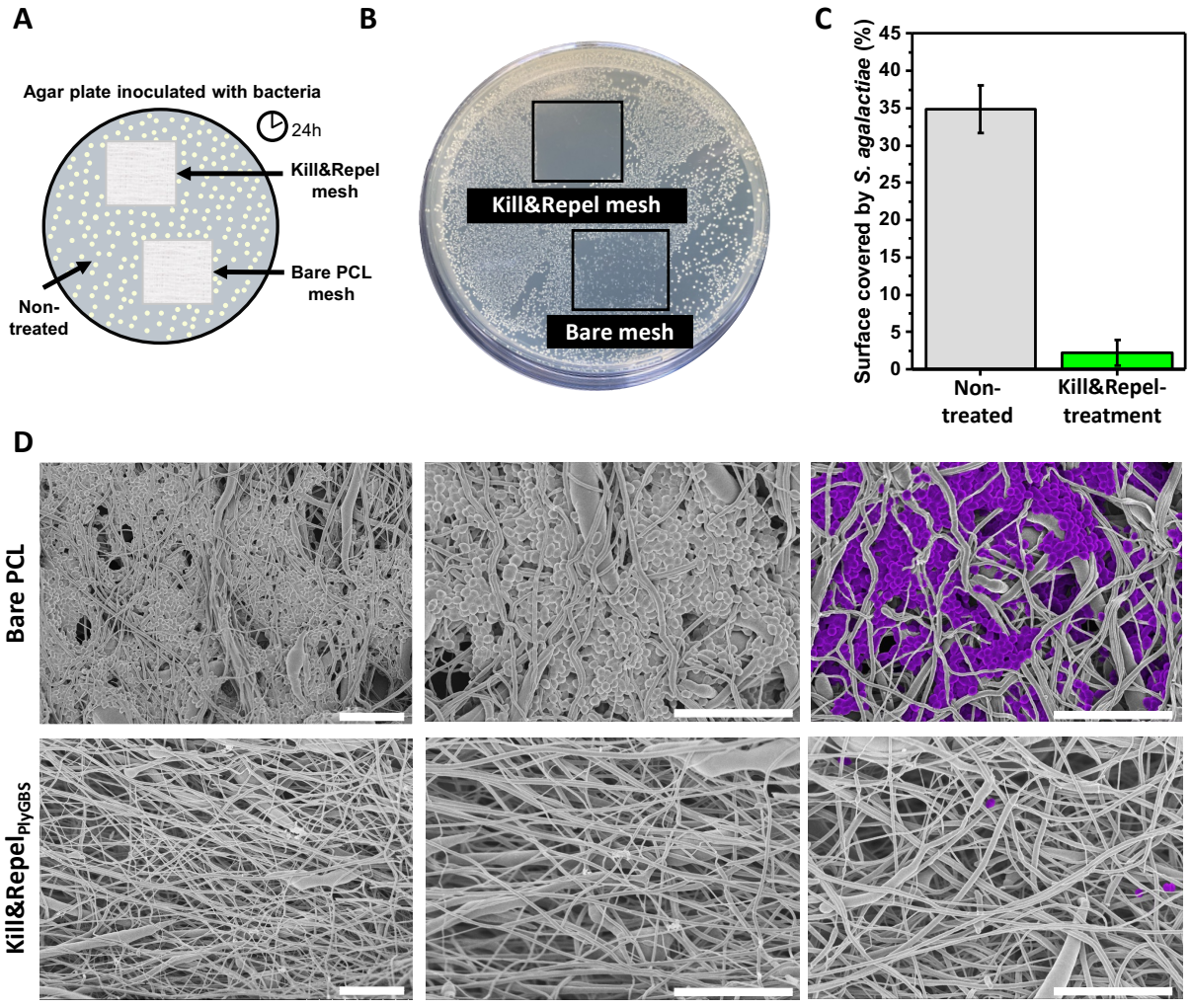

Figure 5.6. (A) Illustration of a simplified *in vitro* would infection on agar plates. (B) Exemplary agar plate after dressing removal showing complete clearance of bacterial contamination by the Kill&Repel coating. (C) Quantification of inhibition zones from images (D) SEM images of the dressings after removal from the agar plates. Scale bars are 10 μm.

After a 24 h incubation period, the wound dressings were carefully removed and a quantification of inhibition zones was conducted (Figure 5.6A and B). It is important to note that although we calculated a 48% bacteria clearance caused by the pristine PCL fibers (Figure S5.6), this is ascribed to the mechanical removal of bacterial colonies during the dressing removal process. This was confirmed by SEM surface analysis that showed significant bacterial colonization with cluster-like biofilm assembly. As evidenced in Figure 5.6B and Figure S5.7, the Kill&Repel$_{PlyGBS94}$ coating successfully eliminated bacteria from the treated area yielding an average clearance of 94%, calculated from the inhibition areas. Notably, the surface of these dressings remained clean from bacterial residues underscoring the synergetic potential of the Kill&Repel coating. While LCI-EndLys successfully kills bacteria, LCI-eGFP-Polymer hinders the accumulation of debris on the surface ensuring constant accessibility of the LCI-EndLys. Importantly, the inhibition zones were constrained to the area under direct contact to the dressing, suggesting no leakage of the coating components.

5.2.3 Antimicrobial Activity Against MRSA

MRSA is at the forefront of antimicrobial resistance and ranks among the deadliest pathogens worldwide.[33] Its resistance to various antibiotics, coupled with a strong biofilm-forming capability, makes it very difficult to treat, leading to high morbidity, substantial economic burden and heightened mortality rates.[34-35] In the last decade, lysins have emerged as promising therapeutic agents against the staphylococci genus. In particular the engineering of chimeric lysins has gained particular attention, as they possess improved bactericidal activity, a broader spectrum of function coupled with increased stability.[36-37] ClyF is a novel chimeric lysin that has demonstrated heightened antimicrobial activity against MRSA in mouse models of bacteremia and burn wound infection.[38]

We advanced our Kill&Repel coating system to mitigate and treat material-related infections caused by MRSA pathogens. To achieve this, we introduced the endolysin ClyF as the bactericidal agent. The advanced version of the Kill&Repel coating comprises 80 mol% LCI-KR2-eGFP-pHPMA hybrids combined with 20 mol% of LCI-KR2-ClyF hybrids (Kill&Repel$_{ClyF}$). We selected the combination of 20 mol% LCI-KR2-ClyF based on preliminary results that demonstrated superior activity compared to other combination ratios, while concurrently maintaining high antifouling properties (KR2-pHPMA$_{912}$/KR2-ClyF, Figure 5.4 and Figure S5.9).

Following the application of this coating to the surface of PCL would dressings, we assessed its ability to eradicate a clinical strain of MRSA (AB 1552009) and prevent biofilm formation, thereby inhibiting infection development.

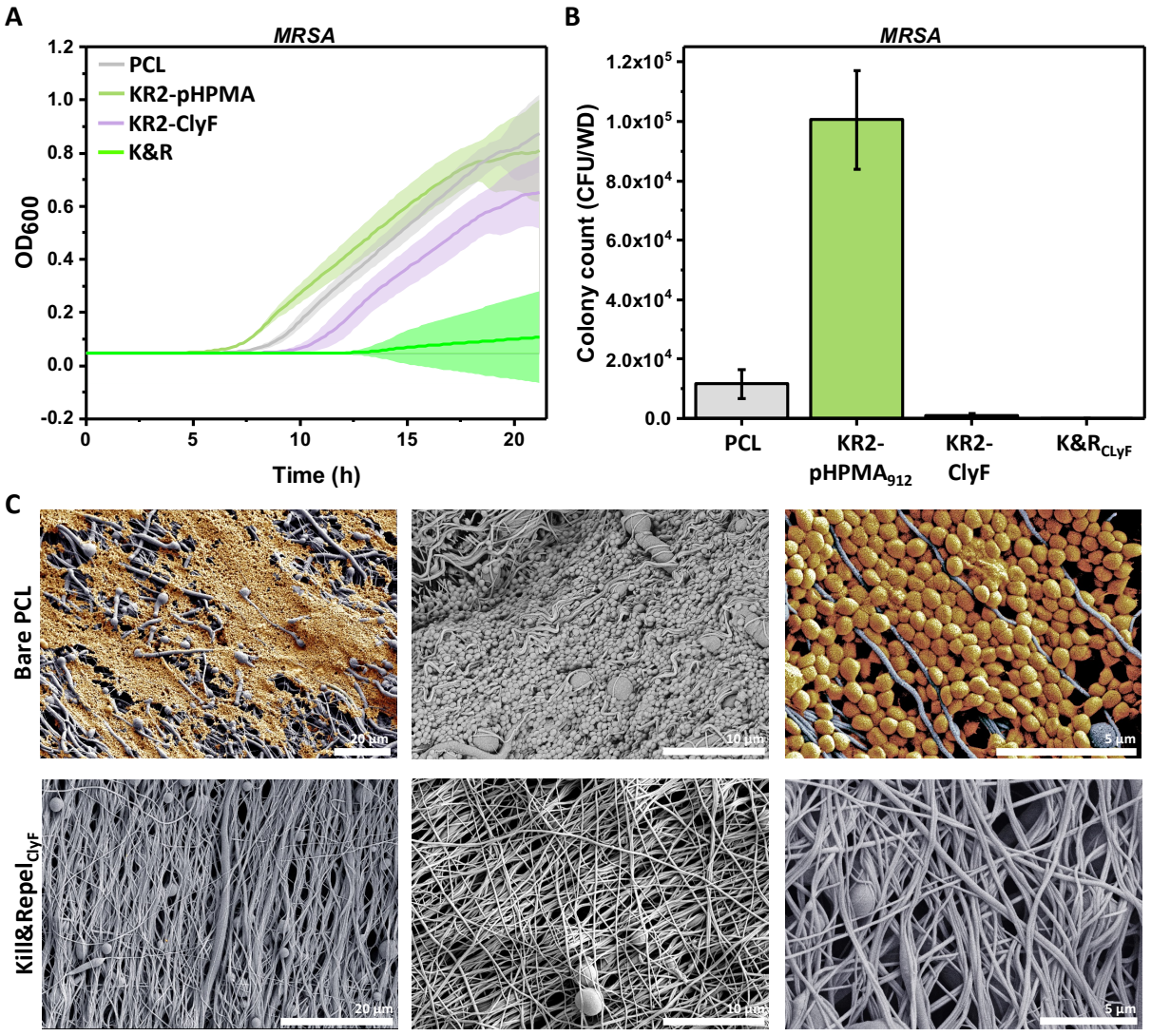

Figure 5.7. (A) Bacterial growth curves showing the antimicrobial activity of the Kill&Repell$_{ClyF}$ coating in comparison to bare PCL wound dressings, LCI-KR2-eGFP-pHPMA coating and LCI-KR2-ClyF coating (B) Colony count to asses log reduction. After 4 h of incubation time, bacteria were harvested com wound dressings and plated. This was followed by CFU count the next day. The Kill&Repell$_{ClyF}$ coating achieved 3.5 log reduction when compared to LCI-KR2-eGFP-pHPMA. (C) SEM images of Kill&Repel$_{ClyF}$ coated and bare wound dressings after antimicrobial activity tests and incubation with MRSA for 9 h.

These experiments involved seeding 10^5 bacteria cells directly onto the wound dressings, followed by static incubation at 25 °C for 4 h. After incubation, MRSA bacteria were carefully

washed off the dressings and further cultivated in solution and agar plates to monitor their concentration and the antimicrobial activity of the dressings after 4 h of direct exposure. Additionally, the dressings underwent further overnight incubation to observe for bacteria regrowth and colonization caused by remaining bacteria attached to the dressing surface. These experiments were conducted using human plasma-like medium (HPLM) with the addition of 10% human serum to simulate conditions closely to the real environment of wound dressings. As illustrated in Figure 5.7, both bare and antifouling (KR2-pHPMA$_{912}$) PCL wound dressings were unable to kill bacteria, resulting in a rapid growth of bacteria from both samples. Strikingly, a higher number of bacteria were recovered from the antifouling wound dressings (KR2-pHPMA) compared to the uncoated dressings (PCL). This can be traced back to the inherent hydrophobic nature of PCL enabling massive protein adsorption and thereby facilitating bacterial adhesion to its surface. Thus, the MRSA bacteria were able to adhere strongly to the PCL dressing already during the exposure period and could not be harvested This resulted in a false reduction in concentration, as seen in the colony count. However, we successfully collected all bacteria following contact with the antifouling dressings, highlighting the outstanding antifouling properties of our LCI-KR2-eGFP-pHPMA hybrid coating. Furthermore, it is noteworthy that after 4 h of direct exposure, our Kill&Repel$_{ClyF}$ coating proved more effective in killing MRSA compared to the pure bactericidal LCI-KR2-ClyF coating. This aligns with previous results, affirming the potentiated activity of our Kill&Repel$_{ClyF}$ coating. Notably, it achieved to eradicate 99.9% (3.5 log reduction) of MRSA. As evidenced by SEM images in Figure 5.7C, the coating not only inhibited bacteria regrowth but also maintained the surface of the coated wound dressings free from invaders and traces of bacterial debris.

5.2.4 Antimicrobial Activity Against S. pyogenes and S. epidermidis

S. epidermidis is the predominant pathogen associated with medical device infections.[39-41] The success of this nosocomial pathogen hinges primary on its remarkable inherent ability to form biofilm on the surfaces of these materials, often accompanied by the development of multidrug resistance.[40, 42] *S. pyogenes* is another aggressive pathogen known for being one of the major bacterial causes of human skin infections. It is sometimes referred to as “flesh-eating bacteria” due to its tissue-destructive nature, capable of causing life-threatening conditions like necrotizing fasciitis.[43] Together with *S. agalactiae*, it is regarded as one of the

most clinically important streptococcal species in humans. Both *S. epidermidis* and *S. pyogenes* pose substantial public health risks, therefore proactive targeting of these pathogens is essential, not only for immediate health concerns but also in the broader context of antibiotic stewardship.

The advanced Kill&Repel$_{ClyF}$ coating demonstrated remarkable antimicrobial efficacy against both of these pathogens, reducing *S. pyogenes* colonization to 0.3% (2.5 log reduction) and achieving complete eradication of *S. epidermidis* (>4 log reduction) within 4 h of contact (Figure 5.8A and B).

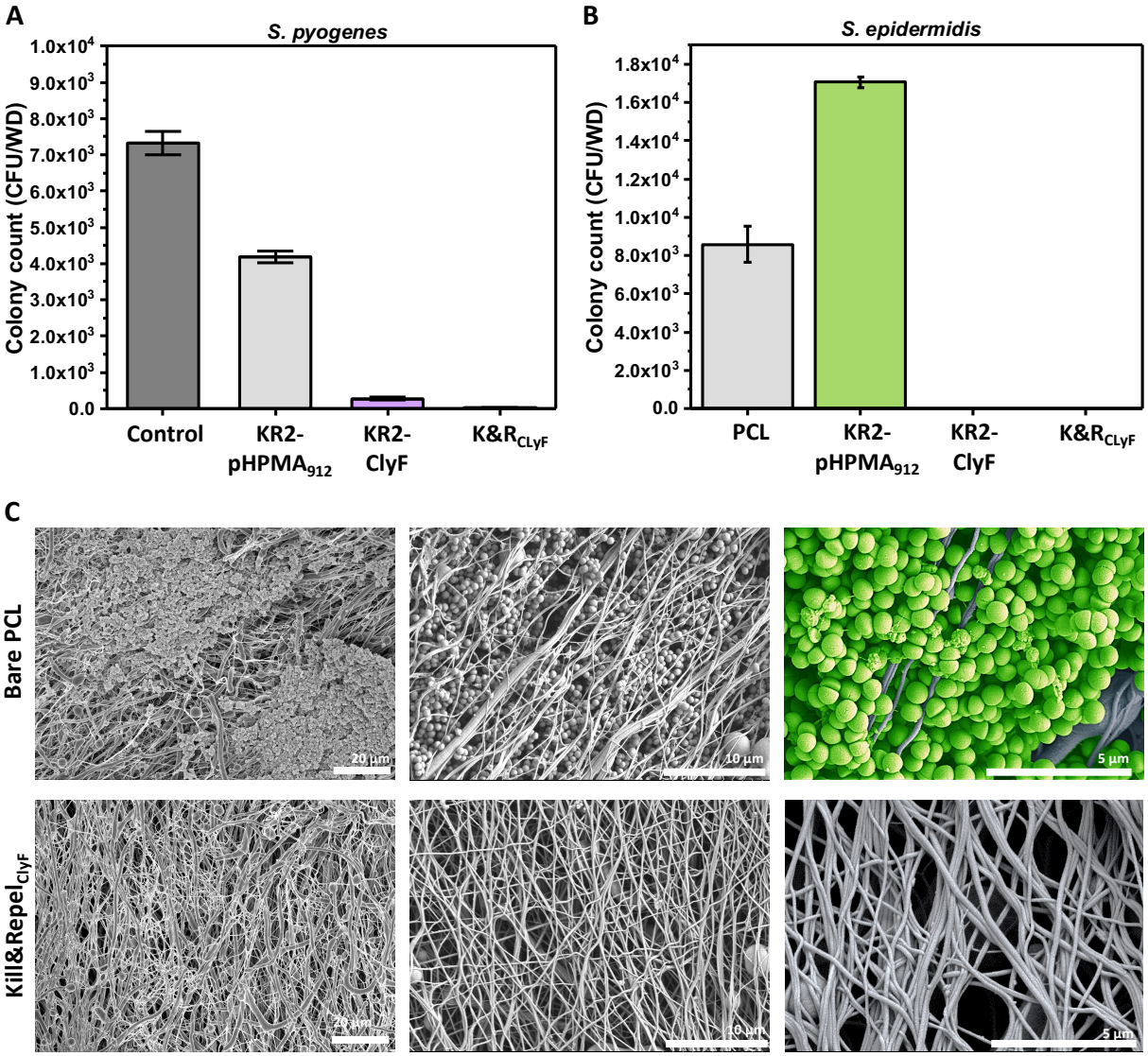

Figure 5.8. Colony count to asses log reduction. Kill&Repel$_{ClyF}$ coating achieved (A) 2.5 log reduction of *S. pyogenes* invaders and (B) complete eradication of *S. epidermidis* pathogens.

(C) SEM images of Kill&Repel$_{ClyF}$ coated and bare wound dressings after antimicrobial activity tests and incubation with *S. epidermidis* for 9-10 h.

Once again, the Kill&Repel$_{ClyF}$ coating exhibited heightened activity compared to the coating consisting or pure bactericidal hybrids (LCI-KR2-ClyF). Moreover, the regrowth of bacteria was also effectively deterred and the surface of the coated wound dressings remained clean from any pathogenic invaders and bacterial residues. On the contrary uncoated wound dressings enabled bacterial adhesion, colonization and biofilm formation (Figure 5.8C), highlighting the critical need to develop surface coatings for medical devices that prevent microbial adhesion, thereby mitigating the risk of infection. Furthermore, it is also crucial to minimize the survival of microorganisms on the surface to effectively prevent their potential transmission and dissemination to the blood stream and other neighboring tissues.

5.2.5 Safety of the Kill&Repel Coating Technology

We investigated the biocompatibility of the Kill&Repel coating by exploring potential irritant or cytotoxic effects using isolated connective tissue fibroblasts and advanced *in vitro* skin models. As a first step, we examined whether any component of the Kill&Repel coatings could potentially induce fibroblast cell death. For these experiments, semiconfluent layers of HDF were exposed to PCL wound dressings modified with antifouling hybrids (100% of LCI-eGFP-Polymer) or bactericidal hybrids (100% of LCI-EndLys). After an incubation period of 24 h, the dressings were carefully removed and the cell monolayers were assessed by the metabolic MTS assay and live/dead staining. The viability of fibroblast cells, assessed through the MTS assay, was not affected by any of the coating components as indicated by viability proportions exceeding 80% for all coatings. Furthermore, live/dead staining confirms the presence of almost exclusively viable cells (green-labelled) with typical spindle-shaped fibroblast morphology. This excellent fibroblast cytocompatibility was observed with both the LCI-KR2-ClyF and LCI-PlyGBS94 endolysin constructs (Figure 5.9. and Figure S5.10).

Thus far, our comprehensive investigation, employing 2D cell monolayers, has unequivocally demonstrated the non-toxic nature of both our antifouling and Kill&Repel coatings to eukaryotic cells (*vide supra*; Chapter 4). While these tests have provided valuable insights into the biological impact of our molecules, it is crucial to note that 2D cell monolayers lack the structural complexity and intricate cellular interactions characteristic of native tissue, thereby

constraining their physiological relevance. Consequently, the translatability of these results to the 3D *in vivo* microenvironment is not always guaranteed. Therefore, we validated the safety of our Kill&Repel coating using advanced 3D models capable of mimicking *in vivo* skin properties, including a multilayered stratum corneum. We utilized the *in vitro* 3D skin model test, EpiDerm™ Skin Irritation Test, which was design for assessing irritation potential in accordance with the EU and GHS classification system. Notably, this testing model has obtained regulatory approval as a viable alternative to equivalent animal models by the EU Reference Laboratory for alternatives to animal testing (EURL ECVAM strategy).

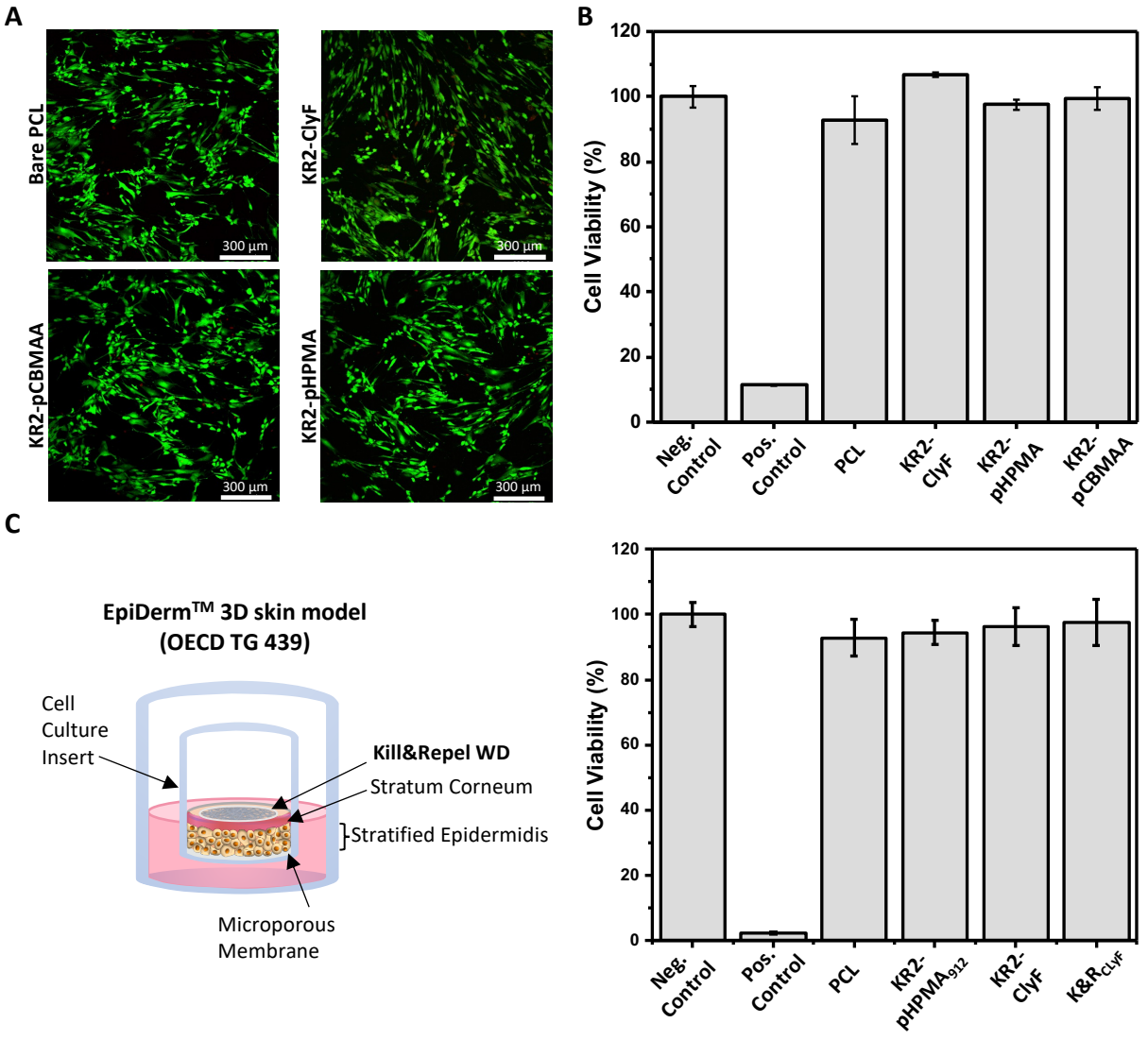

Figure 5.9. (A) Live/dead staining images of fibroblasts after 24 h of direct contact with both coated and bare PCL dressings. (B) Assessment of fibroblast viability using the MTS assay after 24 h of direct contact. Non-treated cells served as the negative control, while latex was used as the positive control. (C) Skin irritation test using the OECD validated EpiDerm™ Skin

Irritation Test. The results indicated that cell viability remained above 90% for all samples, confirming the non-irritative and non-cytotoxic effect of the Kill&Repel coating.

The EpiDerm™ 3D skin model closely replicates the biochemical and physiological properties of the upper layers of human skin. It encompasses proliferative basal cells, the spinous and granular layers and the cornified epidermal layer that are both mitotically and metabolically active (stratified epidermidis).[44] We applied both bare and coated PCL wound dressings to the skin models (stratum corneum) at the liquid-air interface and followed the OECD (Organization for Economic Co-operation and Development) testing method guideline No. 439[45]. Cell viability was then measured as a parameter of toxicity and irritation. As shown in Figure 5.9., cell viability was measures to be above 90% for all samples. This means that none of our coatings exhibited irritant or toxic effects on the skin model, affirming previous observations and underscoring the safety of our Kill&Repel coating strategy as antimicrobial treatment alternative.

Additionally, in collaboration with the research group of Prof. Dr. med Baron at the University Hospital RWTH Aachen, we used 3D full-thickness skin models developed by them, which not only mimic the epidermis but also integrate a fibroblast-collagen matrix layer equivalent to the dermal strata.[46] These full-thickness skin models were treated topically with Kill&Repel PCL wound dressings for three and five days (Figure 5.10). Bare PCL dressings were used as reference control, since PCL is highly biocompatible and non-toxic. Histological analysis with hematoxylin and eosin (HE) staining revealed undamaged models with a well-stratified epidermis arranged in four typical layers: the cornified layer, the granular layer, the spinous layer and basal layer (Figure 5.10A). Moreover, the formation of the basement membrane separating the epidermis from the dermis can be visualize. Notably, the models treated with our Kill&Repel coating displayed a more organized and differentiated epidermis. Furthermore, immunofluorescence staining of the Ki67 protein, a proliferation marker, revealed cells with intact proliferative activity, indicating the unaffected viability of the epidermal layer after treatment with our Kill&Repel coating.

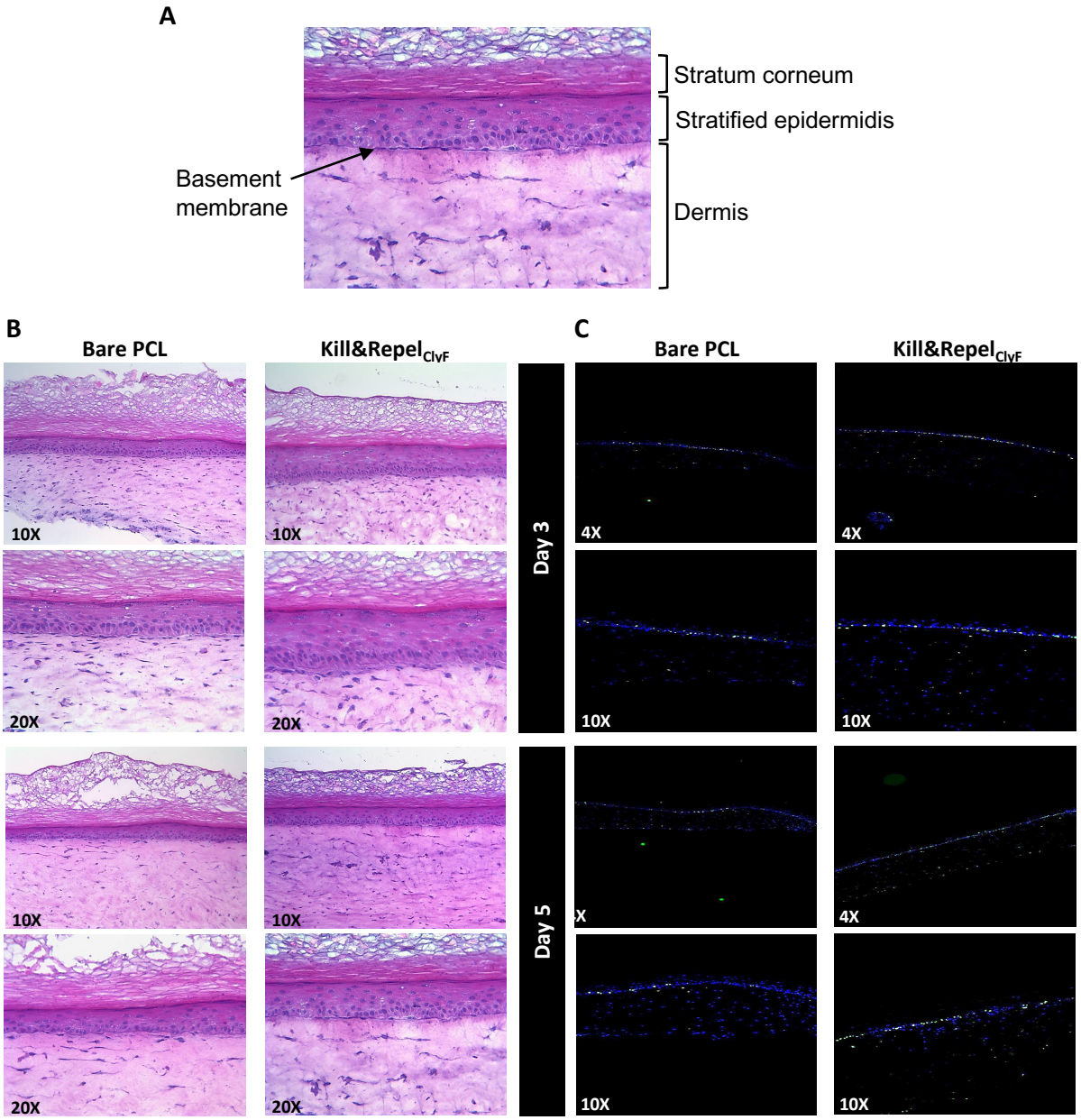

Figure 5.10 (A) HE staining of a 3D full-thickness skin model after exposure for 5 days with Kill&Repel coated PCL wound dressings. Model exerts a well-stratified epidermis. (B) HE staining and (C) Ki67 staining (green) of full-thickness skin models after direct exposure for 3 and 5 days to Kill&Repel coated wound dressings and non-coated dressings as reference. Cells were counterstained with DAPI (blue).

5.2.6 Compatibility with Lyophilization Procedure

In addition, the bactericidal hybrids can be lyophilized into a sterile powder. This powder can be then readily reconstituted in an aqueous solution while retaining its antimicrobial activity (Figure S5.11), streamlining the storage and formulation process of the Kill&Repel coating.

Coupled with its high antimicrobial efficacy and excellent biocompatibility, the Kill&Repel coating strategy emerges as a promising approach for the modification of various medical devices and implants in clinical applications.

5.3 Conclusion

In this chapter, I presented a novel antimicrobial coating termed as the Kill&Repel strategy, which seamlessly integrates antifouling properties with a biorthogonal bactericidal activity. This coating is based on peptide-polymer and peptide-endolysin hybrids, adhering to the surface through the protein moiety and facilitating the functionalization of a diverse range of materials. The Kill&Repel coating harnesses the potent bactericidal activity of bacteriophages, employing the enzyme endolysin to kill bacteria in an efficient, specific and safe manner. By targeting specific regions of the peptidoglycan layer, endolysins may enable targeted antimicrobial activity against specific bacterial strains while sparing non-targeted bacteria, thereby minimizing the risk of disrupting the natural microbiota. This mode of action is particularly valuable in combating antibiotic-resistant strains, with a lower likelihood of bacteria developing further resistance.

The co-immobilization of the endolysins with pHPMA and pCBMAA has a synergistic impact on the endolysin leading to increased enzymatic activity and superior bacteria-killing efficacy when compared to molecularly dissolved endolysins and pure bactericidal dressings (100% endolysin). We hypothesize that a) the close proximity of pHPMA or pCBMAA favorably alters the structure of the endolysin, boosting the activity of the enzyme, b) the high density of immobilized endolysins on the surface may localize the hydrolysis of the bacterial peptidoglycan layer in direct attachment to the surface, heightening bactericidal action and c) the combination with antifouling properties prevents the adhesion of bacterial debris to the surface, thus avoiding the obstruction of endolysin and ensuring sustained antimicrobial activity in the long term. By exchanging the endolysin, we engineered different Kill&Repel coatings that were effective against *S. agalactiae*, *S. epidermidis*, *S. pyogenes* and MRSA. We confirmed using SEM that the surfaces of the coated dressings remained free from bacteria and debris adhesion after antimicrobial activity. Furthermore, the Kill&Repel coating exhibited excellent biocompatibility, with skin cells and tissue viability above 90%.

The Kill&Repel strategy represents a significant advancement in antimicrobial coatings, offering a multifaceted approach that combines efficacy, specificity, and a reduced risk of resistance development, positioning it as a promising solution in the field of antimicrobial technologies. Being able to target antibiotic-resistant bacteria not only addresses immediate

health risks but also contributes to the overall efforts in antibiotic stewardship, combating the antibiotic resistance crisis and contributing to broader public health efforts.

.

5.4 Materials and Methods

5.4.1 Materials

All reagents were of analytical grade and used as received unless otherwise stated. Copper (II) bromide ($CuBr_2$, 99%), ethanol (EtOH, >99.8%), acetone (>99.5%), PBS tablets, bovine serum albumin, citrated Blood plasma, and Poly(ε-caprolactone) (M_n 45,000 g·mol^{-1}) were purchased from Sigma Aldrich Chemie GmbH. Deuterated solvents (99.9%) were purchased from Deuterio GmbH. Dimethyl sulfoxide (DMSO, >99.9%) was obtained from VWR International GmbH. Tris(2-dimethylaminoethyl)amine (Me_6TREN, 99$^+$%) and human plasma-like medium were obtained from ThermoFisher GmbH. Human pooled serum was purchased from MP Biomedicals GmbH. CBMAA and HPMA were synthesized according to literature procedures.[47-48] The maleimide initiator, 2-(2,5-dioxo-2,5-dihydro-1H-pyrrol-1-yl) ethyl 2-bromo-2-methylpropanoate, was synthesized according to literature.[49] MTT assay was purchased from Promega GmbH. Water used in the experiments was provided by a Millipore Milli-Q system. Gold coated SPR sensor slides were purchased from Cenibra GmbH.

Cells and biochemicals. E. coli BL21 Gold (DE3) was used as protein expression system and purchased from Agilent Technologies Inc., Santa Clara, United States. *S. agalactiae* DSM-2134, *S. epidermidis* DSM-1798 and *S. pyogenes* DSM-11728 were obtained from the Leibniz Institute DSMZ-German Collection of Microorganisms and Cell Cultures GmbH, Braunschweig, Germany. MRSA DWI M011 is a clinical strain provided by the University Hospital RWTH Aachen. *S. agalactiae* O90R (ATCC12386) was kindly provided by Prof. Spellerberg, Dept. Med. Microbiology & Hygiene, and University of Ulm, Germany. HDF were purchased from PromoCell GmbH. The EpiDerm™ Skin Irritation Test Kit was purchased from MatTek Life Sciences. HDF and human epidermal keratinocytes (HEK) for 3D full-thickness wound models were isolated from foreskin and biopsies of adult skin obtained from healthy volunteers after cutaneous surgery. DAPI was purchased from Applichem, Darmstadt, Germany. LIVE/DEAD staining kit was purchased from ThermoFisher Scientific, Waltham, United States. Ki67 antibody and antibody diluent were provided by Dako, Glostrup, Denmark. Antibody Alexa Fluor 488 IgG H + L was received from Molecular Probes, Eugene, OR. Collagen I solution was purchased from Vitrogen; Cohesion Technologies, Palo Alto, CA.

5.4.2 Synthetic and Fabrication methods

The production and purification of LCI-eGFP and LCI-KR2-eGFP, synthesis of LCI-eGFP-Polymer and LCI-KR2-eGFP-Polymer hybrids, electrospinning of PCL wound dressings as well as the preparation of a thin layer of PCL on gold-coated SPR sensor chips were carried out as previously described in Chapter 4.

Production and purification of LCI-PlyGBS94: The amplification of 3xGGGGS-LCI was achieved through Polymerase Chain Reaction, and it was subsequently fused to the C-terminus of StrepII-PlyGBS94 using the NEBuilder® HiFi DNA Assembly Kit (New England Biolabs). For overexpression, the resulting plasmid was transformed into chemically competent *E. coli* BL21 (DE3) Gold cells. Successful fusion of LCI and the PlyGBS94 endolysin was confirmed by Sanger sequencing (Eurofins Genomics). 5 mL of LB were inoculated with *E. coli* BL21 (DE3) Gold cells and incubated at 37 °C for 16 h. The working culture (400 mL) was prepared by diluting the inoculum in terrific broth to an optical density of OD_{600} = 0.05 and cultivated for an additional 3 h at 37 °C with aeration at 180 RPM until reaching OD_{600} of 0.6. Protein overexpression was induced by supplementing isopropyl β-D-1-thiogalactopyranoside (0.1 mM final concentration) at 20 °C. After 20 h, cells were harvested by centrifugation at 11,200 g for 30 min and 4 °C. Cell pellets were suspended in Strep-tag II wash buffer and disrupted by sonication on ice (3 min, interval 10 s, 70% amplitude). Soluble proteins were collected after centrifugation at 3,200 g for 45 min at 4 °C. The protein solution was filtered through a 0.45 µm cellulose-acetate filter (Cytiva) and purified using gravity flow chromatography with a prepacked affinity chromatography column (StrepTrap HP, 5 mL, Cytiva). Samples were dialyzed two times against PBS (pH 7.4) using a dialysis tube with a pore size of 3.5 kDa. Protein concentration was determined with the BCA protein assay kit (Novagen, Merck KGaA) and protein homogeneity was analyzed by sodium dodecyl sulfate polyacrylamide gel electrophoresis (SDS-PAGE) using a Tris-Glycine gel (4-20%; NuSep Inc.).

Production and purification of LCI-KR2-*ClyF.* 17x-LCI-KR2 was amplified by Polymerase Chain Reaction and subsequently fused to the C-terminus of 6xHis-ClyF using the NEBuilder® HiFi DNA Assembly Kit (New England Biolabs). For overexpression, the plasmid was then transformed into chemically competent E. coli BL21 (DE3) Gold cells and successful fusion of LCI-KR2 and the ClyF endolysin was confirmed by Sanger sequencing (Eurofins Genomics). 5 mL LB were inoculated with *E. coli* BL21 (DE3) Gold cells at 37 °C for 16 h. The working culture

(800 mL) was prepared by diluting the inoculum in terrific broth to an optical density (OD_{600}) of 0.05 and cultivated for an additional 3 h at 37 °C with aeration at 180 RPM until reaching OD_{600} of 0.6. Protein over-expression was induced by supplementing isopropyl β-D-1-thiogalactopyranoside (0.1 mM final concentration) at 20 °C. After 20 h, cells were harvested by centrifugation at 11,200 g for 30 min and 4 °C. Cell pellets were suspended in 6xHistag wash buffer and disrupted by sonication on ice (3 min, interval 10 s, 70% amplitude). Soluble proteins were collected after centrifugation (x2) at 3,200 g for 20 min (4 °C). The protein solution was filtered through a 0.45 μm cellulose-acetate filter (Cytiva) and purified using gravity-flow chromatography with a prepacked affinity chromatography column (HisTrap HP, 5 mL, Cytiva). Buffer was exchanged against PBS (pH 7.4) using gravity-flow chromatography with a size exclusion column (Sephadex G25 Medium; 125 ml column volume). Protein concentration was determined with the BCA protein assay kit (Novagen, Merck KGaA) and protein homogeneity was analyzed by sodium dodecyl sulfate polyacrylamide gel electrophoresis (SDS-PAGE) using a Tris-Glycine gel (4–20%; NuSep Inc.).

Formation of the Kill&Repel coatings on substrates: Coating solutions were prepared by mixing peptide-polymer hybrid with protein-endolysin hybrids in PBS at different ratios. The final hybrid concentration was adjusted to 27 μM. After 45-60 min of incubation, the meshes were washed with copious amounts of PBS (3 x 5 min). For cell experiments, UV disinfection (254 nm) for 1 h was employed to sterilize all substrates. The coating solution was sterilized by filtration using 0.2 μm cellulose acetate syringe filters (x2). Subsequently, all meshes were washed five times with PBS (5 min each) before use.

5.4.3 Analytical Methods

Nuclear magnetic resonance. ^{1}H- NMR spectra were obtained on a Bruker Avance III 400 spectrometer at 400 MHz. Monomer conversion was determined directly from the crude polymerization solution after the addition of D2O.

Assessment of blood plasma fouling. The amount of blood plasma (BP) protein fouling was assessed by SPR on the MP-SPR NaviTM 210A VASA (BioNavis, Tampere, Finland) with a two-channel microfluidic system enabling measurement at 670 nm as well as 785 nm. The system was used with the SPR-Navi Control software (Version 4.2.5.2). Briefly, a freshly prepared full human BP solution in PBS was injected over the coated SPR sensor at 10 μL·min^{-1} for 60 min.

Subsequently, the surface was flushed with PBS buffer to removed unbound proteins. The data were analyzed with the SPR-Navi Data Viewer (Version 4.3.5.2). Adsorbed protein mass was determined from ΔμRIU before and after injection by multiplication with a conversion factor of 0.0794 ng·cm^{-2} per μRIU for 670 nm.

Enzymatic activity of LCI-PlyGBS94. To assess the enzymatic activity, both free LCI-PlyGBS94 and co-immobilized with LCI-eGFP-pHPMA at ratios of 10:90 and 30:70 mol% were examined. The analysis involved monitoring the increase in fluorescence intensity resulting from the digestion of the pentapeptide (γ-Glu-Lys-D-Ala-Ala-Ala) conjugated to the FRET pair (Abz/Lys(Dnp)). All the samples including bare PCL mesh, PCL meshes coated with LCI-eGFP-pHPMA$_{792}$/LCI-PlyGBS94 at 90:10 and 70:30 mol% ratios, were placed in a 24-well plate. Additionally, molecularly dissolved LCI-PlyGBS94 at a concentration of 3 μM was additionally tested to compare its activity to the co-immobilized one. Tris buffer (50 mM) and 3 μL of pentapeptide (3.2 μM) were added to equal a volume of 500 μL in each well. Incubation was carried out for specified durations at 37 °C. After each incubation period, 100 μL of the solution from each well was transferred to a black 96-well plate and the fluorescence signal was recorded using a Tecan microplate reader (Infinite® M1000 PRO, Tecan, λ_{ex}=325nm, λ_{em}=420nm). The solutions were then returned to the original well plate and left for further incubation. Experiment was conducted in triplicates.

Bactericidal activity against planktonic S. Agalactiae. To initiate bacterial growth, 20 mL of Todd Hewitt broth (THB) was inoculated with a single colony of *S. agalactiae* 090R and statically incubated for 17 h at 30 °C. A 1:100 dilution was prepared and grown statically at 37 °C until reaching an optical density of OD_{550} = 0.4. The experiment was carried out in a 50 mM ammonium acetate buffer containing 10 mM calcium chloride and 1 mM DTT (lysine buffer, pH 6.2). Cells were washed by centrifugation (2x PBS, 1x lysin buffer, 10 min each time) and resuspended in lysin buffer to an optical density OD_{550} of 0.8. For testing the free endolysin, 2 mL Eppendorf tubes were filled with 500 μL of cell suspension (OD_{550} = 0.8) and 500 μl LCI-PlyGBS94 at concentrations of 1 and 2 μM in lysin buffer or 500 μl lysin buffer as control. The Kill&Repel meshes were tested by placing a mesh (3 cm x 2 cm) inside a 2 mL Eppendorf tube and covering it with 750 μL cell suspension (OD_{550} = 0.8) and 750 μL lysin buffer. Samples were incubated for 1 h at 37 °C on a 3D shaker. 900 μL of each sample were

taken and the reduction of optical density (OD_{600}) was measured. Meshes were then analyzed for bacterial adhesion.

Bactericidal activity against sessile S. agalactiae. 20 mL of THB was inoculated with a single colony of *S. agalactiae* DSM-2134 and statically incubated for 17 h at 30 °C. A 1:100 dilution was grown at 37 °C until reaching an optical density of OD_{550} = 0.4. Cells were harvested by centrifugation for 10 min and suspended in THB to OD_{550} = 0.8. A 150 µL aliquot was taken and seeded onto THY agar plates (Todd-Hewitt broth supplemented with 1% yeast extract and 0.5% agar). Pristine and meshes modified with the Kill&Repel coating (2 cm x 2 cm) were carefully placed on top of the seeded agar plates and incubated for 24 h at 37 °C. The efficacy of the coating to clear sessile bacteria colonization was evaluated by the presence of inhibition zones on the contact area. Surface coverage quantification was conducted using ImageJ. Meshes were then analyzed for bacterial adhesion by SEM.

Expose assay. A bacterial preculture was prepared by inoculating a single colony of bacteria in TSY and cultivating it overnight at 37 °C with agitation at 150 rpm. A 1:10000 dilution was then grown at 37 °C and 150 rpm for 6 h. The working bacterial solution was adjusted to an optical density of OD_{600} = 0.25 in human plasma-like medium. Subsequently, the samples are contaminated with 50 µL of the bacterial suspension solution and allowed to incubate for 4 h under ambient conditions. Following the incubation period, the substrates are washed with 2 mL of Mueller Hinton Broth for 20 min at 37 °C and 150 rpm. For monitoring the subsequent bacterial growth based on optical density, 200 µL of the washing solution are transferred to a 96-well plate (in triplicates) and optical density (OD_{600}) is measured for the next 24 h (37 °C with shaking every 10 min). Furthermore, plating is performed to determine CFU of bacteria culture before and after exposure to the pristine or coated substrates, allowing for the analysis of the antimicrobial activity of the Kill&Repel coatings. Wound dressings are then further incubated overnight and fixed using 3% Glutaraldehyde in PBS. Analysis of the substrates surfaces follows using SEM.

Scanning electron microscopy. Images were acquired using the HITACHI-S-3000N and HITACHI-S-4800 (Hitachi High-Technologies, Tokyo, Japan). Before analysis, the samples were sputtered with an 8-10 nm thick conductive layer of Au/Pd.

Adhesion assay of HDF. Bare and modified substrates were incubated overnight in PBS at 37 °C prior to cell adhesion experiments. Cells were cultured until passage 6 in DMEM supplemented with 10% FBS and harvested by trypsinization. PBS was removed and 200,000 fibroblasts in DMEM were seeded onto each substrate (300 µL DMEM). Samples were incubated for 24 h at 37 °C in a humidified atmosphere containing 5% CO_2. Samples were washed twice with DMEM and then cells were fixed with 4% PFA in PBS (pH 7.4) for 15 min at ambient conditions. Cells were washed three times with cold PBS and permeabilized by incubation 0.1% Triton X-100 for 5 mins. Cells were then carefully washed with PBS (3 x 5min) and blocking step proceeded for 30 min with 1% BSA in PBS. Immunostaining was performed using Vinculin Monoclonal Antibody (7F9), eFluor 570 (10 µg·mL^{-1}), Alexa Fluor™ Plus 647 Phalloidin (1 µM) and DAPI (0.1 mg·mL^{-1}). Microscopic evaluation was performed using a Leica TCS SP8 confocal microscope (Wetzlar, Germany).

Viability test by direct contact to HDF. All substrates (1.9 cm^2) were placed on top of a monolayer of HDF cells (80% confluence, 12-well plate) and incubated for 24 h or 48 h at 37 °C in a humidified, 5% CO_2 atmosphere. Cell viability was visualized by live/dead staining and an ApoTome fluorescence microscopy. Cell viability quantification was conducted using the colorimetric MTS assay following the supplier's instructions. Following incubation, the medium was exchanged to equal volumes and 20 µL of MTS reagent (100/20) was added. The microplates containing the treated cells and control were then incubated for 3 h at 37 °C in a humidified, 5% CO_2 atmosphere and the absorbance was recorded at 490 nm using the multi-mode microplate reader SpectraMax® M3. The collected absorbance data were normalized with the untreated cells as the 100% reference.

3D Full-thickness skin models. full-thickness human skin equivalents were generated as described previously.[50] Briefly, the dermis layer was prepared by mixing ice-cold bovine collagen I solution with 10x Hank's balanced salt solution (Gibco/Invitrogen, Darmstadt, Germany) at 8:1 vol%. Following neutralization with 1 M NaOH, 1 vol% of HDF in FBS was added reaching a final concentration of 1 x 10^5 cells·ml^{-1}. Polycarbonate membrane inserts (0.4 µm pore size; ThermoFisher Scientific, Langenselbold, Germany) were filled with 4 mL of the collagen-cell solution. Subsequently, inserts were positioned in 6-well plates. Once the gels completely polymerized, they were covered with DMEM containing 10% FBS, 100 U·ml^{-1} penicillin, and 100 mg·ml^{-1} streptomycin and let to incubate in a humidified atmosphere at

37 °C and 5% CO_2. After 2–5 days, approximately 2×10^6 HEK were seeded on each dermis equivalent. The resulting skin equivalents were cultured in a mixture of DMEM and keratinocyte growth medium (50:50) supplemented with 5% FBS, 100 $U \cdot ml^{-1}$ penicillin, 100 $mg \cdot ml^{-1}$ streptomycin and 50 $mg \cdot ml^{-1}$ ascorbic acid. Following 3-4 days of submerged culture, the skin equivalents were brought to the air-liquid interface and the calcium concentration was increased to 1.2 mM. Full-thickness human skin equivalents were further incubated with medium changes every other day. To test biocompatibility, pristine and Kill&Repel$_{ClyF}$ coated PCL wound dressings were placed onto the models for 3 and 5 days. Following the incubation period, the dressings were carefully removed and skin models were examined through histological as well as immunohistochemistry analyses.

Light microscopy and immunohistochemistry analyses. 4 µm cryosections of the full-thickness human skin equivalents were embedded in Tissue TeK® O.C.T.™ compound and stained with hematoxylin and eosin. Sections were examined using the Leica DM IL photomicroscope (Leica Microsystems, Wetzlar, Germany). For immunohistochemistry analysis, 4 µm cryosections were fixed in acetone for 10 min at 4 °C. The cryosections were then incubated for 1 h with the primary Ki67 antibody (1:50) at ambient conditions. After washing steps with PBS, the cryosections were immersed for 1 h in a solution of the goat anti-mouse IgG Alexa Fluor 488-conjugated secondary antibody. Cell nuclei were counterstained with DAPI. Cryosections were then mounted on glass coverslips utilizing the fluorescent mounting medium (Dako Omnis). Imaging was conducted using the Leica DM IL photomicroscope (Leica Microsystems, Wetzlar, Germany) equipped with epifluorescence illumination and digital photo documentation (DISKUS, Hilgers, Königswinter, Germany).

5.5 Supplementary Results

Molecular adsorption of antifouling (LCI-KR2-pHPMA) and bactericidal (LCI-KR2-ClyF) hybrids.

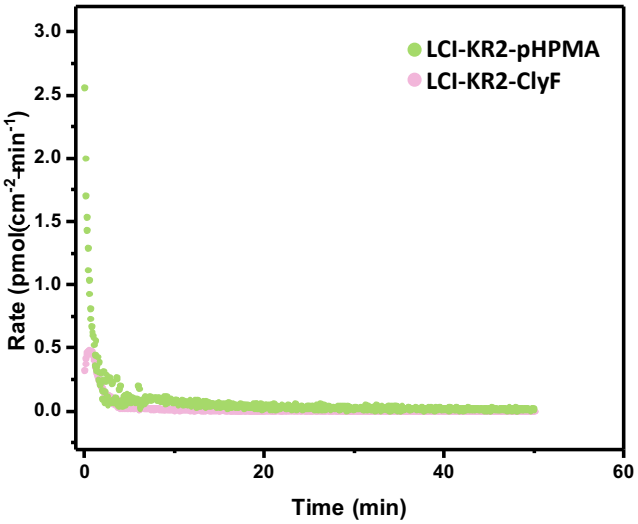

Figure S5.1. Comparison of the adsorption rates of LCI-EndLys (ClyF), LCI-KR2-eGFP-pHPMA measured by SPR spectroscopy, demonstrating that both hybrids exhibit similar adsorption rates across the entire adsorption process.

Blood plasma fouling

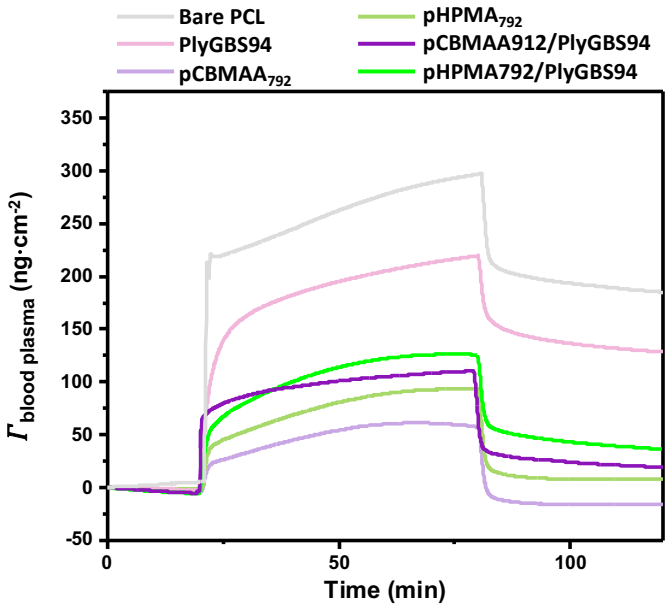

Figure S5.2. SPR sensograms illustrating blood plasma fouling on pristine PCL and PCL coated with the antifouling and bactericidal hybrids as well as the Kill&Repel$_{PlyGBS94}$ coating.

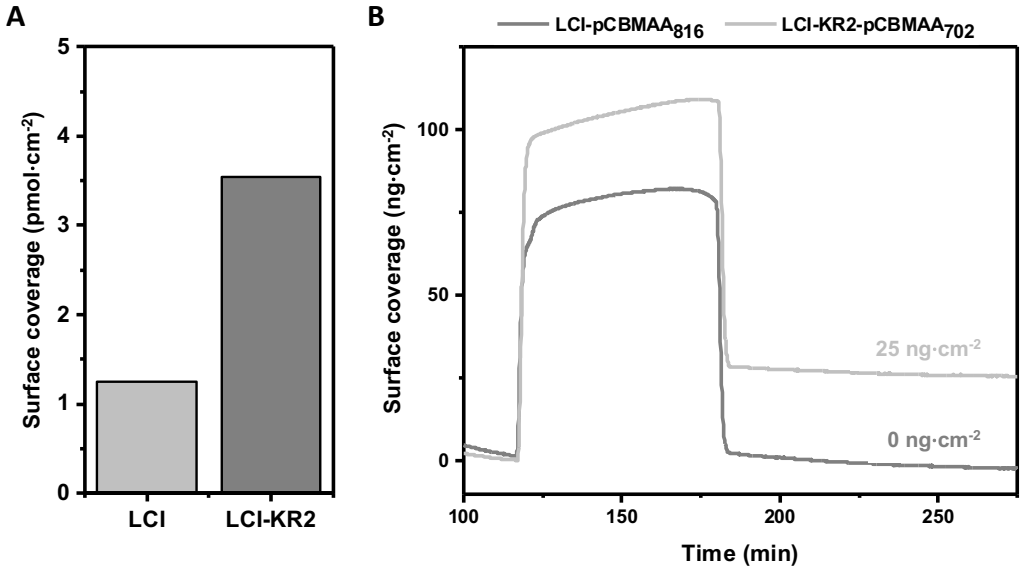

Figure S5.3. (A) Adsorption of LCI-eGFP and LCI-KR2-eGFP on PCL measured and calculated from SPR spectroscopy. (B) SPR sensograms of blood plasma protein fouling on PCL coated with LCI-eGFP-pCBMAA$_{816}$ and LCI-KR2-eGFP-pCBMAA$_{702}$.

Adhesion of fibroblast cells on pristine and coated PCL fibers

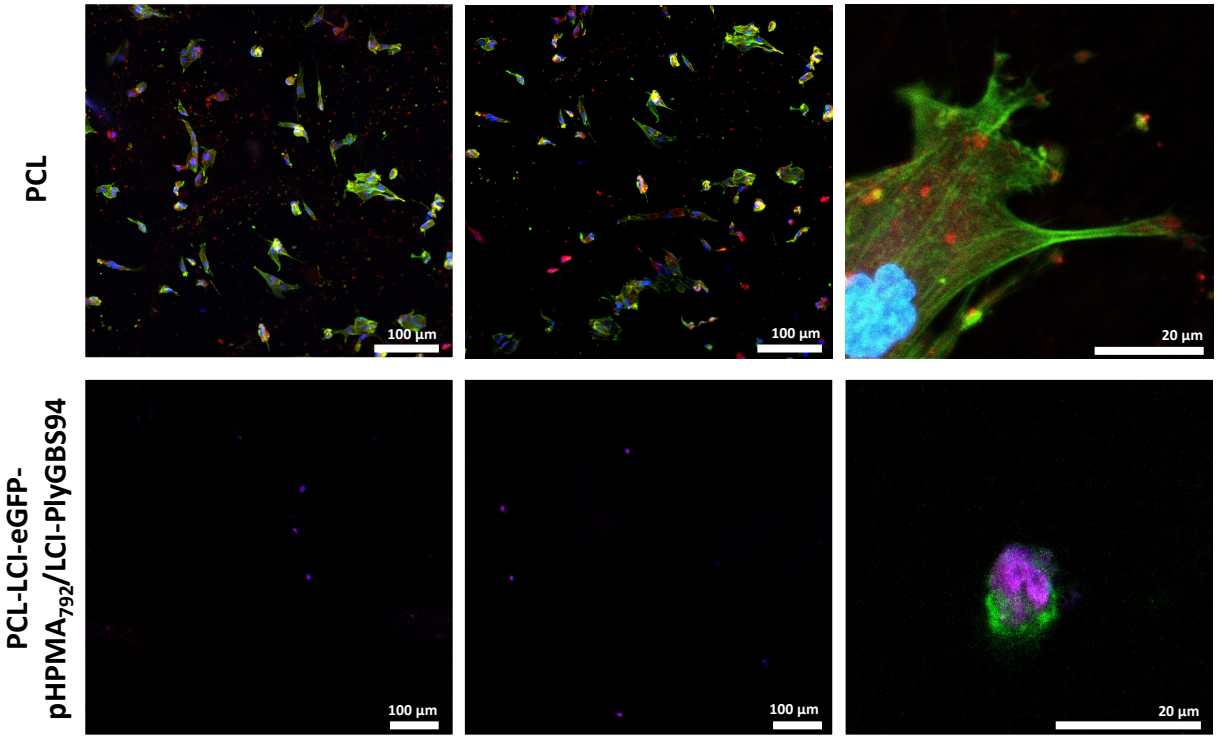

Figure S5.4. Adhesion of dermal fibroblasts on bare and Kill&Repel$_{PlyGBS94}$ coated PCL wound dressings visualized via CLSM (nuclei: blue, actin filaments: green and vinculin: red).

Antimicrobial activity of the Kill&Repel$_{PlyGBS94}$ coating against planktonic *S. agalactiae*

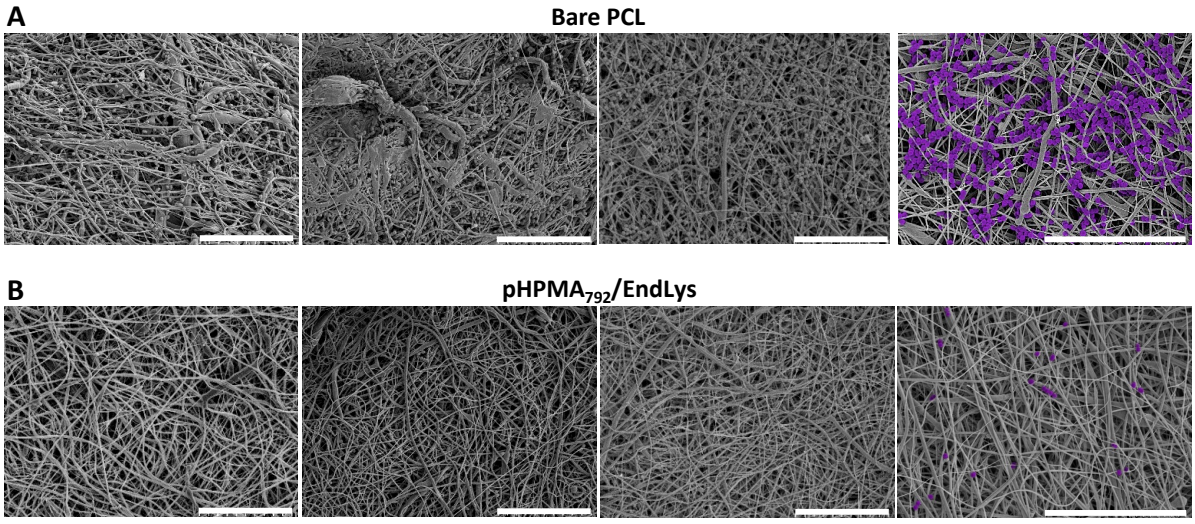

Figure S5.5. Additional images providing a visual representation of substantial bacteria adhesion on bare PCL wound dressings. In contrast, the Kill&Repel$_{PlyGBS94}$ coated dressings effectively prevented bacterial and debris adhesion on the surface.

Antimicrobial activity of the Kill&Repel$_{PlyGBS94}$ coating against sessile *S. agalactiae*

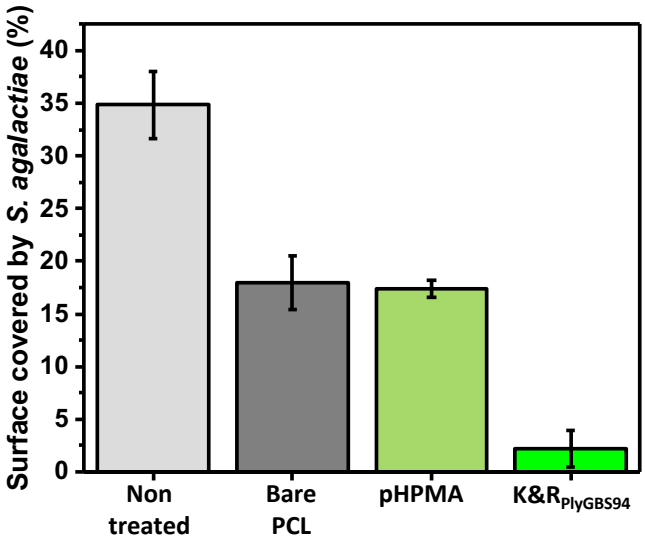

Figure S5.6. Quantification of inhibition zones of the contaminated agar plates with *S. agalactiae* after treatment with bare and coated PCL wound dressings. Non treated surface was used as reference.

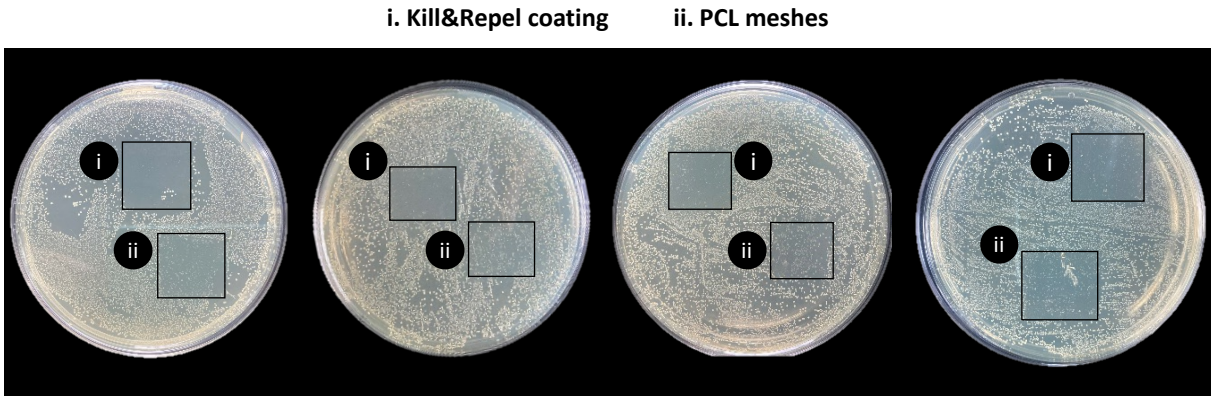

Figure S5.7. Agar plates contaminated with *S. agalactiae* bacteria and treated with bare PCL wound dressings and dressing coated with the Kill&Repel$_{PlyGBS94}$ coating.

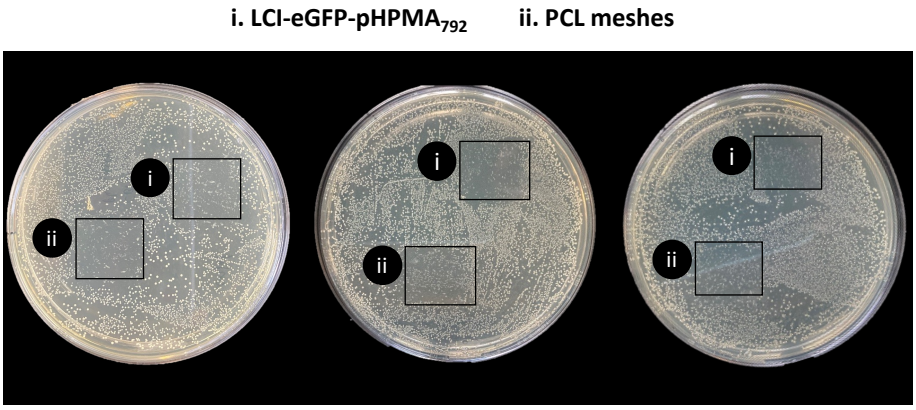

Figure S5.8. Agar plates contaminated with *S. agalactiae* bacteria and treated with bare PCL wound dressings and dressing coated with the LCI-eGFP-pHPMA hybrid coating.

Antimicrobial activity of the Kill&Repel$_{ClyF}$ coating against MRSA

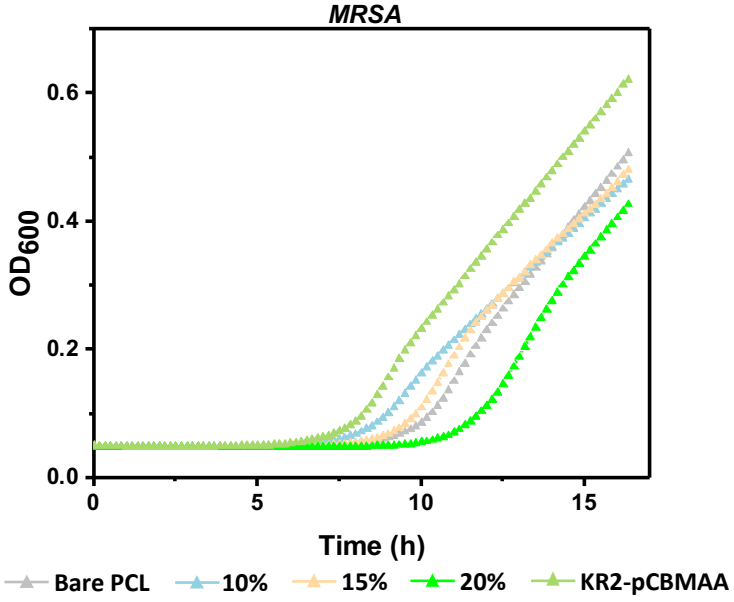

Figure S5.9. Antimicrobial activity of the Kill&Repel$_{ClyF}$ coating containing different ratios of the LCI-ClyF hybrids (10, 15 and 20 mol%).

Biocompatibility of Kill&Repel$_{PlyGBS94}$ coating

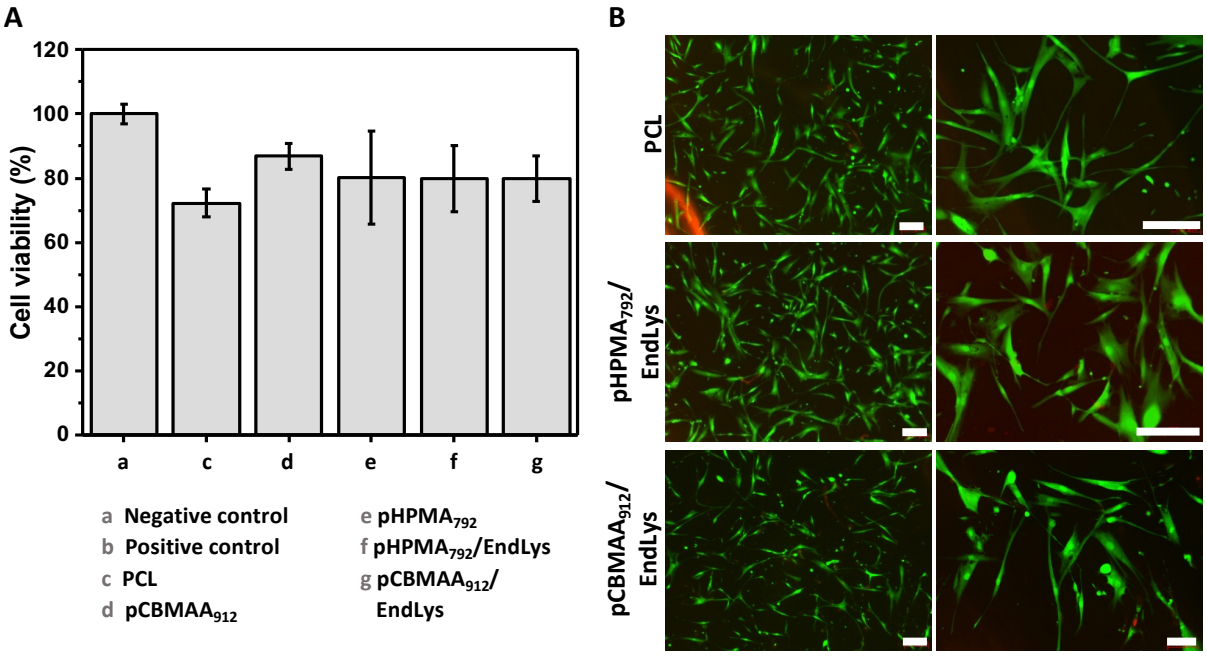

Figure S5.10. (A) HDF viability after direct contact for 48 h determined via MTS assay. No significant statistical difference ($p < 0.05$) between the bare PCL fibers and the coated ones. (B) Live/dead staining images after direct contact for 24 h. Scale bar represent 200 µm.

Lyophilization stability of antimicrobial LCI-EndLys hybrids

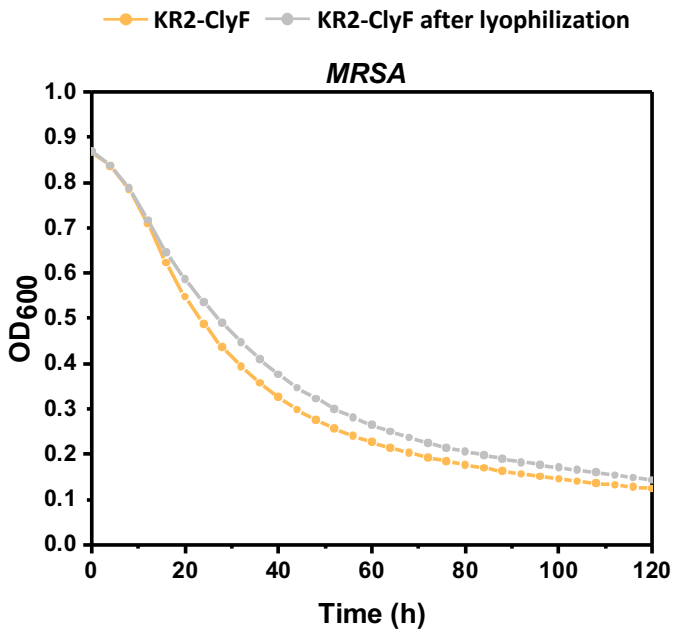

Figure S5.11. The LCI-KR2-ClyF hybrids can undergo lyophilization and subsequent reconstitution into an aqueous solution, preserving their antimicrobial activity.

5.6 Declaration of Contributions

Parts of this chapter were adapted with permission from the publication "Kill&Repel Coatings: The Marriage of Antifouling and Bactericidal Properties to Mitigate and Treat Wound Infections" in Advanced Functional Materials (Garay-Sarmiento, M., Witzdam, L., Vorobii, M., Simons, C., Herrmann, N., De los Santos Pereira, A., Heine, E., El-Awaad, I., Lütticken, R., Jakob, F., Schwaneberg, U., Rodriguez-Emmenegger, C., Kill&Repel Coatings: The Marriage of Antifouling and Bactericidal Properties to Mitigate and Treat Wound Infections. Adv. Funct. Mater. 2022, 32, 2106656; https://doi.org/10.1002/adfm.202106656; Copyright © 2021 The Authors. Advanced Functional Materials published by Wiley-VCH GmbH). Moreover, some of the results were also published in the master thesis entitled "Development of an advanced Kill&Repel coating for polymeric and metallic surfaces" at RWTH Aachen University by Yannik Rutsch.

I introduced the general Kill&Repel concept and performed the following experimental work: polymerization and characterization of the LCI-eGFP-pCBMAA and LCI-eGFP-pHPMA hybrids, all SPR binding and antifouling studies with the first generation of the Kill&Repel$_{PlyGBS94}$ coating, fibroblast adhesion studies, bacterial adhesion assessment against *E. coli,* enzymatic activity studies, bactericidal activity against planktonic *S. agalactiae,* all biocompatibility studies with HDF and imaging analysis by SEM and CLSM. Bactericidal activity against sessile *S. agalactiae* was performed by Rita Gartzen. The interpretation of the data was performed by Prof. César Rodriguez-Emmenegger and me in collaboration with Elisabeth Heine and Prof. Dr. med Rudolf Lütticken. Furthermore, Christian Simons and Niklas Herrmann are acknowledged for their help in the production of LCI-eGFP and LCI-eGFP-PlyGBS94.

The second generation of the Kill&Repel$_{ClyF}$ coating was conceptually and experimentally developed by Niklas Herrmann and me. The synthesis of the LCI-KR2-eGFP-Polymer hybrid macromolecules and SPR measurements to determined hybrid adsorption and BP protein fouling were performed by me and my former master student Yannik Rutsch. The production of LCI-KR2-eGFP and LCI-KR2-ClyF as well as all expose studies were conducted by Niklas Herrmann. The interpretation of the data was performed by Niklas Herrmann, Dr. Felix Jakob, Prof. César Rodriguez-Emmenegger and me. Moreover, I performed SEM imaging after expose experiments. Biocompatibility studies including the EpiDerm^{TM} Skin Irritation Test and the 3D

full-thickness skin models were conducted by the research group of Prof. Dr. med Baron at the University Hospital RWTH Aachen.

Prof. César Rodriguez-Emmenegger and Prof. Ulrich Schwaneberg supervised together all of these projects.

5.7 References

[1] M. Vorobii, R. Teixeira-Santos, L. C. Gomes, M. Garay-Sarmiento, A. M. Wagner, F. J. Mergulhão, C. Rodriguez-Emmenegger, *Progress in Organic Coatings* **2022**, *163*, 106609.

[2] E. L. Cyphert, H. A. von Recum, *Exp Biol Med (Maywood)* **2017**, *242*, 788-798.

[3] X. Chen, J. Zhou, Y. Qian, L. Zhao, *Mater Today Bio* **2023**, *19*, 100586.

[4] J. J. H. Oosterhof, K. J. D. A. Buijssen, H. J. Busscher, B. F. A. M. v. d. Laan, H. C. v. d. Mei, *Applied and Environmental Microbiology* **2006**, *72*, 3673-3677.

[5] B. Gottenbos, D. W. Grijpma, H. C. van der Mei, J. Feijen, H. J. Busscher, *Journal of Antimicrobial Chemotherapy* **2001**, *48*, 7-13.

[6] A. Strassburg, F. Kracke, J. Wenners, A. Jemeljanova, J. Kuepper, H. Petersen, J. C. Tiller, *Macromolecular Bioscience* **2015**, *15*, 1710-1723.

[7] Z. Geng, M. G. Finn, *Journal of the American Chemical Society* **2017**, *139*, 15401-15406.

[8] P. Kotz, J. Fisher, P. McCluskey, S. D. Hartwell, H. Dharma, *Int Wound J* **2009**, *6*, 186-194.

[9] S. Medici, M. Peana, V. M. Nurchi, M. A. Zoroddu, *Journal of Medicinal Chemistry* **2019**, *62*, 5923-5943.

[10] W. Sim, R. T. Barnard, M. A. T. Blaskovich, Z. M. Ziora, *Antibiotics (Basel)* **2018**, *7*.

[11] M. I. Hutchings, A. W. Truman, B. Wilkinson, *Current Opinion in Microbiology* **2019**, *51*, 72-80.

[12] C. Greulich, D. Braun, A. Peetsch, J. Diendorf, B. Siebers, M. Epple, M. Köller, *RSC Advances* **2012**, *2*.

[13] S. Yunoki, M. Kohta, Y. Ohyabu, T. Iwasaki, *Chronic Wound Care Management and Research* **2015**.

[14] S. B. Zou, W. Y. Yoon, S. K. Han, S. H. Jeong, Z. J. Cui, W. K. Kim, *Int Wound J* **2013**, *10*, 306-312.

[15] D. V. Patangia, C. Anthony Ryan, E. Dempsey, R. Paul Ross, C. Stanton, *Microbiologyopen* **2022**, *11*, e1260.

[16] C. L. Ventola, *P t* **2015**, *40*, 277-283.

[17] A. Punjataewakupt, S. Napavichayanun, P. Aramwit, *European journal of clinical microbiology & infectious diseases : official publication of the European Society of Clinical Microbiology* **2019**, *38*, 39-54.

[18] N. A. Hodges, E. M. Sussman, J. P. Stegemann, *Biomaterials* **2021**, *278*, 121127.

[19] C. Ghose, C. W. Euler, *Antibiotics (Basel)* **2020**, *9*.

[20] Q. Cheng, V. A. Fischetti, *Appl Microbiol Biotechnol* **2007**, *74*, 1284-1291.

[21] Y. Briers, R. Lavigne, *Future microbiology* **2015**, *10*, 377-390.

[22] M. U. Rahman, W. Wang, Q. Sun, J. A. Shah, C. Li, Y. Sun, Y. Li, B. Zhang, W. Chen, S. Wang, *Antibiotics (Basel)* **2021**, *10*.

[23] J. R. Baker, C. Liu, S. Dong, D. G. Pritchard, *Applied and Environmental Microbiology* **2006**, *72*, 6825-6828.

[24] M. J. Thiele, M. D. Davari, M. König, I. Hofmann, N. O. Junker, T. Mirzaei Garakani, L. Vojcic, J. Fitter, U. Schwaneberg, *ACS Catalysis* **2018**, *8*, 10876-10887.

[25] M. Heredero, A. Beloqui, *ChemBioChem* **2023**, *24*, e202200611.

[26] A. J. Keefe, S. Jiang, *Nature Chemistry* **2012**, *4*, 59-63.

[27] B. Oyanguren, L. Esteban, M. Guillán, A. de Felipe, A. Alonso Cánovas, E. Navas, C. Quereda, I. Corral, *Neurología (English Edition)* **2015**, *30*, 158-162.

[28] V. N. Raabe, A. L. Shane, *Microbiol Spectr* **2019**, *7*.

[29] T. H. Skoff, M. M. Farley, S. Petit, A. S. Craig, W. Schaffner, K. Gershman, L. H. Harrison, R. Lynfield, J. Mohle-Boetani, S. Zansky, B. A. Albanese, K. Stefonek, E. R. Zell, D. Jackson, T. Thompson, S. J. Schrag, *Clinical Infectious Diseases* **2009**, *49*, 85-92.
[30] N. Y. Lee, J. J. Yan, J. J. Wu, H. C. Lee, K. H. Liu, W. C. Ko, *Clinical Microbiology and Infection* **2005**, *11*, 577-579.
[31] F. Al Akhrass, L. Abdallah, S. Berger, R. Hanna, N. Reynolds, S. Thompson, R. Hallit, P. M. Schlievert, *Medicine (Baltimore)* **2013**, *92*, 10-14.
[32] P. Sendi, L. Johansson, A. Norrby-Teglund, *Infection* **2008**, *36*, 100-111.
[33] E. World Health Organization, *and development of new antibiotics* **2017**.
[34] J. K. Ortwine, K. Bhavan, *Hosp Pract (1995)* **2018**, *46*, 64-72.
[35] A. H. S. J. Koirala, StatPearls [Internet], Treasure Island (FL): StatPearls Publishing, **2023**.
[36] H. Yang, J. Yu, H. Wei, *Frontiers in Microbiology* **2014**, *5*.
[37] H. Yang, Y. Zhang, J. Yu, Y. Huang, X.-E. Zhang, H. Wei, *Antimicrobial Agents and Chemotherapy* **2014**, *58*, 536-542.
[38] H. Yang, H. Zhang, J. Wang, J. Yu, H. Wei, *Scientific Reports* **2017**, *7*, 40182.
[39] M. M. Severn, A. R. Horswill, *Nat Rev Microbiol* **2023**, *21*, 97-111.
[40] M. T. McCann, B. F. Gilmore, S. P. Gorman, *J Pharm Pharmacol* **2008**, *60*, 1551-1571.
[41] M. Otto, *Nat Rev Microbiol* **2009**, *7*, 555-567.
[42] S. Águila-Arcos, I. Álvarez-Rodríguez, O. Garaiyurrebaso, C. Garbisu, E. Grohmann, I. Alkorta, *Frontiers in Microbiology* **2017**, *8*.
[43] P. Cleary, Q. Cheng, in *The Prokaryotes: Volume 4: Bacteria: Firmicutes, Cyanobacteria* (Eds.: M. Dworkin, S. Falkow, E. Rosenberg, K.-H. Schleifer, E. Stackebrandt), Springer US, New York, NY, **2006**, pp. 108-148.
[44]https://www.mattek.com/mattekproduct/epiderm/#:~:text=EpiDerm%20exhibits%20human%20epidermal%20tissue,are%20mitotically%20and%20metabolically%20active. 2023, Nov 28.
[45] OECD, *Test No. 439: In Vitro Skin Irritation: Reconstructed Human Epidermis Test Method*, **2021**.
[46] Y. Marquardt, P. M. Amann, R. Heise, K. Czaja, T. Steiner, H. F. Merk, C. Skazik-Voogt, J. M. Baron, *Lasers in Surgery and Medicine* **2015**, *47*, 257-265.
[47] C. Rodriguez-Emmenegger, E. Brynda, T. Riedel, M. Houska, V. Šubr, A. B. Alles, E. Hasan, J. E. Gautrot, W. T. S. Huck, *Macromolecular Rapid Communications* **2011**, *32*, 952-957.
[48] M. Vorobii, A. de los Santos Pereira, O. Pop-Georgievski, N. Y. Kostina, C. Rodriguez-Emmenegger, V. Percec, *Polymer Chemistry* **2015**, *6*, 4210-4220.
[49] C. Rodriguez-Emmenegger, C. M. Preuss, B. Yameen, O. Pop-Georgievski, M. Bachmann, J. O. Mueller, M. Bruns, A. S. Goldmann, M. Bastmeyer, C. Barner-Kowollik, *Adv. Mater.* **2013**, *25*, 6123-6127.
[50] M. M. Neis, A. Wendel, T. Wiederholt, Y. Marquardt, S. Joussen, J. M. Baron, H. F. Merk, *Skin Pharmacology and Physiology* **2010**, *23*, 29-39.

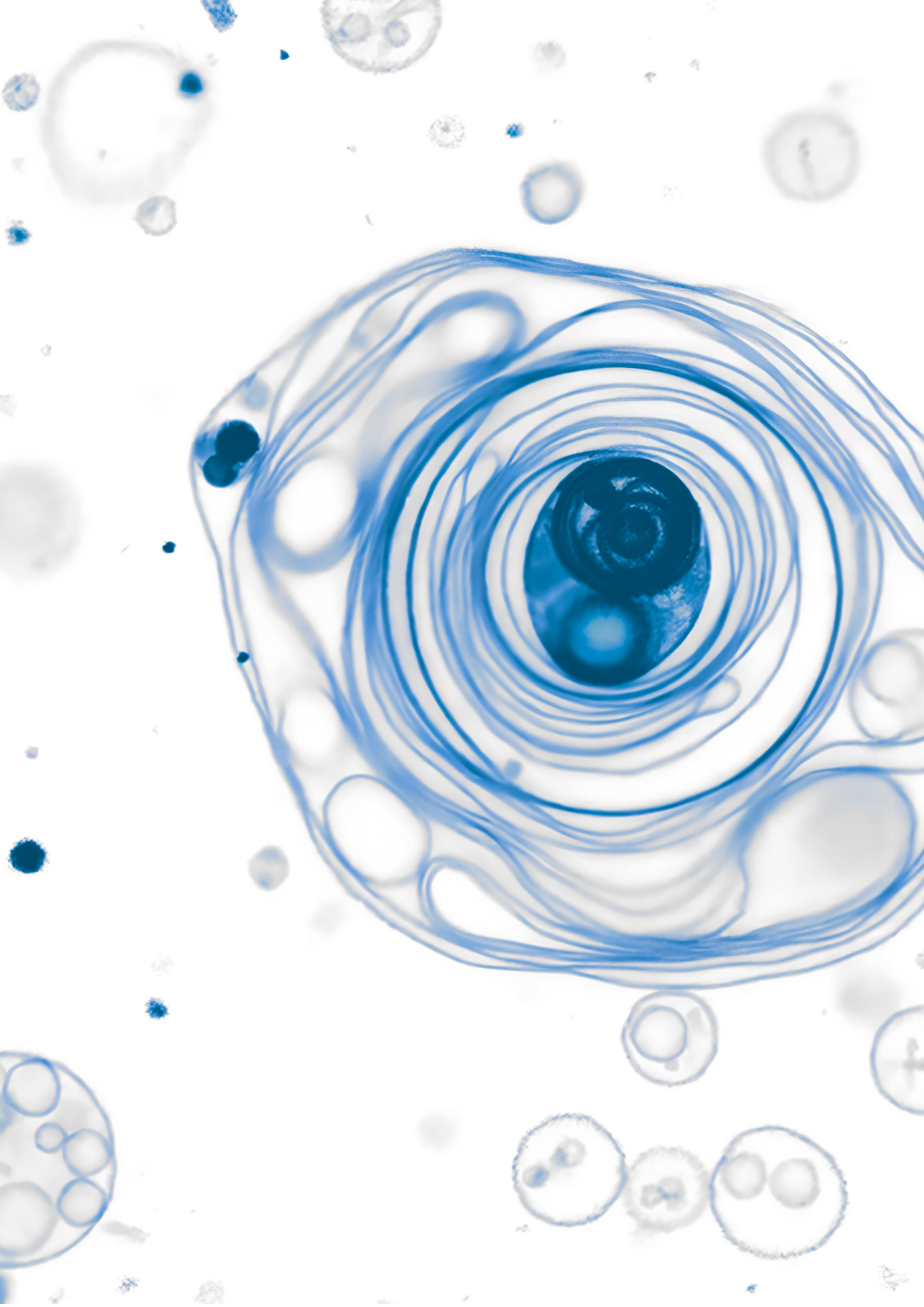

Chapter 6

Unlocking the Phagocytic Potential of Synthetic Cells

6.1 Introduction

Phagocytosis is the biological process through which living cells engulf and internalize particulate matter. In protists, phagocytosis serves as an efficient nutritional strategy, while in multicellular organisms, it functions as a unique scavenging mechanism instrumental for the selective clearance of apoptotic cells and pathogenic invaders.[1-3] Notably, a primitive form of phagocytosis is considered to be the driving force behind the evolution of eukaryotic cells, according to Margulis's theory of endosymbiosis.[4] As such, phagocytosis stands as a hallmark of eukaryotic cells, being fundamental for nutrient uptake, tissue homeostasis and innate immunity. In fact, phagocytosis is one of the most effective defense strategies against microbes, preventing infection.[5]

During phagocytosis, the cell membrane undergoes significant deformation and bending as it engulfs and internalizes matter. This intricate process relies on a sophisticated cellular machinery that orchestrates the tight interplay of several proteins, lipids and enzymes involved in the dynamic remodeling of the actin cytoskeleton.[1, 3] Phagocytosis initiates upon receptor-based recognition and binding of the targeted particle to the membrane. These binding events activate signaling pathways, leading to the formation of pseudopods that wrap the particle. The process continues with the inward bending of the membrane, forming a pocket known as phagosome, which ultimately undergoes fission into the cell's cytoplasm. Subsequently, the phagosome goes through a series of maturation steps, that ultimately result in the digestion and elimination of the engulfed matter.[2, 6] The refinement and efficiency of this process has captured significant attention in the field of bottom-up synthetic biology, where scientists aim to recreate an artificial form of phagocytosis using minimal synthetic cells devoid of complex machinery. Specially, in the biomedical field and environmental remediation, artificial phagocytosis can emerge as a means to scavenge disease-causing microorganism and foreign objects from the environment. Indeed, the pioneering concept of non-living predators capable of capturing and eating objects was firstly introduced by the scientific group of Stephen Mann.[7-9] Early systems exemplifying this concept include membranelles coacervate microdroplets that devour proteinosomes mediated by electrostatic attraction or preferential solubility of the proteinosome surface within the hydrophobic environment of the coacervate.[7-8] Furthermore, both membraneless[9] and membranized[10] coacervate microdroplets as well as porous microcapsules[11] have been

employed to capture and lyse bacterial cells. Additionally, strategies like cell membrane-mimicking nanodecoys[12] and DNA hollow cages have proven successful in neutralizing viruses.[13] Nonetheless, none of these systems faithfully replicate the phagocytic process of living cells. Theoretical studies have indicated that giant unilamellar vesicles (GUVs) have the capability to mimic a rudimentary form of engulfment observed during phagocytosis. In the simplest model that considers the membrane as a continuous elastic body, engulfment occurs when the adhesion energy ($\Delta G^{adhesion}$) between object and membrane is sufficiently high to surpass the elastic energy of the membrane, i.e., bending energy ($\Delta G^{bending}$) and tension ($\Delta G^{tension}$) energies, as stated in Equation 1.[14-20]

$$|\Delta G^{adhesion}| > |\Delta G^{bending}| + |\Delta G^{tension}| \qquad \textbf{Equation 6.1}$$

Equation 1, gives rise to a critical radius R_c, where k is the bending stiffness:

$$R_c = \sqrt{\frac{2k}{\Delta G^{adhesion}}} \qquad \textbf{Equation 6.2}$$

Thus, artificial engulfment is favored by very flexible membranes or strong adhesion energies. To date, most of the empirical studies on particle engulfment have been carried out with liposomes assembled from natural lipids or polymersomes derived from amphiphilic block copolymers. The latter are known for their high stability but at the expense of high membrane thickness along with low flexibility (high bending rigidity).[21-24] These properties lead to a higher resistance of the membrane to bending and stretching, thereby demanding higher adhesion energies. Conversely, liposomes have highly flexible membranes, making engulfment thermodynamically feasible. However, despite their superior flexibility, accomplishing complete nanoparticle engulfment has only been successful under specific conditions that required the addition of salts to reduce the high energy barrier caused by the inability of liposomes to readily accommodate the intermediate steps of engulfment.[25-27] Furthermore, in the case of micrometer-sized particles, the incorporation of charge or strong, irreversibly binding receptors, such as avidin-biotin binding, was a prerequisite for engulfment to occur.[28-34] Yet, even in such cases, engulfment lacked efficiency. Ultimately, neither liposomes nor polymersomes from block copolymers are able to fully engulf particles in an efficient manner; if invagination is successful, completion to membrane fission still remains a challenge.[35-36] This challenge arises from the complex dynamics of membrane curvature

changes during intermediate stages (Figure 6.1). Even if the overall engulfment process is thermodynamically plausible, intermediate stages with strong non-zero membrane curvatures pose energetic barriers. Hence, complete engulfment requires overcoming these barriers. Liposomes, while highly flexible, consist of single amphiphilic molecules with zero spontaneous curvature, not being able to compensate for strong membrane bending and therefore stall at partial engulfment stages.[34, 36]

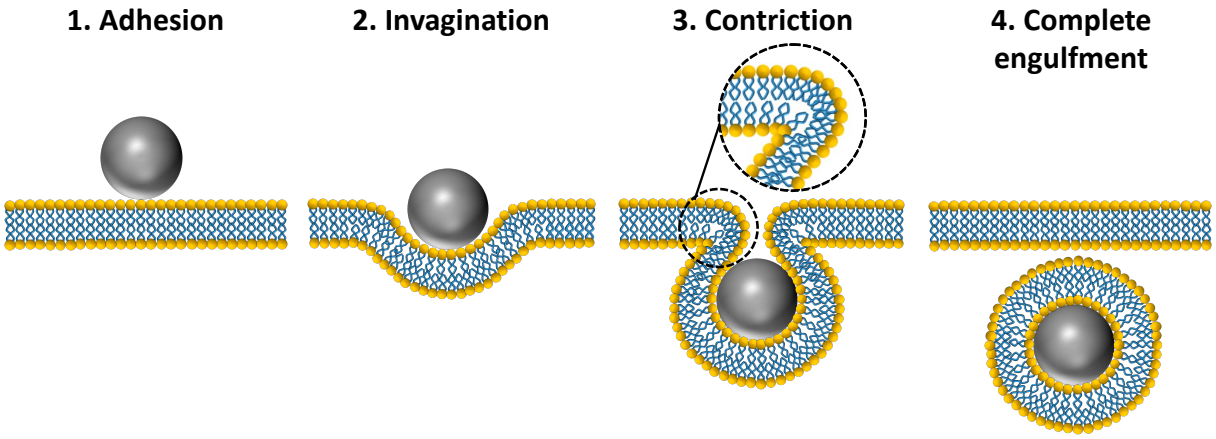

Figure 6.1. Interaction of a particle with a liposome membrane depicting during the engulfment process. Intermediate stages with strong non-zero membrane curvature behave as kinetic traps.

Hence, alternative membrane assemblies are needed that can more effectively balance the interplay between adhesion energy, membrane elastic energy and membrane stability, facilitating spontaneous engulfment with high efficiency. Our group demonstrated the enhanced feasibility of engulfing nanoparticles and even microscopic objects, such as *E. coli* bacteria, using dendrimersomes assembled from Janus dendrimers.[37] Dendrimersomes exhibit flexibility similar to that of liposomes[38-39]; however, it is their macromolecular structure that is crucial for their higher capability to engulf. Accordingly, they exhibit greater conformational freedom than liposomes and can therefore better accommodate the high-energy intermediate stages of engulfment, reducing the kinetic barrier and leading to complete internalization of *E. coli* inside a phagosome. These observations, led us to hypothesize that a way to achieve “accelerated artificial phagocytosis”, may involve devising a means to lower kinetic barriers encountered during the intermediate stages of engulfment.

In this chapter, we pioneered the concept of “accelerated artificial phagocytosis”. For this, we proposed the use of a new family of cell mimics known as i-combisomes, which self-assemble from amphiphilic ionically-linked comb polymers (iCPs).[40] As described in [40], the iCPs are supramolecular polymers with a hydrophilic backbone comprising zwitterionic and cationic monomers. Hydrophobic ligands (tails) are linked to this backbone by electrostatic interactions. Upon self-assembly of the iCPs in water into i-combisomes, the hydrophobic tails zip together, forming a bilayer where the backbone is restricted to the two-dimensional water interface. Notably, the membrane thickness is decoupled from the DP and depends only on the height of the amphiphilic repeating unit. The non-entangled nature and the non-covalent ligation of hydrophilic and hydrophobic domains result in more degrees of freedom, granting the i-combisomes with the dynamic ability to locally reconfigure their molecular topology. For example, in i-combisomes, the ionically linked hydrophobic tails can freely move and exchange between neighboring chains. When necessary, this process can induce transient changes in packing, such as an increase in the local density of the hydrophobic ligands allowing for a better accommodation of non-zero membrane curvatures and, consequently, reducing the kinetic barriers for complete engulfment. Accordingly, I hypothesize that the inherent molecular flexibility of the i-combisomes will enable them to accommodate the high energy intermediate stages of engulfment, thereby reducing the kinetic barrier and ultimately leading to a rapid and efficient engulfment capability, i.e. accelerated artificial phagocytosis. To examine this, we studied the ability of i-combisomes to engulf SiO_2 and polystyrene (PS) micro- and nanoparticles using CLSM, cryogenic transmission electron microscopy (cryo-TEM) and dynamic light scattering (DLS). These results were benchmarked against the performance of 1,2-dioleoyl-sn-glycero-3-phosphocholine (DOPC) liposomes as well as poly(butadiene)-*block*-poly(ethylene oxide) (PB_{33}-*b*-PEO_{73}) and poly(dimethylsiloxane)-*graft*-poly(ethylene oxide) (PDMS-*g*-PEO) polymersomes and highlighted the massive engulfment capability of our i-combisomes. Furthermore, I will elaborate on our discoveries, revealing that the polymeric sequence heterogeneity of iCPs is truly responsible for the "accelerated artificial phagocytosis" performance exhibited by our i-combisomes.

6.2 Results and Discussion

6.2.1 Synthesis of iCPs

The iCPs were synthesized according to literature.[40] First, the hydrophilic backbone was synthesized by SET-LRP of CBAA and DMAPAA from the water-soluble 2,3-dihydroxypropyl 2-bromo-2-methylpropanoate initiator (Scheme 6.1A). The SET-LRP was conducted in water at 0 °C via the *in situ* reduction of Cu(II)Br_2/Me_6TREN to Cu(0) by $NaBH_4$. As it was published in [40], the reaction kinetics revealed a pseudo-first order kinetic behavior with uniform chain growth, where the probability for the addition of CBAA or DMAPAA into the growing chain is similar for both and remains constant throughout the entire polymerization time. This results in a poly(CBAA-*co*-DMAPAA) chain where both monomers are randomly distributed along the chain. The molar ratio of DMAPAA (N) and the DP are adjusted by tuning the CBAA:DMAPAA and monomer:initiator molar feed composition, respectively. Additionally, their composition and molecular weight were verified by NMR and SEC (Figure S6.1, Figure S6.2 and Figure S6.3).

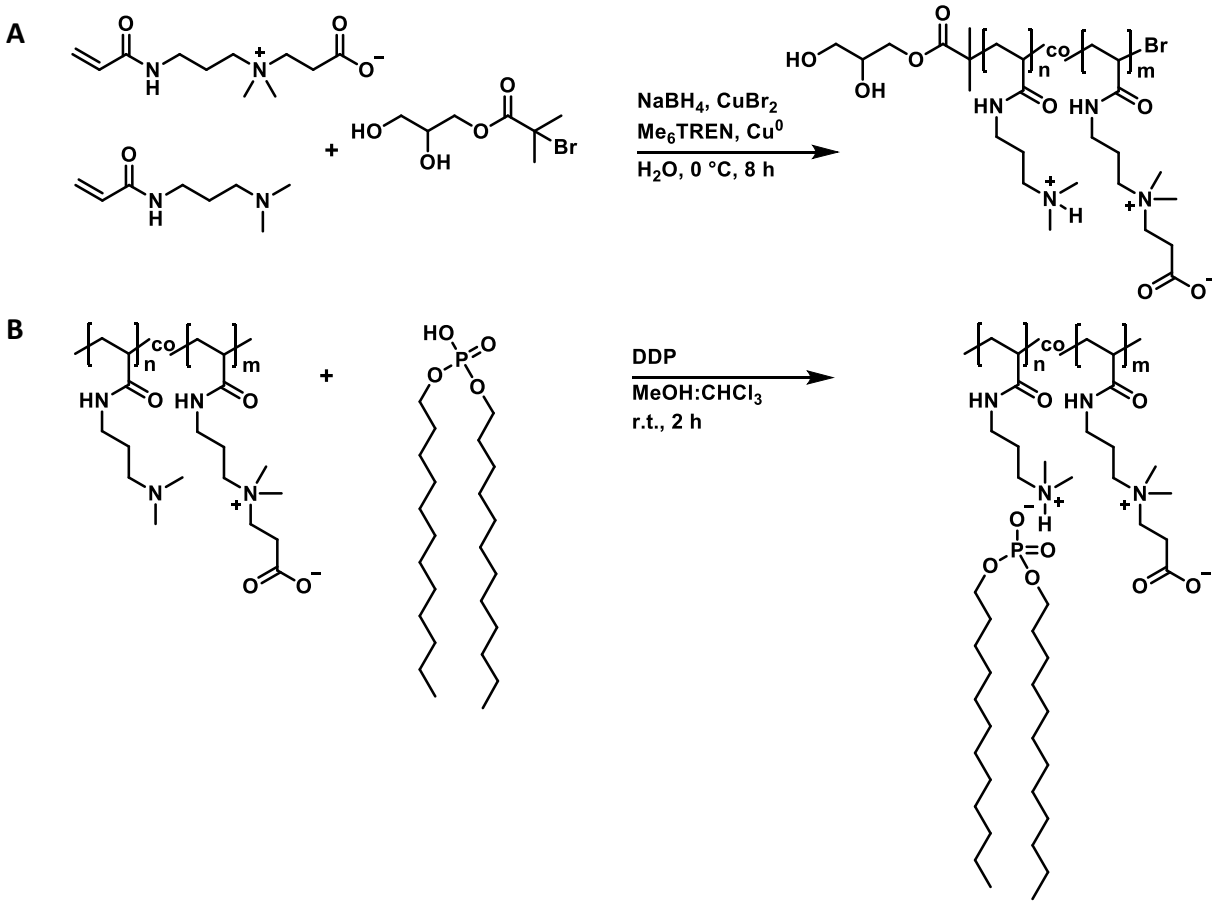

Scheme 6.1. Overview of the synthetic pathway of the iCPs. (A) SET-LRP of poly(CBAA-*co*-DMAPAA) and (B) Complexation with DDP.

In a second step, lipid-like hydrophobic side tails were appended to the hydrophilic poly(CBAA-*co*-DMAPAA) backbone by the electrostatic complexation of the free amine groups stemming from DMAPAA with didodecyl hydrogen phosphate (DDP, Scheme 6.1B) via an acid-base binding reaction. The ratio of DDP was adjusted accordingly to the desired degree of substitution (DS). For the following work, I chose iCPs with $DP_{85}N_{57}DS_{100}$.

6.2.2 Self-Assembly into GUVs and Characterization

We assembled GUVs from i-combisomes, DOPC liposomes, PDMS-*g*-PEO and PB_{33}-*b*-PEO_{73} polymersomes by the thin-film hydration (TFH) or electroformation method, incorporating 0.1 mol% of a membrane dye. In both of these methods, a thin polymer film is deposited from a good solvent onto a substrate, followed by solvent evaporation. Subsequent hydration of the film with an aqueous solution induces swelling and detachment of the layers, leading to spontaneous vesicle formation. During electroformation, film rehydration is supported by the application of an alternating electric field. As visualized by CLSM, the TFH method resulted in the formation of GUVs with a broad size distribution, which is a typical outcome for this method (Figure 6.2A). The membranes were then characterized by standard biophysical methods (Figure 6.2). The i-combisome membrane thickness was measured to be 4.6 ± 0.5 nm and similar to that of DOPC liposomes (5.3 ± 0.6 nm) and PDMS-*g*-PEO polymersomes (5.8 ± 1.1 nm). Conversely, polymersomes assembled from the block copolymer PB_{33}-*b*-PEO_{73} displayed a higher membrane thickness of 8.2 ± 1.1 nm (Figure 1.2C). Contrary to other polymeric cell mimics, where the membrane thickness is strongly dependent on the degree of polymerization of the amphiphiles, the membrane thickness of i-combisomes is mainly governed by its hydrophobic moiety, namely DDP.[40] Therefore, although having a DP of 85 and a molecular weight of about 73,000 $g \cdot mol^{-1}$, the i-combisomes display a bilayer thickness comparable to that of natural cell membranes.[41] As a comparison, PB_{33}-*b*-PEO_{73} has a much smaller polymer chain length with a molecular weight of 5000 $g \cdot mol^{-1}$, however it displays a thickness nearly double that of the i-combisomes. In the case of the graft polymersomes, the graft PDMS-*g*-PEO copolymer consists of a hydrophobic, low molecular weight and flexible PDMS backbone, to which two chains of PEO are grafted.[42] The high flexibility of the siloxane chains together with the low density of the PEO graft chains enables the backbone to bend forming loops and generating a liquid-like hydrophobic core with PEO chains organize into mushroom-like structure facing the aqueous solution.[43] Moreover, the flexibility of the

backbone accommodates for optimal amphiphilic packing unit and assembly into a lamellar lyotropic phase. These special polymersomes exert a high degree of biomimicry, showcasing membrane thickness comparable to natural cells.[41] Moreover, they can seamlessly integrate functional components of natural membranes.[42, 44-45]

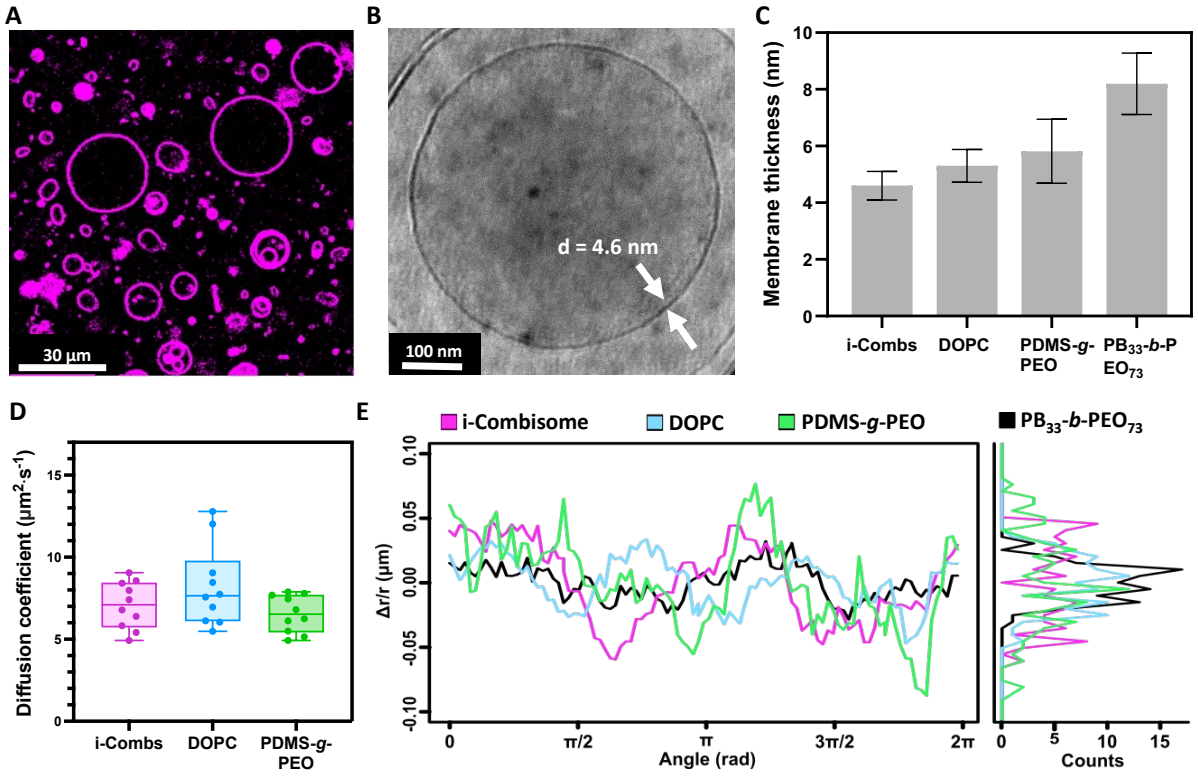

Figure 6.2. (A) Self-assembly of iCPs into i-combisomes by the TFH method visualized via CLSM. The bilayer was fluorescently labeled by addition of 0.1 mol% BODIPY (B) The membrane thickness of i-combisomes determined from multiple cryo-TEM images revealing a biomimetic thickness of 4.6 nm. (C) Membrane thicknesses compared to liposomes (DOPC) and polymersomes (PDMS-*g*-PEG and PB_{33}-*b*-PEO_{73}). (D) Boxplots for the diffusion coefficients of Liss Rhod-PE determined by fluorescence recovery after photobleaching (FRAP) analysis. The line represents the median and the whiskers show the standard deviation. (E) Angular fluctuation of radii (Δr(ϕ)') and distribution of the fluctuations (left).

Furthermore, we assessed the membrane fluidity by measuring the lateral diffusion of a fluorescently labeled lipid (Liss Rhod-PE) within the membrane leaflets using the standard FRAP technique (Figure 6.2D). Notably, the i-combisomes display lateral diffusion coefficients (D) of $D = 7 \pm 1.4\ \mu m^2 \cdot s^{-1}$, which is in the same range as for the DOPC liposomes ($8.2 \pm 2.5\ \mu m^2 \cdot s^{-1}$) and PDMS-*g*-PEO polymersomes ($6.5 \pm 1.1\ \mu m^2 \cdot s^{-1}$). It should be mentioned

that under our experimental conditions we could not measure D for the PB_{33}-*b*-PEO_{73} polymersomes. However, similar polymersomes in the literature display $D = 0.0144 \pm 0.006\ \mu m^2 \cdot s^{-1}$, which is approximately two orders of magnitude smaller than that of i-combisomes.[26] Such a low diffusion coefficient is attributed to the entanglement of the polymer chains, which becomes more pronounced with increasing molecular weight and membrane thickness in the case of polymersomes derived from block copolymers.[26] To have an idea on the flexibility of our i-combisomes in comparison to the other GUV systems, we assessed membrane flexibility by analyzing the shape fluctuations of the membrane using contour analysis. Figure 6.2E shows the angular distribution of the radii ($\Delta r(\varphi)$') after subtraction of the shape and size. The i-combisomes display highly fluctuating membranes similarly to DOPC liposomes, which are known to have a membrane bending rigidity of $\kappa = 19\ \kappa_B\ T$. Consistent with the literature, in our experiments PDMS-*g*-PEO polymersomes exhibited even stronger fluctuating vesicles. This is not surprising since they exhibit a bending rigidity of $\kappa = 11.7\ \kappa_B\ T$, which is almost half that of DOPC liposomes.[44-45] Furthermore, polymersomes of PB_{33}-*b*-PEO_{73} showed hardly any fluctuations, indicating a low flexibility. Monroy et al. and Hammer et al. reported a bending stiffness of $\kappa = 35\ \kappa_B\ T$ and $\kappa = 34\ \kappa_B\ T$, respectively, for similar PB-*b*-PEO polymersomes, indicating a rather rigid system, in agreement with our observations.[46-47] Once again, the higher bending stiffness of this system is attributed to the interdigitation and entanglement of the chains.

Importantly, a high level of fluidity and flexibility have been proven to be decisive membrane factors influencing the feasibility of engulfment. Notably, our i-combisomes exhibit a high level of biomimicry, featuring thickness, lateral mobility and flexibility akin to those observed in liposomes and graft polymersomes. Thus, from a thermodynamic point of view, engulfment of an object should be plausible with all of these systems.

6.2.3 Artificial Phagocytosis of Silica Nanoparticles

In this section, we investigated the ability of i-combisome GUVs to spontaneously engulf nano-sized silica (SiO_2) particles (SNPs) via CLSM, DLS as well as cryo-TEM and benchmarked it against DOPC liposomes, PB_{33}-*b*-PEO_{73} and PDMS-*g*-PEO polymersomes.

6.2.3.1 Visualizing the i-combisome-SNP Interactions by CLSM

The interaction between i-combisomes and 50 nm carboxylated SNPs was observed in real-time using CLSM. As shown in Figure 6.3A, the engulfment of SNPs by the i-combisomes was immediately evident upon contact, indicated by the cyan fluorescence originating from the SNPs located inside the GUVs (magenta fluorescence). During a contact period of 30 min, we observed the majority of the i-combisomes containing engulfed particles in their lumen (Figure 6.3B). Notably, as shown by the 3D reconstruction image in Figure 6.3C, some of the i-combisomes were even completely filled with SNPs, underscoring their exceptional engulfment efficiency. The co-localization of both the SNP and membrane fluorescence indicates that the SNP internalization process followed the engulfment pathway, which involves membrane wrapping around the SNP and fission of the neck leading to the endosome release inside the GUV. Endosome fission can be confirmed by observing freely diffusing SNPs within the GUV lumen (Figure 6.3Aiii).

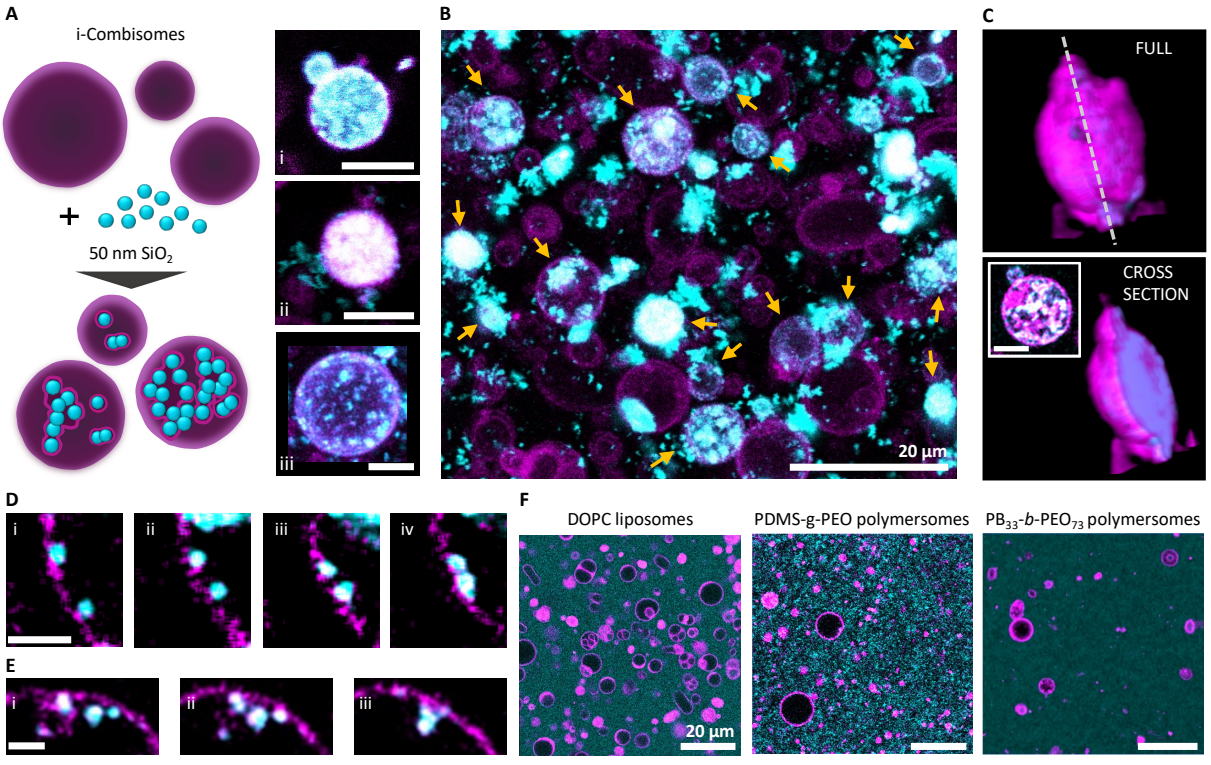

Figure 6.3. Interaction between i-combisomes and SNPs. (A) Schematic (left) and CLSM images immediately after mixture of SNPs with i-combisomes. Scale bars represent 5 µm. (B) Maximal intensity projection image giving an overview about SNP engulfment efficiency by i-combisomes. Co-localization of membrane fluorescence with SNP fluorescence corroborates wrapping of the SNPs. (C) 3D reconstruction of a single i-combisome (magenta) containing

multiple engulfed particles (cyan) in its lumen in full and cross-sectional view. (D) Attraction and distance reduction and (E) attraction and binding, resulting in cooperative engulfment. Scale bars represent 5 μm (F) Overview images depicting interaction of SNPs with DOPC liposomes, PDMS-*g*-PEO and PB-*b*-PEO polymersomes. Only very little to no interactions could be observed.

Furthermore, the formation of SNP aggregates at the membrane and their cooperative engulfment could be observed (Figure 6.3D). Particles protrude into the lumen of the GUVs and co-localization of the particle fluorescence with the membrane fluorescence indicates a wrapped state of the SNPs. Within seconds, the SNP complexes move towards each other and, in some cases, eventually bind together and are engulfed as a whole (Figure 6.3E). This sort of membrane mediated cooperative engulfment process has been previously described and observed in literature with GUV systems consisting of lipids.[48-53] When the particles indent into the interior of the GUV lumen, they cause local membrane deformation, bending it inwards. This perturbs the global membrane curvature and increases the bending energy of the membrane. This curvature change mediates long-range attractive forces between the particle complexes with the goal to minimize the membrane curvature energy. Consequently, a strong attractive potential can surpass short-ranged repulsion leading to a membrane-mediated particle assembly and formation of bigger aggregates at the bilayer membrane. Importantly, in the absence of i-combisomes, SNP aggregation was not observed. In stark contrast to these results, no particle engulfment was observed when SNPs were brought into contact with GUVs formed from DOPC lipids, PDMS-*g*-PEO and PB_{33}-*b*-PEO_{73} copolymers. This was expected in the case of PB_{33}-*b*-PEO_{73} polymersomes, which have thicker and more rigid membranes that require significantly higher adhesion energies for the onset of engulfment. Nevertheless, PDMS-*g*-PEO polymersomes and DOPC liposomes have highly flexible membranes with κ values of 11.7 $\kappa_B T$ and 19 $\kappa_B T$, respectively. As mentioned earlier, while engulfment may be thermodynamically plausible, especially for highly flexible membranes, the successful completion of the process is often hindered due to kinetic barriers imposed by the intermediate stages. Namely, these stages include strong curvature inversion during membrane wrapping and neck formation (Figure 6.1) and crossing the inverse micellar intermediate during fission of the neck. Notably, to the best of our knowledge, in spite of the highly flexible nature of liposomes, they achieved complete nanoparticle engulfment only above a threshold salt concentration of 10 mM.[54] In this case, the addition of ions shields the

repulsion of the zwitterionic headgroups, which allows them to come closer together and better accommodate the extreme curvatures of the intermediate stages.[25-27] Therefore, it can be concluded that flexibility is essential but in itself not sufficient for predicting engulfment.

6.2.3.2 Visualizing the i-combisome-SNP Interactions at the Nanoscale

To gain more insight into the phagocytic uptake process of SNPs by the i-combisomes, we followed the transport process across the membrane at the nanoscale using cryo-TEM. In addition, we intend to verify whether the other GUV systems really did not achieve engulfment or whether imaging with CLSM failed due to the small size of the particles, which requires highly concentrated particle regions for visualization. Before vitrification, GUVs were mixed with the SNPs and let to incubate for 3 min. In the case of DOPC liposomes, PDMS-*g*-PEO and PB-*b*-PEO polymersomes, we did not observe particle engulfment as shown in Figure S6.6. In the case of the i-combisomes, it was possible to visualize intermediate steps in the engulfment of individual or an assembly of SNPs, allowing us to further detail-down the mechanism of SNP internalization. As shown in Figure 6.4A, a sufficiently strong attractive interaction between the SNP and the membrane triggers an inward bending of the membrane and leads to a more profound invagination of the membrane. The particle becomes almost fully wrapped forming a narrow membrane neck (constriction). Specially this intermediate step requires extreme curvatures, which our i-combisomes appear capable of accommodating. Furthermore, complete engulfment requires the fission of the membrane rims around the particle (neck fission) so that it can detach from the main membrane. The 3D intensity plot image in Figure 6.4A clearly shows that particles engulfed within the lumen are surrounded by an i-combisome membrane (blue), confirming successful neck fission and crossing of all engulfment intermediate stages. Furthermore, it can be observed that even smaller vesicles are able to completely engulf multiple SNPs (Figure 6.4C), which underscores the significant potential of the i-combisomes to execute accelerated artificial phagocytosis. Notably, when the local concentration of the SNPs is very high, complete engulfment was impeded in some of the cases (Figure 6.4D). This is due to the substantial contribution of area expansion to the membrane's elastic energy. When multiple SNPs interact at the same time with the membrane, the indentation of these particles on the membrane consumes

membrane leading to an increase in tension, which ultimately hinder the complete engulfment of these particles.

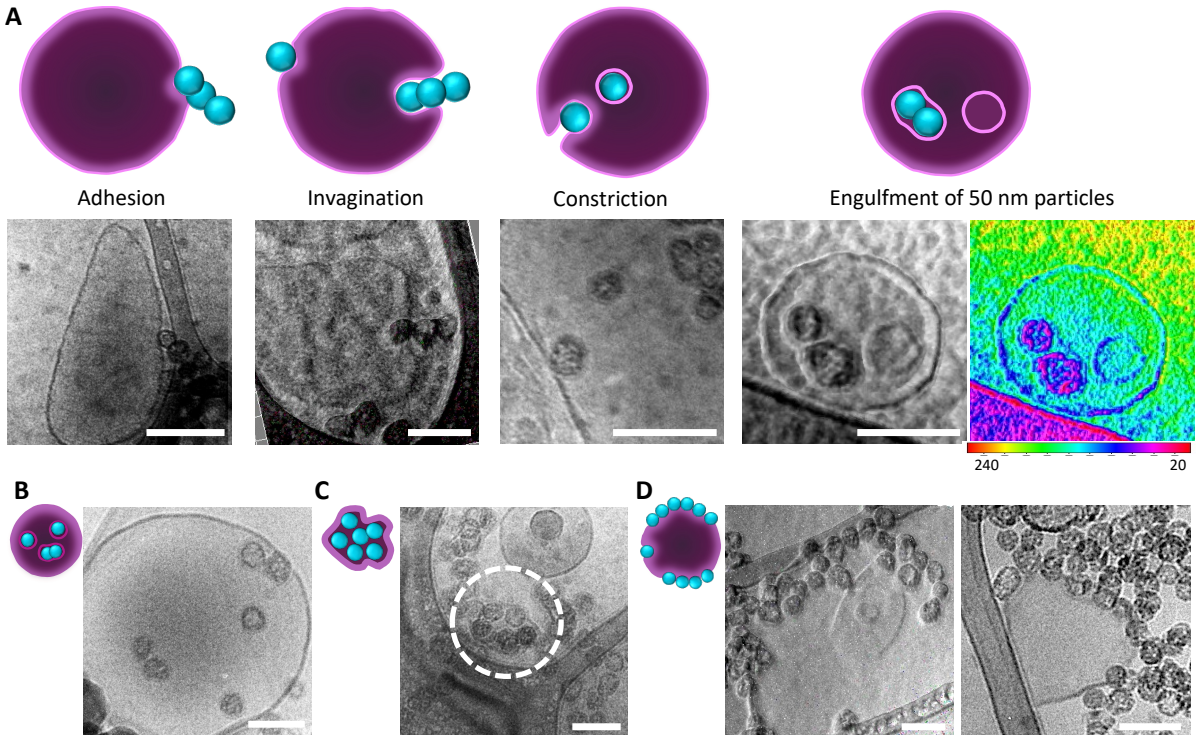

Figure 6.4. Cryo-TEM micrographs depicting the process of phagocytic uptake of SNPs. (A) i-combisome before interaction with SNP, adhesion step of SNP (bending of the bilayer membrane at the contact point), invagination and complete engulfment with release of endosomes with SNPs inside the i-combisome. With an increasing local concentration of SNPs, we observed (B) internalization of single or grouped SNPs , (C) deformed i-combisome membranes after internalization of several SNPs, (D) hindered engulfment due to a reduction of the excess membrane area by the high number of membrane-bound SNPs. Scale bars represent 100 nm.

In a smaller fraction of our samples, we observed SNPs tightly enveloped by an i-combisome bilayer, yet located outside the vesicle lumen, moving in the vicinity of the GUV (Figure 6.5B). Based on the visualization of intermediate steps, we hypothesize that the initial stage involves an SNP adhering to the i-combisome membrane. As the particle becomes partially wrapped by the membrane, the membrane lacerates, likely in a region with the highest curvature, causing a local perturbation of the bilayer (Figure 6.5A). The complete wrapping of the particle then continues until the wrapped particle detaches from the main vesicle and the membrane pieces reattach (Figure 6.5B). It is important to note, that this mechanism was rarely observed

and only a small number of particles were found wrapped outside the vesicles, in comparison to the high rate of particles that are internalized within intact vesicles (see CLSM and cryo-TEM images, Figure 6.3 and Figure 6.4). Furthermore, we believe that this process appears to cause only a transient local laceration of the membrane, rather than a complete rupture of the i-combisome.

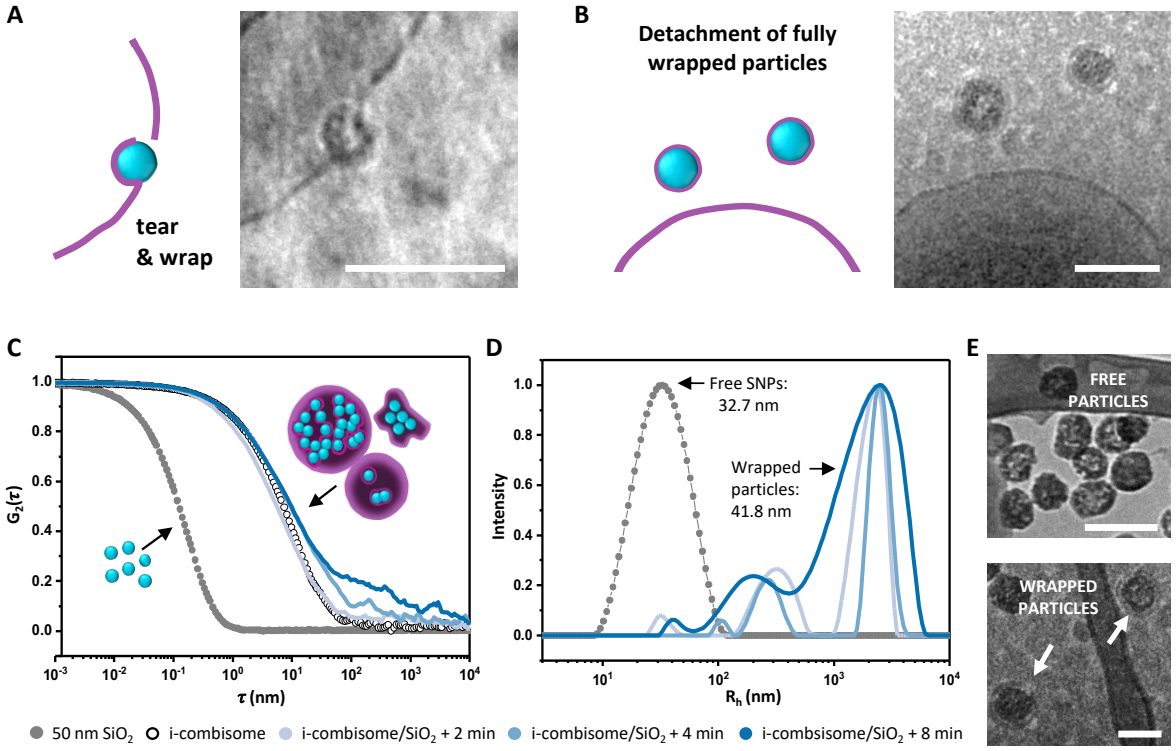

Figure 6.5. Schematic representation and cryo-TEM micrographs of (A) the membrane laceration event while wrapping process and (B) detachment of completely wrapped SNP by the bilayer. Scale bars represent 100 nm. (C) Normalized DLS-ALV correlation functions and (D) size distribution of SNPs (grey filled dots), i-combisomes (black hollow dots), mixture of SNPs with i-combisomes measured after 2 min (light blue), after 4 min (sky blue) and after 8 min (dark blue). (E) Cryo-TEM micrographs show free SNPs and SNPs wrapped with i-combisome bilayer (endosome) coinciding with DLS-ALV results. Scale bars represent 50 nm.

6.2.3.3 Dynamics and Efficiency of SNPs Uptake

We further investigated the dynamics and efficiency of engulfment by the i-combisomes using DLS. The DLS autocorrelation functions and size distribution profiles are illustrated in Figure 6.5 and Figure S6.7. For the experiments, 0.2 mL of the GUV solution with $c_{polymer}$ = 1 mg·mL^{-1} was added to 1.5 mL of a SNPs solution with a concentration of 0.26 mg·mL^{-1}. Measurements

were run every two minutes during one hour. A pure dispersion of SNPs in water showed a mono exponential relaxation corresponding to the simple diffusion of particles with a mean hydrodynamic radius of 32.7 nm. When the i-combisomes were mixed with the SNPs, an immediate shift of the correlation function toward longer decay times of the i-combisomes was observed. Strikingly, this is accompanied by an almost complete disappearance of the size peak corresponding to the population of free SNPs (32.7 nm), indicating that the DLS signals are dominated by a population bigger than the SNPs. These results indicate rapid and extensive interactions between the SNPs and the i-combisomes. Most importantly, when combined with our observations from CLSM and cryo-TEM (*vide supra*), these findings indicate an efficient and accelerated ability of our i-combisomes to perform engulfment. Furthermore, after 8 min there is a shift of the peak corresponding to the free SNPs to 41.8 nm. We attributed this shift to the process of the wrapping of the remaining SNPs with an i-combisome bilayer, as shown in Figure 6.5B and E (wrapped particles). In stark contrast, when comparing the interactions of SNPs with DOPC liposomes, size distribution shows the presence of two distinct populations, namely free SNPs and liposomes. Furthermore, no changes in the SNP size distribution were observed over time, indicating no interaction events between liposomes and SNPs even after prolonged incubation. As a result, the autocorrelation function falls into an intermediate region between the signals of the free SNPs and the liposomes. In a similar vein, when utilizing block and graft polymersomes, no interactions could be identified (Figure S6.7).

6.2.4 Artificial Phagocytosis of Microparticles

Furthermore, we investigated whether the i-combisomes could also efficiently engulf micron-sized particles (MPs). For these experiments, we used silica (SiO_2), carboxyl-functionalized PS and amine-functionalized PS MPs with a diameter of 1 µm.

The i-combisomes were able to engulf the carboxyl-functionalized SiO_2 MPs immediately after mixing as observed by CLSM. As shown in Figure 6.6.B, most of the i-combisomes contained one or multiple particles in their lumen. Notably, the engulfed particles were tightly wrapped with an i-combisome bilayer, confirming MP uptake through the endocytic process, including invagination, membrane wrapping until formation of a closed membrane neck and neck fission with endosome release as depicted in Figure 6.6.A. This highlights the exceptional

capability of the i-combisomes to progress successfully through all intermediate stages of engulfment, culminating in the successful release of the endosome.

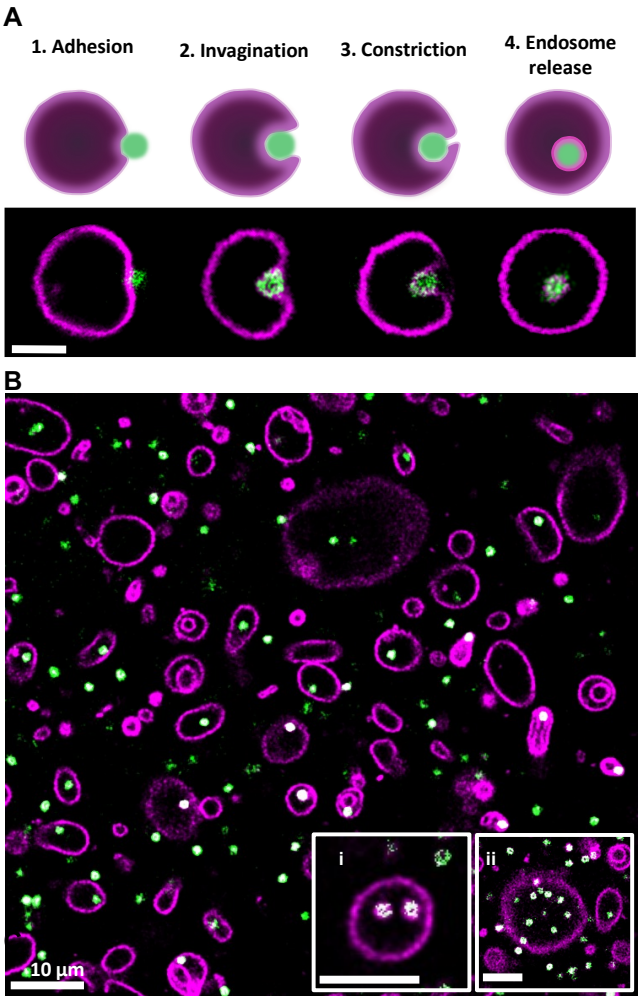

Figure 6.6. (A) Schematic representation and CLSM images depicting the mechanism and sequence of MP (green) engulfment by i-combisomes (magenta): 1) Adhesion, 2) invagination, 3) complete wrapping with neck formation and 4) neck fission with release of an endosome. (B) Overview image showing a large population of i-combisomes containing at least one engulfed microparticle in their lumen. i) Engulfed Silica MPs are wrapped by a i-combisome bilayer, ii) large i-combisomes are capable of engulfing many particles. Scale bars represent 6 µm.

Furthermore, we also observed a rapid and high rate of engulfment of PS MPs. Co-localization of membrane fluorescence with particle fluorescence from CLSM images demonstrated that 74% and 98.5% of the carboxyl- and amine-functionalized PS MPs, respectively, were wrapped with an i-combisome bilayer. However, we also observed a great number of wrapped particles outside the vesicle lumen. We hypothesize, that during engulfment of these particles, the

membrane lacerates due to an increase in membrane tension. It should be noted, that the i-combisome membrane gradually increases its surface tension, due to membrane consumption upon the engulfment of particles. Thus, we analyzed if deflated membranes with a reduced membrane tension, are able to engulf more particles to their interior. The GUVs were formed by the electroformation method in a 25 $mOsm \cdot kg^{-1}$ sucrose solution. These GUVs were then dispersed in a glucose solution with a slightly hypertonic value of 27 $mOsm \cdot kg^{-1}$. This slight osmotic imbalance drives the deflation of the vesicles, resulting in very low tensions. These floppy GUVs were then mixed with carboxyl-functionalized PS MPs.

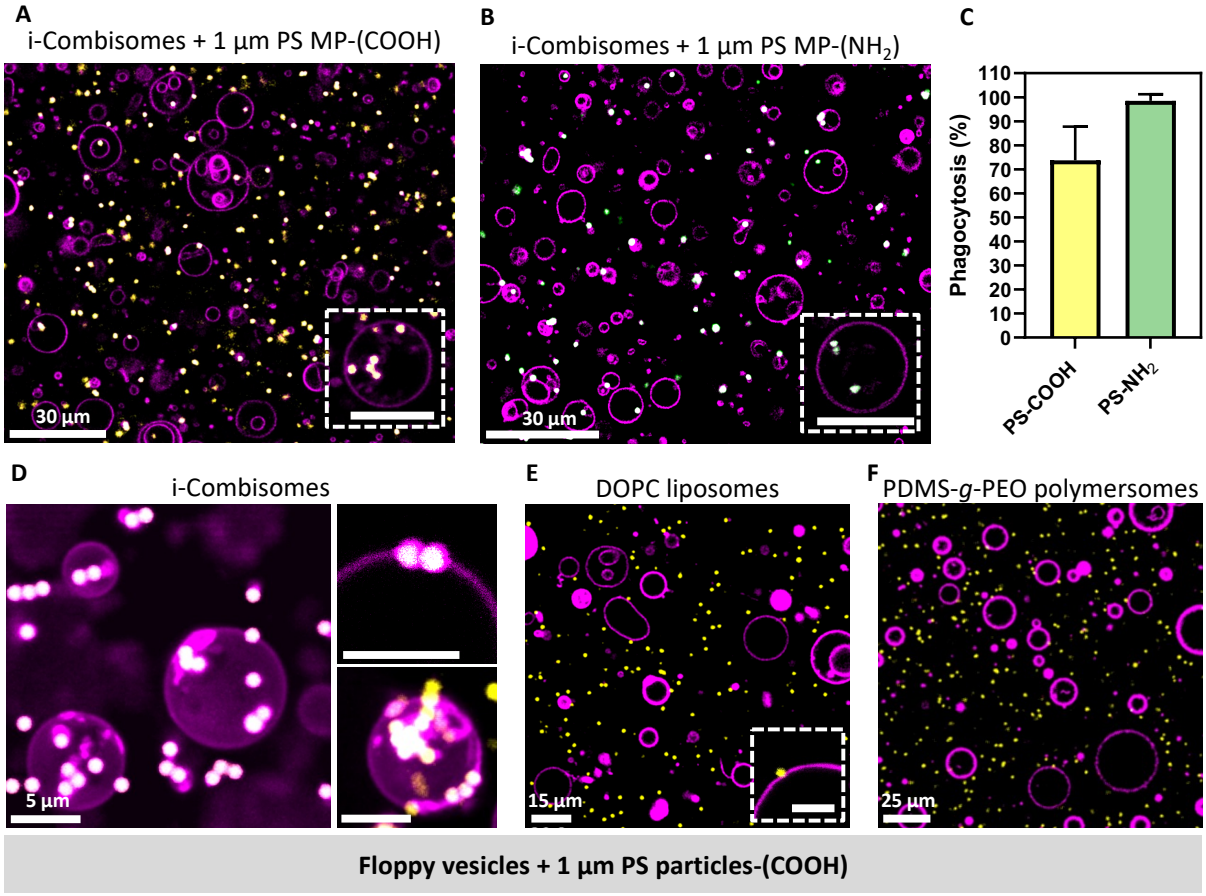

Figure 6.7. Engulfment of (A) carboxyl-functionalized and (B) amine-functionalized PS MPs. Scale bars in zoom-ins represent 10 µm. (C) Quantification of particle wrapping from the co-localization of membrane (magenta) and particle fluorescence (yellow and green) from CLSM images. Engulfment of carboxyl-functionalized particles by floppy GUVs from (D) i-combisomes, (E) DOPC liposomes and (F) PDMS-*g*-PEO polymersomes. Scale bars in zoom-ins represent 5 µm.

As shown in Figure 6.7D, we observed i-combisome GUVs with multiple particles engulfed inside their lumen. Moreover, we could also visualize the cooperative engulfment of particle assemblies as it was described before. From CLSM analysis, we estimate to find more particle engulfed inside the GUVs compared to previous observation utilizing tense GUVs (*vide supra*). However, further quantification studies need to be performed to reach a more precise conclusion. Nevertheless, in the case of DOPC liposomes and PDMS-*g*-PEO polymersomes, we did not observe MP engulfment even in the presence of floppy GUVs (Figure 6.7E and F).

6.2.5 Unraveling the Mechanism Underlying the Superior Phagocytic Ability of the i-combisomes

Our i-combisomes demonstrate remarkable and unparalleled engulfment efficiency for nano- and microparticles with different surface chemistries. Notably, high efficiencies were observed within just a few minutes of contact. When comparing our results to other cell mimics, even those that are equally or more flexible than our i-combisomes, it is evident that i-combisomes exhibit a distinct superiority for the execution of accelerated artificial phagocytosis. But, how do i-combisomes achieve this quantitative, spontaneous phagocytic uptake? Our initial hypothesis proposed that the non-directional nature of the ionic bonds between hydrophilic and hydrophobic parts allows for dynamic local reorganization of the iCPs, which helps the i-combisomes to better accommodate the intermediate steps of engulfment, potentially reducing the kinetic barrier and facilitating successful complete engulfment. While this mechanism certainly contributes to the heightened engulfment capacity of our i-combisomes, our remarkable results prompt us to consider the possibility of another overriding factor at play.

In a recent publication, Anđela Šaric et al. demonstrated that the sparse inclusion of membrane components with positive and negative spontaneous curvature, such that the total spontaneous curvature of the multicomponent membrane remains at zero, can strongly influence the engulfment capacity of membranes.[55] They explained that especially the inclusion of components with negative curvature are the ones that are recruited to the membrane wrapping region during engulfment and are able to reduce the energetic cost of engulfment by several tens of $\kappa_B T$. As such, the expression of curved inclusion within the membrane represents a compelling general mechanism for modulating particle engulfment in

synthetic cells. And in fact, living cells possess inherently heterogeneous membranes characterized by an asymmetric distribution of lipids, proteins and sugars with diverse geometrical properties. The interplay among these molecules with distinct geometrical shapes plays a fundamental role in modulating membrane curvature and facilitating shape transformation.[55-58]

This led us to wonder if there was a similar effect behind the greater ability of our i-combisomes to engulf. The iCPs were designed to have a density of hydrophobic tails (DDP) and a packing arrangement that leads to flat membranes with zero spontaneous curvature. However, the nature of the copolymerization inevitably leads to a statistical ensemble of the poly(CBAA-*co*-DMAPAA) chains, placing our iCPs within the family of random heteropolymers. This entails that both monomers are arranged in a random order with no specific sequence along the polymer chains with local regions rich in CBAA or DMAPAA (intra-chain heterogeneity, Figure 6.8) and the presence of molecules with different sequence and percentages of CBAA and DMAPAA monomers (interchain heterogeneity). Upon the complexation with the hydrophobic DDP ligand, this results in iCPs with different distributions and contents of hydrophobic moieties within one batch. As shown in Figure 6.8B, the heterogeneous iCPs are symmetrically distributed around the average desired molecule composition, which represents the majority and has zero curvature. However, there are also molecules at the opposite extremes of the distribution that exhibit extreme proportions of the hydrophobic ligand, which is due to their different DMAPAA contents. These molecules have opposing molecular topology with packing parameter (PP) different than 1 and can be visualized as wedges imparting positive (PP < 1) or negative curvature (PP > 1).

Hence, we hypothesize that the self-assembly of iCPs into i-combisomes in water results in bilayers of heterogeneous composition with a combination of different amphiphile topologies, leading to membrane regions with local spontaneous curvatures different from the global membrane curvature, i.e., local-mean mismatch of curvature.[59-60] In the membrane, the curved molecules are forced into a strained non-ideal conformation that may be considered as “loaded springs”, i.e., the membrane stores elastic potential that favor the engulfment process (Figure 6.8.C).

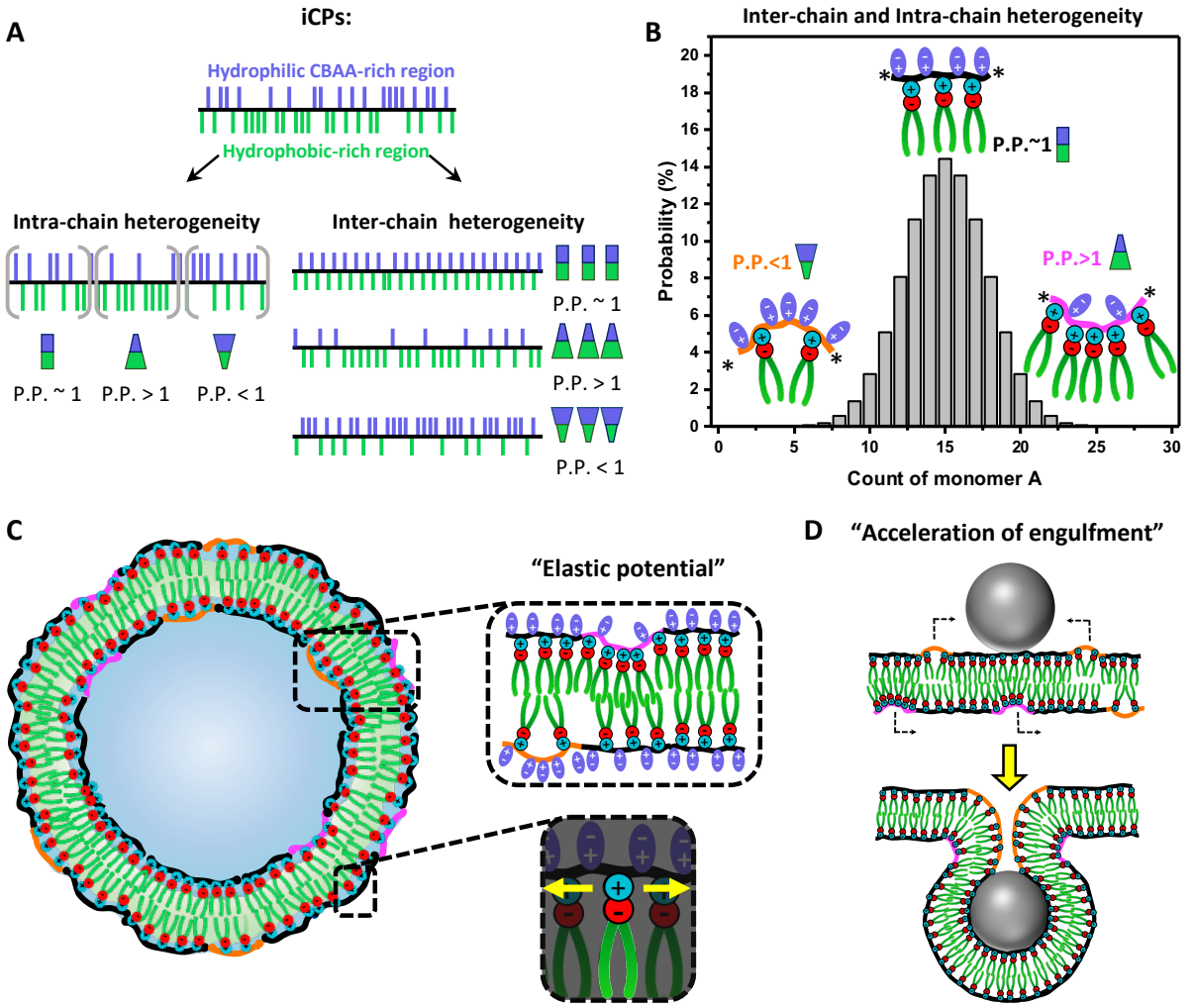

Figure 6.8. (A) Schematic representation and (B) probability calculation of the polymer sequence heterogeneity of the iCPs forming a combination of different amphiphile topologies. (C) Self-assembly of iCPs into i-combisomes forms membranes with local regions of positive and negative curvature. (D) Upon engulfment process, polymer chains with desirable curvature are recruited to the contact area facilitating bending of the membrane and thereby reducing energy barriers for engulfment.

We hypothesize that during the engulfment process, these molecules can migrate towards the regions on non-zero curvature and release their stored potential energy, facilitating local deformations of the membrane and consequently reducing the energy barriers for engulfment, as shown in Figure 6.8.D. We believe that this effect, coupled with high flexibility and lateral mobility, gives the i-combisomes the outstanding ability for accelerated "Artificial Phagocytosis". This concept is unprecedented and establishes our i-combisomes as a pioneering system of "Phagocytic Synthetic Cells" (PSCs).

6.3 Conclusion

We introduced a new family of “Phagocytic Synthetic Cells” based on iCPs that exhibit unprecedented accelerated engulfment capabilities. Using CLSM, cryo-TEM and DLS, we demonstrated massive engulfment of nano- and micron-sized particles with different surface chemistries based exclusively on physical interactions and without the need of external energy input. From these experiments, we discovered that the mechanism underlying their improved engulfment capabilities does not only rely on its excellent flexibility akin to natural membranes, but is rather based on the heterogeneous composition of the membrane including different amphiphile topologies. The nature of the radical polymerization of our iCPs give rise to molecules with a random sequence distribution and compositional polydispersity. The opposing extremes of this distribution is represented by a small population of iCPs that are rich on either hydrophilic CBAA or hydrophobic DDP moieties giving rise to molecules with different packing parameters and opposing spontaneous curvature. The mixture of these molecules with the mean average molecule exhibiting zero curvature leads to membranes that contain local-mean mismatches of curvature. In the membrane, these curved molecules are in a strained non-ideal configuration, endowing the membrane with an elastic potential. During the process of engulfment, these molecules migrate towards the contact area, facilitating membrane deformation necessary for the engulfment process.

Notably, our results agree with theoretical and experimental analysis accounting for the formation of local bilayer curvature mismatches induced by a heterogeneity in polymer sequence[61] and enhanced cargo trafficking with membranes including components with curvature.[55]

We envision that the unparalleled phagocytic potential of our PSCs could open up a new approach to combat pathogenic microbes.

6.4 Materials and Methods

6.4.1 Materials

All reagents were of analytical grade and used as received unless otherwise stated. Solketal, D,L-1,2-Isopropylideneglycerol, Copper(II) bromide, Me_6TREN, BODIPY FL, Nile Red, Sucrose and Glucose were purchased from Sigma Aldrich Chemie GmbH. CBAA was synthesized according to literature procedures.[62] DMAPAA, 2-Bromoisobutyryl-bromide and anisole were purchased from TCI Deutschland GmbH. Anhydrous THF was purchased from Fisher Scientific GmbH. Anhydrous methanol, chloroform, DMSO and triethylamine were obtained from Acros Organics™. DOPC and 16:0 LissRhod PE lipids were purchased from Avanti Polar Lipids, Inc. PB_{33}-*b*-PEO_{73} was acquired from Polymer Source, Inc. PDMS-*g*-PEO (DOWSIL™ OFX-5329 Fluid) was kindly provided by Dow Chemical. Sicastar® SNPs and MPs particles were supplied by Micromod Partikeltechnologie GmbH. PS MPs were purchased from Polysciences, Inc.

DOWSIL™ OFX-5329 Fluid. Dow Corning 5329 was a kind gift from Down Corning and it consists of a PDMS chain decorated with two arms of PEO, each averaging about 12 monomers in length. According to the data provided by the supplier, the weight fraction of ethylene oxide is 47% and the average viscosimetric molecular weight is 3000 $g \cdot mol^{-1}$.

6.4.2 Synthesis and Fabrication Methods

Synthesis of the CBAA-co-DMAPAA copolymer. A Schlenk flask was equipped with a magnetic stirring bar and $NaBH_4$ (1.4 mg, 0.03 mmol, 0.4 eq.) as well as $CuBr_2$ (16.6 mg, 0.074 mmol, 0.8 eq.) were added. In a separate vial Milli-Q-water (1.00 mL) and Me_6TREN (29.8 µL, 0.111 mmol, 1.2 eq.) were mixed. Both vessels were sealed and degassed by sparging with argon for 30 min. The degassed solution was transferred under inert atmosphere to the solids under vigorous stirring and the formation of Cu(0)-particles was allowed to proceed for 30 min at 0 °C. Simultaneously, (3-Acryloylamino-propyl)-(2-carboxy-ethyl)-dimethyl-ammonium (CBAA; 9, 15 and 21 eq.), *N*-[3-dimethylamino)propyl] acrylamide (DMAPAA; 9, 15 and 21 eq.) and the initiator (22.4 mg, 0.093 mmol, 1.0 eq.) were dissolved in water (2.48 mL), degassed with argon for 30 mins at 0 °C and transferred under inert gas atmosphere to the Cu(0)-particles. The polymerization was stirred at 0 °C for 30 min. The polymerization was rapidly quenched by bubbling with air and freezing with liquid nitrogen. The polymer was purified by

removal of the Cu(0)-particles and dialysis for 2 days against an aqueous hydrochloride solution (pH = 5, 3x water change/day, MWCO = 1 kDa). Freeze-drying yielded the purified copolymer as colorless solid.

Synthesis of PSCs. CBAA-*co*-DMAPAA copolymer ($DP_{85}N_{57}$, 10 mg, 0.053 mmol, 0.03 $mmol_{DMAPAA}$, 1 eq.) was dissolved in MeOH at 10 $mg \cdot mL^{-1}$ and added to a vial with a magnetic stir bar. DDP (13.23 mg, 0.03 mmol, 0.57 eq.) was dissolved in $CHCl_3$ at 40 $mg \cdot mL^{-1}$ and added dropwise to the copolymer solution while stirring to form iCPs via acid-base reaction. After 2 h of stirring the solvent was evaporated yielding the iCPs as a colorless gel. Finally, the iCPs were dissolved in $CHCl_3$ at 10 $mg \cdot mL^{-1}$. Quantitative substitution was achieved by mixing molar equivalents of the DDP and DMAPAA.

Vesicle preparation by thin-film rehydration. GUVs from iCPs, DOPC, PB_{33}-*b*-PEO_{73} and PDMS-*g*-PEO were self-assembled via TFH. Polymers and lipids were dissolved in $CHCl_3$ at 10 $mg \cdot mL^{-1}$. 30 µL of the solution were then mixed with 0.1 mol% of dye and deposited on a roughened Teflon plate. The plate was dried at room temperature, followed by 2 h in vacuo. Afterwards, it was placed in a small vial and 300 µL of Milli-Q water were added to rehydrate the dry film yielding a vesicle solution of $c_{polymer}$= 1 $mg \cdot mL^{-1}$. The vial was then placed at 60 °C overnight. For PB_{33}-*b*-PEO_{73} polymersomes the vial was placed overnight at 80 °C.

6.4.3 Analytical Methods

Nuclear magnetic resonance spectroscopy. NMR spectra were recorded at room temperature using a Bruker AvanceIII 400. MestReNova V.12.0.1 was used for Spectra analysis. The chemical shifts are reported in δ units relative to the solvent residual peak (D_2O: δ_H = 4.79 ppm, $CDCl_3$: δ_H = 7.26 ppm, δ_C = 77.16 ppm, CD_3OD: δ_H = 3.31 ppm, δ_C = 49.0 ppm)[63].

Size exclusion chromatography (SEC). The weight-average molecular weight (M_wSEC), the number-average molecular weight (M_nSEC), and the polydispersity index (M_n/M_w; PDI) were determined by SEC. Samples were measured on an Agilent-1200 system, equipped with a degasser, isocratic pump, manual injection valve and refractive index detector. A Novema Max Lux column (PSS) was used with NaCl (0.1 M), TFA (0,3 Vol%) and NaN_3 (0,01w%) as eluent to achieve separation. Calibration was performed with commercial poly(ethylene glycol)

standards in the range from 238 Da to 504 kDa. Ethylene glycol (Sigma Aldrich) was used as internal standard. Samples of 25 µL were injected at room temperature with a concentration of 5 mg·mL^{-1}. Data analysis was done with PSS WinGPC UniChrom software (Version 8.1.1).

Determination of membrane thickness by cryo-TEM. Vesicle membrane thickness was determined from cryo-TEM micrographs taken on a Zeiss Libra® 120 transmission electron microscope (Oberkochen, Germany). 4 µL of the aqueous vesicle dispersion (1 mg·mL^{-1}) was deposited onto a plasma-treated lacey grid and plunge frozen in liquid ethane using a FEI Vitrobot (Model Mark IV. The vitrified specimens were transferred to a Gatan-910 cryo-holder. Images were recorded using an incolumn Omega energy filter with a CCD detector at a temperature of −168 °C with an applied electron beam acceleration voltage of 120 kV. The bilayer thickness was determined at 15 different spots utilizing ImageJ.

Determination of membrane fluctuation. We determined the undulations of the different GUV membranes by CLSM as previously described by our group.[40] GUVs of i-combisomes, DOPC liposomes, PB_{33}-*b*-PEO_{73} and PDMS-*g*-PEO polymersomes were prepared by TFH with the addition of 0.1 mol% BODIPY as fluorescent probe. 16 µL of the vesicle solution in water (1mg mL^{-1}) were mixed with 4 µl of 10 mM HEPES to obtain deflated and fluctuating vesicles. The vesicles were then transferred to a chamber consisting of two precision cover glasses and a 2 mm thick Teflon spacer. The GUVs were observed with a 63x/1.40 glycerol-immersion objective and images of the fluctuations were acquired at a resolution of 512 x 512 pixels and a scanning speed of 1000 Hz. Contour analysis will be discussed below in the section of

Determination of lateral mobility. The diffusion coefficient was determined from the analysis of FRAP as previously reported.[40] Vesicles were prepared by electroformation with the addition of 0.1 mol% of 16:0 LissRhod PE as fluorescent probe. Floating vesicles were imaged at a resolution of 256 x 256 pixel frame in the bidirectional scan mode at a scanning speed of 1800 Hz. Using a nominal bleaching radius of r_n = 2.5 µm bleaching was performed for 10 frames using maximum laser power. Subsequently, fluorescence recovery was recorded at an attenuated laser power of 1%. The calculation of D from the obtained FRAP data will be discussed in the Supplementary Data section.

Engulfment of SNPs and MPs by CLSM. Images were recorded on a Leica TCS SP8 confocal microscope (Wetzlar, Germany) with a 63x/1.40 glycerol-immersion objective and PMT or HyD

detectors. Temperature was kept constant at 22 °C. In the case of SNP, interactions were studied at different NP concentrations . For high concentration studies, 18 µL of the aqueous GUV dispersion ($c_{polymer}$ =1 mg·mL^{-1}) was mixed with 2 µL on the NPs solution in Milli-Q water at c = 10 mg·mL^{-1} and measured immediately. Further, SNP were prepared at c = 2 mg·mL^{-1} and 4 µL of this solution was spiked with 16 µL of the GUV dispersion. Lastly, low concentration experiments were performed by mixing 2 µL of the SNP solution at c = 2 mg·mL^{-1} with 18 µL of the GUV dispersion. In the case of the SiO_2 MP 18 µL of the vesicles ($c_{polymer}$ = 1 mg·mL^{-1}) was mixed with 2 µL on MP solution in Milli-Q water at c = 5 mg·mL^{-1} and measured immediately. Post-corrections of all images were performed with the Fiji-ImageJ software.

Engulfment of SNPs by Cryo-TEM. Experiments were conducted by mixing 10 µL of GUVs ($c_{polymer}$ = 1 mg·mL^{-1}) with 75 µL or 1 µL of the SNP at c = 0.2 mg·mL^{-1} and 5 mg·mL^{-1}, respectively. The samples were incubated at room temperature for 5 min and then shaken to avoid sedimentation before preparation for cryo-TEM. Samples were measured at -168 °C with an applied electron beam acceleration voltage of 120 kV on a Zeiss LibraTM 120 transmission electron microscope (Oberkochen, Germany) in cryogenic mode. The samples were vitrified using a FEI Vitrobot (model Mark IV) immersion freezing station by the deposition of 5 µL of the GUV or GUV/particle mixture onto plasma-treated Lacey grids. After blotting and shock freezing in liquid ethane, the samples were transferred to a Model 910 Cryo transfer stage (Gatan, Pleasanton, California). Images were captured using an incolumn Omega energy filter with a CCD detector. 3D intensity-plotting images were created using ImageJ.

Engulfment of SNPs by *DLS.* Experiments were performed at 25.0±0.2 °C using an ALV/CGS3 compact goniometer equipped with an ALV/LSE-7004 Tau Digital Correlator and a JDE Uniphase HeNe laser (wavelength: 632.8 nm) and toluene index matching bath. For the experiments, 0.2 mL of the GUV dispersion ($c_{polymer}$ = 1.0 mg·mL^{-1}) were mixed with 1.5 mL of the SNP dispersion (c = 0.26 mg·mL^{-1}). The glass cuvette was then carefully shaken to allow homogeneous mixing and the measurement was started. Data were collected in automatic mode at 90º scattering angle every 60 s.

6.5 Supplementary Results

Synthesis and molecular characterization of iCPs

Molecular characterization was carried out by SEC (Figure S6.1), ^{1}H-NMR (Figure S6.2) and ^{13}C-NMR (Figure S6.3). The composition as well as the DP of the purified copolymer were calculated from ^{1}H-NMR using the initiator signal 17+18 (1.03 ppm, 6H, 2x CH_3) together with signal 9 of CBAA (3.43 ppm, 2H, CH_2) and signal 14+15 of DMAPAA (2.75 ppm, 6H, 2x CH_3). SEC-analysis in water revealed a PDI = 1.81.

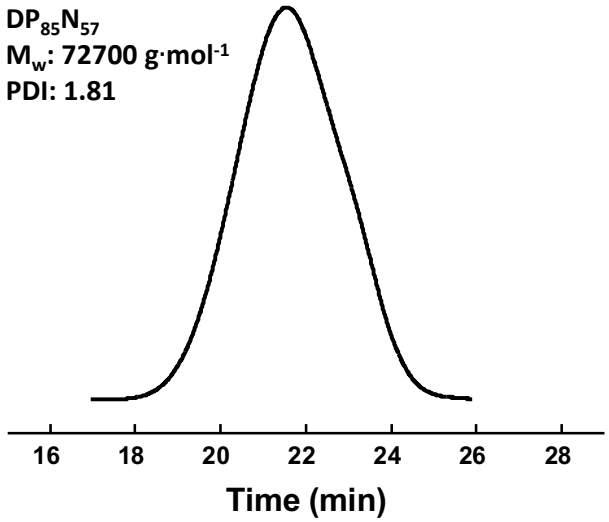

Figure S6.1. SEC elugram for $DP_{85}N_{57}$

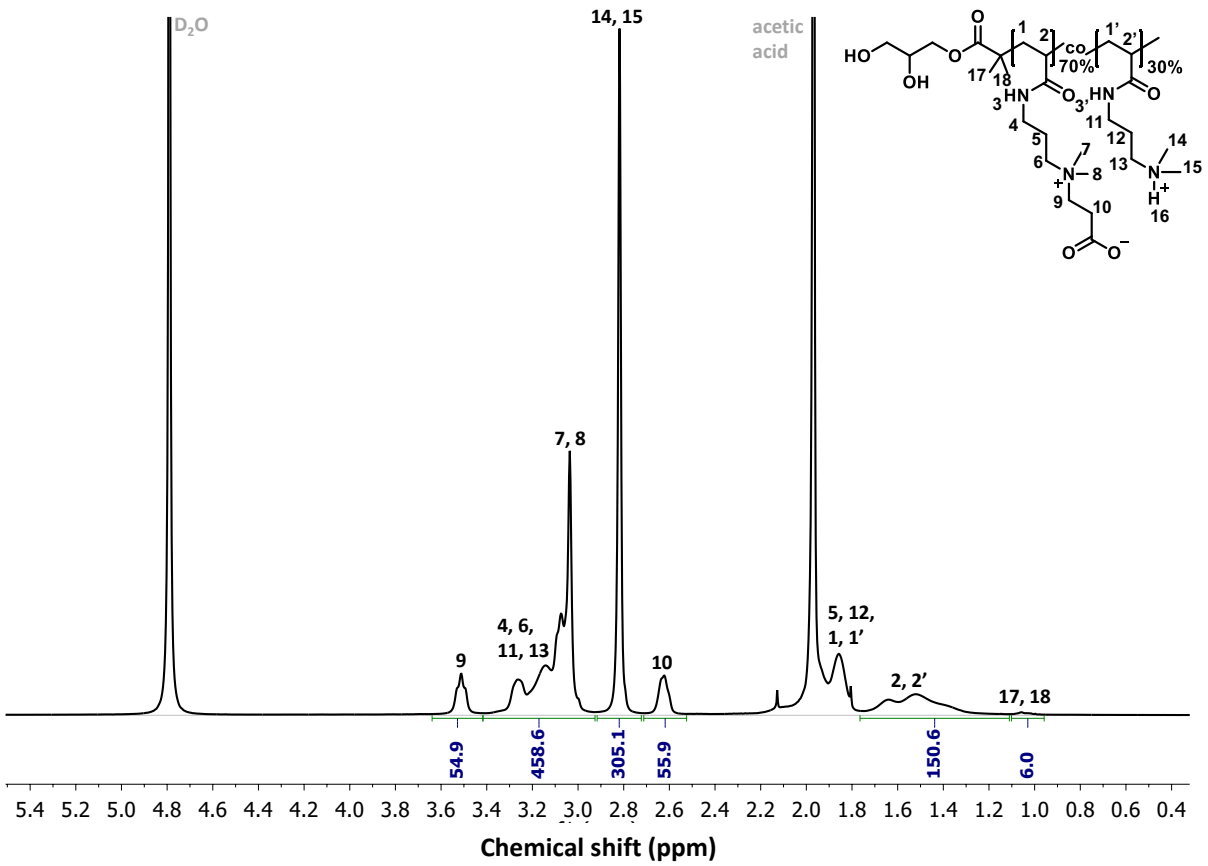

Figure S6.2. ^{1}H-NMR of the synthesized poly(CBAA-*co*-DMAPAA) ($DP_{85}N_{57}$) in D_2O.

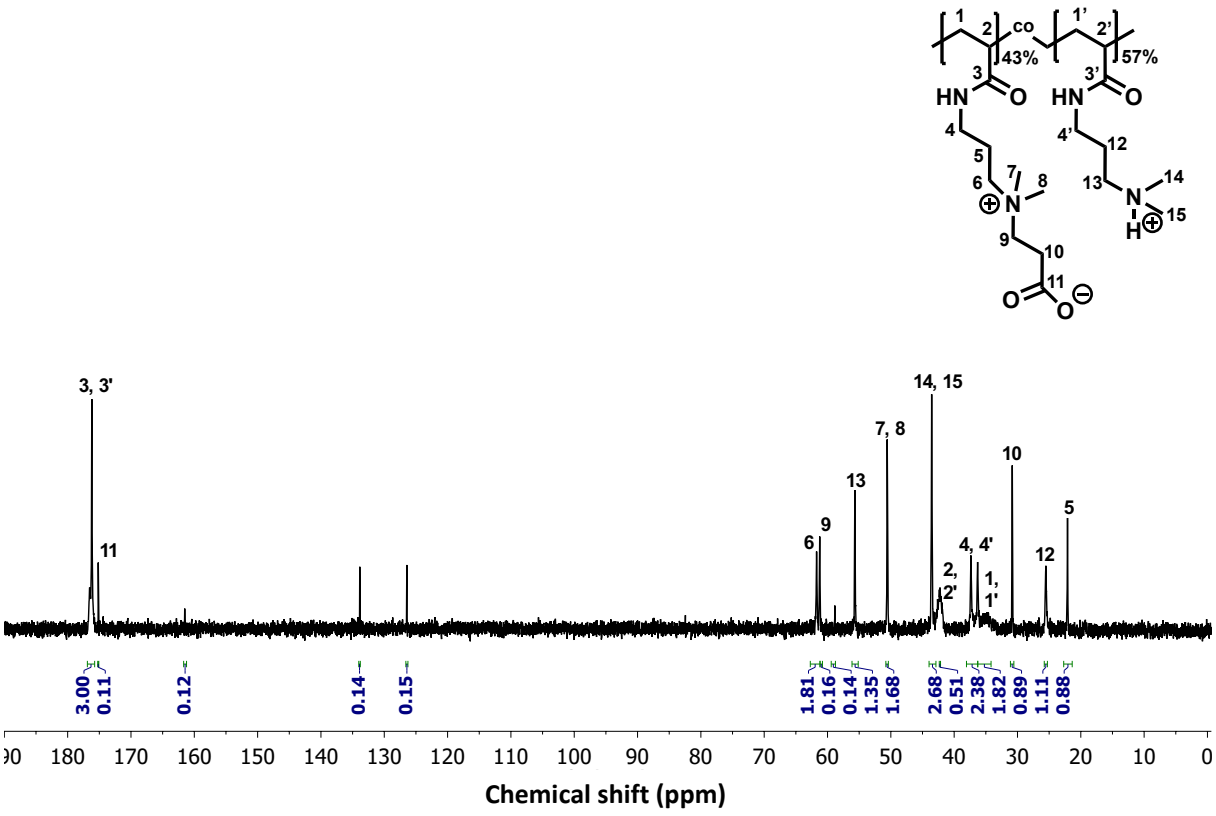

Figure S6.3. ^{13}C-NMR of the synthesized poly(CBAA-*co*-DMAPAA) ($DP_{85}N_{57}$) in D_2O.

Analysis of Membrane Fluctuations

CLSM imaging showed constantly undulating membranes after deflation. To assess the fluctuations, we processed single CLSM images of undulating GUVs with similar size using a custom-made Python script based on a general procedure.[64-65] Objects around the studied GUVs were removed prior to processing with the Fiji ImageJ software.[66] A background image was created for each sample by convolution of a Gaussian kernel (window size of 61 pixels, width σ = 10 pixels). Subsequently, this background was subtracted from the original image. The obtained negative pixels were set to zero. And a second Gaussian kernel (window size of 21 pixels, width σ = 3 pixels) was applied to smoothen the image (Figure S6.4.). A binary image was then created from the results by applying a threshold calculated according to the Otsu´s method.[67] Confluent images with a predefined size range were selected from the binary images. The size range was typically from 500-15000 pixels area for each image, with the center of the mass defining the center of the object. The pixel coordinates were then transformed into polar coordinates and angles relative to the center of the object. A range of angles from 0 to 2π rad was defined with 100 data points. For each of the defined angle bins, the maximum was identified and a local straight line was fitted in both directions from the maximum. The crossing point was used as the corresponding radius.[68] The exported profiles were further processed using R. The mean radius was subtracted from each data set ($\Delta r = r - \langle r \rangle$), which allowed for comparison of the angular profiles. By shifting of $\Delta r(\varphi)$, the zero angle was set to the maximum of the curve (main axis of a prolate) for each vesicle. Afterwards $\Delta r(\varphi)$ was fitted with a series of cosine functions with integer harmonics, where φ is the angle obtained from the data set:

$$\Delta r = \sum_{i=1}^{N} \alpha_i \cdot cos(i\varphi)$$

In the next step, the shape contributions were removed to show the individual fluctuation independent of size and shape.[69-70] To achieve this, the two first harmonics of the cosine series were subtracted, generating $\Delta r(\varphi)'$ from $\Delta r(\varphi)$.

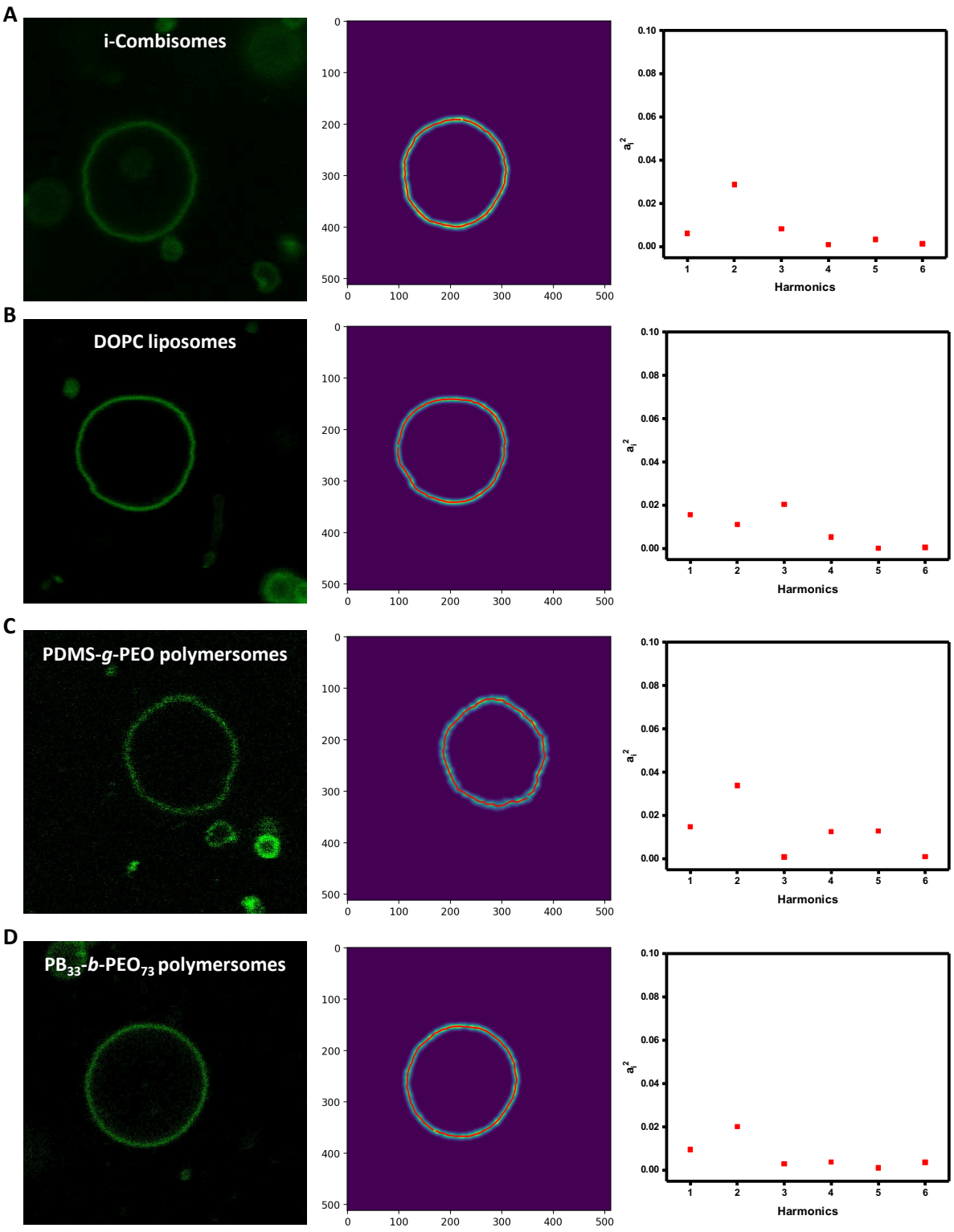

Figure S6.4. Confocal images of an (A) i-combisome, (B) DOPC liposome, (C) PDMS-*g*-PEO and (D) PB_{33}-*b*-PEO_{73} polymersomes (left column). Binary images (central column) and amplitude of the harmonics (right column).

Analysis of the Lateral Mobility

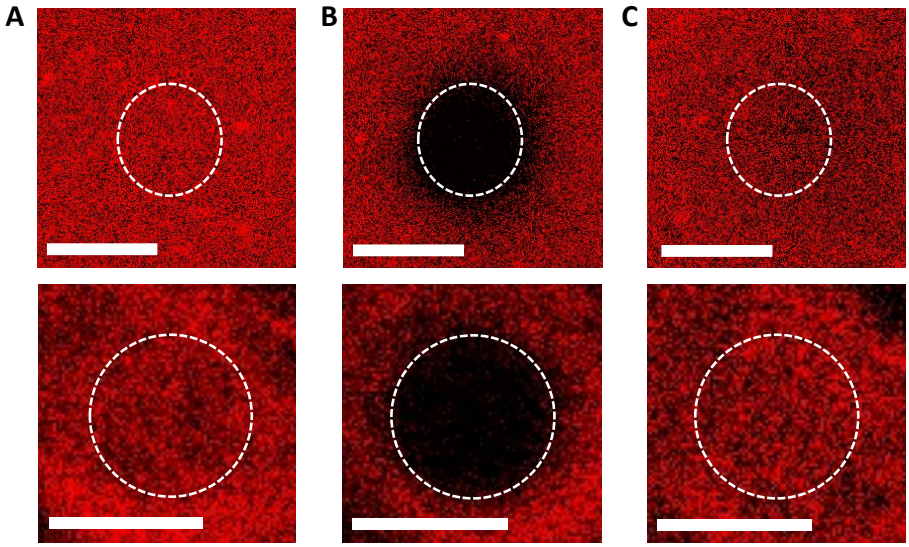

Figure S6.5. FRAP microscopy images of an i-combisome GUV. The stages include (A) pre-bleach (B) photo bleaching and (C) fluorescence recovery. Scale bars represent 5 μm.

The effective bleaching radius r_e was determined from the intensity line profile across the center of the first bleaching spot by using the following fitting equation:

$$f(x) = 1 - K \cdot e^{-\frac{2x^2}{{r_e}^2}} \qquad \textbf{Equation6.3}$$

where K is the bleaching depth. We calculated the time $t_{1/2}$ until half of the fluorescence intensity $F_{1/2}$ recovered from the normalized intensity FRAP curve, using the equation:

$$F_{1/2} = \frac{F_0 + F_\infty}{2} \qquad \textbf{Equation6.4}$$

where F_0 is the fluorescence intensity in the bleached spot of the first frame after bleaching and F_∞ is the intensity after recovery. Using the values for r_e and $t_{1/2}$, we calculated the diffusion coefficients as follows:

$$D = \frac{{r_e}^2 + {r_n}^2}{8t_{1/2}} \qquad \textbf{Equation6.5}$$

Engulfment of SNPs

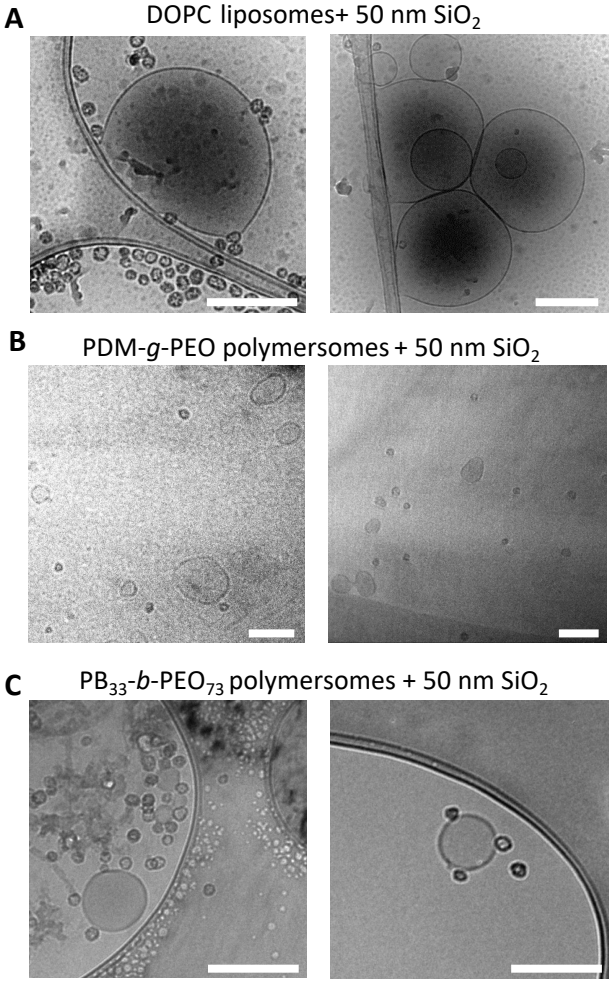

Figure S6.6. Cryo-TEM images after mixing GUVs of (A) DOPC liposomes, (B) PDMS-*g*-PEO and (C) PB_{33}-*b*-PEO_{73} polymersomes with SNPs. No engulfment could be observed.

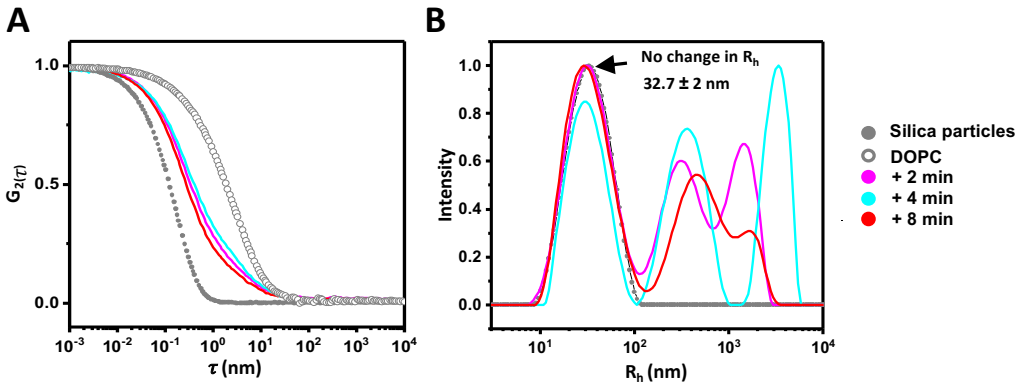

Figure S6.7 (A) Normalized DLS-ALV correlation functions and size distribution of SNPs (grey filled dots), DOPC liposomes (grey hollow dots), mixture of SNPs with DOPC liposomes measured after 2 min (magenta), after 4 min (cyan) and after 8 min (red).

Engulfment of Silica MPs

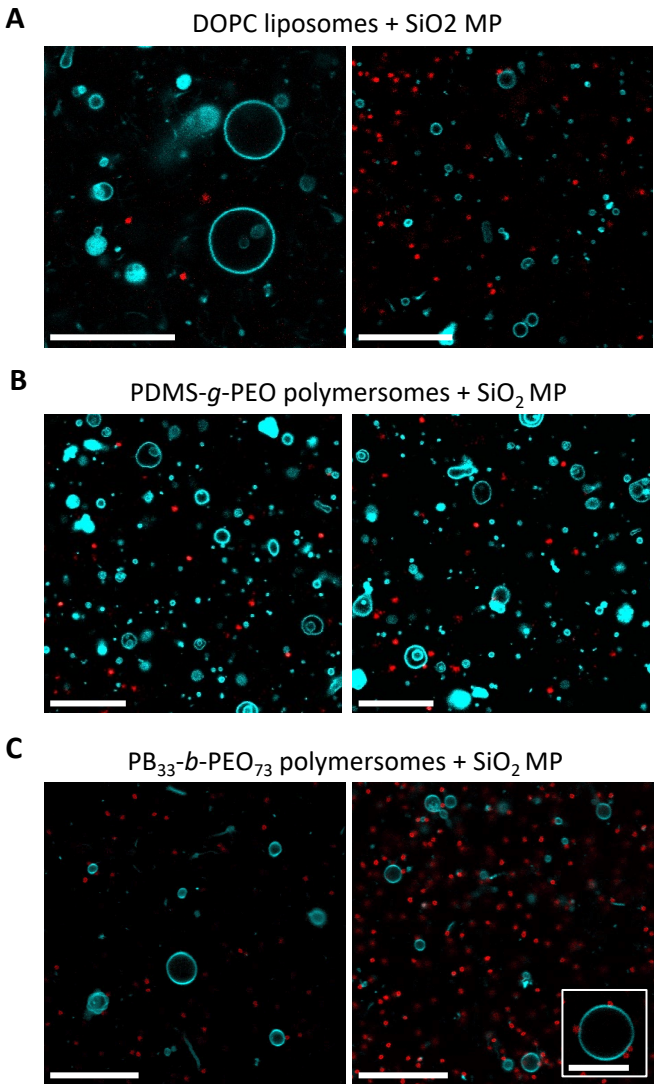

Figure S6.8. CLSM images showing no engulfment of Silica MPs by (A) DOPC liposomes, (B) PDMS-*g*-PEO and (C) PB_{33}-*b*-PEO_{73} polymersomes. Scale bars represent 20 μm. Zoom-in scale bar represents 10 μm.

6.6 Declaration of Contributions

Jonas Quandt synthesized the iCPs and performed NMR and SEC analysis. Anna M. Wagner conducted the FRAP studies and analysis of diffusion coefficients. Membrane fluctuation analysis was conducted by Dominik Söder and Dr. Tamás Haraszti. I performed the cryo-TEM studies for the determination of membrane thicknesses and elucidation of the engulfment process. Additionally, I conducted CLSM experiments including the SNPs. I acknowledge the help of Dr. Nina Kostina in recording and editing the 3D reconstruction image in Figure 6.3C. Furthermore, I conducted CLSM engulfment studies including silica MPs, liposomes as well as polymersomes and PS MPs with i-combisomes, liposomes and polymersomes. The engulfment studies, including the Silica MPs and the i-combisomes were conducted by Fabian Wirtz and me as part of his research internship in our group. DLS experiments were conducted by Dr. Tamás Haraszti and me. Additionally, I would like to acknowledge the assistance of Dr. Tamás Haraszti for the quantification analysis of engulfment from CLSM images.

Data interpretation and conceptual discussions were conducted by Prof. César Rodriguez Emmenegger, Dr. Nina Kostina and me.

Prof. César Rodriguez-Emmenegger supervised this project.

6.7 References

[1] R. C. May, L. M. Machesky, *Journal of Cell Science* **2001**, *114*, 1061-1077.
[2] E. Uribe-Querol, C. Rosales, *Frontiers in Immunology* **2020**, *11*.
[3] S. Kumari, S. Mg, S. Mayor, *Cell Research* **2010**, *20*, 256-275.
[4] M. W. Gray, *Mol Biol Cell* **2017**, *28*, 1285-1287.
[5] L. Wu, L. Li, A. Gao, J. Ye, J. Li, *Aquaculture and Fisheries* **2022**.
[6] K. A. Beningo, Y.-l. Wang, *Journal of Cell Science* **2002**, *115*, 849-856.
[7] N. Martin, J. P. Douliez, Y. Qiao, R. Booth, M. Li, S. Mann, *Nat Commun* **2018**, *9*, 3652.
[8] Y. Qiao, M. Li, R. Booth, S. Mann, *Nat Chem* **2017**, *9*, 110-119.
[9] C. Xu, N. Martin, M. Li, S. Mann, *Nature* **2022**, *609*, 1029-1037.
[10] C. Zhao, J. Li, S. Wang, Z. Xu, X. Wang, X. Liu, L. Wang, X. Huang, *ACS Nano* **2021**, *15*, 10048-10057.
[11] R. Luo, S. Pashapour, O. Staufer, I. Platzman, J. P. Spatz, *Advanced Functional Materials* **2020**, *30*, 1908855.
[12] Z. Li, Z. Wang, P.-U. C. Dinh, D. Zhu, K. D. Popowski, H. Lutz, S. Hu, M. G. Lewis, A. Cook, H. Andersen, J. Greenhouse, L. Pessaint, L. J. Lobo, K. Cheng, *Nature Nanotechnology* **2021**, *16*, 942-951.
[13] C. Sigl, E. M. Willner, W. Engelen, J. A. Kretzmann, K. Sachenbacher, A. Liedl, F. Kolbe, F. Wilsch, S. A. Aghvami, U. Protzer, M. F. Hagan, S. Fraden, H. Dietz, *Nature Materials* **2021**, *20*, 1281-1289.
[14] A. H. Bahrami, M. Raatz, J. Agudo-Canalejo, R. Michel, E. M. Curtis, C. K. Hall, M. Gradzielski, R. Lipowsky, T. R. Weikl, *Adv Colloid Interface Sci* **2014**, *208*, 214-224.
[15] J. Agudo-Canalejo, R. Lipowsky, *ACS Nano* **2015**, *9*, 3704-3720.
[16] J. Agudo-Canalejo, R. Lipowsky, *Soft Matter* **2017**, *13*, 2155-2173.
[17] J. Agudo-Canalejo, R. Lipowsky, *Nano Lett* **2015**, *15*, 7168-7173.
[18] J. Agudo-Canalejo, in *Multiresponsive Behavior of Biomembranes and Giant Vesicles*, **2019**, pp. 195-227.
[19] S. Dasgupta, T. Auth, G. Gompper, *Soft Matter* **2013**, *9*, 5473-5482.
[20] M. Deserno, T. Bickel, *Europhysics Letters (EPL)* **2003**, *62*, 767-774.
[21] H. Bermudez, D. A. Hammer, D. E. Discher, *Langmuir* **2004**, *20*, 540-543.
[22] R. Dimova, U. Seifert, B. Pouligny, S. Förster, H. G. Döbereiner, *The European Physical Journal E* **2002**, *7*, 241-250.
[23] A. Mecke, C. Dittrich, W. Meier, *Soft Matter* **2006**, *2*, 751-759.
[24] E. Rideau, R. Dimova, P. Schwille, F. R. Wurm, K. Landfester, *Chem Soc Rev* **2018**, *47*, 8572-8610.
[25] F. G. Strobl, F. Seitz, C. Westerhausen, A. Reller, A. A. Torrano, C. Bräuchle, A. Wixforth, M. F. Schneider, *Beilstein J Nanotechnol* **2014**, *5*, 2468-2478.
[26] A. C. Greene, I. M. Henderson, A. Gomez, W. F. Paxton, V. VanDelinder, G. D. Bachand, *PLOS ONE* **2016**, *11*, e0158729.
[27] C. Contini, J. W. Hindley, T. J. Macdonald, J. D. Barritt, O. Ces, N. Quirke, *Commun Chem* **2020**, *3*, 130.
[28] H. T. Spanke, R. W. Style, C. François-Martin, M. Feofilova, M. Eisentraut, H. Kress, J. Agudo-Canalejo, E. R. Dufresne, *Physical Review Letters* **2020**, *125*, 198102.
[29] H. T. Spanke, J. Agudo-Canalejo, D. Tran, R. W. Style, E. R. Dufresne, *Physical Review Research* **2022**, *4*, 023080.
[30] E. J. Ewins, K. Han, B. Bharti, T. Robinson, O. D. Velev, R. Dimova, *Chemical Communications* **2022**, *58*, 3055-3058.

[31] C. van der Wel, A. Vahid, A. Šarić, T. Idema, D. Heinrich, D. J. Kraft, *Scientific Reports* **2016**, *6*, 32825.
[32] A. Azadbakht, B. Meadowcroft, T. Varkevisser, A. Šarić, D. J. Kraft, *Nano Letters* **2023**, *23*, 4267-4273.
[33] C. van der Wel, D. Heinrich, D. J. Kraft, *Biophysical Journal* **2017**, *113*, 1037-1046.
[34] T. Eierhoff, B. Bastian, R. Thuenauer, J. Madl, A. Audfray, S. Aigal, S. Juillot, G. E. Rydell, S. Müller, S. de Bentzmann, A. Imberty, C. Fleck, W. Römer, *Proceedings of the National Academy of Sciences* **2014**, *111*, 12895-12900.
[35] K. A. Smith, D. Jasnow, A. C. Balazs, *J Chem Phys* **2007**, *127*, 084703.
[36] M. Wang, A. M. Mihut, E. Rieloff, A. P. Dabkowska, L. K. Månsson, J. N. Immink, E. Sparr, J. J. Crassous, *Proceedings of the National Academy of Sciences* **2019**, *116*, 5442-5450.
[37] N. Y. Kostina, K. Rahimi, Q. Xiao, T. Haraszti, S. Dedisch, J. P. Spatz, U. Schwaneberg, M. L. Klein, V. Percec, M. Moller, C. Rodriguez-Emmenegger, *Nano Lett* **2019**, *19*, 5732-5738.
[38] A. Joseph, A. M. Wagner, M. Garay-Sarmiento, M. Aleksanyan, T. Haraszti, D. Söder, V. N. Georgiev, R. Dimova, V. Percec, C. Rodriguez-Emmenegger, *Advanced Materials* **2022**, *34*, 2206288.
[39] V. Percec, D. A. Wilson, P. Leowanawat, C. J. Wilson, A. D. Hughes, M. S. Kaucher, D. A. Hammer, D. H. Levine, A. J. Kim, F. S. Bates, K. P. Davis, T. P. Lodge, M. L. Klein, R. H. DeVane, E. Aqad, B. M. Rosen, A. O. Argintaru, M. J. Sienkowska, K. Rissanen, S. Nummelin, J. Ropponen, *Science* **2010**, *328*, 1009-1014.
[40] A. M. Wagner, J. Quandt, D. Söder, M. Garay-Sarmiento, A. Joseph, V. S. Petrovskii, L. Witzdam, T. Hammoor, P. Steitz, T. Haraszti, I. I. Potemkin, N. Y. Kostina, A. Herrmann, C. Rodriguez-Emmenegger, *Advanced Science* **2022**, *9*, 2200617.
[41] K. Mitra, I. Ubarretxena-Belandia, T. Taguchi, G. Warren, D. M. Engelman, *Proceedings of the National Academy of Sciences* **2004**, *101*, 4083-4088.
[42] J. F. Le Meins, C. Schatz, S. Lecommandoux, O. Sandre, *Materials Today* **2013**, *16*, 397-402.
[43] R. M. Hill, M. He, Z. Lin, H. T. Davis, L. E. Scriven, *Langmuir* **1993**, *9*, 2789-2798.
[44] N. Marušič, Z. Zhao, L. Otrin, R. Dimova, I. Ivanov, K. Sundmacher, *Macromolecular Rapid Communications* **2022**, *43*, 2100712.
[45] N. Marušič, L. Otrin, Z. Zhao, R. B. Lira, F. L. Kyrilis, F. Hamdi, P. L. Kastritis, T. Vidaković-Koch, I. Ivanov, K. Sundmacher, R. Dimova, *Proceedings of the National Academy of Sciences* **2020**, *117*, 15006-15017.
[46] R. Rodríguez-García, M. Mell, I. López-Montero, J. Netzel, T. Hellweg, F. Monroy, *Soft Matter* **2011**, *7*, 1532-1542.
[47] B. M. Discher, Y.-Y. Won, D. S. Ege, J. C.-M. Lee, F. S. Bates, D. E. Discher, D. A. Hammer, *Science* **1999**, *284*, 1143-1146.
[48] C. Yolcu, R. C. Haussman, M. Deserno, *Advances in Colloid and Interface Science* **2014**, *208*, 89-109.
[49] T. R. Weikl, M. M. Kozlov, W. Helfrich, *Physical Review E* **1998**, *57*, 6988-6995.
[50] P. G. Dommersnes, J. B. Fournier, P. Galatola, *Europhysics Letters* **1998**, *42*, 233.
[51] I. Koltover, J. O. Rädler, C. R. Safinya, *Physical Review Letters* **1999**, *82*, 1991-1994.
[52] M. M. Müller, M. Deserno, J. Guven, *Physical Review E* **2005**, *72*, 061407.
[53] P. A. Kralchevsky, K. Nagayama, *Adv Colloid Interface Sci* **2000**, *85*, 145-192.
[54] F. G. Strobl, F. Seitz, C. Westerhausen, A. Reller, A. A. Torrano, C. Bräuchle, A. Wixforth, M. F. Schneider, *Beilstein Journal of Nanotechnology* **2014**, *5*, 2468-2478.

[55] T. Curk, P. Wirnsberger, J. Dobnikar, D. Frenkel, A. Šarić, *Nano Letters* **2018**, *18*, 5350-5356.
[56] A. Gupta, T. Korte, A. Herrmann, T. Wohland, *J Lipid Res* **2020**, *61*, 252-266.
[57] N. Y. Kostina, A. M. Wagner, T. Haraszti, K. Rahimi, Q. Xiao, M. L. Klein, V. Percec, C. Rodriguez-Emmenegger, *Soft Matter* **2021**, *17*, 254-267.
[58] T. Schubert, W. Römer, *Biochimica et Biophysica Acta (BBA) - Molecular Cell Research* **2015**, *1853*, 2992-3005.
[59] I. Jayapurna, Z. Ruan, M. Eres, P. Jalagam, S. Jenkins, T. Xu, *Biomacromolecules* **2023**, *24*, 652-660.
[60] M. Shin, H. Kim, G. Park, J. Park, H. Ahn, D. K. Yoon, E. Lee, M. Seo, *Nature Communications* **2022**, *13*, 2433.
[61] M. Shin, H. Kim, G. Park, J. Park, H. Ahn, D. Yoon, E. Lee, M. Seo, *Nature Communications* **2022**, *13*, 2433.
[62] C. Rodriguez-Emmenegger, E. Brynda, T. Riedel, M. Houska, V. Šubr, A. B. Alles, E. Hasan, J. E. Gautrot, W. T. S. Huck, *Macromolecular Rapid Communications* **2011**, *32*, 952-957.
[63] G. R. Fulmer, A. J. M. Miller, N. H. Sherden, H. E. Gottlieb, A. Nudelman, B. M. Stoltz, J. E. Bercaw, K. I. Goldberg, *Organometallics* **2010**, *29*, 2176-2179.
[64] J. D. Hunter, *Computing in Science & Engineering* **2007**, *9*, 90-95.
[65] C. R. Harris, K. J. Millman, S. J. van der Walt, R. Gommers, P. Virtanen, D. Cournapeau, E. Wieser, J. Taylor, S. Berg, N. J. Smith, R. Kern, M. Picus, S. Hoyer, M. H. van Kerkwijk, M. Brett, A. Haldane, J. F. Del Rio, M. Wiebe, P. Peterson, P. Gerard-Marchant, K. Sheppard, T. Reddy, W. Weckesser, H. Abbasi, C. Gohlke, T. E. Oliphant, *Nature* **2020**, *585*, 357-362.
[66] C. A. Schneider, W. S. Rasband, K. W. Eliceiri, *Nat Methods* **2012**, *9*, 671-675.
[67] N. Otsu, *IEEE transactions on systems, man, and cybernetics* **1979**, *9*, 62-66.
[68] H. A. Faizi, C. J. Reeves, V. N. Georgiev, P. M. Vlahovska, R. Dimova, *Soft Matter* **2020**, *16*, 8996-9001.
[69] H. P. Duwe, E. Sackmann, *Physica a-Statistical Mechanics and Its Applications* **1990**, *163*, 410-428.
[70] R. Dimova, *Adv Colloid Interface Sci* **2014**, *208*, 225-234.

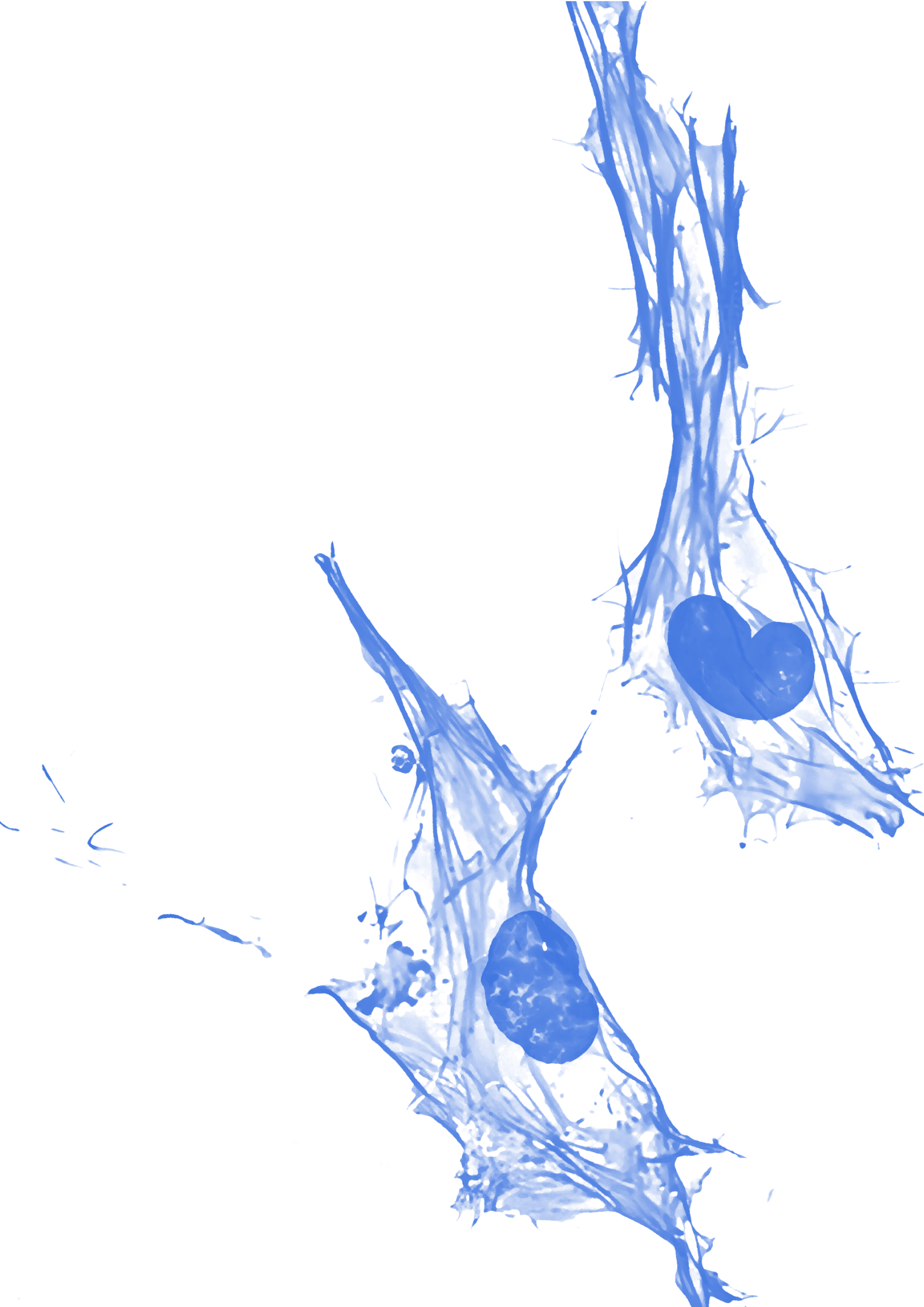

Chapter 7

Harnessing Synthetic Cells as Bacterial Predators

7.1 Introduction

In the previous chapter, we demonstrated that i-combisomes are able to achieve enhanced engulfment of nano- and micro-sized objects. In this chapter, we go beyond the engulfment of inanimate objects and demonstrate how the unparalleled engulfment behavior of our i-combisomes can be harnessed for the "Artificial Phagocytosis" of bacteria as a potential therapeutic approach to combat resistant infections (Figure 7.1). "Artificial Phagocytosis" is accomplished through the concerted process of pathogen engulfment, coupled with a killing mechanism inspired by the bactericidal action of HDPs and HDP-mimicking polymers. In this manner, killing proceeds only after engulfment and the debris of the killed bacteria remains encapsulated, thereby protecting the environment from harmful endotoxins, such as lipopolysaccharides (LPS). The engulfment process follows the same physical principles outlined in Chapter 6. The adhesion energy between the bacterium and the membrane drives the onset of engulfment, which is then favored by the presence of small fractions of molecules with non-zero spontaneous curvature. Subsequently, we propose that the bactericidal mechanism employed by our i-combisomes is based on the close apposition of their bilayer membrane to the bacterium upon engulfment and the insertion of their lipid-like hydrophobic tails into the bacterial membrane, thereby disrupting membrane integrity, causing leakage and consequently cell death. This mechanism of cell membrane disruption is analogous to that known for HDPs and HDP-mimicking polymers, which have been shown to be effective against both Gram-positive and Gram-negative bacteria due to their general mode of action targeting the bacterial membrane and not specific components.[1-6] Moreover, this non-specific bacteria-killing pathway acting on essential structures, such as the bacterial membrane, is promising because bacterial mutations are unlikely to result in fundamental changes of the membrane, thereby restricting the development of resistance.[1, 7-9] Furthermore, we hypothesize that hydrophobic tail insertion is feasible only when the i-combisome membrane closely apposes to the bacterial membrane. This suggests that the killing action is exclusively unleashed through bacterium engulfment, making it less harmless to eukaryotic cells, which are typically larger (10-100 µm in diameter) and cannot be engulfed.

This chapter presents the first report on the complete realization of "Artificial Phagocytosis" by cell mimics. The process includes complete engulfment of the pathogen with subsequent deactivation. The high level of biomimicry of our system is envisioned to serve as a

groundbreaking novel antimicrobial platform that can be applied to both Gram-positive and Gram-negative bacteria without compromising the integrity of surrounding mammalian cells and tissue.

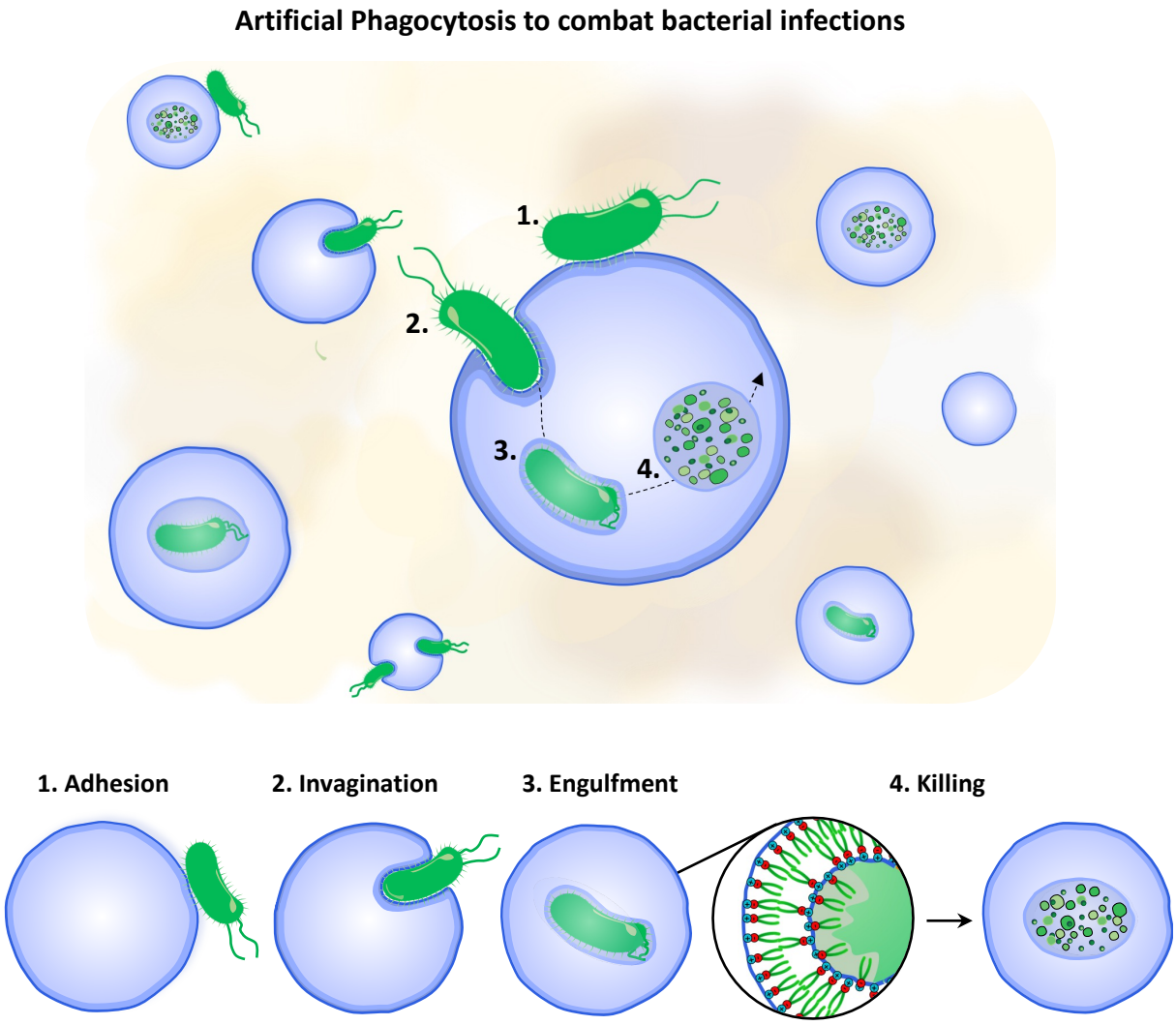

Figure 7.1. "Artificial Phagocytosis" performed by our i-combisomes to combat bacterial pathogens. The i-combisomes ingest the bacterium through an engulfment process including invagination, wrapping with a narrow membrane neck, neck fission and release of endosome. Lastly, bacterial death is induced through the insertion of the hydrophobic tails into the bacterial membrane disrupting membrane integrity.

7.2 Results and Discussion

7.2.1 Engulfment of Bacteria

In a first stage, we aimed to validate the phagocytic behavior of our i-combisomes against bacteria. For this purpose, we used the non-pathogenic strain *E. coli* BL21 (DE3) as a model bacterium. Prior to mixing the bacteria with the i-combisomes, these were stained with the live-cell nucleic acid stain NucBlue™ (Hoechst 33342). This allowed us to track their localization and possible engulfment in real time using CLSM.

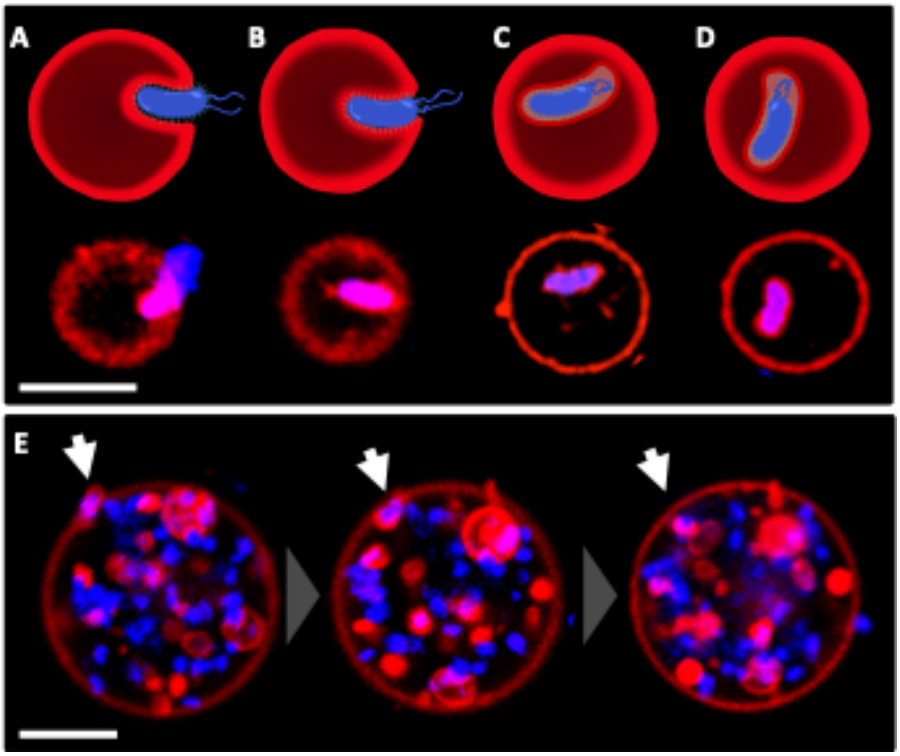

Figure 7.2. CLSM images demonstrate the engulfment of bacteria (blue) by our i-combisomes (red). (A) Invagination of i-combisome membrane, (B) complete engulfment with closed neck and (C) neck fission with release of endosome containing living bacterium into the lumen. (D) Free diffusion of engulfed bacterium inside lumen. (E) Charged i-combisomes containing multiple engulfed E. coli cells. White arrows indicate the engulfment of an additional bacterium. Scale bars represent 5 μm.

As shown in Figure 7.2, our i-combisomes are able to ingest the E. coli cells through the engulfment process, which involves membrane invagination (Figure 7.2A), bacteria wrapping with a narrow membrane neck (Figure 7.2B) and neck fission with subsequent endosome

release (Figure 7.2C). The endosome membrane is visible by the red fluorescent around the engulfed bacterium. Finally, the free diffusion of the engulfed bacterium inside the lumen can be observed (Figure 7.2D), confirming the complete release of the endosome. Moreover, when utilizing charged i-combisomes self-assembled from cationic $DP_{85}N_{57}DS_{80}$ iCPs, we observed GUVs containing a high concentration of engulfed *E. coli* cells in their lumen, as depicted in Figure 7.2E. It should be noted that these results were obtained within the first 30 min of contact time. Possibly, the positive charge of these i-combisomes, derived from the free amine residues of DMAPAA, drives strong electrostatic attraction and adhesion between the membrane and the negatively charged bacteria, resulting in even more efficient engulfment.

7.2.2 Killing of Bacteria

Our aim is to achieve the deactivation of the bacterial pathogen in a concerted manner with engulfment. In that way, the killing mechanism is unleashed only during engulfment and otherwise remains dormant. This enables the specific targeting of microbes while reduced toxicity to surrounding eukaryotic cells. For the killing mechanism, we exploit a mechanism inspired in the bactericidal action of HDPs and HDP-mimicking polymers, involving the insertion of the hydrophobic tails of the i-combisomes into the bacterial membrane. This process is anticipated to disrupt the integrity of the bacterial membrane, leading to leakage and, ultimately, cell death. To confirm the mechanism of action, we examined the ability of our i-combisomes to induce leakage of the fluorescent eGFP protein from *E. coli* bacteria. For these experiments, we utilized *E.coli* BL21 cells expressing eGFP in their cytosol. Figure 7.3A shows the engulfment of these *E. coli* bacteria (cyan fluorescence) as the first step upon contact with the i-combisomes. Subsequently, we observed events of eGFP leakage (cyan fluorescence) during the engulfment process (Figure 7.3B). These provides first evidence of the killing mechanism indicating the permeabilization of the bacterial cell wall and membrane upon interaction with our i-combisomes. This is consistent with our hypothesis that the hydrophobic tails of the i-combisomes insert into the bacterial membrane upon close contact, disrupting membrane integrity, causing leakage and consequently cell death. After an incubation period of approximately 2 h, we find that almost all i-combisomes carry eGFP fluorescence on their membrane, indicating interactions between the eGFP and the i-combisome membrane and a strong leakage of eGFP (Figure 7.3C). Interestingly, we also

evidence a morphological change of the wrapped bacteria from rod-shaped to spherical (Figure 7.3D). Such a shape transition to a spheroplast is known in *E. coli* cells, whose cell wall has been disrupted[10], further confirming our proposed killing mechanism.

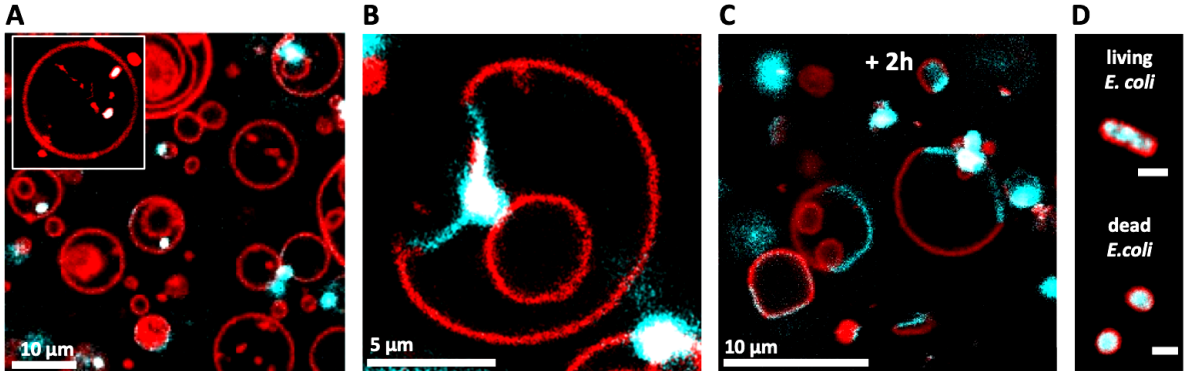

Figure 7.3. (A) Overview image showing engulfment of eGFP-expressing *E. coli* bacteria by i-combisomes. (B) The release of eGFP from the interior of *E. coli* suggests the permeabilization of the bacterial membrane upon engulfment. (C) Overview image after 2 h of contact time showing almost all i-combisomes exerting eGFP fluorescence at their membranes. (D) After bacteria wrapping, the wrapped bacterium changes morphology from rod-shaped to spherical indicating cell wall disruption. Scale bars represent 1 µm.

Additionally, another notable observation is the presence of phase separation into curved and faceted region within the GUVs after prolonged incubation with the *E. coli* bacteria (Figure 7.3C). This leads us to propose that the killing mechanism of our i-combisomes may also involve the fusion between the i-combisome membrane and the bacterial membrane. Phase separation could be explained due to the binary membrane mixture of the i-combisomes with bacterial outer membrane fragments and the asymmetric outer membrane of the *E. coli* bacteria, where the external leaflet is rich in rigid liposaccharides and probably drives the segregation from the iCPs forming phase-separated stable patches. These assumptions are in agreement with our previous work, where we reported the ability of the i-combisomes to readily undergo fusion with both lipid and complex bacterial membranes.[11] Furthermore, the differences in membrane composition, including the presence of transmembrane proteins and sugars as well as hydrophobic mismatches, could also be behind phase separation. In this context, further studies are needed to confirm and explore the fusogenic behavior involved in the killing process.

7.2.3 Antimicrobial Efficiency Against Gram-Positive and Gram-Negative Bacteria

We quantified the bactericidal efficiency of our i-combisomes by performing viable cell count reduction with the CFU method. We assessed their antimicrobial efficiency not only against the *E. coli* model bacterium but also against the Gram-negative bacterium *Pseudomonas aeruginosa* (*P. aeruginosa*) and the Gram-positive bacterium MRSA. Notably, both of these germs were clinical isolates and highly resistant to several antibiotics. Additionally, *P. aeruginosa* as well as MRSA are major pathogens behind chronic wound infection[4, 12-13] and have been classified by the WHO as two of the most dangerous and high-priority superbugs, for which new antimicrobial therapies are urgently needed.[14]

The i-combisomes were mixed with the different bacterial strains for 2 h under ambient conditions. Subsequently , plating at different dilutions was carried out and the plates were further incubated for 48 h under optimal conditions for bacterial cell growth. Counting for CFU was performed, as shown in Figure 7.4. As a control, the bacteria were mixed with the same volume of pure water and bacterial concentration was determined by CFU count before and after incubation for 2 h. Notably, our i-combisomes completely eradicated the model *E. coli* BL21 bacteria upon contact. Based on CFU counts, we calculated that approximately 10^6 cells were incubated with 10 µL of the i-combisomes dispersion ($c_{polymer}$ = 1.0 mg·mL^{-1}), resulting in a 6-log reduction. As shown in Figure 7.4B, the growth of *P. aeruginosa* on the agar plates occurred in the form of a biofilm, causing a typical greenish staining without classical colony formation, so that CFU quantification could not be performed. However, the absence of a greenish biofilm on the agar plates after treatment indicates that no viable cells remained after incubation, demonstrating the great bactericidal ability of our i-combisomes against this superbug. Remarkably, the i-combisomes also showed effective bactericidal activity against the Gram-positive MRSA, achieving complete eradication of the bacteria, equivalent to a 4-log reduction (Figure 7.4C). Collectively, these results emphasize the robust antimicrobial activity of our i-combisomes against superbugs. By mimicking the bactericidal mode of action seen in HDPs and HDP-mimicking polymers, they target the bacterial membrane, displaying a broad-spectrum effect and minimizing the potential for resistance development.

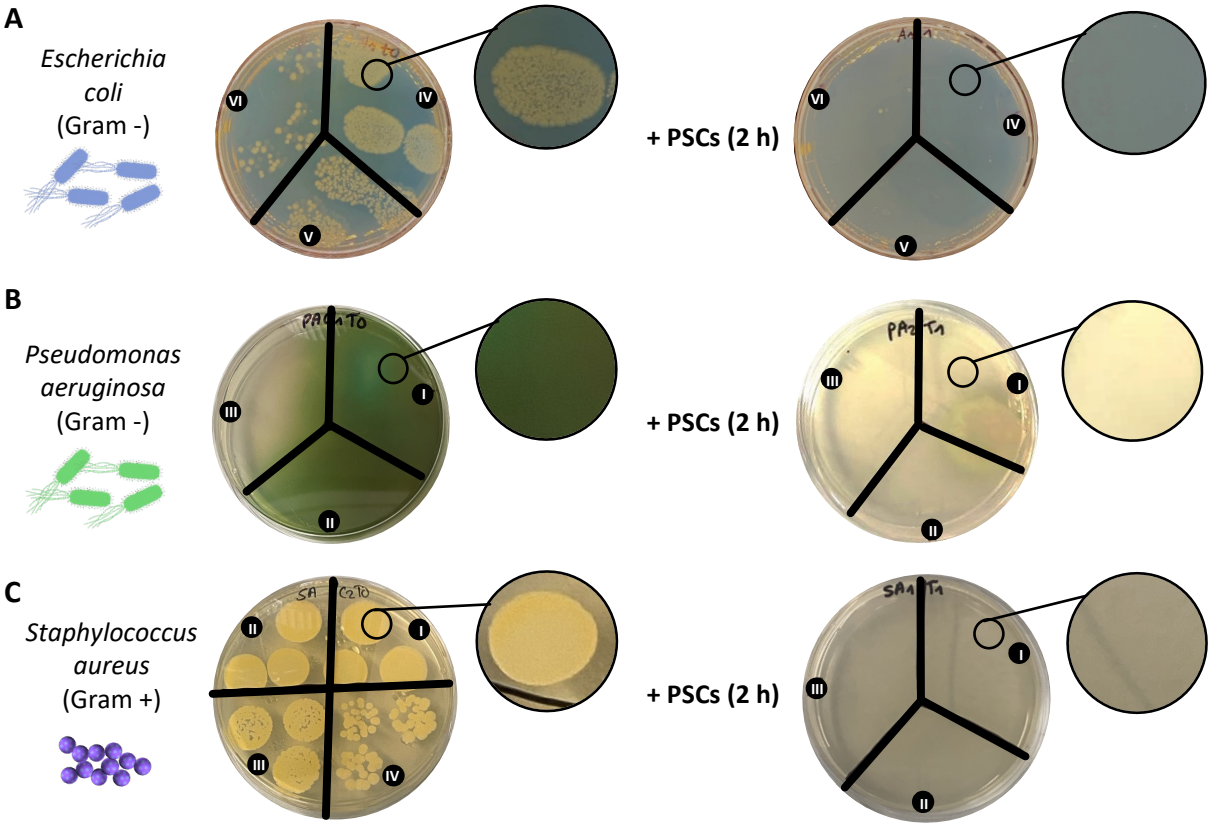

Figure 7.4. Images of agar plates after plating and 48 h of incubation depicting the CFUs of (A) *E. coli*, (B) *P. aeruginosa* and (D) MRSA. Control samples are shown on the left, while samples mixed with i-combisomes and incubated for 2 h are depicted on the right.

7.2.4 Biocompatibility of i-combisomes

The high level of antimicrobial activity of our i-combisomes suggests great potential as anti-infective treatment. However, for such an application, the goal is not only to achieve exceptional bactericidal activity, but also to minimize toxicity to mammalian cells to ensure a safe application. Hence, we investigated the *in vitro* biocompatibility of our i-combisomes against mammalian cells using human kidney organoids. Organoids are 3D tissue-like structures that anatomically and functionally resemble organs in the living body.[15] Importantly, 3D organotypic tissues have proven to be more sensitive to drug-induced toxicity, allowing a better prediction of drug safety in real applications.[16] In particular, kidney organoids have been leverage in the last decade for drug-induced toxicology studies.[15] We incubated kidney organoids with our i-combisomes and monitored potential interactions in real time for 2 h using CLSM (Figure 7.5A, B and C). For this purpose, the cells were labeled with Calcein AM (green) and Hoechst 33342 (blue) as nuclear staining. Furthermore, the

i-combisome GUVs were prepared by the electroformation method in a 300 mM sucrose solution with the addition of 0.1 mol% Rhod-PE (magenta) for membrane labeling. As shown by the Z-stack images, we do not observe major interactions between the i-combisomes and the organoid cells as has been previously observed in the case of bacterial cells (*vide supra*). Occasionally, some adhesion of the GUVs to the organoids was observed, but overall, this was a rare observation. That said, the engulfment of mammalian cells by our i-combisomes is not feasible due to their large sizes. For comparison, our i-combisomes prepared by TFH can have sizes between 2-25 μm,[11] while typical mammalian cell size can range between 7-100 μm [17] in diameter. Even in the case of the smallest cells, the engulfment of such big objects would be impeded due to the large contribution of area expansion to the elastic energy. Moreover, mammalian cells often exhibit complex, intricate structures and shapes, which would pose additional barriers for engulfment.

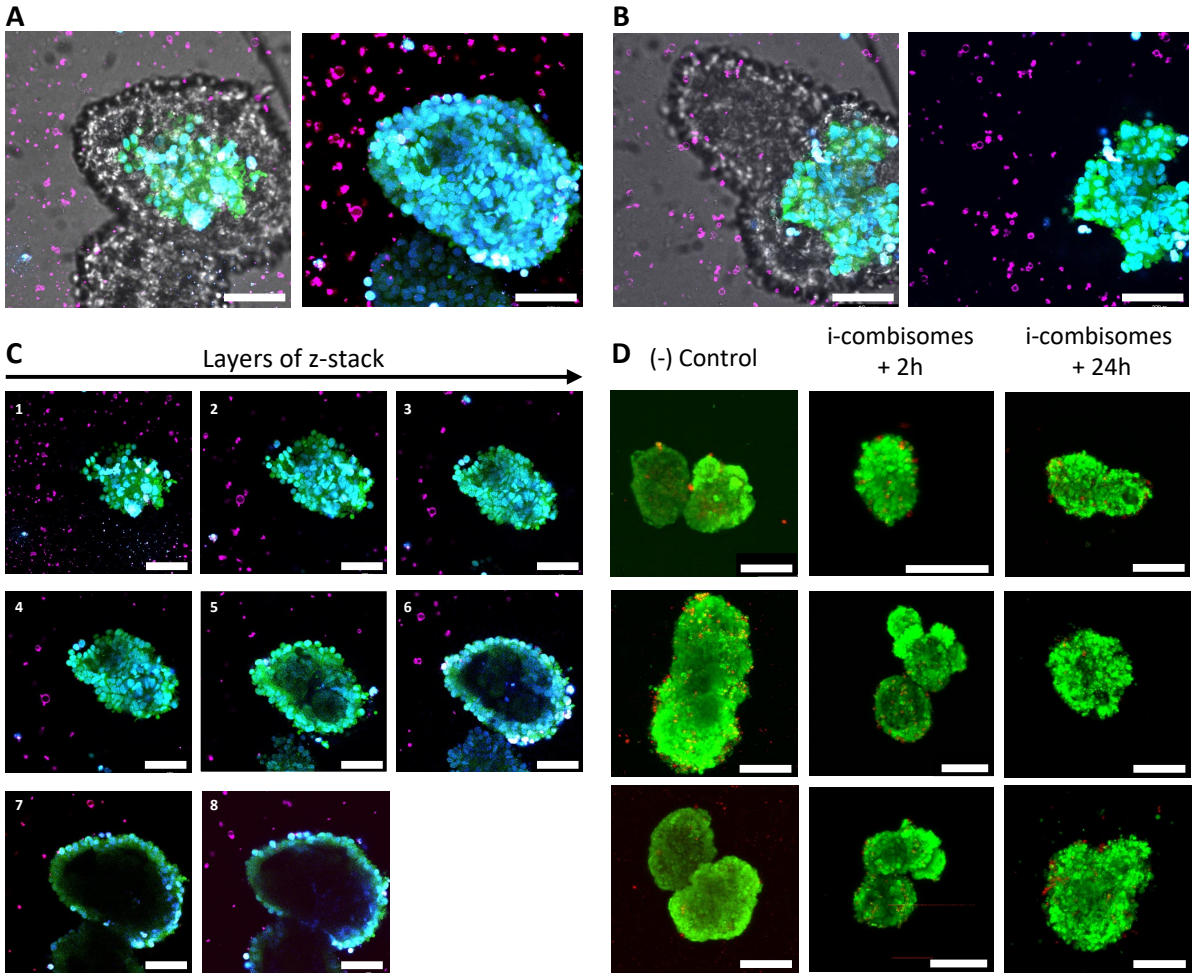

Figure 7.5. (A), (B) Maximum intensity projection images of kidney organoids treated with i-combisomes directly after mixture and after 2 h of incubation. (cell nuclei: blue, cytosol: green and i-combisome membrane: magenta). (C) Z-axis scans from top to bottom (1-8) of the

kidney organoids and i-combisomes showing minimal interactions. (D) Live/dead staining of untreated kidney organoids (control) and those treated with i-combisomes for 2 h. Scale bars represent 100 μm.

After a prolonged incubation period of 24 h, we assessed cell viability by live/dead staining. As shown in Figure 7.5D, the vast majority of cells exhibited a green calcein staining, characteristic for viable cells. Only a small number of cells showed a red staining, which is indicative for cell death. This was comparable to control organoids, that were treated with a 300 mM sucrose solution and also exhibited a small number of dead cells. Consequently, we can conclude from these first experiments that the i-combisomes did not induce toxicity towards the kidney organoids.

The ability of the killing mechanism to be coupled in a concerted manner with the engulfment process is a critical feature of our i-combisomes. This coupling ensures that the membrane-disruptive action is unleashed specifically on the engulfed pathogen. In this context, the possibility of eukaryotic cells, which are typically larger than 10 μm in diameter, being engulfed is minimal. Thus, this targeting mechanism enhances the safety profile of our i-combisomes, minimizing the risk of unintended effects on eukaryotic cells.

7.3 Conclusion

In this chapter, we introduced a new concept for an antimicrobial therapeutic approach based on synthetic cell mimics that are able to perform complete “Artificial phagocytosis”. In proof-of-concept experiments, we demonstrated that, similar to the professional phagocytes of our innate immune system, our i-combisomes were capable of engulfing and subsequently inactivating bacteria in a concerted manner. Their bactericidal mechanism targeting the disruption of the bacterial membrane integrity is analogous to the one known for HDPs and HDP-mimicking polymers[1-5], endowing our i-combisomes with a broad antimicrobial spectrum against Gram-positive and Gram-negative bacteria. In this regard, the i-combisomes were able to completely eradicate *P. aeruginosa* and MRSA bacteria after only 2 h of contact time. By means of a cytosolic protein leakage assay, we confirmed that the killing mechanism is based on membrane permeabilization, which ultimately leads to bacterial death. It is important to note that despite their non-specific mode of action, the i-combisomes did not induce toxicity in mammalian cells. Kidney organoid cell viability remained unaffected even after prolonged incubation periods with the i-combisomes. These findings allowed us to propose that the concerted dual mode of action enabled the bactericidal action of our i-combisomes to be unleashed only against the engulfed pathogens, while preserving the integrity of surrounding mammalian cells that are not engulfed. That said, in order to make more precise conclusions and in-depth evaluate the specificity of our i-combisomes, further tests need to be performed with co-cultures of bacteria and mammalian cells. Additionally, biocompatibility studies, including the use of specific biomarkers for drug-induced tissue injury, are necessary to assess the biocompatibility of the i-combisomes more accurately.

Nevertheless, the findings presented in this chapter provide, for the first time, insight into a sophisticated form of “Artificial Phagocytosis” performed by synthetic cells. It is envisioned that i-combisomes may provide a new platform for the development of minimal Phagocytic Synthetic Cells that can aid in the fight against resistant infections while preserving the integrity of surrounding healthy cells. Owing to its general membrane-disrupting mechanism, our cell mimics may also be effective against viruses and fungi.

7.4 Materials and Methods

7.4.1 Materials

All reagents were of analytical grade and used as received unless otherwise stated. Nile Red and NucBlue™ Live ReadyProbes™ Reagent were purchased from Sigma Aldrich Chemie GmbH. 16:0 LissRhod PE lipid was purchased from Avanti Polar Lipids, Inc. iCPs were synthesized according to literature procedures.[18]

Cells and Biochemicals. E. coli strain BL21-Gold (DE3) was purchased from Agilent Technologies Inc., USA. The plasmids pET28a(+) and pEGFP were purchased from Novagen, Germany and Clontech Laboratories Inc., USA, respectively. *P. aeruginosa* and MRSA are clinical strains obtained from the University Hospital Aachen, Germany. *E. coli* and *P. aeruginosa* were grown in LB containing 10 $g \cdot L^{-1}$ tryptone, 5 $g \cdot L^{-1}$ yeast extract and 10 $g \cdot L^{-1}$ NaCl, purchased from AppliChem GmbH. *MRSA* was grown in MHB obtained from Sigma Aldrich Chemie GmbH. Live/dead staining kit was purchased from ThermoFisher Scientific, Waltham, United States.

7.4.2 Synthetic and Fabrication Methods

GUV preparation by thin-film rehydration. iCPs were dissolved in $CHCl_3$ at 10 $mg \cdot mL^{-1}$. 30 µL of the solution were then mixed with 0.1 mol% of dye and deposited on a roughened Teflon plate. The plate was dried at room temperature, followed by 2 h in vacuo. Afterwards, it was placed in a small vial and 300 µL of Milli-Q water were added to rehydrate the dry film yielding a vesicle solution of $c_{polymer}$ = 1 $mg \cdot mL^{-1}$. The vial was then placed at 60 °C overnight.

GUV preparation by electroformation. iCPs were dissolved in $CHCl_3$ at 10 $mg \cdot mL^{-1}$ and mixed with 0.1 mol% of Liss Rhod-PE as membrane dye. Subsequently, 15 µL of this solution were spread as a thin film on two conductive ITO-coated glasses (ITO film thickness < 100 nm, resistance 50 Ω; Präzisions Glas & Optik, Iserlohn, Germany). The glasses were dried at room temperature in vacuo for 2 h. The chambers were then prepared by placing a Teflon spacer between the two glasses. The chamber was filled with 1.8 mL of a sucrose solution (300 mM) and electroformation was performed at 10 Hz and 1.1 mV (sine wave shaped) for 2 h at ambient conditions. The GUVs were then collected with a 1 mL micropipette tip and mixed with a 300 mM glucose solution at a 1:1 volume ratio. Subsequently, GUVs were spun down

for 2 min at 2000 g. Supernatant was carefully removed yielding a final GUV dispersion with an amphiphile concentration of $c_{polymer}$ = 1 mg·mL^{-1}. Prior to experiments with kidney organoids, the GUVs were sterilize by UV disinfection (254 nm) for 40 min.

eGFP expressing E. coli cell culture. Precultures of *E. coli* BL21-Gold (DE3) cells containing the plasmid pET28:EGFP were incubated in 10 mL LB for 16 h at 37°C and 210 rpm. Then a working culture of OD_{600} = 0.05 was prepared and 0.1 mM of kanamycin was added. The working culture was led to incubate for 2.5 h at 37 °C and 210 rpm until an OD_{600} = 0.6 was reached. Subsequently, protein overexpression was induced by adding IPTG to a final concentration of c = 0.1 mM. Incubation for 24 h proceeded at 20 °C. Before experiments, the OD was adjusted to OD_{600} = 3.5. Then 1.5 mL of the cell solution was transferred into a 2 mL reaction tube and spun down at 11,363 g for 15 s at 20 °C using an Eppendorf centrifuge 5424 R (Eppendorf AG, Hamburg, Germany). The cells were then resuspended in sterile-filtered tap water and washed 2 times by spinning down.

Nuclear staining of E. coli cells. E. coli BL21-Gold (DE3) cells were cultured in LB for 24 h at 37 °C and 210 rpm. Subsequently, the OD was measured and normalized to OD_{600} = 3.5. Then 1.5 mL of the cell solution was transferred into a 2 mL reaction tube and spun down at 11,363 g for 15 s at 20 °C using an Eppendorf centrifuge 5424 R (Eppendorf AG, Hamburg, Germany). The cells were then resuspended in sterile Milli-Q water and washed 2 times by spinning down. Then, 2 drops of NucBlue™ Live ReadyProbes™ Reagent were added to 1 mL of bacterial solution and allowed to incubate for 30 min at room temperature before use.

7.4.3 Analytical Methods

CLSM studies with E.coli cells. i-combisome GUVs were either stained with 0.1 mol% of Liss Rho-PE or Nile red. 40 μL of the GUV dispersion was then mixed with 8 μL of the bacterial solution (OD_{600} = 3.5) in a reaction tube and 20 μL were directly transferred to the microscope observation chamber. Images were recorded on a Leica TCS SP8 confocal microscope (Wetzlar, Germany) with a 63x/1.40 glycerol-immersion objective and PMT or HyD detectors. Temperature was kept constant at 22 °C. Post-corrections of all images were performed with the Fiji-ImageJ software.

Bacterial spot plating assay. Precultures of *E. coli*, *P. aeruginosa* and *S. aureus* were prepared by inoculating a single colony into 10 mL of the respective cell broth and culture for 12 h at 37 °C and 180 rpm. Following incubation, the working cultures were adjusted to an OD_{600} of 3.5. 10 mL of the bacterial solution were then transferred into 15 mL reaction tubes and spun down at 3500 g for 10 min. Bacterial sediment was resuspended in 10 mL sterile-filtered tap water and washing was carried out for two more times. i-combisomes GUV were prepared by the TFH method without the addition of any cell membrane dye. Subsequently, 8 μL of the bacteria in tap water were mixed with 40 μL of the i-combisomes dispersion in a reaction tube and let to incubate for 2 h at ambient conditions. Control samples were prepared by the mixture of 8 μL of bacterial solution with 40 μL of sterile tap water. Cell spot platting was carried out directly after mixture (t_0) and after 2 h of incubation period (t_1). For spot platting, serial dilutions were prepared and 20 μL of these solutions were plated in triplicates.

CLSM studies with kidney organoids. i-combisome GUVs were formed by the electroformation method with the addition of 0.1 mol% of Liss Rho-PE as membrane dye. The organoids were stained by mixing 1 mL of the organoid dispersion with 0.5 mL of a calcein AM solution (1 μM). Subsequently, cell nuclei staining was carried out by adding three drops of the NucBlue™ Live ReadyProbes™ Reagent. Incubation at ambient conditions proceeded for 30 min before imaging with a Leica TCS SP8 confocal microscope (Wetzlar, Germany) equipped with a 63x/1.40 glycerol-immersion objective and PMT or HyD detectors. Post-corrections of all images were performed with the Fiji-ImageJ software.

Viability of kidney organoids. Cell viability was visualized by live/dead staining after at 37 °C in a humidified, 5% CO_2 atmosphere. For these experiments, i-combisomes were formed by the electroformation method without the addition of a membrane dye. Live/dead staining solution was prepared according to the manufacturer's procedure. Briefly, component A (Calcein AM as live cell indicator) was transferred into component B (BOBO-3 Iodide as dead cell indicator). 50 μL of this solution were then transferred into 100 μL of the i-combisomes-organoid mixture and incubated for 30 min at ambient conditions before imaging. Images were recorded on a Leica TCS SP8 confocal microscope (Wetzlar, Germany) with a 63x/1.40 glycerol-immersion objective and PMT or HyD detectors. Temperature was kept constant at 22 °C. Post-corrections of all images were performed with the Fiji-ImageJ software.

7.5 Declaration of Contributions

I conducted engulfment studies by CLSM, the bacteria killing experiments and the assessment of biocompatibility with kidney organoids. I would like to acknowledge Dominik Söder for his assistance during the CLSM experiments with the eGFP-producing *E. coli* bacteria as well as Jonas Quandt for the synthesis of the iCPs. The kidney organoids were kindly provided by Prof. Nuria Monserrat from the Institute for Bioengineering of Catalonia in Barcelona, Spain. The interpretation of the data and conceptual discussions were carried out by Prof. César Rodriguez-Emmenegger, Dr. Nina Kostina and me.

Prof. César Rodriguez-Emmenegger supervised this project.

7.6 References

[1] H. Etayash, R. E. W. Hancock, *Pharmaceutics* **2021**, *13*, 1820.

[2] M. Concilio, R. Garcia Maset, L. P. Lemonche, V. Kontrimas, J.-I. Song, S. K. Rajendrakumar, F. Harrison, C. R. Becer, S. Perrier, *Advanced Healthcare Materials* **2023**, *12*, 2301961.

[3] A. M. Bapolisi, P. Kielb, M. Bekir, A.-C. Lehnen, C. Radon, S. Laroque, P. Wendler, H. M. Müller-Werkmeister, M. Hartlieb, *Macromolecular Rapid Communications* **2022**, *43*, 2200288.

[4] R. Garcia Maset, A. Hapeshi, S. Hall, R. M. Dalgliesh, F. Harrison, S. Perrier, *ACS Applied Materials & Interfaces* **2022**, *14*, 32855-32868.

[5] A. C. Engler, J. P. K. Tan, Z. Y. Ong, D. J. Coady, V. W. L. Ng, Y. Y. Yang, J. L. Hedrick, *Biomacromolecules* **2013**, *14*, 4331-4339.

[6] K. Lienkamp, A. E. Madkour, A. Musante, C. F. Nelson, K. Nüsslein, G. N. Tew, *Journal of the American Chemical Society* **2008**, *130*, 9836-9843.

[7] M. Riool, V. Patrulea, C. Monteiro, *Pharmaceutics* **2022**, *14*.

[8] P. Pham, S. Oliver, C. Boyer, *Macromolecular Chemistry and Physics* **2023**, *224*, 2200226.

[9] D. Liu, S. Choi, B. Chen, R. J. Doerksen, D. J. Clements, J. D. Winkler, M. L. Klein, W. F. DeGrado, *Angewandte Chemie International Edition* **2004**, *43*, 1158-1162.

[10] D. Ranjit, K. Young, *Journal of bacteriology* **2013**, *195*.

[11] A. M. Wagner, J. Quandt, D. Soder, M. Garay-Sarmiento, A. Joseph, V. S. Petrovskii, L. Witzdam, T. Hammoor, P. Steitz, T. Haraszti, Potemkin, II, N. Y. Kostina, A. Herrmann, C. Rodriguez-Emmenegger, *Adv Sci (Weinh)* **2022**, *9*, e2200617.

[12] M. Fazli, T. Bjarnsholt, K. Kirketerp-Møller, B. Jørgensen, A. S. Andersen, K. A. Krogfelt, M. Givskov, T. Tolker-Nielsen, *Journal of Clinical Microbiology* **2009**, *47*, 4084-4089.

[13] U. Trivedi, S. Parameswaran, A. Armstrong, D. Burgueno-Vega, J. Griswold, S. Dissanaike, K. P. Rumbaugh, *Journal of Pathogens* **2014**, *2014*, 173053.

[14] G. Mancuso, A. Midiri, E. Gerace, C. Biondo, *Pathogens* **2021**, *10*.

[15] T. Matsui, T. Shinozawa, *Front Genet* **2021**, *12*, 767621.

[16] T. M. DesRochers, L. Suter, A. Roth, D. L. Kaplan, *PLOS ONE* **2013**, *8*, e59219.

[17] R. Milo, R. Phillips, N. Orme, *Cell Biology by the Numbers*, Garland Science, Taylor & Francis Group, **2016**.

[18] A. M. Wagner, J. Quandt, D. Söder, M. Garay-Sarmiento, A. Joseph, V. S. Petrovskii, L. Witzdam, T. Hammoor, P. Steitz, T. Haraszti, I. I. Potemkin, N. Y. Kostina, A. Herrmann, C. Rodriguez-Emmenegger, *Advanced Science* **2022**, *9*, 2200617.

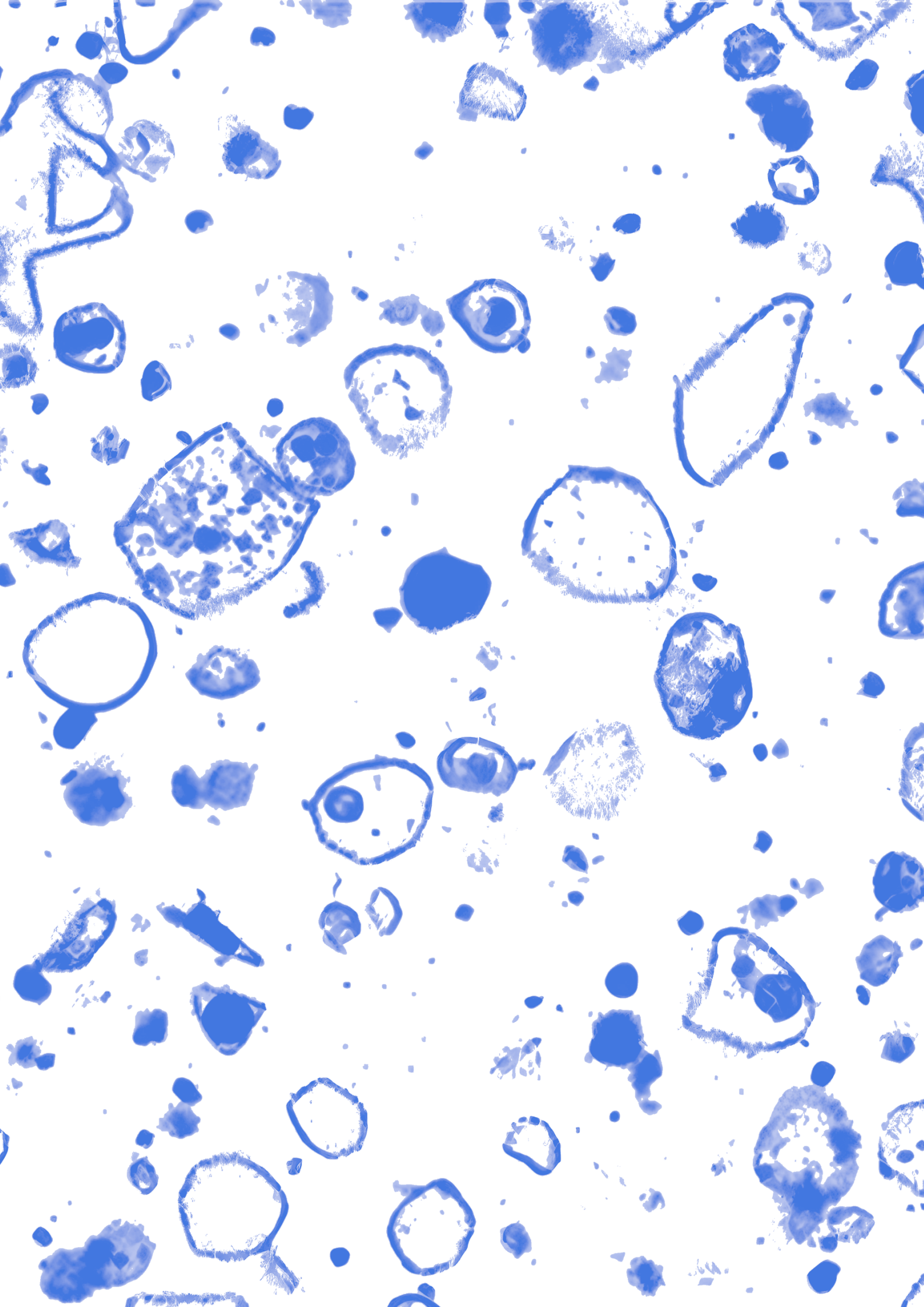

Chapter 8

Outlook

This dissertation presents the design and development of two innovative antimicrobial strategies, that show great promise for combating infections and the growing crisis of antibiotic-resistant pathogens. These strategies include the “Kill&Repel” coating and “Phagocytic Synthetic Cells” (PSCs). The former is a nanoscale surface coating that synergistically combines antifouling properties with the bio-orthogonal bactericidal activity of bacteriophages. This specific dual mode of action enables the eradication of bacterial pathogens while preserving the integrity of surrounding eukaryotic cells, thus offering a completely biocompatible antimicrobial approach. Additionally, it concurrently prevents the adhesion of bacterial debris and other cells from the surrounding environment to the surface. The cooperative mechanism of killing and repellency not only provides superior protection, mitigating the development of infections, but also maintains the activity and accessibility of the antimicrobial surface for an extended period during treatment. In developing this coating, two biohybrids consisting of the surface binding peptide LCI were synthesized. To achieve antifouling hybrids, CBMAA or HPMA polymer chains were grafted from the peptide by SET-LRP. Bactericidal hybrids were produced by the genetic fusion of the LCI peptide with a bacteriophage endolysin that cleaves the peptidoglycan layer of bacteria. The precise combination of these hybrids enabled the formation of the “Kill&Repel” coating on a wide array of polymeric and metallic medical devices driven solely through the physisorption of the hybrids from an aqueous solution onto the surface. This approach allowed for an easy application without the need for strenuous surface treatment steps or special machinery, under conditions that can be readily adjusted to clinical settings. Notably, the “Kill&Repel” coating displayed antifouling properties on par with the best grafting-from polymer brushes synthesized via the complex process of surface-induced SET-LRP. Moreover, it was highly effective against several multidrug-resistant bacterial pathogens, including *S. agalactiae*, *S. pyogenes*, *S. epidermidis* and *S. aureus*. Proof-of-concept experiments with wound dressings demonstrated the coating’s ability to successfully resolve a simulated infection and keep the surface clean from debris adhesion. Additionally, initial studies using 3D human skin models confirmed the outstanding biocompatibility and safety of the “Kill&Repel” coating, reinforcing its potential for infection management and wound healing. Future research on the “Kill&Repel” coating should include validation of its efficacy under more physiologically relevant conditions, for example using 3D infected tissue models of wounded skin or small animal models that resemble infected skin wounds. These models should allow for the

investigation of protection against biofilm formation, pathogenic clearance, assessing inflammatory response, and tissue regeneration. Additionally, future efforts should be dedicated to developing a next-generation “Kill&Repel” coating capable of targeting both Gram-positive and Gram-negative bacteria. The endolysins employed in this work induce bacterial death by degrading the peptidoglycan layer. Gram-positive bacteria lack an outer membrane, exposing their peptidoglycan layer directly to the cell exterior. This makes them susceptible to the action of endolysins. In contrast, Gram-negative bacteria have an outer membrane that contains LPS and serves as a robust barrier that limits the bactericidal activity of the endolysin. However, this challenge has recently been shown to be efficiently circumvented by protein engineering.[1-6] Endolysins have been successfully fused to a wide variety of outer membrane permeabilizing peptides, enabling them to permeabilize the membrane of Gram-negative bacteria and degrade their peptidoglycan layer. Some of these engineered lysins have already proven effective against *P. aeruginosa* and *Acinetobacter baumannii* in *in vivo* studies.[1-2] Therefore, they could provide a promising platform for the development of a new generation of advanced “Kill&Repel” coatings with a broad antibacterial activity.

The latter strategy presented in this dissertation, involved the developed of bioinspired PSCs. Similar to the professional phagocytes of our immune system, PSCs has been shown to engulf and subsequently neutralize pathogenic invaders while preserving the integrity of surrounding mammalian cells. These PSCs are formed by the self-assembly of iCPs in water. They exhibit a high degree of biomimicry, exerting membrane thickness, membrane flexibility and lateral diffusion similar to that of natural cells.[7-8] Empirical studies have shown that PSCs have a unique ability to accelerate engulfment, making them efficient at internalizing inanimate nano- and micron-sized objects as well as bacterial pathogens. This ability surpassed that of other cell mimics based on liposomes, polymersomes and dendrimersomes. It was discovered that their underlying mechanism for accelerated engulfment is attributed to their capacity to store elastic energy, which is released at the moment of contact, reducing kinetic barriers and driving the engulfment process. Additionally, the PSCs are shown to be equipped with a membrane-disrupting mechanism inspired by the antimicrobial activity of HDPs. This mechanism enabled the PSCs to efficiently eradicate contaminations of multidrug-resistant *P. aeruginosa* and *S. aureus*. Importantly, in preliminary biocompatibility experiments, it was observed that the PSCs did not induce toxic effects on kidney organoids. This suggests that

their bactericidal mechanism becomes activated only upon engulfment and the close apposition of the PSC's membrane with the bacterial membrane. Thus, engulfment and killing occur in a concerted manner, similar to phagocytosis in living cells. Although, the current PSCs are still in the early stages of development and there are still some mechanistic questions that need clarification, they validate the novel concept of "Artificial Phagocytosis" performed by synthetic cells devoid of complex cell machinery. Specially, their ability to perform accelerated engulfment is unprecedented in the field and is reported here for the first time. Future work should encompass basic research that integrates computational copolymer composition analysis and simulations, to gain deeper insights into the influence of iCP composition on the resulting membrane properties. Understanding these molecular design principles will enable the precise engineering of more advanced PSCs with augmented phagocytic abilities in the future. Moreover, it could help to shed light on how engulfment is controlled in biological membranes and understand the influence of membrane composition. Furthermore, future work may incorporate the concept of superselectivity[9-10] into "Artificial Phagocytosis". This advancement would not only allow for the selective scavenging of objects and pathogens but could also extend to the precise targeting of disease-causing cells, such as cancer cells, based on the surface density of specific receptors.[9-10] Superselectivity would enable controlled engulfment with a more precise targeting of specific pathogenic cells, reducing off-target interactions and contributing to an overall improved safety profile of the PSCs.

8.1 References

[1] Y. Briers, M. Walmagh, V. V. Puyenbroeck, A. Cornelissen, W. Cenens, A. Aertsen, H. Oliveira, J. Azeredo, G. Verween, J.-P. Pirnay, S. Miller, G. Volckaert, R. Lavigne, *mBio* **2014**, *5*, 10.1128/mbio.01379-01314.

[2] Y. Briers, R. Lavigne, *Future Microbiology* **2015**, *10*, 377-390.

[3] Y. Briers, M. Walmagh, B. Grymonprez, M. Biebl, J.-P. Pirnay, V. Defraine, J. Michiels, W. Cenens, A. Aertsen, S. Miller, R. Lavigne, *Antimicrobial Agents and Chemotherapy* **2014**, *58*, 3774-3784.

[4] H. Yang, M. Wang, J. Yu, H. Wei, *Frontiers in Microbiology* **2015**, *6*.

[5] H. Gerstmans, D. Grimon, D. Gutiérrez, C. Lood, A. Rodríguez, V. van Noort, J. Lammertyn, R. Lavigne, Y. Briers, *Science Advances* **2020**, *6*, eaaz1136.

[6] T. H. Jeong, H. W. Hong, M. S. Kim, M. Song, H. Myung, *Viruses* **2023**, *15*.

[7] K. Mitra, I. Ubarretxena-Belandia, T. Taguchi, G. Warren, D. M. Engelman, *Proceedings of the National Academy of Sciences* **2004**, *101*, 4083-4088.

[8] K. Jacobson, Y. Hou, Z. Derzko, J. Wojcieszyn, D. Organisciak, *Biochemistry* **1981**, *20*, 5268-5275.

[9] G. V. Dubacheva, T. Curk, R. P. Richter, *Accounts of Chemical Research* **2023**, *56*, 729-739.

[10] T. Curk, J. Dobnikar, D. Frenkel, in *Multivalency*, **2018**, pp. 75-101.